Cold Gas Dynamic Spraying of Titanium Coatings

Timothy Simon Price, MEng (Hons)

Thesis submitted to the University of Nottingham for the Degree of Doctor of Philosophy, May 2008

Abstract

Cold gas dynamic spraying, CGDS, is a relatively new technique used to deposit materials onto the surface of a substrate. It differs to the majority of other thermal spray techniques as the substrate and particles are not exposed to high temperatures during the spraying process. This makes CGDS particularly advantageous for spraying materials such as titanium which react at high temperature. The aim of this project was to investigate the potential use of titanium coatings by CGDS as a surface treatment for medical prostheses. Titanium powder was deposited onto Ti6Al4V substrate using helium gas at room temperature. Titanium coatings were also produced by a competing spray technique, shrouded arc spraying, to allow for a comparison of the two techniques to be made. Mechanical properties of the titanium coatings were measured and the influence of subsequent heat treating on the mechanical properties was also investigated. The coatings were characterised by investigating properties such as their bond strength, residual stress and stiffness, as well as the influence of the cold spray titanium coating on the fatigue life of a sprayed substrate. Scanning electron microscopy and optical microscopy techniques were also used to characterise the deposits. To further develop and optimise the CGDS process aluminium and copper coatings were also deposited and their mechanical properties compared to that of the titanium deposits. Additionally particle image velocimetry, PIV, was used to improve general understanding of the cold spray process and the effect that spray parameters have on the particle impact velocity.

In the case of fatigue endurance limit and despite a compressive residual stress state measured in the titanium CGDS coatings, a 15% reduction in fatigue endurance limit was observed following the application of a CGDS titanium coating to the as-received substrate, but no significant reduction was observed on its application to the grit blasted substrate. By four point bend testing it was observed that the ratio of the modulus of the titanium deposit to that of the corresponding bulk material (the modulus ratio) was 0.17, significantly below unity. For copper and aluminium, also deposited by cold spray, a modulus ratio of 0.41 and 0.16 was observed. The volume

fraction and aspect ratio of porosity in each deposit was measured by SEM. However, an Eshelby equivalent homogeneous inclusion model supplied with these data was not able to predict the low modulus ratios observed. Instead, imperfect inter-particle bonding within the deposit (akin to through-thickness cracks) is the source of the low modulus ratios, with the tenacious oxide on the titanium and aluminium powder particles being more effective at preventing oxide disruption and formation of metallurgical bonds between particles upon impact, hence the lower modulus ratio for these material types.

A method was developed to visually show the imperfect inter-particle bonding expected to be found within the CGDS deposits. Although porosity levels are low within cold spray deposits, individual particles are found to not be well bonded to each other which results in low coating moduli. By increasing the primary gas pressure in the cold spray process an increase in the degree of inter-particle bond formation occurred.

Heat treating of the titanium coating at 1150 °C was found to improve the bond strength of the coating but drastically reduced the fatigue endurance limit. The same heat treatment temperature was found to increase the modulus ratio of the coating to 0.36 and this is attributed to a greater level of inter-particle bonding within the titanium coating occurring by diffusion bonding. However a reduction in the fatigue endurance limit was observed. This is most likely due to phase changes of the Ti6Al4V substrate, the stress relaxation nature of heat treating and oxygen embrittlement occurring, despite an argon furnace used.

Diagnostic tools such as particle velocity measurements are also used to gain a further general understanding of the CGDS process. Particle velocity measurements were made for titanium and copper powders using helium and nitrogen gas and a range of spray parameters. Particles of less than 9 μm in diameter were found to have the slowest particle velocities for both the copper and titanium powders. For the titanium powder up to a 200 m s^{-1} variation was found between the smallest and largest sized particles. This knowledge may be used in the future to optimise the size

distribution of a powder feedstock prior to being used for cold spray deposition. Overall the titanium powder produced the highest particle velocities compared to the copper powder due to its lower density and therefore being easier to accelerate by the gas flow. A particle model was used to predict particle velocities. Generally the model predicted higher particle velocities then the maximum measured particle velocities and this is due to the model not taking into consideration of particles interacting with one another, the external walls of the nozzle, or the external atmosphere. These factors would all lead to particle deceleration.

In comparison to titanium coatings produced by the shrouded arc process, the titanium CGDS coatings performed admirably. The shrouded arc coatings had a considerably lower fatigue endurance limit, due to tensile residual stresses within the coating, forming as particles cool on impact. However, the shrouded arc coatings showed a higher modulus ratio of approximately 1/3, which is comparable to coatings produced by other thermal spray methods.

Acknowledgements

This research was funded by the Nottingham Innovative Manufacturing Research Centre (NIMRC) and the Engineering and Physical Sciences Research Council (EPSRC).

I would first like to thank my supervisors Professor Philip Shipway and Professor Graham McCartney for their invaluable support, advice and mentoring throughout the three years of my PhD. I would also like to thank Keith Dinsdale, Rory Screaton, Graham Malkinson and Deen Zhang for all the equipment training, their specialist knowledge, technical support and solving of many hands on issues. A further thank you is extended to Deen Zhang and Tiziana Marocco for the many hours spent with myself in the lab producing coatings.

I am also very grateful for the proof reading and encouragement given by Alice, Mum and my sister, Emily. Finally a thank you to the other postgraduates, staff and friends for their encouragement throughout my time at The University of Nottingham.

Contents

List of Figures

List of Tables

Abbreviations

3PB – Three Point Bending

4PB – Four Point Bending

AOM – Automated Optical Microscopy

Al – Aluminium

APS – Atmospheric Plasma Spray

AR – As-Received Surface Finish

BSE – Backscattered Electron Imaging

CFD – Computational Fluid Dynamics

CGDS – Cold Gas Dynamic Spray

Cu – Copper

CVD – Chemical Vapour Deposition

FOV – Field of View

GB – Grit Blasted Surface Finish

HA – Hydroxyapatite

HVOF – High Velocity Oxy-Fuel

LD – Laser Diffractometer

LDV – Laser Doppler Velocimetry

L2F – Laser Two-Focus Method

OM – Optical microscope

PIV – Particle Image Velocimetry

PMMA– Poly(methyl methacrylate)

PVD – Plasma Vapour Deposition

SA – Shrouded Arc

SE – Secondary Electron Imaging

SEM – Scanning Electron Microscope

SOD – Stand Off Distance

TEM – Transmission Electron Microscope

Ti – Titanium

TWA – Transferred Wire Arc

VPS – Vacuum Plasma Spray

WA – Wire Arc Spray

Nomenclature

A^* – Nozzle cross-sectional area at throat

A – Nozzle cross-sectional area

A_e – Nozzle exit cross-sectional area

A_p – Surface area of particle

A_{pixel} – Pixel area

a – Speed of sound of a fluid

a – Distance between loading rollers and support rollers

d – Sample thickness

d' – Spacing between planes in the atomic lattice

f – Porosity volume fraction

f_n – Normalised pore volume fraction

C – Micron per pixel ratio

C_C – Composite stiffness tensor

C_D – Drag coefficient

C_I – Inclusion stiffness

C_p – Specific heat of gas with constant pressure

C_M – Stiffness tensor of material

C_v – Specific heat of gas with constant volume

C_1 – Maximum composition content measured across a diffusion boundary

C_2 – Minimum composition content measured across a diffusion boundary

c_p – Specific heat of particle

D^* – Nozzle throat diameter

D – Diffusion coefficient

D_a – Particle diameter of equivalent circular area

D_e – Nozzle exit diameter

D_0 – Pre-exponential constant

d_{crit} – Particle critical diameter for deposition to occur

d_p – Particle diameter

E – Young's modulus of a uniform beam

E_c – Coating Young's modulus

E_s – Substrate Young's modulus

E_y – Beam Young's modulus as a function of position

E_{1C} – Transverse Young's modulus

E_{3C} – Axial Young's modulus

H – Enthalpy

H – Substrate thickness

h – Coating thickness

h_t – Heat transfer coefficient

I – Second moment of area

L – Distance between outer support rollers

Ma – Mach number

M – Moment generated within sample due to residual stress

m – Gradient of graph used to calculate residual stress by X-Ray diffractometry

$\dot{m}$ – Mass flow rate

m_p – Particle mass

N_f – Number of cycles to fatigue failure

Nu – Nusselt number

n – Number of moles

P – Applied load per loading point as shown by Figure 4.23

P_l – Force applied to give continuity of length

P^* – Gas pressure at the nozzle throat

P_0 – Stagnation gas pressure

P – Gas pressure

Q – Activation energy

Q – Amount of heat transfer

R – Radius of curvature of a sample associated with residual stress generation

R – Specific gas constant

R_a – Average surface roughness

Re – Reynolds number

S – Entropy

S – Eshelby 'S' tensor

S – Molecular speed ratio

T^* – Gas temperature at the nozzle throat

T_0 – Stagnation gas temperature

T – Temperature of the gas

T_i – Particle impact temperature

T_m – Particle melting temperature

T_p – Temperature of the particle

T_t – Gas temperature at the nozzle throat

t – Time

U – Internal energy of system

u^* – Gas velocity at the nozzle throat

u_c – Particle critical velocity

u_g – Gas velocity

u_p – Particle velocity

u_t – Gas velocity at the nozzle throat

V – Volume

v – Mid-point displacement

W – Work done by the system

w – Diffusion distance / Intermetallic thickness

w – Normal distribution

w – Width of modulus sample

w' – Equivalent width of coating with modulus E_s

X – A log normal random variable

x – Distance

y_1 – Distance between neutral axis and coating top surface

z – Distance from nozzle exit (Stand off distance)

γ – Adiabatic index

ε_a – Strain acting due to applied load

ε^C – Constrained strain

ε_c – Coating strain

ε_s – Substrate strain

ε^T – Transformation strain

θ – Angle between the incident ray and the scattering plane

θ – Mean of distribution

λ_g – Thermal conductivity of the gas

λ_p – Thermal conductivity of the particle

λ – X-Ray wavelength

μ_g – Dynamic viscosity

μ_x – Standard deviation of X

ρ^* – Gas density at the nozzle throat

ρ_0 – Stagnation gas density

ρ – Density

σ – Stress in beam

σ_a – Stress acting due to applied load

σ^b – Background stress which satisfies the stress balance

σ_c – Coating stress

σ_f – Maximum stress level of the final block of cycles where fatigue failure occurred

σ_I – Inclusion stress

σ_{pr} – Maximum stress level of the prior block of cycles where no fatigue failure occurred

σ_s – Substrate stress

σ_u – Particle ultimate strength

σ_x – Standard deviation of X

σ_{10^7} – Applied stress for fatigue failure to occur at 10^7 cycles

σ_φ – Specimen residual stress calculated by X-Ray diffractometry

υ – Poisson's ratio

ω – Standard deviation of a distribution

Chapter 1 – Introduction

1.1. Introduction

Surface coatings are utilised widely in engineering design and manufacture. Coatings may be applied to a component for a number of reasons including improvement of surface properties, such as wear resistance, and to provide protection to the main bulk of the component from the operating environment, for example corrosion resistance. Surface coatings are also used to improve aesthetic appearance and to reduce material costs. Reductions in material costs can be made if a low cost substrate is used for the main bulk of the component, such as steel or many metal alloys. Often the material chosen for the substrate is selected due to superior mechanical properties, but will not interact with the operating environment positively and will therefore require a coating to protect the main bulk of the component from the operating environment. There are different methods of surface coating and they differ in the manner in which the coatings are applied, thickness of coating, nature of bonding, materials coated and temperature during coating process.

The choice of the surface coating process used for a particular engineering application depends upon a number of requirements. Firstly, the coating-surface treatment should not impair the properties of the bulk material. For example, there is little point in applying a coating for corrosion protection if the fatigue or mechanical properties of the bulk material are adversely affected and these properties are also important. Secondly the deposition process must be capable of coating the component, in terms of both size and shape. One major disadvantage of all spray methods is that they are line of sight processes. Therefore complex geometries are often difficult to spray as great care must be taken in initial design stages to ensure that the component can be sprayed. In contrast, chemical vapour deposition (CVD) and electroless nickel plating are noted for their ability to coat complex shaped components with a layer of uniform thickness. Finally the surface treatments must be cost-effective, taking into account factors such as reduced downtime and improved product quality, in addition to the coating cost. For example, the improvement in surface finish, which occurs through the use of a coated tool, may give an additional

benefit in that a subsequent finishing operation may be omitted [1]. The decision to use a particular coating process therefore will depend upon the capabilities and limitations of the process and benefits versus cost analysis of the coating applied.

The biomedical industry uses coatings on prosthetic implants. All implants are considered as a foreign body to the surrounding living cells and body tissues. When considering a material to be used as a foreign body it is important to consider its biocompatibility. Biocompatibility is the ability of a material to perform with an appropriate response in a specific application [2]. For example, the prosthetic must not interact harmfully with the host's body. For load bearing applications the implant must meet or exceed the mechanical properties of bone. The mechanical properties of bone vary greatly depending on age and location within the body but its stiffness has been found to vary from between 14 – 20 GPa with a tensile load applied. During bending the stiffness can reduce to as low as 5.4 GPa [3]. Whilst materials such as polymers and composite more closely resemble the properties of bone only metals are suitable materials for load bearing implants due to their higher strength. Currently many implants are produced from cobalt chrome and titanium alloys (e.g. Ti6Al4V). These materials are chosen due to having a relatively low stiffness (compared to other metals), high mechanical strength and commercial availability. To improve the biocompatibility of the implant the surface properties are modified, by applying a coating, to increase the level of tissue interaction and bone attachment.

Fixation of the majority of prosthetic implants in the past has been performed using bone cement such as poly(methyl methacrylate), PMMA. Bone cement is able to conform to the shape of its surroundings before self curing. It acts as cement between the bone and implant and allows even distribution of any loads between implant and bone [4]. However, bone cement is sometimes not favoured due to poor bonding between bone and cement sometimes being observed. Wear particles, originating from the acetabular cup, may then build up between the bone and prosthetic, causing inflammatory reactions. These shortfalls often lead to aseptic loosening or as a worst case scenario prosthetic failure [5]. To prevent prosthetic failure revision surgery is routinely required and in 1995 18% of the 40,000 hip replacement operations performed in the UK were revision surgery due to aseptic

loosening occurring [5]. Alternatives to bone cement are hydroxyapatite, HA, and other calcium phosphate coatings which allow a direct chemical bond between the coating and bone to occur, leading to decreased healing times and increase of the longevity of the prosthetic [4, 6-9]. As life expectancies increase the life spans of the implants are too short and replacement surgery is routinely required; also a greater number of organs, joints and other critical body parts are being replaced by artificial implants to maintain a good quality of life. Implants are expected to deliver greater levels of comfort and increased life spans as on going improvement continues, and so the prosthetic implant market is growing rapidly [10].

As an alternative to HA and other calcium phosphate coatings, pure titanium is also regarded to have a high level of biocompatibility, low levels of toxicity and high resistance to corrosion by body fluids. The reason for this is due to the presence of a protective oxide layer. This oxide layer is regarded to be self-protecting and is quickly re-established after being locally destroyed, for example by mechanical action [10]. However the fatigue and yield strength of pure titanium makes it unsuitable for use as the bulk material for implants and therefore can only be used as a surface coating.

Spraying of pure titanium as a surface coating can be applied using current thermal surface coating technologies (for example, high velocity oxy fuel spraying, HVOF, and plasma spraying). However in these processes the pure titanium powder is heated to a semi-molten state and propelled towards the substrate to be coated. By heating the pure titanium, oxidation can readily occur which will affect its final properties. To prevent this from occurring, inert atmospheres (i.e. vacuum or low pressure plasma spray) must be employed. This greatly increases the cost and reduces the flexibility of coating application. Another problem is the creation of residual stresses within the coating after it has been applied due to the coating and substrate cooling at different rates. This causes the coating to contract after spraying and tensile residual stresses will form at the coating top surface. Tensile residual stresses at the surface are generally regarded as unwanted due to aiding crack growth and therefore, reducing the fatigue life of the component.

Cold gas dynamic spraying, CGDS, is a relatively new spray technique. This process is potentially attractive compared with the current manufacturing methods due to the fact that no significant heating of the titanium powder is required, eliminating the problem of oxidation and possibly reducing residual stresses within the deposit. Titanium powder particles in the CGDS process are typically accelerated to speeds in excess of 600 m s^{-1}. On impact with the substrate the particles plastically deform, bond together and form a mechanical bond to the substrate. This project seeks to investigate optimisation of the CGDS process for deposition of titanium onto a Ti6Al4V substrate by examination of mechanical properties and microstructural characterisation of titanium deposits produced. Diagnostic tools such as modelling and particle velocity measurements are also made to gain a further general understanding of the CGDS process.

This chapter provides a brief introduction as to why titanium is inherently biocompatible, why HA is currently used and finally the case for using titanium as an alternative to HA and calcium phosphate coatings. Chapter two describes the spray methods commonly used to deposit titanium as well as cold spraying. Chapter three considers particle velocity measurement in cold spray and its important role in determining if bonding occurs. Finally chapter four characterises the titanium coating produced during this project both mechanically and microstructurally.

1.2. Titanium in Medicine

The mechanical properties of titanium make it suitable for medical applications, including its high strength to weight ratio and low Young's modulus. Titanium alloys, such as Ti6Al4V, have even better strength to weight ratios than pure titanium, and since the late 1960s it has become the most popular implant material [11]. Ti6Al4V is a dual phase ($\alpha+\beta$ phases) alloy. The alloying additions, the relative grain size of the α and β phases and heat treatment conditions rates are the reasons why the Ti6Al4V alloy has a much higher ultimate tensile stress than pure titanium shown in Table 1.1 [12].

	Density / kg m^{-3}	Young's Modulus / GPa	Yield Strength / MPa	Ultimate Tensile Strength / MPa
Titanium	4500	120	170	240
Ti6Al4V	4400	115	800-900	900-1000

Table 1.1 – Material properties of titanium and Ti6Al4V [13].

It is the surface properties of titanium that allow it to be a suitable candidate as a highly regarded biocompatible material. Titanium oxidises within nanoseconds in a variety of media [see 14]. The oxidised surface layer consists of predominantly TiO_2, the most stable titanium oxide [14]. The oxide film grows due to oxygen ions migrating towards the metal where they react at the base of the oxide layer, the metal-oxide interface [15]. It is this oxide layer that provides titanium with superior corrosion resistant properties compared to most other metals. Figure 1.1 shows a schematic of *in vivo* corrosion resistance versus tissue reaction for various metals. Figure 1.1 shows that metals of similar corrosion resistance (for example cobalt chrome and titanium) do not necessarily offer the same level of tissue reaction. Cobalt chrome has a less favourable tissue reaction compared to titanium due to the effect of the toxic nickel and cobalt. Similarly Ti6Al4V shows a slightly poorer tissue reaction compared to titanium, due to the low levels of vanadium that have high toxicity and are able to produce a prominent foreign body reaction [15].

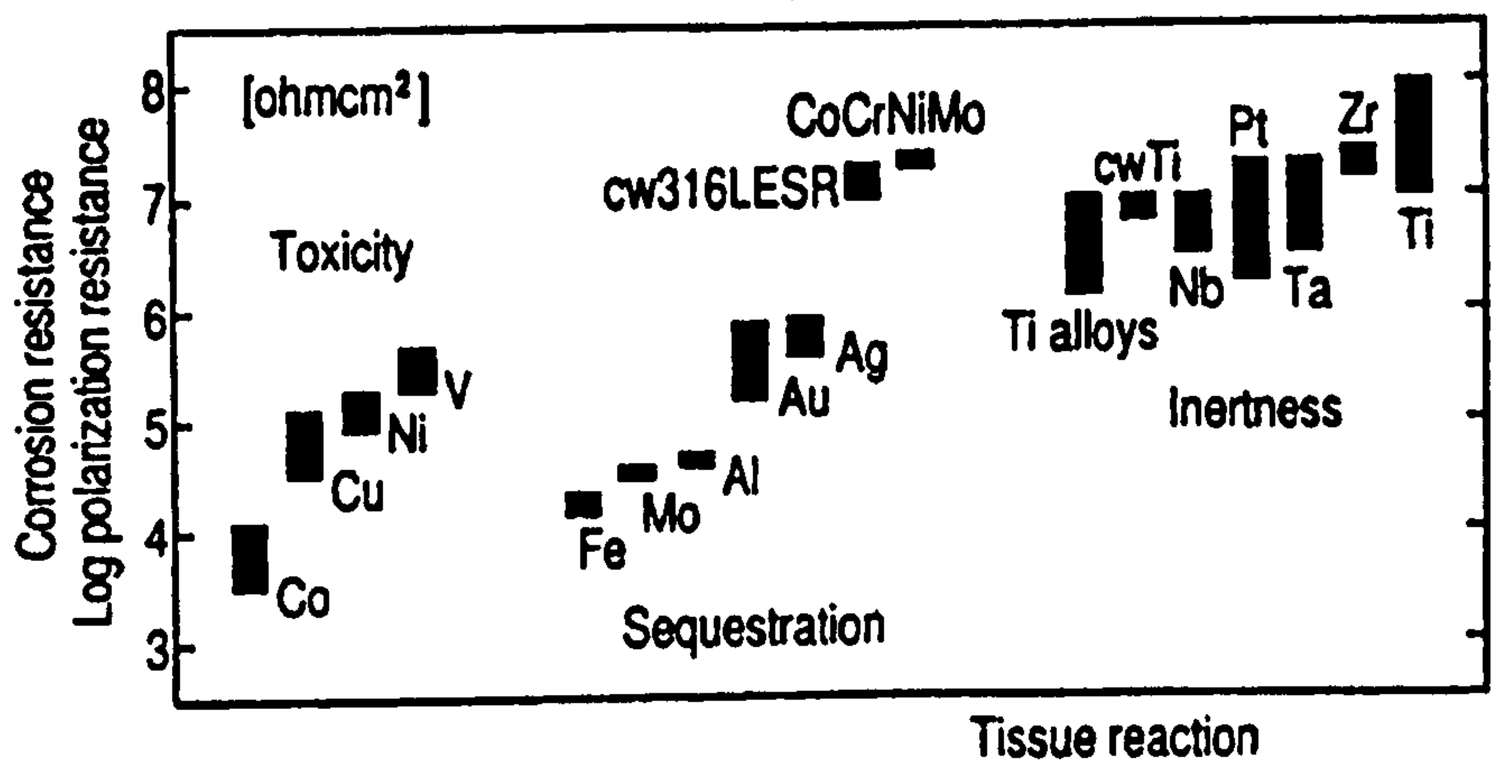

Figure 1.1 - Corrosion resistance versus tissue reaction of various metals. Those materials to the left of the figure are regarded as toxic whereas those to the right are regarded as bio-inert [15].

Steinemann [15] also presented work concerning the effect of metals in close proximity to fibroblast and osteoblast cells. Fibroblast cells give rise to connective

tissue whereas osteoblast cells are required to help bone formation. A range of metals were tested including copper, vanadium, aluminium and titanium. It was found that copper and vanadium were toxic to fibroblast cell growth and corroding molybdenum strongly reduces the cell proliferation rate. Only the titanium and zirconium metal discs showed little or no growth inhibition for both fibroblast and osteoblast cells. This suggests that only these two metals have the capacity for osseointegration to occur (the direct attachment of tissue to the implant surface).

1.3. Hydroxyapatite

Hydroxyapatite, HA, is a synthetic material that is able to promote bone growth without the need for bone cement. It bonds directly to bone with greater fixation strength than PMMA and in a smaller time scale thus reducing the required healing time [16]. HA is mechanically bonded to the implant and currently, the only clinically approved method to apply the coating is by plasma spraying. Plasma spraying is also advantageous because of its simplicity and high deposition rates [17]. The plasma spray process projects heated calcium phosphate particles at high velocity in a gas stream onto the implant to build up the coating. The thickness of the coating typically ranges from 50-75 μm. The temperature of the plasma flame is normally up to 10000 K [10]. Some of this heat energy is distributed to the accelerated particles and the fact that the substrate is in close proximity to the gun can lead to heating of the substrate that could affect its microstructure and ultimately its mechanical strength. The plasma spray process can occur in atmospheric (APS) or vacuum conditions (VPS). Other novel techniques for the application of HA coatings include chemical vapour deposition, dip coating and pulsed laser deposition [9]. These techniques offer advantages over plasma spraying due to greater control over the final chemical composition of the coating and minimisation of defects within the coating.

An ideal HA coating requires strong cohesive strength, good adhesion to the substrate, a high degree of crystallinity and high chemical purity and phase stability [18]. A porous and rough coating surface will allow bone growth to occur more readily between the stem and bone and improve the bonding strength further [9, 19,

20]. HA coatings are required to have a tensile strength of 50.8 MPa and a shear strength greater than 22.2 MPa [9, 21]. No criterion is set for the stiffness of the HA coating [21].

The plasma spray technique normally used to apply HA coatings does not permit accurate control of the chemical composition, crystallographic structure and crystallinity of the coating. As a result, the HA coating can be mechanically and chemically unstable [22] and the HA coatings' consistency and reliability is sometimes questioned [17]. The brittle nature of HA coatings leads to concerns of coating failure and research to optimise coating and spray parameters is ongoing [23]. Nevertheless HA coatings have been successfully used in many biomedical situations and successfully help improve substrate-bone bonding [24].

It is universally agreed that HA does increase speed, strength and amount of bony attachment to an implant in the early stages of fixation especially in regions of an implant which is not in press contact with the bone. These areas require HA to allow bony growth to bridge the gap between implant and bone which otherwise would not be possible. However there may be other factors that help long term implant survival such as optimised implant design, loading conditions and most critically surface roughness [7, 16, 25-35]. There are two main methods of surface modification; modification of the surface texture and chemical modifications, usually by application of a coating. The aim of texture modifications, such as pores or patterns, is to improve mechanical interlocking between bone and titanium implant.

Many studies have compared the biocompatibility of different surface roughness of titanium surfaces with HA coatings [26, 27, 33-35]. Generally, results found a higher amount of bone fixation immediately after insertion (< 4 weeks) for HA coated implants. However after longer periods of time similar amounts of bone fixation were found when comparing HA and non-HA coated implants. Those implants that were not HA coated were found to perform best if a rough surface finish was employed. This highlights the importance of HA during the early stages of bone fixation. However over time it appears a non-HA implant may offer similar levels of fixation.

Of particular note is the work carried out by Hacking et al. [33]. Tests were carried out on canine femoral implants. Four types of implant were used for the study with different average surface roughness values (R_a). The average surface roughness refers to the mean height of the valleys and peaks of the surface profile and therefore it is possible for surfaces of differing surface profile to have identical Ra values. Alternatives to characterising a samples surface include determining the maximum and minimum peak and valley heights of the surface, the waviness or pitch of the profile and the number of peaks within the sample. Nevertheless R_a is used routinely to characterise surface profiles. The four types of implant in the study were, i) polished surface, R_a = 0.09μm, ii) grit blasted surface, R_a = 3.64μm, iii) HA coated, R_a = 5.58μm and iv) HA coated and masked with titanium, R_a = 5.58μm. The HA coating was applied by plasma spraying. For the final type of implant a plasma vapour deposition, PVD, technique was used to apply the dense, homogeneous and thin (<100nm) titanium mask. The surface topographies of the HA coated and HA and titanium masked implants were shown to be near identical and allowed the role of the HA surface topography to be investigated without the benefits of the HA itself. Results after 12 weeks insertion found the polished and grit blasted surfaces to have the lowest bone apposition of 3% and 23% respectively compared to the highest bone apposition of 74% for the HA coated implant. The HA coated implant with the titanium mask showed bone apposition of 59%. This is significantly higher than the 3% bone apposition of the polished surface. Although the HA coated implant showed statistically significantly higher bone apposition compared to the HA coated and titanium masked implant, the role of the surface topography can not be disputed [33].

The specific surface topography required to influence bone apposition is unknown. Although Hacking et al. [33] quantify the sizes of peaks and valleys, by calculating roughness average values (R_a), between the different implants, it could also be other unknown factors that are influencing the level of bone apposition. For example characteristics of as yet undefined individual features such as their spatial distribution or radii curvature could be significant. Other factors may also be responsible such as total surface area and relative plane of implant surface compared to the bone.

Greater research into the role of surface topography on implant fixation is required and the search for new prosthetic surfaces is justified. CGDS inherently leaves a rough surface and it has therefore been identified as a potential method for the application of pure titanium coatings or titanium-HA coatings which may prove very desirable in terms of biocompatibility [36].

Chapter 2 – Spray Methods

2.1. Introduction

This chapter will give a brief introduction of the spray methods routinely used to deposit titanium coatings. All thermal spray methods operate on the same basic principle of providing the coating particles with sufficient kinetic and thermal energy so that when they impact the substrate they will form a bond. As subsequent particles impact the substrate these will also deform and bond to the previously deposited splats. This creates a slow build up of the coating, typically up to 100 – 1000 μm thick. The major disadvantage of all spray methods is that they are line of sight processes. Therefore complex geometries are often difficult to spray as great care must be taken in initial design stages to ensure that the component can be sprayed. By heating the particles, semi-molten droplets can form and this makes it easier for the particles to deform when impacting the substrate. It is expected that a molten particle hitting a surface with sufficient kinetic energy is deformed into a disc like splat with an enlarged diameter of 2.5 times the original particle diameter or more. At the same time the disc thickness is reduced to $1/5^{th}$ or less of the original particle diameter. The exact deformation depends on the velocity and temperature of the particles at the point of their impact [14].

Cold gas dynamic spraying, CGDS, differs from thermal spray processes in that the particles are sprayed at much lower temperatures, typically in the range from room temperature to 500 °C. This coating process relies on achieving much higher velocities, compared to thermal spray techniques, to create a well bonded and cohesive coating.

Figure 2.1 shows the variation in gas temperature and particle velocities between some of the main spray processes. Despite the different gas temperature and particle velocities a number of these processes are suitable for creating titanium coatings. This chapter will concentrate on describing the spray processes identified in Figure 2.1 that are capable of spraying titanium; namely, high velocity oxy fuel (HVOF), vacuum plasma spray, shrouded arc spraying, (a derivative of wire arc spraying), and CGDS.

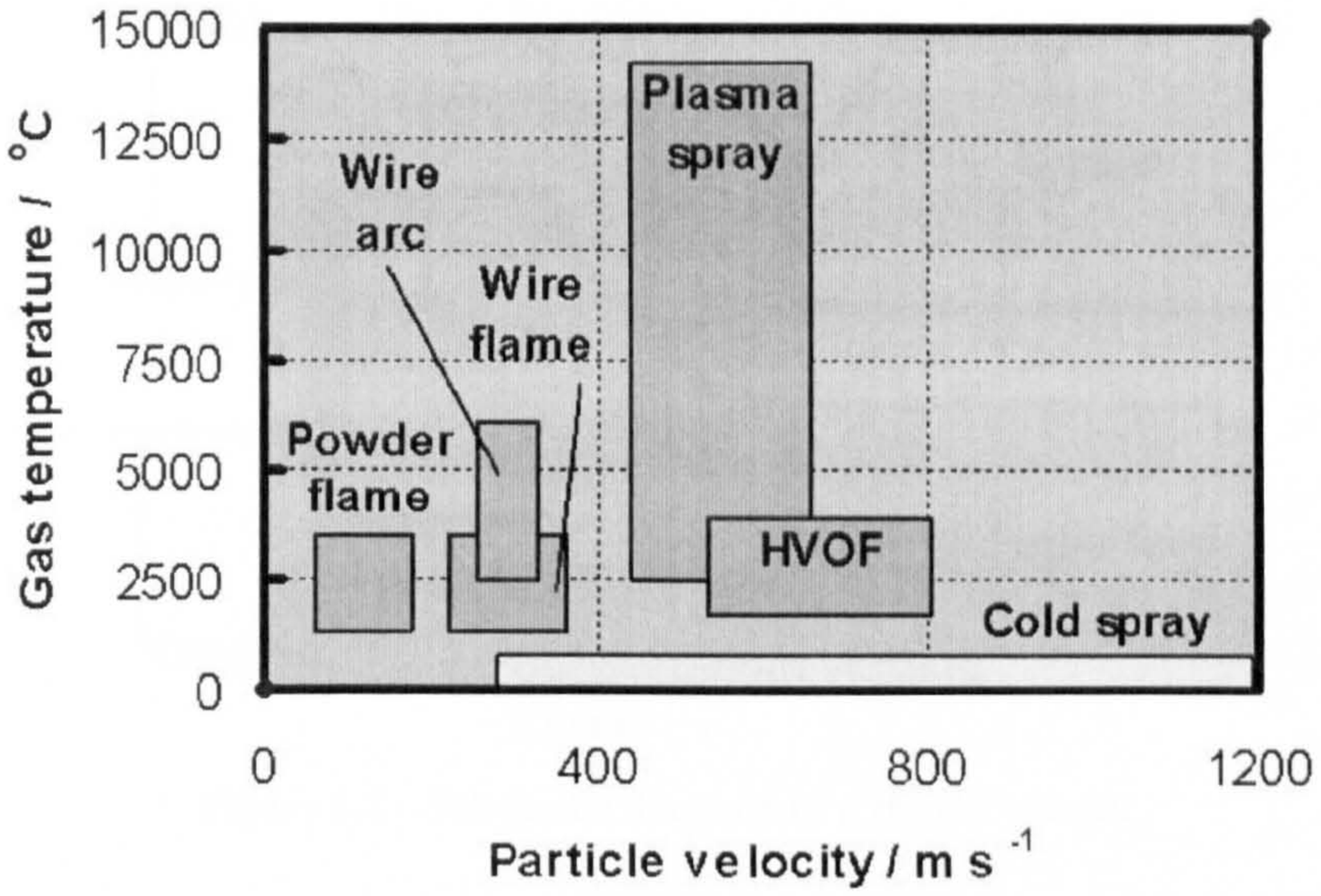

Figure 2.1 – Schematic illustration of the ranges of gas temperatures and particle velocities of the main spray processes [37].

2.2. High Velocity Oxy Fuel, HVOF, Spraying

HVOF processes and its variants have some of the highest particle velocities of all thermal spray processes. A specially designed nozzle and combustion chamber accelerates the particles to supersonic velocities within the nozzle. Figure 2.2 shows a schematic of a HVOF nozzle. The two main variants are differentiated by whether they use liquid (HVOLF) or gas fuel (HVOGF). Particle velocities are greater in a liquid fuel gun compared to a gas fuel gun and therefore result in denser, lower porosity coating structures [38].

HVOF has been successfully used for spraying titanium despite the high temperatures involved and the consequent oxidation of the powder during spraying [39, 40]. Spraying of titanium is possible at atmospheric conditions due to the high particle velocities, typically 650 m s^{-1}, and therefore the particles are exposed to the high temperature for only a short period of time and so their temperature remains relatively low.

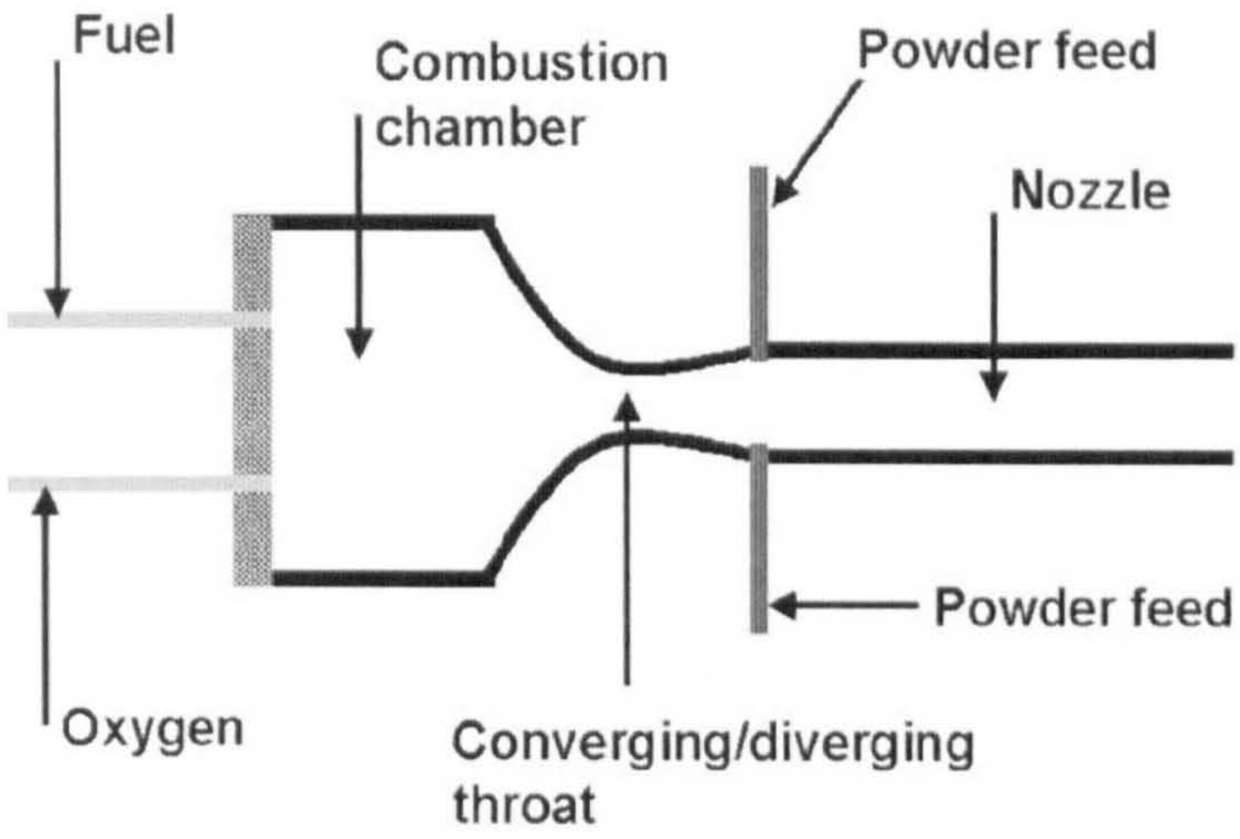

Figure 2.2 – Schematic diagram of a HVOF nozzle.

2.3. Vacuum Plasma Spray, VPS

VPS originally derives from air plasma spraying (APS) but is carried out in a low pressure or inert atmosphere. This eliminates the detrimental oxidation effect seen during HVOF spraying but at increased cost and reduced process flexibility.

During VPS the powder particles gain their thermal and kinetic energy from a plasma jet. Particle temperatures are significantly higher than those developed in HVOF but particle velocities are significantly lower. Figure 2.3 shows typical temperatures and velocities gained within a plasma spray system. VPS is routinely used for spraying titanium, including for biomedical applications [14].

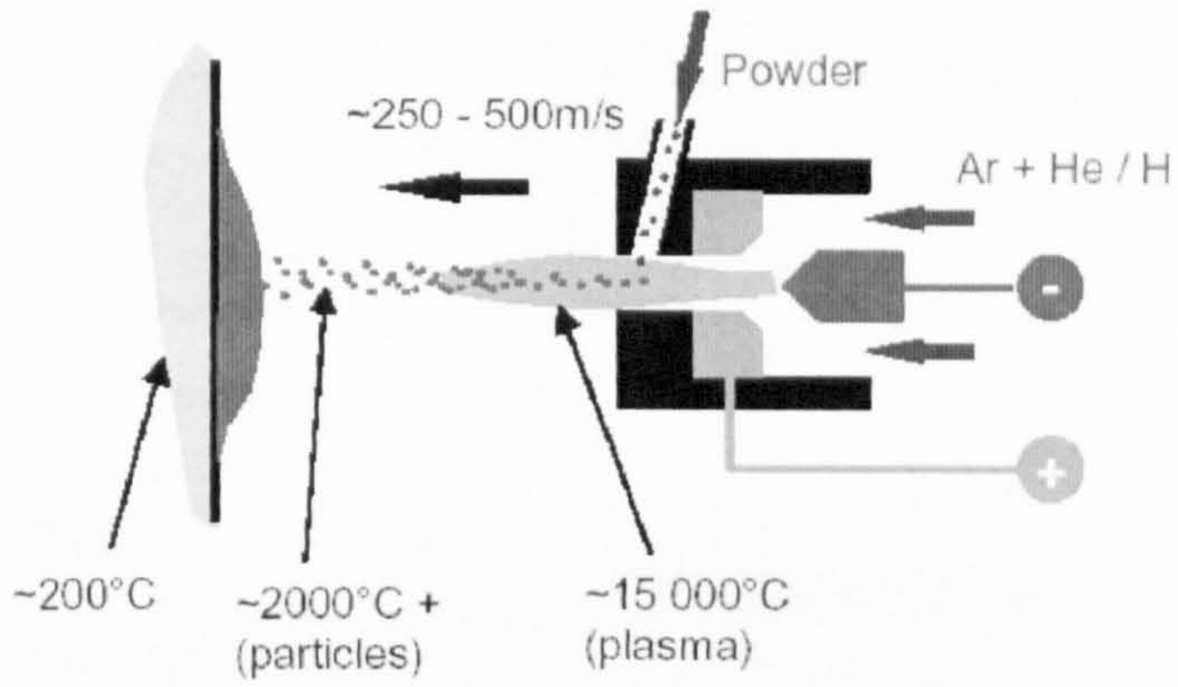

Figure 2.3 – Schematic diagram of the VPS system.

2.4. Shrouded Arc, SA, Spraying

Shrouded arc spraying is a derivative of wire arc spraying. A direct current, DC, electric arc is struck between two consumable wire electrodes and form the spray material. The material is atomised into fine droplets by a compressed gas and propelled towards the substrate. By using an inert gas as a shroud between the nozzle and substrate, oxidation effects can be minimised and deposition efficiencies are improved but at increased cost.

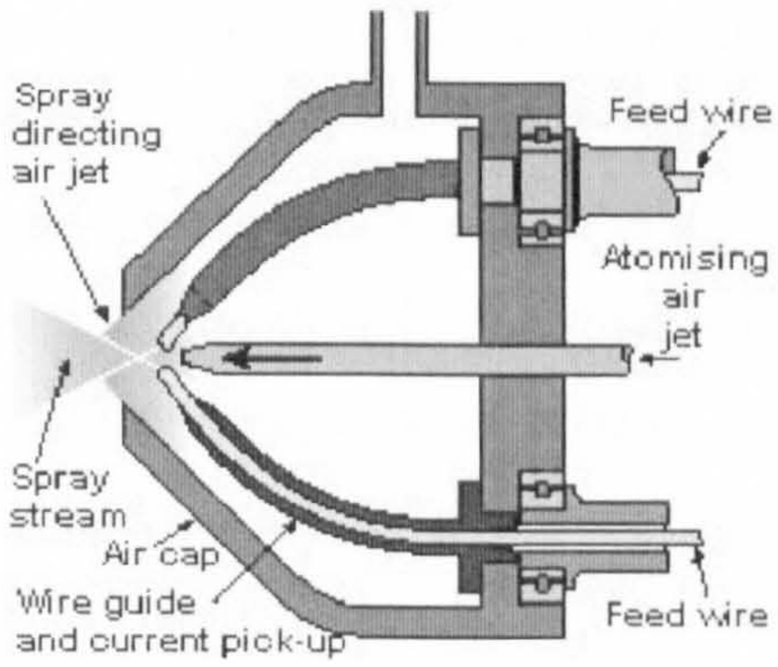

Figure 2.4 – Schematic diagram of the shrouded arc spraying equipment [41].

2.5. Cold Gas Dynamic Spraying, CGDS

CGDS is a relatively new process. It was developed in the mid-1980s at the Institute of Theoretical and Applied Mechanics of the Siberian Division of the Russian Academy of Science in Novorsibirsk while performing supersonic wind tunnel tests [42]. The CGDS process uses a specifically designed gun, a converging-diverging nozzle, termed a de Laval nozzle. A schematic of a cold spray nozzle is shown in Figure 2.5. The area of the nozzle between the converging and diverging sections is termed the throat.

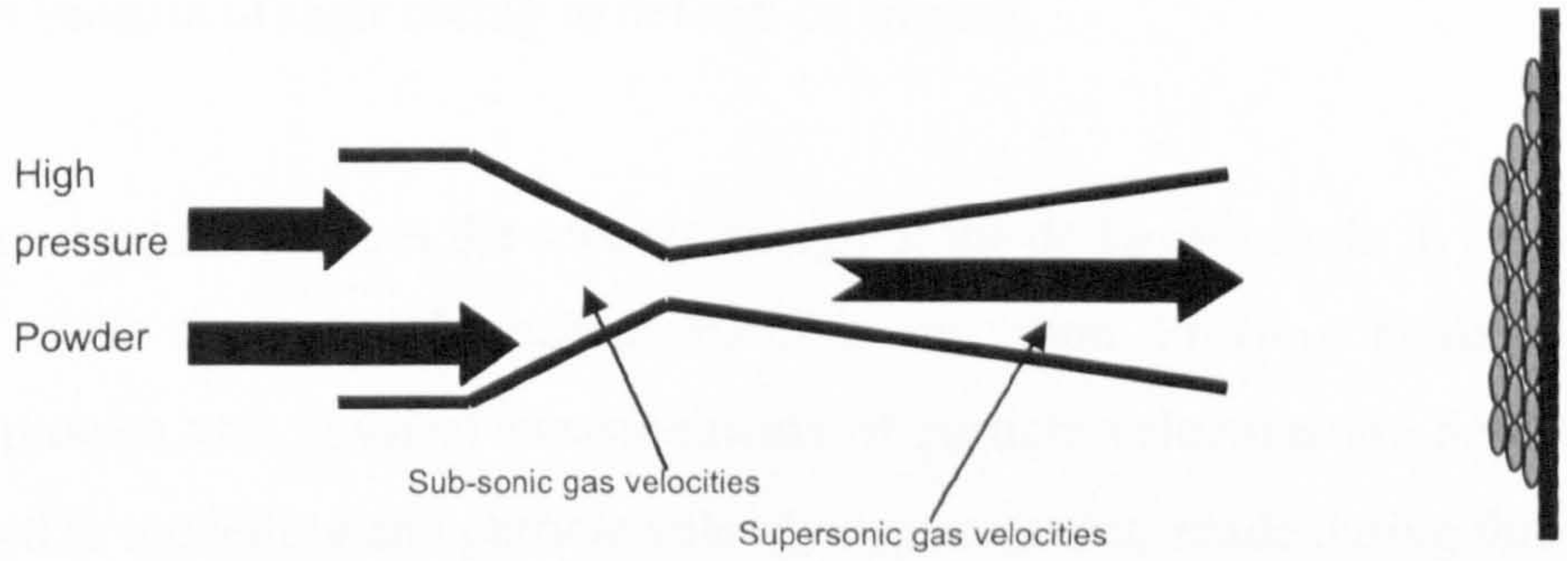

Figure 2.5 – Schematic diagram of the CGDS de-Laval nozzle.

High pressure gas (generally up to 30 bar [42]) is fed into the rear of the de Laval nozzle. The powder particles are fed by a high pressure powder feeder into the back of the nozzle before the throat. It is expected that the gas reaches sonic conditions at the throat. Within the diverging section of the nozzle the gas continues to accelerate to supersonic velocities. As particles pass along the nozzle, they gain kinetic energy from the supersonic gas and this allows them to be accelerated by the gas. Higher gas and particle velocities can occur if the gas is heated typically to 500 K prior to entering the de Laval nozzle. In contrast to thermal spray processes, the particles remain solid during the whole process [43]. This is highly advantageous as the phase makeup of the spray powder is not affected and it prevents unwanted effects, such as oxidation, from occurring. A substrate is placed at a typical stand off distance of between 5 and 40 mm from the nozzle exit. A further advantage of CGDS is that due to minimal heating, the substrate experiences little or no temperature variation and therefore its mechanical properties are not affected.

For bonding between the substrate and particles to occur, the particle impact velocity is required to exceed a critical velocity. The critical velocity is determined by a number of factors such as particle type and size. Critical particle velocities of Cu, Fe, Ni, Al and Ti has been experimentally measured to be approximately 540-580, 620-640, 630-690, 660-700 and 680-750 m s^{-1} respectively [44-48]. If the particle impact velocity is less than the critical velocity there is insufficient kinetic energy for bonding to occur. Instead, the particles will either rebound or erode the substrate surface similar to a sand blasting process [43, 47, 49-52]. The more the particle impact velocity exceeds the critical velocity the greater the likelihood and the stronger the bond formed within the coating and between the substrate and coating itself. Materials that are suitable for cold spraying include copper, aluminium and titanium because of their ability to deform on impact.

The next chapter describes the specific design of the de Laval nozzle in greater detail as well as the concept and mechanisms of its operation. Previous modelling of the CGDS process and physical measurements of particle velocities are described and compared to modelling and particle velocity measurements made during this project.

Chapter 3 – Gas Flow and Particle Velocity in Cold Spraying

3.1. Introduction

As described previously cold spraying involves the use of a converging-diverging nozzle referred to as a de Laval nozzle. The role of the nozzle is to generate supersonic gas flow and allow particle injection. If particles are accelerated to an impact velocity greater than a critical velocity this allows particle bonding and coating build up to occur. The greater the particle impact velocity and mass, and therefore the greater the kinetic energy, the denser the coating and the greater the level of bonding between splats is expected to be. This generally leads to an increase in the strength of particle to particle bonding and therefore improves the coatings' mechanical properties. The other important criterion to be considered is the deposition efficiency. The deposition efficiency is defined as the ratio of the weight of the deposited coating (the weight gain of the substrate prior to spraying) to the weight of the powder incident to the surface. Evidently, to achieve a viable process the deposition efficiency must be as large as possible and this is accomplished by the correct choice of powder size distribution, process parameters and nozzle design, to achieve the desired particle velocity. Examples of typical deposition efficiencies observed in cold spraying are described in Section 4.3.

The effect of particle size distribution, nozzle design and spray parameters, such as gas pressure and temperature, on particle velocity can be investigated both experimentally and theoretically through process modelling [47, 53-57]. One dimensional and more complex two and three dimension modelling techniques (computational fluid dynamics) are commonly used to predict expected particle velocities along the length of the nozzle, the nozzle exit, and just prior to impact with the substrate. The present chapter will review fundamental concepts of compressible gas flow and particle acceleration relevant to cold spraying. Also reviewed will be modelling work, predicted and measured particle impact velocities carried out by other workers. The experimental work undertaken in the present project will then be discussed in detail and results reported. Part of the present work involved

modification of a one dimensional isentropic model and the modelling carried out will be described. The isentropic model assumes that the gas flow is frictionless, occurs without loss or gain of heat and that external forces acting on the gas flow are negligible. The limitations of the model are discussed in further sections. Finally a discussion section will consider the results and where relevant compare measured and modelled results.

3.2. Fundamental Principles of Compressible Flow

This section describes the key equations used for describing the gas dynamics expected within a de Laval nozzle and is based on the application of fundamental flow equations presented by Oosthuizen and Carscallen in the text book "Compressible Fluid Flow" [58]. Within this section only the key equations are shown with their full derivation available in Appendix 1. Section 3.5.2. considers the key process parameters and their predicted effect on coating deposition.

A de Laval nozzle consists of converging and diverging sections. The smallest area section of the nozzle is called the throat. The de Laval nozzle operates because gases are highly compressible fluids. The flow is accelerated or decelerated by changing flow areas and compressing the gas. As the gas passes through the throat it is compressed sufficiently so that it will reach sonic velocity (Mach number equal to one). The gas continues through the throat and accelerates and within the first third of the divergent section 90% of the gas acceleration is expected to occur [59]. As the gas accelerates, the temperature and pressure decrease from their original stagnation values. The ratio of exit area to throat area is approximately 8-10 for sufficient supersonic gas velocities to be reached in the diverging section of the nozzle for deposition to occur. This section highlights the main equations used to carry out modelling of the gas characteristics along the length of a nozzle (pressure, temperature, density, velocity), referred to as the gas model, and is then used to model the particle characteristics as it travels within the gas flow.

3.2.1. Compressible Fluid Flow within the de Laval Nozzle

Gas flow within the de Laval nozzle can be modelled if a number of assumptions are made. These are:

i) The gas flow whilst within the nozzle is assumed to be one dimensional. Therefore the gas flow properties (pressure, temperature and velocity) will vary only along one dimension, x, parallel to the nozzle axis (i.e. p=p(x), T=T(x) etc).

ii) The gas flow is assumed to be continuous, i.e. the motion of individual molecules does not have to be considered. This is valid under most conditions, except under conditions of low pressure or a vacuum.

iii) It is assumed that flow properties are uniform across any given cross section area of the nozzle, and therefore the gas flow is isentropic (adiabatic and frictionless).

iv) No chemical changes occur in the flow.

v) Gravitational effects on the gas flow are negligible.

vi) The gas is approximated as a perfect gas with constant specific heat.

vii) It is assumed that external forces are negligible. These include frictional forces within the gas flow and the boundary layer between the nozzle wall and the gas flow.

The analysis of compressible fluids also relies on the principles of conservation of mass, momentum and energy to the flow. Once the gas properties within the nozzle are known, it is possible to calculate its effect on the momentum of a particle passing through the gas flow within the nozzle as shown in Section 3.3.

3.2.2. Isentropic State Relationships

The isentropic state relationships (equation 3.1 and A44) show how the temperature, T, pressure, P, density, ρ, and speed of sound, a, of a fluid passing through the de

Laval nozzle between any two points (x_1 and x_2) are related. γ is the adiabatic index of the fluids (the ratio of specific heats).

$$\frac{a_2}{a_1} = \left(\frac{T_2}{T_1}\right)^{\frac{1}{2}} = \left(\frac{\rho_2}{\rho_1}\right)^{\frac{\gamma-1}{2}} = \left(\frac{P_2}{P_1}\right)^{\frac{\gamma-1}{2\gamma}} \qquad \text{(Eq. 3.1)}$$

By considering energy conservation between any two points within a de Laval nozzle it is possible to find the temperature, pressure and density of the fluid in the gas flow in terms of the corresponding Mach number (*Ma*) of the gas as shown by equations 3.2 to 3.4 (Equations A47 and A48):

$$\frac{T_2}{T_1} = \frac{1+\frac{1}{2}(\gamma-1)Ma_1^2}{1+\frac{1}{2}(\gamma-1)Ma_2^2} \qquad \text{(Eq. 3.2)}$$

$$\frac{P_2}{P_1} = \left[\frac{1+\frac{1}{2}(\gamma-1)Ma_1^2}{1+\frac{1}{2}(\gamma-1)Ma_2^2}\right]^{\frac{\gamma}{\gamma-1}} \qquad \text{(Eq. 3.3)}$$

$$\frac{\rho_2}{\rho_1} = \left[\frac{1+\frac{1}{2}(\gamma-1)Ma_1^2}{1+\frac{1}{2}(\gamma-1)Ma_2^2}\right]^{\frac{1}{\gamma-1}} \qquad \text{(Eq. 3.4)}$$

3.2.3. Relationship between Critical and Stagnation Conditions

Critical conditions within a de Laval nozzle occur at the throat where the gas is expected to reach sonic velocities. Stagnation conditions exist isentropically when the flow is brought to rest, i.e. no gain or loss of heat. A large reservoir of gas can be considered as possessing stagnation conditions. Critical and stagnation conditions are denoted with the superscript * and subscript $_0$ respectively. By setting Ma_1 equal to zero (stagnation conditions) and Ma_2 to one (critical conditions at throat) in equations 3.2 the relationships between stagnation and critical conditions are generated as shown by equation 3.5. Equation 3.5 (Equations A53 to A56) show the

relationships between stagnation and critical conditions of the temperature, speed of sound of the fluid, pressure and density.

$$\frac{T^*}{T_0} = \frac{2}{\gamma+1} \text{ and } \frac{a^*}{a_0} = \sqrt{\frac{2}{\gamma+1}} \text{ and } \frac{P^*}{P_0} = \left(\frac{2}{\gamma+1}\right)^{\frac{\gamma}{\gamma-1}} \text{ and } \frac{\rho^*}{\rho_0} = \left(\frac{2}{\gamma+1}\right)^{\frac{1}{\gamma-1}} \quad \text{(Eq. 3.5)}$$

3.2.4. Variable Area Flow

Equation 3.6 (Equation A60) shows the relationship between velocity change of the fluid and area change in an isentropic duct flow.

$$\frac{du_g}{u_g} = \frac{dA}{A}\frac{1}{Ma^2-1} = -\frac{dP}{\rho u_g^{\ 2}} \quad \text{(Eq. 3.6)}$$

This equation shows property changes are of opposite sign for subsonic and supersonic flow because of the term Ma^2-1. There are four combinations of area change and Mach number summarised below:

i) dA > 0 (Increasing duct area) and Ma < 1 (Subsonic)

Then du_g < 0 (deceleration) and dp > 0 (Increasing pressure)

ii) dA > 0 (Increasing duct area) and Ma > 1 (Supersonic)

Then du_g > 0 (acceleration) and dp < 0 (Decreasing pressure)

iii) dA < 0 (Decreasing duct area) and Ma < 1 (Subsonic)

Then du_g > 0 (acceleration) and dp < 0 (Decreasing pressure)

iv) dA < 0 (Decreasing duct area) and Ma > 1 (Supersonic)

Then du_g < 0 (deceleration) and dp > 0 (Increasing pressure)

For a de Laval nozzle option ii) occurs after the gas has passed through the throat of the nozzle with sufficient stagnation pressure. This will cause the gas to continue to accelerate as it passes along the nozzle.

3.2.5. Area-Mach Relationships

Equations 3.2 to 3.4 can be used to calculate gas flow properties (temperature, pressure and density) at any point within the nozzle if the gas Mach number is known at that point and the flow properties are also known at an alternative point within the nozzle. To calculate the gas Mach number at any point along the nozzle, a relationship between the nozzle dimensions at that point and the throat is created. Equation 3.7 (Equation A82) relates the Mach number of the gas at any location within the nozzle as a function of the local nozzle area, A, to the sonic throat area, A^*.

$$\left(\frac{A}{A^*}\right) = \frac{1}{Ma}\left[\frac{2}{\gamma+1}\left(1+\frac{\gamma-1}{2}Ma^2\right)\right]^{\frac{\gamma+1}{2(\gamma-1)}} \qquad \text{(Eq. 3.7)}$$

Figure 3.1 shows a plot of area ratio (A/A*) against Mach number for helium gas. During the converging region of the nozzle the gas is subsonic (Ma < 1), and as the local nozzle area, A, approaches the sonic throat area, A* (A/A* approaches 1), a steady increase in the gas Mach number occurs. At A/A* equals one the gas reach transonic velocity (Ma = 1). In the diverging section of the nozzle the ratio of A/A* will increase rapidly.

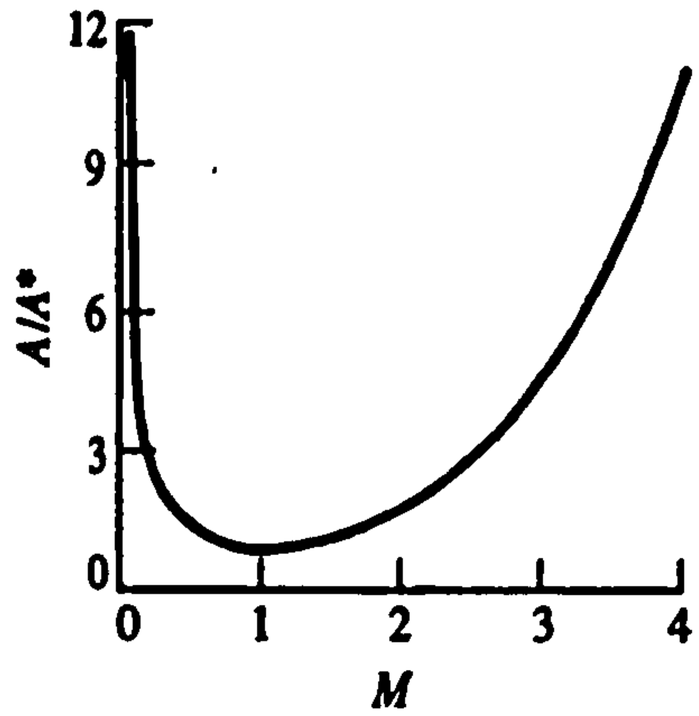

Figure 3.1 – Variation of area ratio with Mach number for helium gas (γ =1.6) [58].

Equations 3.2 to 3.4 are used to calculate the gas pressure, temperature, velocity and density. *Ma* is set to the gas Mach number at the point in the nozzle under consideration, calculated by equation 3.7, and Ma_2 is set to zero to represent stagnation conditions; therefore equations 3.2 to 3.4 become:

$$T = \frac{T_o}{\left[1+\left(\frac{\gamma-1}{2}\right)Ma^2\right]} \quad \text{(Eq. 3.8)}$$

$$\rho = \frac{\rho_o}{\left[1+\left(\frac{\gamma-1}{2}\right)Ma^2\right]^{\frac{1}{\gamma-1}}} \quad \text{(Eq. 3.9)}$$

$$P = \frac{P_o}{\left[1+\left(\frac{\gamma-1}{2}\right)Ma^2\right]^{\frac{\gamma}{\gamma-1}}} \quad \text{(Eq. 3.10)}$$

To calculate the gas velocity the following equation is used:

$$u_g = Ma\sqrt{\gamma RT} \quad \text{(Eq. 3.11)}$$

3.3. Particle Motion and Heating in a Flowing Gas

It is not the gas properties that determine the effectiveness of the cold spray process, but the resulting particle velocities, as they pass within the gas flow. The gas characteristics described in the previous section may be used to calculate the particle velocity. It is assumed that external forces are negligible, such as interactions between particles within the flow that may lead to particle deceleration. Whilst calculating a particle velocity, it is assumed to be isolated within the gas flow and therefore surrounding particles have no influence on the particle velocity. Moreover, no frictional or energy losses and collisions between particles and nozzle walls, which could lead to particle deceleration, are considered. Finally, particles are assumed to have a uniform temperature at all times. These approximations will lead to over estimation of the particle velocity found within the nozzle.

The particle velocity as it travels along the nozzle is determined using Newton's second law. All forces acting on the particle other than drag forces due to relative motion between gas and particle are neglected. Therefore:

$$m_p \frac{du_p}{dt} = \frac{1}{8} A_p \rho_g C_D \left|u_g - u_p\right| \left(u_g - u_p\right) \quad \text{(Eq. 3.12)}$$

The acceleration of a particle is therefore equal to:

$$\frac{du_p}{dt} = \frac{3\rho_g}{4d_p\rho_p} C_D \left|u_g - u_p\right|\left(u_g - u_p\right) \qquad \text{(Eq. 3.13)}$$

There are a number of drag coefficient, C_D, equations available in the literature for compressible and incompressible gas flows. In the case of incompressible gas flows, the drag coefficient is calculated depending on the relative Reynolds number of the particle at a specific point. The drag coefficient equations employed in this case are as follows as described by Clift et al. [60]:

$$C_D = \frac{24}{\mathrm{Re}_r} \qquad (Re_r < 0.2) \qquad \text{(Eq. 3.14)}$$

$$C_D = \frac{24}{\mathrm{Re}_r}\left(1 + \frac{3}{16}\mathrm{Re}\right) \qquad (0.2<Re_r<2) \qquad \text{(Eq. 3.15)}$$

$$C_D = \frac{24}{\mathrm{Re}_r}\left(1 + 0.11\,\mathrm{Re}^{0.81}\right) \qquad (2<Re_r<20) \qquad \text{(Eq. 3.16)}$$

$$C_D = \frac{24}{\mathrm{Re}_r}\left(1 + 0.1935\,\mathrm{Re}^{0.6305}\right) \qquad (20<Re_r<260) \qquad \text{(Eq. 3.17)}$$

$$C_D = 10^{1.645 - 1.1242w + 0.1588w^2} \qquad (Re_r>260) \qquad \text{(Eq. 3.18)}$$

Where:

$$w = \frac{\log \mathrm{Re}_r}{\log 10} \qquad \text{(Eq. 3.19)}$$

Where Re_r is the relative Reynolds number and calculated by:

$$\mathrm{Re}_r = \frac{\rho d_p \left|u_g - u_p\right|}{\mu} \qquad \text{(Eq. 3.20)}$$

However, it has been reported previously that the drag coefficients of a particle travelling within a compressible gas flow will also depend on the gas Mach number [61-64]. The Mach number of a gas is calculated by the following equation:

$$Ma = \frac{u_g}{\sqrt{\gamma RT}} \qquad \text{(Eq. 3.21)}$$

Re is the gas Reynolds number and calculated by:

$$\mathrm{Re} = \frac{\rho_g d_p u_g}{\mu_g} \qquad \text{(Eq. 3.22)}$$

And S is the molecular speed ratio calculated by:

$$S = M\sqrt{\frac{\gamma}{2}} \qquad \text{(Eq. 3.23)}$$

The subscript r is used to refer to relative conditions and therefore u_g in equations 3.21 to 3.23 is replaced by $|u_g - u_p|$. Using the work of Henderson et al. [63] and Walsh et al. [64] the following drag coefficient equations are proposed. If $Ma_r < 1$ then:

$$C_D = 24\left[\mathrm{Re}_r + S_r\left\{4.33 + \left(\frac{3.65 - 1.53\frac{T_p}{T}}{1 + 0.353\frac{T_p}{T}}\right)\exp\left(-0.247\frac{\mathrm{Re}_r}{S_r}\right)\right\}\right]^{-1}$$
$$+ \exp\left(-\frac{0.5Ma_r}{\sqrt{\mathrm{Re}_r}}\right)\left[\frac{4.5 + 0.38\left(0.03\mathrm{Re}_r + 0.48\sqrt{\mathrm{Re}_r}\right)}{1 + 0.03\mathrm{Re}_r + 0.48\sqrt{\mathrm{Re}_r}} + 0.1Ma_r{}^2 + 0.2Ma_r{}^8\right] \qquad \text{(Eq. 3.24)}$$
$$+ \left[1 - \exp\left(-\frac{Ma_r}{\mathrm{Re}_r}\right)\right]0.6S_r$$

If $Ma_r > 1$ then:

$$C_D = \frac{0.9 + \frac{0.34}{Ma^2} + 1.86\sqrt{\frac{Ma}{\mathrm{Re}}}\left[2 + \frac{2}{S^2} + \frac{1.058}{S}\sqrt{\frac{T_p}{T}} - \frac{1}{S^4}\right]}{1 + 1.86\sqrt{\frac{Ma}{\mathrm{Re}}}} \qquad \text{(Eq. 3.25)}$$

T_p is the temperature of the particle and T is the temperature of the gas at that given point.

Whereas the methods developed by Clift et al. [60] do not consider the role of Mach number, equations 3.24 and 3.25 do. Therefore equations 3.14 and 3.18 predict little variation in the drag coefficient when a gas flow changes from subsonic to supersonic velocity. However experimental work by Bailey and Hiatt [61], shown in Figure 3.2, found that for Reynolds numbers in the region of 200 to 1500 the drag

coefficient will increase abruptly from ~0.5 to ~1.2 as the Mach number increases from ~0.8 to ~1.5. Therefore it is crucial to use the correct drag coefficient equations when predicting particle velocities as they pass within the gas flow.

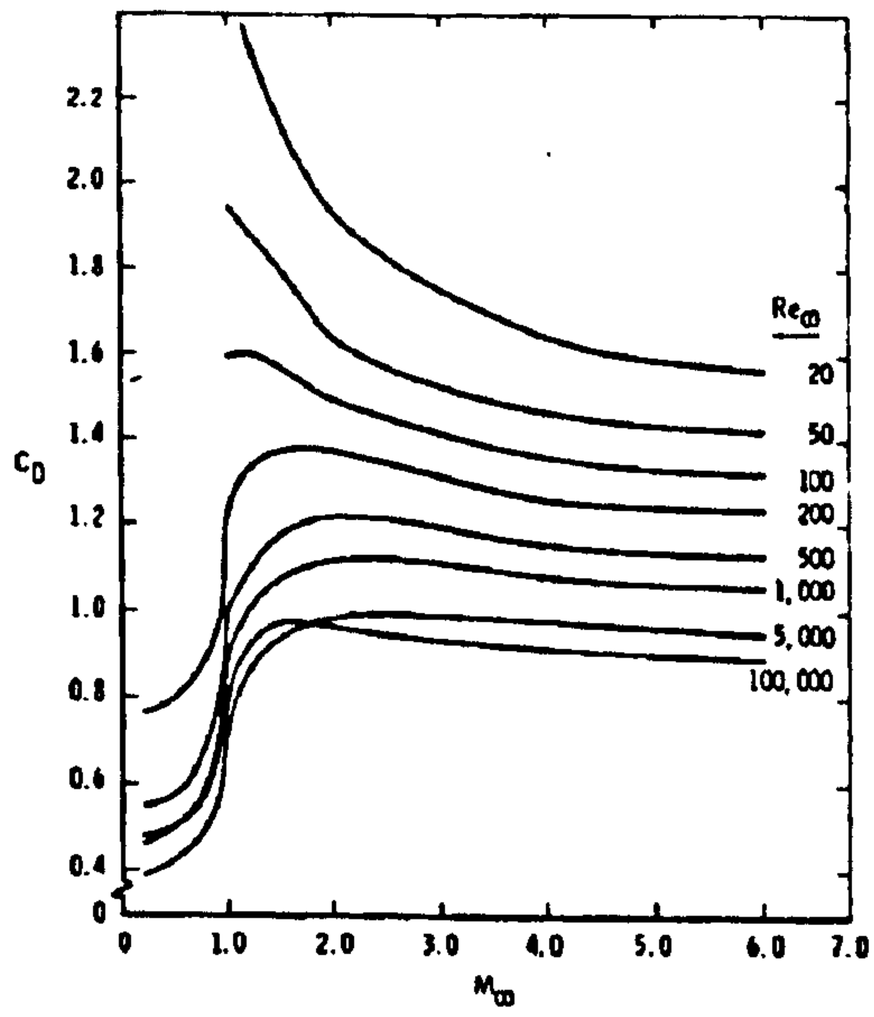

Figure 3.2 – Variation of sphere drag coefficient with Mach number at subsonic and supersonic speeds and $T_w/T \approx 1$ [61].

Heat transfer to a particle is described by a heat transfer coefficient, h_t, which is a function of the Nusselt number, *Nu*. The Nusselt number refers to the ratio of convective to conductive heat transfer across a boundary. A Nusselt number close to unity (where the amount of conductive and convective heat transfer is similar) is characteristic of a laminar flow. For turbulent flows, convection heat transfer occurs more readily and a larger Nusselt number is obtained. By considering the conservation of energy, the equation for the temperature change in a particle is [65]:

$$m_p C_p \frac{dT_p}{dt} = h\left(T - T_p\right)A_p \qquad \text{(Eq. 3.26)}$$

The heat transfer coefficient is given by:

$$h = \frac{Nu\lambda_g}{d_p} \qquad \text{(Eq. 3.27)}$$

Combining equations 3.26 and 3.27, the rate of change of temperature of a particle is:

$$\frac{dT_p}{dt} = \frac{6\lambda_g Nu(T - T_p)}{d_p^2 \rho_p C_p} \qquad \text{(Eq. 3.28)}$$

To determine the temperature and velocity of a spherical particle as it moves along the nozzle, equations 3.13 and 3.28 are solved numerically in a series of time steps. At the end of each time step, the new velocity, new temperature, and new position of the particle are calculated [65].

3.4. Modelling of Gas and Particle Behaviour in CGDS

The basic equations and assumptions made relating to isentropic one dimensional flow and the interaction of a gas flow with injected particles have been described previously. The simplest form of modelling the cold spray process is based on solving these one dimensional flow equations. More complex analysis uses computational fluid dynamics which is able to include factors such as wall friction and the influence of the free jet nozzle external to the nozzle. In the simplest case, modelling of particle velocity is calculated by first calculating the gas velocities as they pass along the length of the nozzle and secondly the interactions between particles and the gas flow [42, 54, 65, 66].

Dykhuizen and Smith [42] were the first researchers to publish work on predicting cold spray particle velocities using a one dimensional isentropic model. Modelling was carried out using the equations and assumptions described previously. Modelling was carried out for a particle of 10 μm diameter with a density of 8×10^3 kg m^{-3}. Although no information was provided referring to the nozzle dimensions, an exit particle velocity of 1080 m s^{-1} was predicted when utilising helium gas. It is noted by the authors that the particle velocity is strongly influenced by the gas type and properties, particle material density and size. It was also predicted that particles of smaller diameter are expected to have the highest velocities at the nozzle exit, due to small particles accelerating faster than larger particles whilst travelling within the gas flow. The nozzle length was also found to influence the particle velocity but not the nozzle shape. However, if the nozzle length is too large then the gas pressure

within the nozzle will reduce to less than ambient pressure and therefore cause a shock wave to form within the nozzle, abruptly reducing the gas velocity.

Further one dimensional flow modelling was carried out by Van Steenkiste et al. [54]. The variation in gas and particle velocities and temperatures along the nozzle axis for copper particle diameters ranging from 1 to 50 μm, utilising air as the main driving gas with a stagnation pressure of 2.0 MPa and temperature of 527 °C, was calculated. The variation of gas and particle velocities and temperatures along the nozzle axis are shown in Figure 3.3(a) and (b). Once again similar trends to those identified by Dykhuizen and Smith [42] are identified; mainly, increasing particle velocity with decreasing particle size. Whilst modelling was carried out for particles of similar density, lower particle velocities, of size 10 μm, were found by Van Steenkiste et al. [54] compared to Dykhuizen and Smith [42]. This can be explained due to the utilisation of different gas types as well as the potential variation in nozzle dimensions.

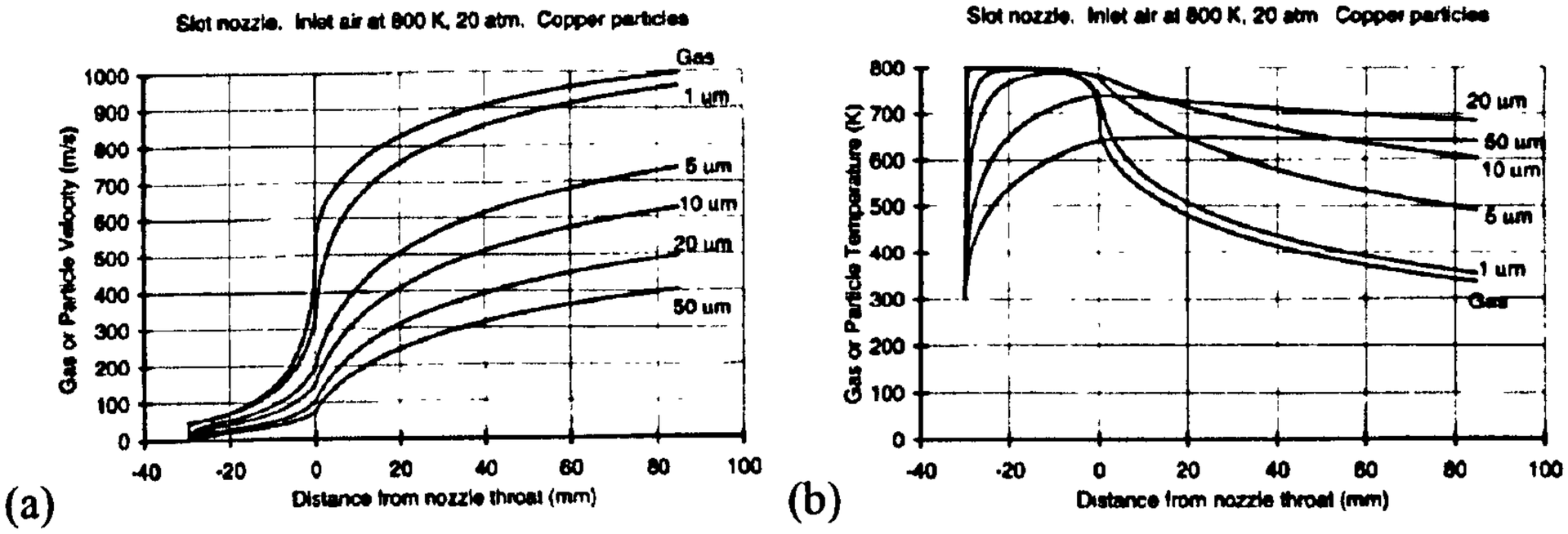

Figure 3.3 – (a) Velocity and (b) temperature profile along the nozzle axis utilising air as the process gas for various copper particle diameters, To = 527°C, po = 2.0 MPa [54].

Whilst one dimensional isentropic analysis helps to provide physical understanding of the spraying process, a number of potentially important factors are ignored. With one dimensional flow modelling the effect that the ambient atmosphere (upon leaving the nozzle and prior to the particle impacting the substrate) has on the final particle impact velocity can not be predicted accurately. It may be expected that turbulence of the gas flow at the nozzle exit will influence the gas velocity and therefore may affect the particles velocity on leaving the nozzle. Additionally, boundary layers that change the working dimensions of the nozzle and friction at the

nozzle walls may also influence the particles velocity. Computational fluid dynamics (CFD) provides more detailed analysis of particle velocities than isentropic flow analysis as it is able to take these parameters into account [48, 54, 56, 66, 67].

Comparisons between isentropic flow and CFD analyses have been made previously [66]. For their particular nozzle geometry, the particle nozzle exit velocity of a 15 μm copper particle travelling through a heated nitrogen gas flow was 50 m s^{-1} higher when calculated by isentropic flow equations compared to CFD modelling [66]. The increased particle exit velocity is due to the basic assumptions made by isentropic models, for example, no frictional losses throughout the system. However, the authors also believe that the particles will continue to accelerate on leaving the nozzle and therefore the particle impact velocity for a typical stand off distance of 30 mm may in fact more closely resemble the particle exit velocity calculated by the isentropic flow equations.

Stoltenhoff et al. [48] calculated the gas and temperature and velocity of the particles along the length of the nozzle for a copper powder travelling within a nitrogen gas flow using CFD as shown in Figure 3.4. The authors did not divulge the nozzle length. The majority of the gas acceleration takes place in the area of the nozzle throat and the first third of the divergent section. At the same time the gas temperature is predicted to decrease to values below room temperature. At the nozzle exit, the gas velocity suffers from shockwaves and changes irregularly. However it is predicted to have little influence on the particle velocity on leaving the nozzle.

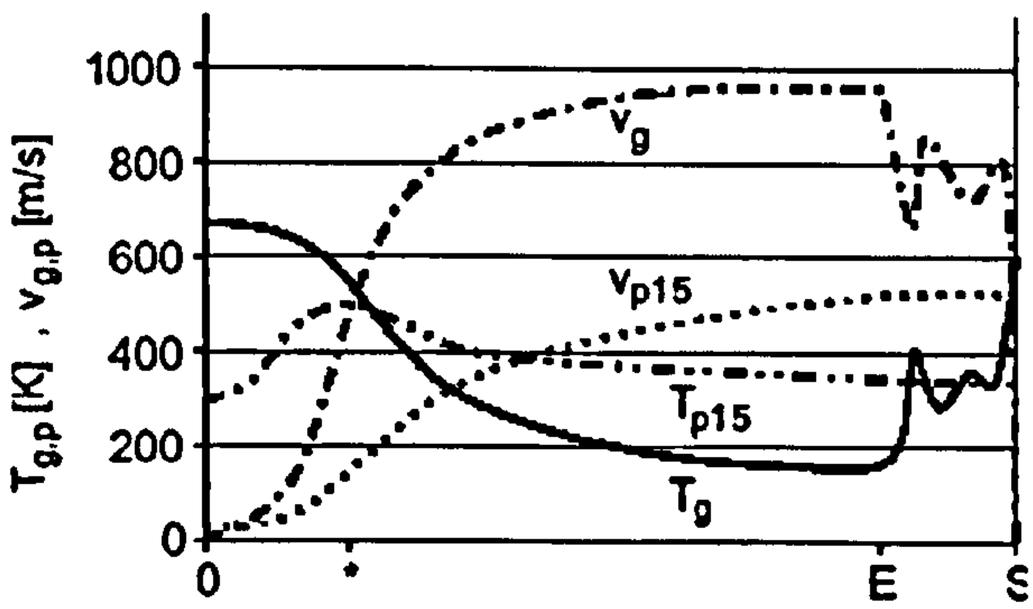

Figure 3.4 – Temperature and velocity profile along the nozzle axis utilising nitrogen as the process gas and a 15 μm Cu particle, To = 320 °C, po = 2.5 MPa (* = nozzle throat, E = nozzle exit, S = substrate, V_g = gas velocity, T_g = gas temperature, V_{p15} = particle velocity, T_{p15} = particle temperature) [48].

The effect of varying gas temperature, gas pressure, stand off distance and particle size on particle exit velocity and temperature was also evaluated. By increasing gas temperature (Figure 3.5(a)) and gas pressure (Figure 3.5(b)) a monotonic increase in particle velocity at the nozzle exit was found. The stand off distance is predicted to have a minimal effect on the particle velocity as shown by Figure 3.5(c). Finally, for a typical powder size distribution (+5-25 μm) an increasing particle velocity is found with decreasing particle size and shown in Figure 3.5(d). This is due to the slower acceleration of the particle as its mass increases. Further modelling of potential shockwaves that may occur at the nozzle exit have been made by Jodoin et al. [67] using CFD analysis. For their particular spray setup, shock waves were expected when using nitrogen and helium over a range of gas pressures and temperatures. Shock waves were found to reduce the gas velocity drastically and therefore influence the particle exit velocity. By considering the effect of shockwaves at the nozzle exit, the particle velocity model was found to be in good agreement with captured velocity data.

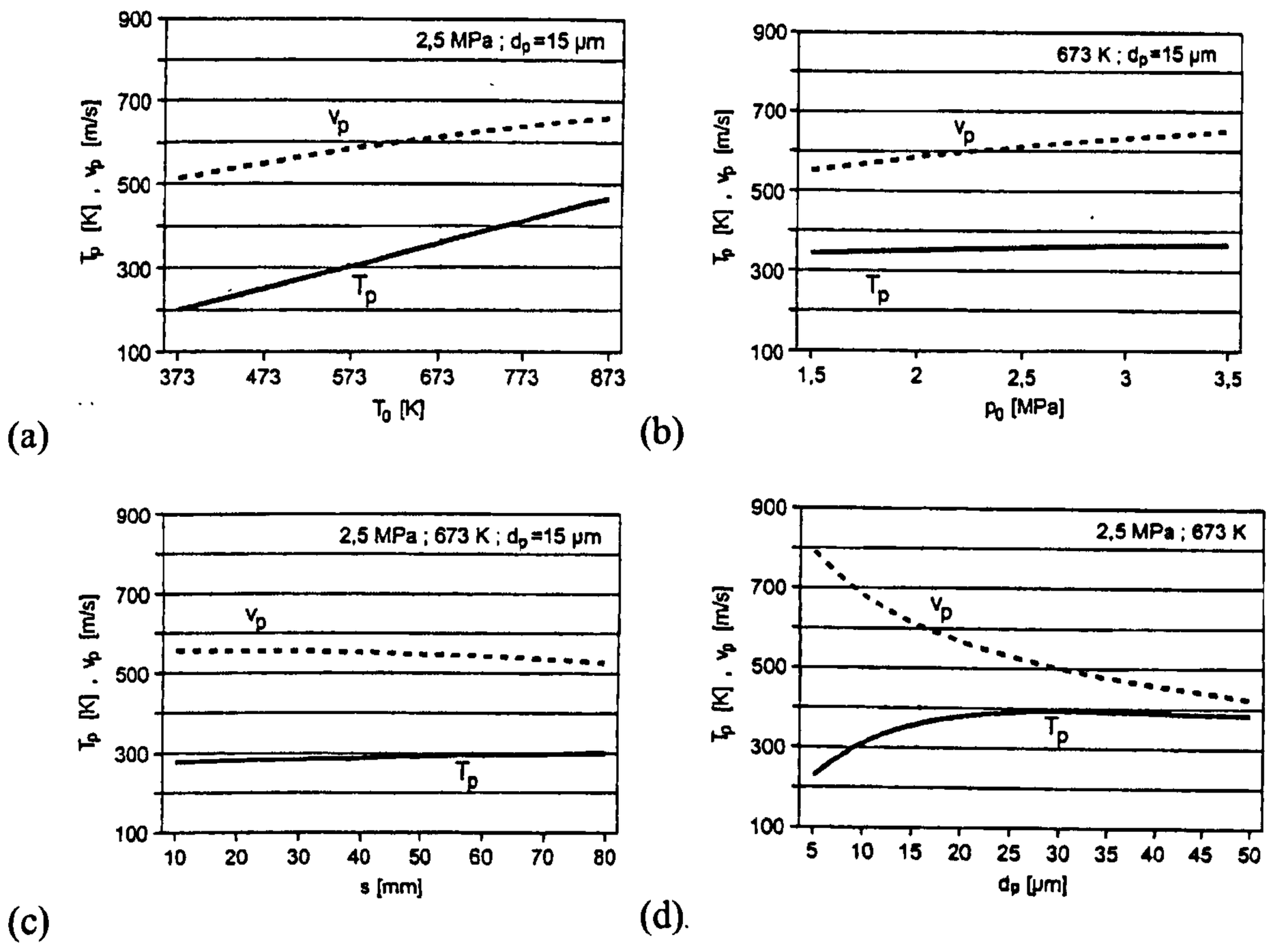

Figure 3.5 – Predicted effect of (a) gas temperature, T_o, (b) stagnation pressure, P_o, (c) stand off distance, s, and (d) particle diameter, d_p, on particle velocity, V_p, and particle temperature, T_p for copper particles travelling within a nitrogen gas flow [48].

An area where results vary between one dimensional flow modelling and CFD analysis is the effect of particle size on particle velocity. One dimensional isentropic modelling predicts that the smallest particles will offer the largest particle velocities at the nozzle exit due to being easier to accelerate. Grujicic et al. [68] and Schmidt et al. [47] predict that particles of small diameter will have a reduced particle impact velocity. This is shown schematically in Figure 3.6. Grujicic et al. [68] modelled the impact velocities of copper and aluminium particles travelling within a helium and nitrogen gas flow using analytical analysis. They predict particle velocities to reduce for particle diameters less than 1 μm for a copper particle travelling within a helium gas flow. The particle diameter, at the point where particle velocities begin to reduce, is larger for aluminium within a helium gas flow as shown by Figure 3.7. From Figure 3.7 it appears that the particle diameters where impact velocities are expected to reduce are generally smaller than a typical powder size distribution and therefore this effect may not be an issue when creating a coating by cold spray deposition. Particle velocities reduce for particles of a small volume and mass, compared to larger particles, because of faster deceleration on leaving the nozzle, thus reducing the impact velocity [47, 68].

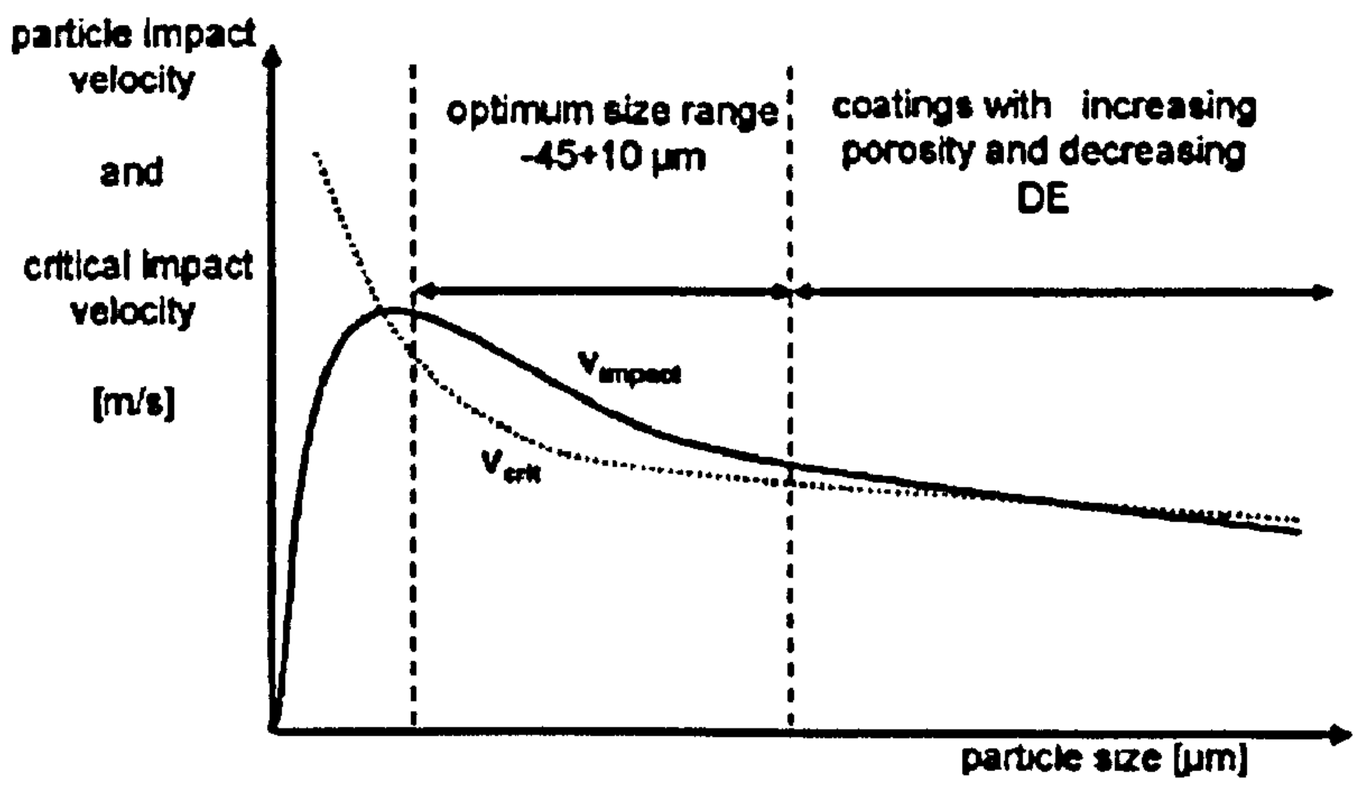

Figure 3.6 – Schematic of critical and impact velocity versus particle size [47].

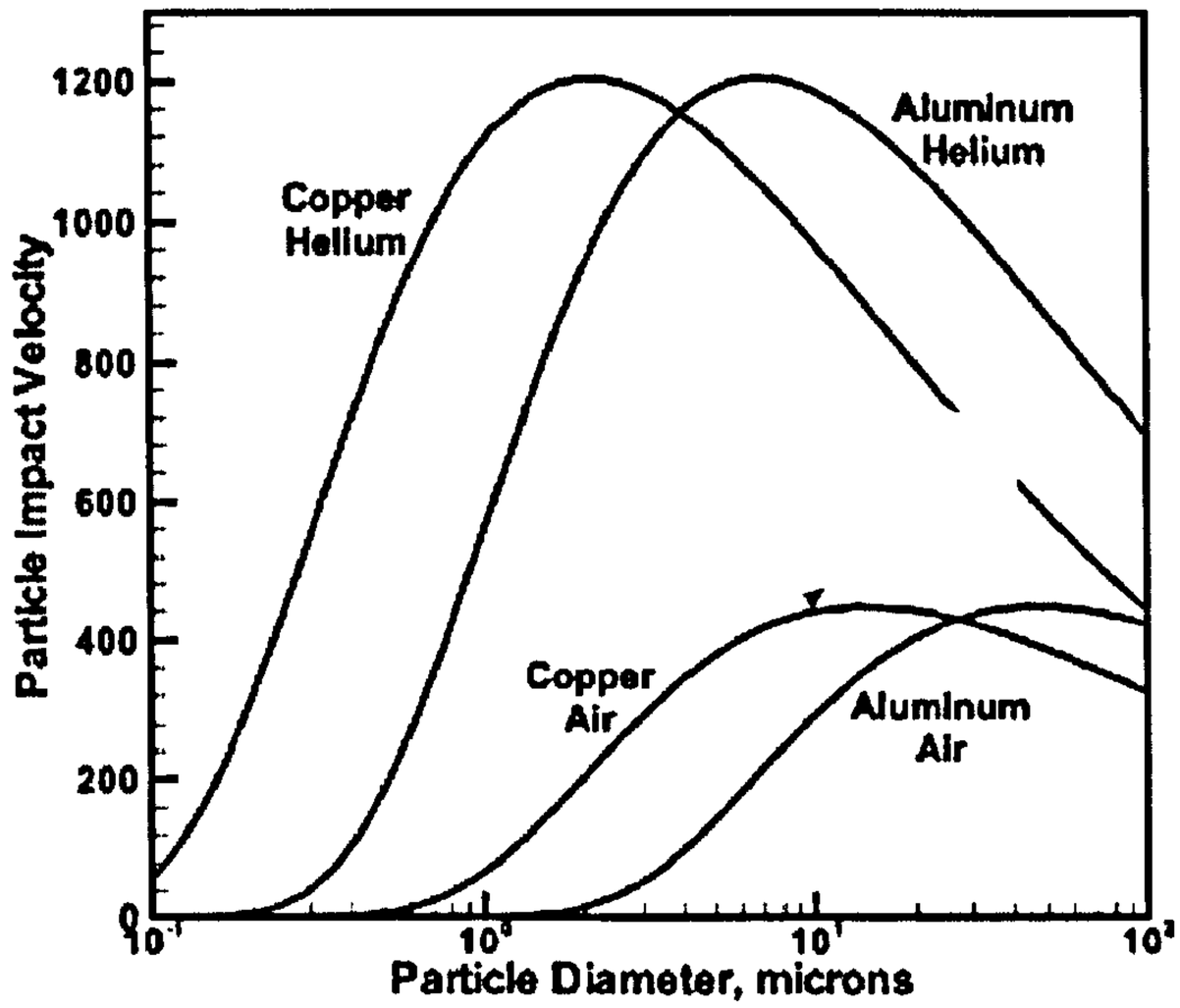

Figure 3.7 – Effect of the particle size, the powder material and the carrier gas on the particle impact velocity [68].

3.5. Measurement of Particle Velocities

Whilst modelling of particle velocities is important in the development of the cold spray process, physical measurement of particle velocities is also important; at the very least to validate and verify modelling output. Firstly, this section will discuss the general methods available for measuring particle velocities. Secondly, measurements of particle velocities from cold spray made by other workers are then described.

3.5.1. Particle Velocity Measurement Techniques

There are various methods available to measure particle flows within fluids; the three methods routinely employed are:

i) Laser Doppler Velocimetry (LDV)

ii) Laser Two-Focus Method (L2F)

iii) Particle Image Velocimetry (PIV)

LDV is based on the fact that coherent light waves show a Doppler shift when scattered by moving boundary layers, and therefore carry velocity information. A laser beam is split into two partial waves that are then focussed by the use of a convex lens. At the point of intersection of the laser beams interference fringes will form. Flowing particles that pass through the point of intersection will cause the interference fringes to scatter. A detector (photomultiplier) collects data referring to the frequency of the interference fringes that can be directly related to the particles velocity [69].

The L2F method uses two laser beams to focus within the particle flow at two points of known separation distance. The focal points act as a light barrier in the flow. Two photomultipliers detect the light scattered by particles as they pass the measuring points allowing the particle velocity to be calculated. The L2F method has some advantages over the LDV method, such as requiring lower laser power and a larger velocity measurement range [69]. Similar to the LDV method it is not possible for particle sizes to be measured simultaneously. An example of a commercially available L2F measuring system for cold spraying is the Polytec Optronics (Polytec Optronics Ltd., Costa Mesa, CA, USA) L2F velocimeter [70].

PIV uses a monochromatic light source to illuminate a large area (typically up to several square centimetres) of the particle flow. The laser light flashes in quick succession illuminating the travelling particles. A digital camera and computer record images of the particles illuminated by the backscattered flashing laser light. PIV systems will typically illuminate the particle flow twice for every time the digital camera produces an image. This causes a double exposed image to be produced with each particle appearing on the image twice. The particle velocity may then be calculated by computer software as the time duration between the firing of the lasers is known and the distance between paired particles may be measured.

There are various commercial PIV systems available for cold spraying. One of the most common PIV systems routinely used to measure particle velocities in cold spraying is the SprayWatch system (Oseir Ltd., Tampere, Finland) [57, 67, 71, 72],

but other examples include the Control Vision dual strobe system (Control Vision, Idaho Falls, ID, USA) [55] and the Oxford Laser VisiSizer (Oxford Lasers, Didcot, UK).

The SprayWatch system consists of a camera that captures images of the particles as they are illuminated by a laser light source. For each camera exposure of typically $1/10^{th}$ to $1/100^{th}$ second, the light source is pulsed so that the particles are illuminated for a short time period (~ 50 ns). During this time period the particle movement will normally not be frozen due to sufficiently high particle velocity. Figure 3.8 is a schematic of the SprayWatch system. Whilst this time period may not be short enough to "freeze" the particle movements, the particle velocity may be calculated from the particle streaks. This is due to knowing the pulse time-interval and the measuring the distance travelled between pulses by subsequent image analysis. For PIV to accurately measure particle velocity it must be able to accurately and reliably control the time delay between the firing of the two lasers, typically 300 ns. Whilst the Oxford Lasers system operates using the same basic time of flight principle it is advantageous over the SprayWatch equipment as it is able to "freeze" the particle movement, due to a laser illumination time of approximately 6 ns, allowing the particle velocity and size to be measured simultaneously. The Oxford Lasers system was used for this project to carry out particle velocity and size measurements and is explained in greater detail in Section 3.7.4.

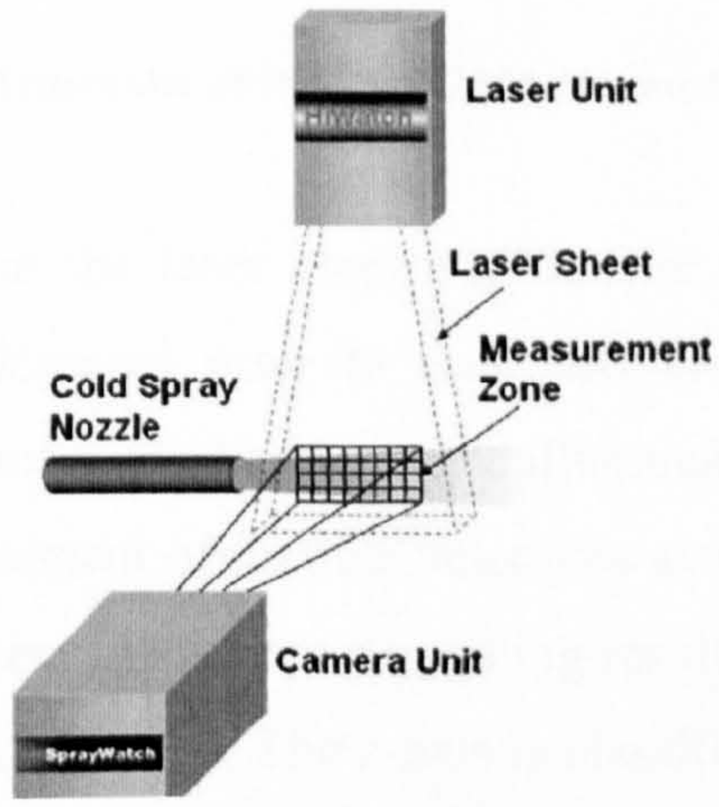

Figure 3.8 – Schematic of the SprayWatch diagnostic system [72].

A final note is made to the Tecnar DPV-2000 (Tecnar Automation Ltd., St. Bruno, QC, Canada) [73-75]. This system is not strictly a PIV system as it records the time taken for particles to travel a known distance. A laser light source is used to illuminate the measurement volume area. Particles travel in front of two slits and the reflected light coming from the particles passes through the slits and an optical fibre to a detector. The distance between the two slits is fixed and the time taken for a particle to traverse the distance between the slits is determined by measuring the time interval between two signal peaks formed. This allows the particle velocity to be determined. Individual particle sizes may also be determined by analysis of the laser light diffraction pattern generated. Figure 3.9 is a schematic of the DPV-2000 diagnostic system.

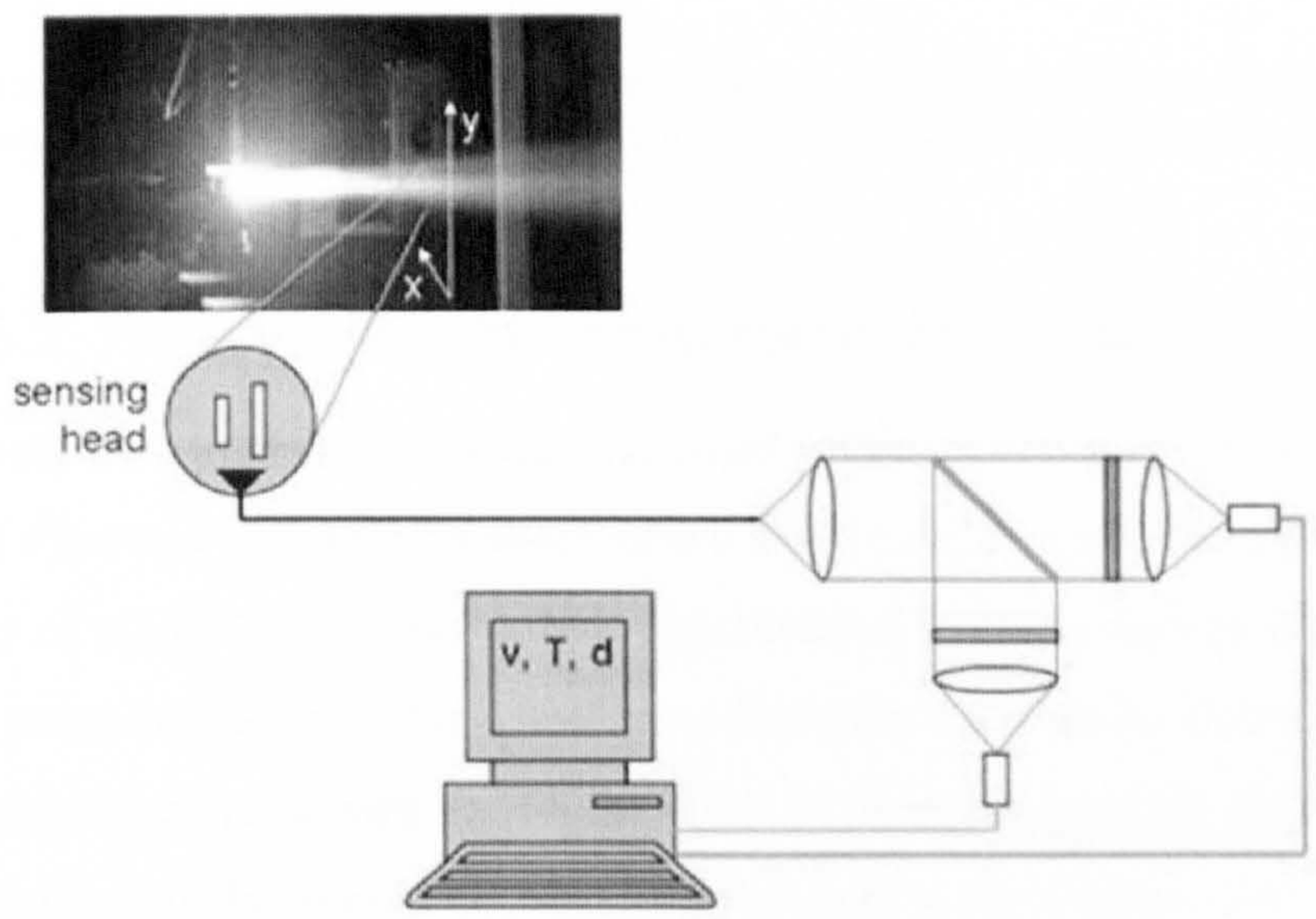

Figure 3.9 – Schematic of the DPV-2000 diagnostic system [76].

In all cases radiation from the laser employed can be dangerous and means that safety issues must be addressed prior to their use. Generally with any velocity measurement, system the measuring and particle illumination system are mounted on a traverse to allow measurement of particle velocities at any point within the plume. Definition of the axis system used when describing results from previous workers is shown schematically in Figure 3.10. The z-axis is classified as the distance from the nozzle exit. Typically velocity measurements are made with a stand off distance (z-axis) of between 5 and 40 mm, to replicate typical stand off distances when

depositing material. If gravitational effects on the particles velocity are assumed to be negligible, then the plume can be classed as axisymmetric and therefore there should be little variation in velocity data when comparing measurements carried out in the x and y axis. Changing the vertical position (x-axis) requires a traverse capable of lifting the weight of the measuring system. It is often simpler and cheaper to change the horizontal axis (y-axis) where no load requires lifting.

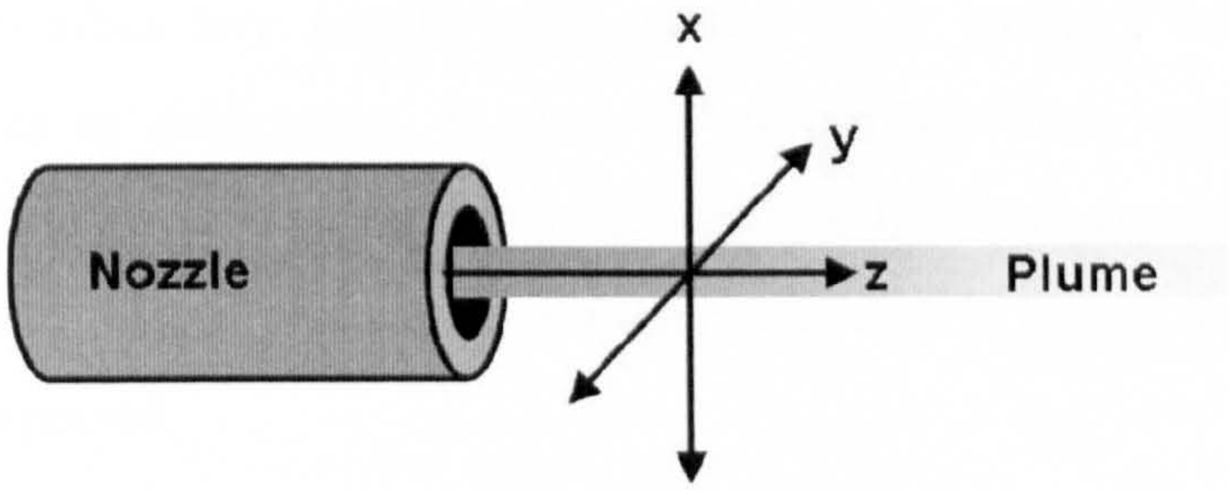

Figure 3.10 – The three axis coordinate system used to define where PIV measurements are made from. (Z = 0 at the nozzle exit, X & Y = 0 at the centre of the plume).

3.5.2. Particle Velocity Measurements in Cold Spray

Velocity measurements made at a specific point within a plume are often represented in terms of a normal or Gaussian distribution. For example, Lee at al. [57] measured the velocity of a Cu-Sn alloy and group experimental velocity data taken at a single measuring point into 20 m s^{-1} bins, and show that their data can be characterised by a normal distribution, as shown by Figure 3.11. It is not surprising that a range of velocity results will be measured at any point within the plume. For mono-sized particles, a velocity distribution exists due to particles interacting with each other, the nozzle walls and the surrounding atmosphere. Furthermore a real powder often contains particles of various sizes, and therefore mass. Particles of varying size will have different velocity profiles due to different rates of acceleration and deceleration as described in Section 3.4.

The majority of the literature concentrates on showing the effects of process parameters on velocity and not how powder parameters (i.e. its size distribution) affects particle velocities. This is due to limitations of the majority of velocity measurement techniques that only allow for the measurement of particle velocity and

not simultaneous measurements of their size. Therefore velocity data are generally evaluated by identifying the effect of parameter variation, for example gas pressure [57, 67, 70, 71, 74] or temperature [55, 57, 67, 70, 71, 74], versus the mean particle velocity. Capturing of individual particle size and velocity data simultaneously makes it possible theoretically to identify trends relating the particle size to its velocity.

This section describes key results produced by other workers when measuring particle velocities in cold spray. It must be noted that when analysing particle measurements from various workers it is generally difficult to compare data output due to the effect of differing process parameters and nozzle design, however similar trends may be expected.

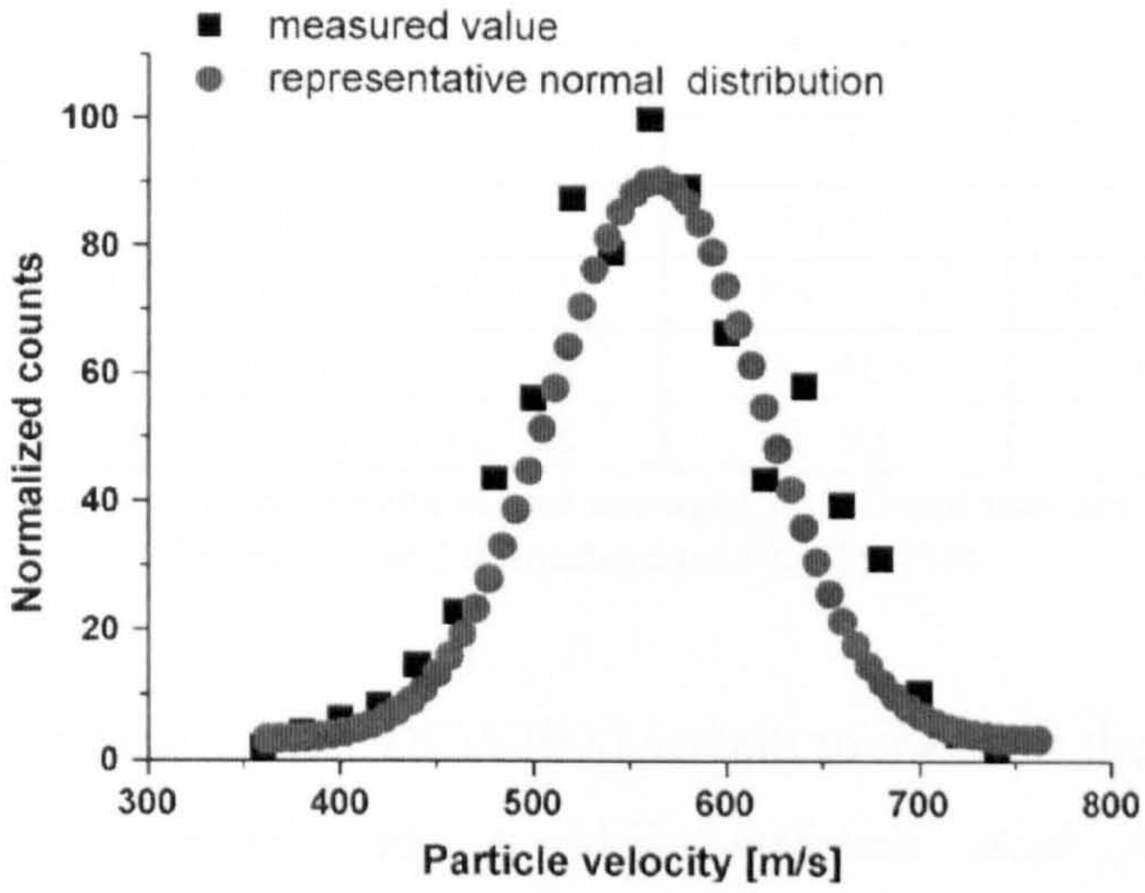

Figure 3.11 – Particle distribution curves of a Cu-Sn alloy using nitrogen gas at an operating pressure of 2.9 MPa and at a temperature of 400 °C. The distribution of measured particle velocities has been estimated as a normal distribution [57].

3.5.2.1. Process Gas Type

Currently industrial standard helium, nitrogen and air can be suitably used for the cold spraying process. Helium is preferentially used due to higher compressibility and higher speed of sound, compared to nitrogen or air and therefore will have a higher velocity at the throat region of the nozzle.

As the gas passes along the remaining diverging part of the nozzle and continues to accelerate, higher velocities can be expected with helium gas compared to nitrogen or air, despite the lower gas density. Assuming that sonic velocities are reached at the throat, the speed of the gas at the throat, u_t, is determined by equation 3.29 (Equation A43):

$$u_t = \sqrt{\gamma RT} \qquad \text{(Eq. 3.29)}$$

Where γ is the adiabatic index of the gas, R the gas specific constant and T is the temperature of the gas. Table 3.1 summarises the critical gas constants of helium and nitrogen gas. Helium has a higher ratio of gas specific heats (adiabatic index) and lower molecular weight compared to nitrogen. Equation 3.29 shows that increasing the ratio of specific heats (adiabatic index) and the specific gas constant, by reducing the molecular weight of the gas, will produce a higher gas velocity.

Gas Constants	He	N_2
Specific Gas Constant / J kg^{-1} K^{-1}	2079	296.8
Adiabatic Index	1.667	1.404
Dynamic Viscosity / kg m^{-1} s^{-1}	1.86×10^{-5}	1.67×10^{-5}
Thermal Conductivity / W m^{-1} K^{-1}	0.1468	0.025
Specific Heat Capacity / J kg^{-1} K^{-1}	5193	1039

Table 3.1 – The gas constants of helium and nitrogen gas. Constants are taken from the Handbook of Chemistry and Physics [77].

Vlcek et al. [75] used the Tecnar DPV-2000 system to measure the particle velocity and diameter simultaneously for a 316L stainless steel powder using a helium/nitrogen mixture at 793 K. Results are shown in Figure 3.12. They found that for any given particle diameter, there was a large variation in particle velocities. Presenting individual particle diameters and their corresponding velocities (Figure 3.12) makes it difficult to analyse the data and in fact the author makes no attempt to predict trends between particle diameter and velocity.

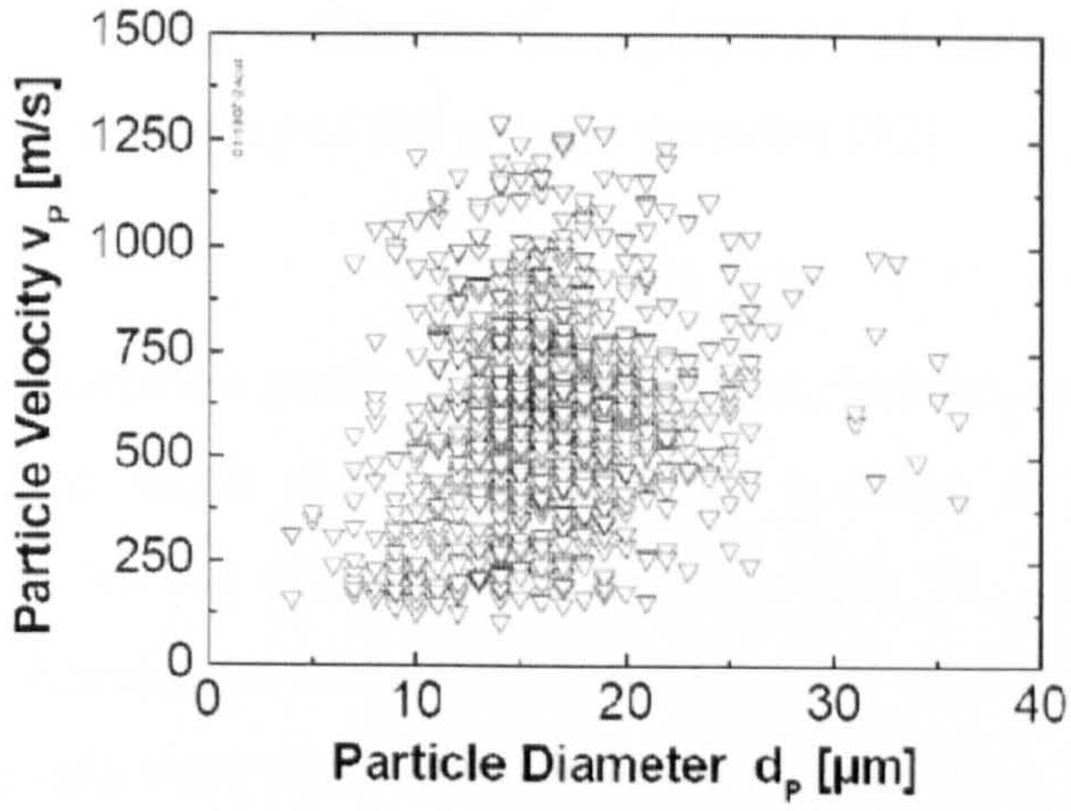

Figure 3.12 – Particle velocities measured by the Tecnar DPV-2000 for -25 µm 316L stainless steel powder at a nozzle distance of 20 mm; temperature of helium/nitrogen mixture 793 K [75].

Comparisons between helium, nitrogen and air as the main driving gas have been made by PIV analysis. Despite the lower gas density of helium, higher particle velocities were found compared to if nitrogen or air was utilised. Gilmore et al. [70] compared the velocity of a copper powder utilising helium and air as the driving gas. Measurements taken at a stand off distance of 30 mm and gas temperature of 200 °C, showed a mean particle velocity of approximately of 400 m s^{-1} when using air, and 650 m s^{-1} with helium. Comparisons between helium and nitrogen have also been made by Jodoin et al. using a nickel powder [67]. At a gas temperature of 500 °C the helium gas gave a mean velocity of 800 m s^{-1} compared to 510 m s^{-1} for nitrogen gas. These results were in good agreement with a CFD model produced by the authors.

3.5.2.2. Gas Pressure

Increasing the gas stagnation pressure, and therefore gas density, will increase the mass flow rate of the gas as shown by equation 3.30:

$$\dot{m} = \rho_g A u_g \qquad \text{(Eq. 3.30)}$$

Gas pressures of between 15 to 30 bar have been successfully employed for depositing various materials [48]. Increasing gas pressure will theoretically have no influence on the gas velocity but due to an increase in gas density an increase in the drag force acting on the powder particles is experienced resulting in more rapid acceleration [42]. Additionally the use of high gas inlet pressures reduces the risk of

shock waves from occurring within the diverging part of the nozzle which would significantly reduce the velocity of the gas and particles [42].

Increasing the gas stagnation pressure, be it nitrogen, helium, or air, has routinely shown to increase the mean particle velocity for a range of spherical powders including Al-Si [71], bronze (Cu-Sn) [57], copper [55, 70, 72], nickel [67] and stainless steel [74]. Results are summarised in Table 3.2. The stand off distance (z-axis) that measurements were taken at is also given in the table. Measurements that have been made using the Oseir Ltd. SprayWatch [57, 67, 71] have given results for a larger section of the plume, up to 20mm across, compared to typically 1 or 2mm for other measurement systems. In these cases the stand off distance shown in Table 3.2 is given as the centre of the measuring area.

Whilst it is difficult to compare actual values from one worker to another, due to different nozzle designs, powders and spray parameters, similar trends are apparent. Figure 3.5(b) has previously shown that modelling predicts a relatively linear increase of particle velocity with increasing gas pressure. Therefore it is possible to calculate the velocity percent increase per 1 MPa increase in stagnation pressure, as shown in Table 3.2, as a method of comparing the influence of pressure on particle velocities for the various studies considered. Whilst this basic assumption may have limited validity it does allow simple comparisons between the data to be made. It is found that generally helium gives the largest percentage increase in particle velocity per 1 MPa stagnation pressure increase compared to nitrogen or air.

Powder Size Distribution / µm	Gas Type	z / mm	A_e/A^*	Gas Temperature & Pressure	Mean Velocities / m s^{-1}	Vel. % Increase per MPa	Ref.
Al-Si -45 +5	N_2	30	- (CGT)	2.1 – 2.9 MPa 500 °C	675 – 820	+24 %	[71]
Cu-Sn -40 +5	N_2	30	- (CGT)	1.7 – 2.9 MPa 500 °C	523 – 593	+11 %	[57]
Cu -30 +10	He	10	6.4	1.5 – 2.7 MPa 300 °C	425 – 500	+15 %	[70]
Cu -30 +10	Air	10	6.4	1.5 – 2.7 MPa 300 °C	325 – 375	+13 %	[70]
Ni -45 +10	He	8	10.4	2.0 – 2.4 MPa 500 °C	740 – 800	+20 %	[67]
Ni -45 +10	N_2	8	10.4	2.0 – 2.4 MPa 500 °C	570 – 610	+18 %	[67]
316L -44 +16	He	20	-	1.5 – 3.0 MPa 200 °C	475 – 625	+21 %	[74]
316L -44 +16	N_2	20	-	1.5 – 3.0 MPa 300 °C	450 – 540	+13 %	[74]
Cu +1 -50	N_2	14	- (CGT)	2.0 – 10.0 MPa 150 °C	271 – 430	+7 %	[72]

Table 3.2 – Effect of gas stagnation pressure on mean spherical particle velocities at constant spray temperature for various gas types and powders. All measurements were taken in the central portion of the plume.

3.5.2.3. Gas Temperature

An increase in the gas temperature will increase the gas velocity as shown by equation 3.29 and therefore higher exit velocities at the end of the nozzle are attained, despite the reduction in gas density. The reduction in gas density will mean that momentum is passed to the particles at lower efficiency due to less drag. Pre heating of nitrogen gas allows the potential for nitrogen gas to be used due to sufficiently increasing the particle velocity to allow bonding [45, 48, 56].

Results of experimental measurements carried out by other workers are summarised in Table 3.3. The velocity percent increase per 100 K increase in gas temperature is also shown in the table. This assumes a linear increase of particle velocity with increasing temperature as shown to be predicted previously by modelling in Figure 3.5(a). By comparing Table 3.2 and Table 3.3 it can be seen that generally a 300 °C

to 400 °C increase in gas temperature is required to give a similar increase in particle velocity to when a 1 MPa increase in gas stagnation pressure is applied. Results by Gilmore et al. [70] suggest that a larger percentage increase in particle velocity per 100 °C in gas temperature may be expected when using air rather than helium, although the absolute particle velocity when using helium remains higher.

Powder Size Distribution / µm	Gas Type	z / mm	A_e/A^*	Gas Temperature & Pressure	Mean Velocities / m s^{-1}	Vel% Increase per 100 K	Ref.
Al-Si -45 +5	N_2	30	- (CGT)	2.9 MPa 300 – 500 °C	705 – 820	+8 %	[71]
Cu-Sn -40 +5	N_2	30	- (CGT)	2.9 MPa 300 – 500 °C	544 – 593	+5 %	[57]
Cu -30 +10	He	10	6.4	2.1 MPa 25 – 500 °C	600 – 690	+3 %	[70]
Cu -30 +10	Air	10	6.4	2.1 MPa 25 – 500 °C	350 – 450	+6 %	[70]
Cu +50	Air	5	2.8	2.4 MPa 204 – 371 °C	~ 320	N/A	[55]
Ni -45 +10	He	8	10.4	2.4 MPa 300 – 500 °C	760 – 810	+4 %	[67]
Ni -45 +10	N_2	8	10.4	2.4 MPa 300 – 500 °C	570 – 610	+4 %	[67]

Table 3.3 – Effect of gas temperature on mean spherical particle velocities at constant stagnation pressure for various gas types and powders. All measurements were taken in the central portion of the plume.

3.5.2.4. Plume Position

The stand off distance (z-axis (Figure 3.10)) is the distance from the exit point of the de Laval nozzle to the substrate. It is typically 10 - 40 mm in length. As with most spray systems, the in flight particle characteristics and deposition efficiency for cold spray coatings change very little when varying the stand off distance between typical stand off distances of 5 and 20 mm [70, 78]. Shukla et al. [see 78] observed that instabilities in spray flume, such as shock waves, are enhanced as the stand off distance is increased. An increase in shock waves would be expected to reduce the deposition efficiency of the coating due to a potential reduction in the particle impact velocity. Generally stand off distances of no greater than 30 mm are employed. As

the stand off distance is increased the particle velocity is expected to decrease slightly due to interactions between the particles and the surrounding environment.

Gilmore et al. [70], Wu et al. [71] and Lee et al. [57] have all investigated the effect of the measuring position within the plume on the mean particle velocity. Work carried out by Gilmore et al. [70] investigated the effect of changing the z-axis position. A copper powder was used and tests were carried out using helium and air at a constant pressure of 2.1 MPa and 200 °C. It was found that the copper powder continues to accelerate upon leaving the nozzle up to a z position of 30 mm with helium as the main driving gas but when air is used this does not occur, as shown by Figure 3.13. Momentum transfer between air and the particles is greater than when the helium is used because of the higher density of air. Therefore particles travelling within the helium gas flow take longer to attain their maximum velocity.

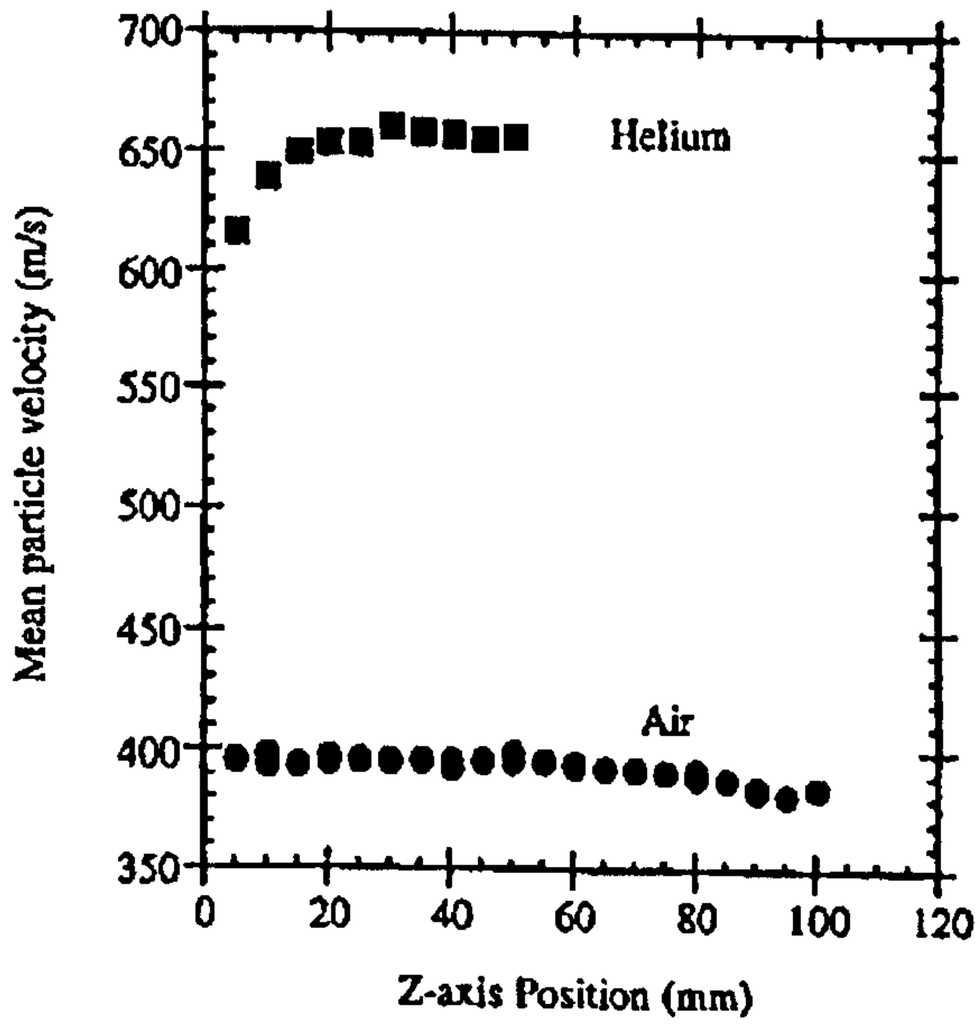

Figure 3.13 – Measured mean particle velocity versus z-axis position (x=o, y=0) for a copper powder for helium and air process gases. Measurements were made using the Polytec Optronics L2F system. Pressure and temperature of process gas is kept constant at 2.1 MPa and 200 °C respectively [70].

Lee et al. [57] considered the impact of the x position on particle velocity for a bronze powder, the results are shown in Figure 3.14. The authors suggest that a reduction in the mean particle velocity is found at the extremities of the plume which

is attributed to gas flow boundary layers along the nozzle walls, where the gas velocity is lower than the central axis value [57]. Furthermore at the extremities of the gas plume the gas velocity can be expected to decelerate as it interacts with the surrounding atmosphere.

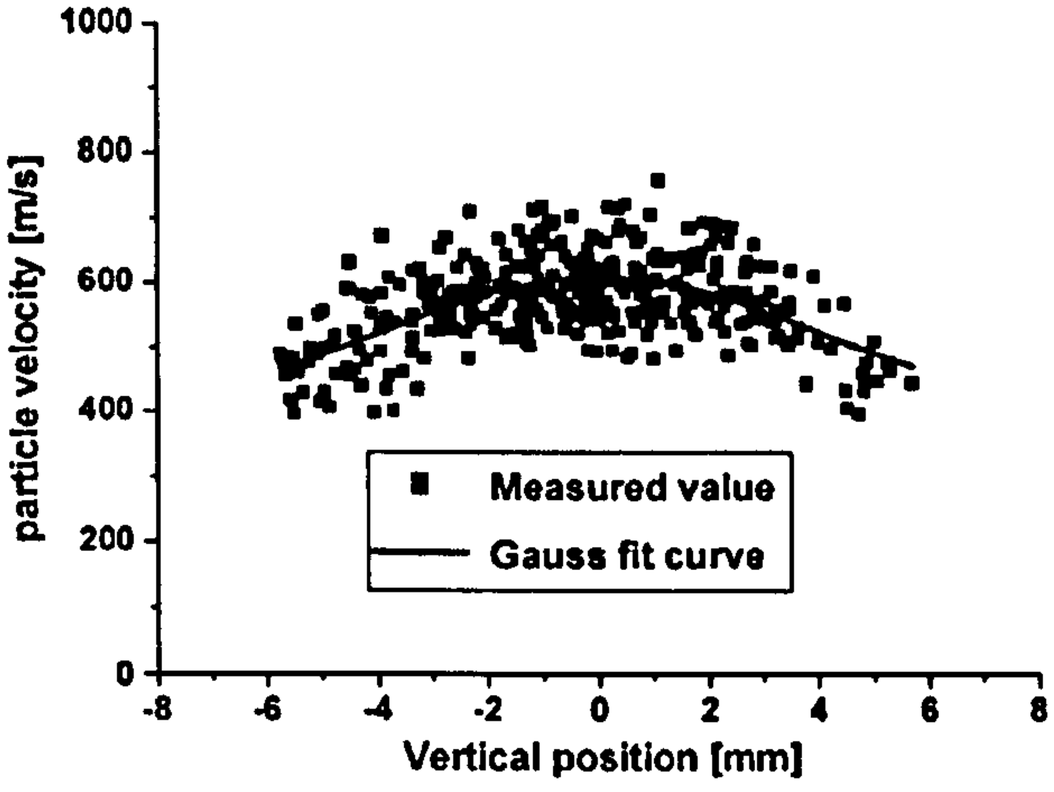

Figure 3.14 – Measured particle velocities using the Oseir SprayWatch system for a bronze powder using nitrogen gas at 2.9 MPa and 400 °C (z = 30mm) [57].

3.5.2.5. The Effect of Particle Shape

Comparisons of the particle velocities for spherical and angular powders were made by Fukanuma et al. [74]. A 316L stainless steel powder available in spherical and angular form of similar size distribution was chosen for the analysis. It was found that angular particles had higher velocities than spherical ones. The author suggests that angular particles are able to reach higher velocities due to a larger drag coefficient and therefore a greater likelihood of momentum being transferred from the gas flow to the particle [74].

3.6. Conclusions of Literature Review

By completing this literature review the following conclusions can be made:

i) The one dimensional isentropic relationships for a compressible flow provide a good starting point for predicting gas velocities within cold spray. However, it is agreed that when predicting particle velocities using the isentropic relationships that an over estimation of particle velocity will be made. This is due to interactions that particles have with the walls of the nozzle, other particles and the external atmosphere are not considered by this modelling process. CFD modelling allows for these effects to be considered. For a heated nitrogen gas flow a 50 m s^{-1} reduction in the predicted velocity of a 15 μm copper particle was found when modelling using the isentropic relationships compared to using CFD analysis [66]

ii) Velocity measurement techniques routinely used do not allow for simultaneous measurement of particle velocity and size.

iii) The majority of modelling results and subsequent velocity measurements have successfully summarised the effect that various spray parameters have on particle velocity.

The following areas may be identified in the science of cold spray where gaps exist in the present knowledge:

i) Few measurements exist of particle velocity and size. This is fundamental to optimising the powder size range of a feedstock to be used for cold spraying.

ii) The majority of modelling carried out to date only allows for the particle velocity at the nozzle exit to be predicted. Despite this, there has been very little literature examining the effect of stand off distance on particle velocity.

The present work will attempt to increase the general understanding of particle diameter on particle velocity and more specifically carry out velocity measurements of a titanium and copper powder used frequently for cold spray. A model, based on the one dimensional isentropic relationships, originally created at The University of Nottingham, will be further developed to improve general understanding of the cold spray process and the factors involved that influence particle velocity.

3.7. Experimental Methods

In this section experimental techniques for characterising the powder powders and measuring particle velocities are described. Section 3.7.1. describes the techniques for characterising the powder morphology, Section 3.7.2. explains the processes for analysing the powder size, Section 3.7.3. describes the cold spray method of coating deposition and finally Section 3.7.4. describes the PIV technique for measuring particle velocities. Definition of the axis system used for PIV measurements for this project is shown schematically in Figure 3.10.

For the PIV analysis a spherical copper and angular titanium powder were employed. The powder suppliers, and manufacturers nominal size distributions, are summarised in Table 3.4. The copper and aluminium powders were both spherical in nature and produced by gas atomisation. The titanium powder was produced using the hydride-dehydride process. This process hydrogenates the Ti6Al4V to make it brittle, milled to produce a fine powder, and finally heated in a vacuum to extract the hydrogen [79].

Material	Nominal Size Range / µm	Supplier
Copper	+5 -25	Sandvik Osprey Ltd. (Neath, UK)
Titanium	+5 -45	Active Metals Ltd. (Sheffield, UK)

Table 3.4 – Powder materials employed in this study.

3.7.1. Powder Morphology

Particle morphology was investigated using a FEI XL-30 (FEI Imaging, Eindhoven, The Netherlands) utilising secondary and backscattered electron imaging techniques (SE and BSE techniques respectively). The powder was applied onto an adhesive

carbon disc and mounted within the scanning electron microscope, SEM. Care was taken to ensure that the powder particles were evenly distributed and that a sufficient number of the particles had not agglomerated so that sufficient images could be captured.

3.7.2. Powder Size Analysis

Particle size analysis of the copper and titanium powders was carried out using a laser diffractometry technique, Malvern Instruments Laser Mastersizer S (Malvern Instruments, Worcestershire, UK). For comparison of the size distribution data measured by the laser diffractometry technique, an automated optical measurement sizing system, the Malvern Morphologi G2 (Malvern Instruments, Worcestershire, UK), was additionally used with the spherical copper powder. Powder size analysis is also able to be measured by manual particle size measurement, using the SEM, and the sizing function of the particle image velocimetry equipment. The operation of the PIV equipment is described in Sections 3.7.4. To manually measure particle sizes, up to 5 captured SE images of the powders, at a magnification of 1500 x, were analysed in ImageJ (U.S. National Institutes of Health, Bethesda, Maryland, USA) using the sizing function. This was a labour intensive method and allowed for typically up to 150 particles to be sized for each powder type.

3.7.2.1. Laser Diffractometry

A schematic of the laser diffractometer sizing system, Laser Mastersizer S, is shown in Figure 3.15. The process is based on the phenomenon that particles in a laser beam scatter light during the sizing operation at angles that are related to the particle size. To prevent particle agglomeration a representative sample of each powder is suspended in fluid, normally propanol, during testing. The laser light is scattered by the particles at various angles and is measured by a multi-element detector and numerical values relating to the scattering pattern are then recorded for subsequent analysis. This is then transformed, using an appropriate optical model, to yield a volumetric particle size distribution.

The system software uses the Mie light scattering theory to obtain the light energy distribution of the particles to produce particle size analyses. This is supported by the ISO-13320 standard, which advises that Mie theory provides a rigorous method for measuring particle diameters below 50 μm. A He-Ne light source with a wavelength of 632.8 nm is used, which means that the measurable particle size limit is 1 μm. Prior to performing the measurements, the system calibration was checked by using a sample powder with known size distribution. After that, two measurements were taken for each powder and the mean calculated.

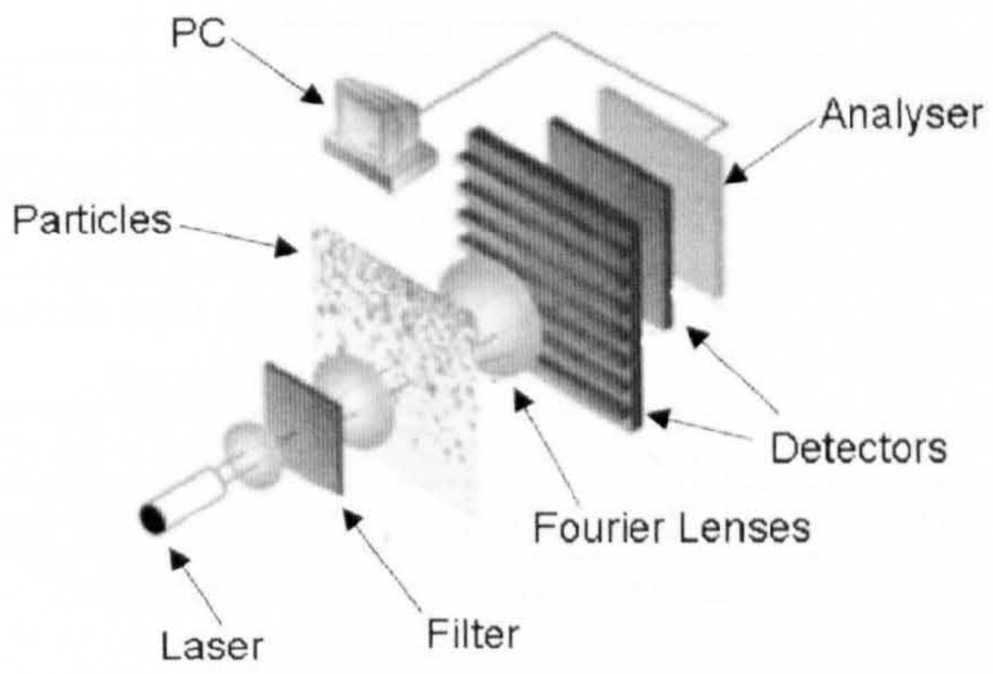

Figure 3.15 – Schematic of the Malvern sizing system.

3.7.2.2. Automated Optical Microscopy

The automated optical microscopy equipment, the Malvern Morphologi G2, differs from the system described above because it uses an optical measuring system to characterise the powder size distribution. A mono-layer of the powder is dispersed onto a glass microscope slide and placed under the optical microscope. The system uses a 2 megapixel CCD to capture images of the individual particles for analysis. An automated controlled 3-axis traverse system allows particle images to be captured at a quicker rate than the laser diffractometer. Additionally, there is reduced risk of particle agglomeration as suspension of the powder in a fluid is not required. The area of each particle is measured and then the diameter for a circle of equivalent area is calculated and recorded. This technique will offer less accuracy for a powder that is not spherical, for example the titanium powder used in this study.

3.7.3. Description of Cold Spray Equipment and Parameter Settings

Cold gas dynamic spraying (CGDS) was carried out at The University of Nottingham using an in-house designed system. A de Laval nozzle, 100 mm in length with a throat diameter of 1.35 mm, was employed. The nozzle was manufactured from hardened steel. Table 3.5 summarises the nozzle dimensions.

Nozzle Dimensions	
Throat Diameter (D*) / mm	1.35
Entrance Nozzle Diameter / mm	13
Exit Nozzle Diameter (D_e) / mm	4
Nozzle exit area (A_e) / Nozzle throat area (A*)	8.79
Length of Converging Section / mm	10
Length of Diverging Section / mm	100

Table 3.5 – The nozzle dimensions (Nozzle I).

Nitrogen was used as the carrier gas and helium for the main driving gas supply. Carrier gas pressures were employed for the different powder types; typically 30 bar and approximately 1 bar above that of the main driving gas. A high pressure powder feeder (1264HP, Praxair, USA) was employed. For the spherical copper powder a '120 hole' feed wheel was used. Due to the angular morphology of the titanium powder the powders flowability is less than that of the copper powder. Therefore for the titanium powder, a '12 slot' feed wheel was used. This feed wheel consists of larger apertures, compared to the '120 hole' feed wheel, and therefore helps to feed the titanium powder to the de Laval nozzle. A powder feed wheel speed of 2 rpm for the titanium powder and 4 rpm for the copper powder was employed. When carrying out PIV analysis, the nozzle was mounted in a horizontal position to allow enough room for the PIV equipment to be installed and operated as described in the next section.

3.7.4. PIV Measurement Methodology

Particle velocities and diameters were measured by PIV. PIV was carried out using the VisiSizer system produced by Oxford Lasers (Oxford Lasers, Didcot, UK). Particle size and velocity distributions were measured by a technique called Particle /

Droplet Image Analysis or PDIA. The system uses a monochromatic light source, to illuminate the spray plume, supplied by a 532 nm Nd:YAG laser connected to a diffuser, and a digital camera to capture images of the spray plume. A schematic of the system is shown in Figure 3.16. The working distance between the camera lens and focusing plane is 37 mm. Lens magnifications of between 1 x and 7 x are available that will alter the field of view (FOV, the captured image width) between 324 and 3910 μm. The smallest object/particle that the camera can resolve is typically $1/200^{th}$ of the FOV and therefore increasing the lens magnification, and reducing the FOV, will increase the ability to resolve smaller objects/particles. For this project a lens magnification of 2x was used giving a FOV of approximately 1134 μm x 1134 μm. This gave an ability to size particles accurately that are between 5.8 μm and 378 μm in diameter.

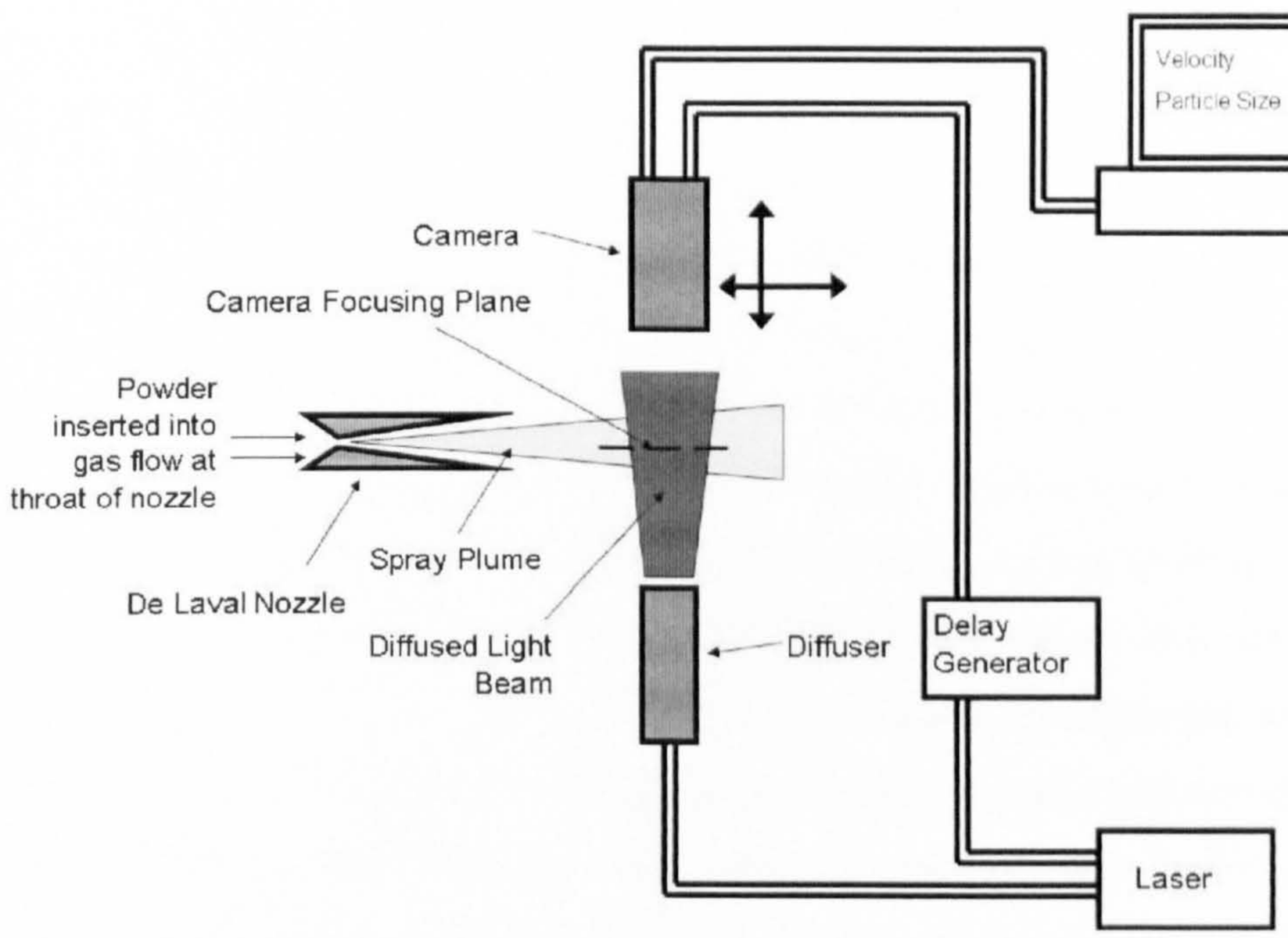

Figure 3.16 – Schematic representation of the PIV system

The laser fires twice for every frame captured by the camera to create a double exposed image as shown by Figure 3.17. The laser illuminates the spray plume for approximately 6 ns so that it is able to "freeze" the particles movement. The delay generator controls the time delay between the two lasers firing and is typically set to 300 ns to allow for sufficient displacement of the particles between the two lasers firing.

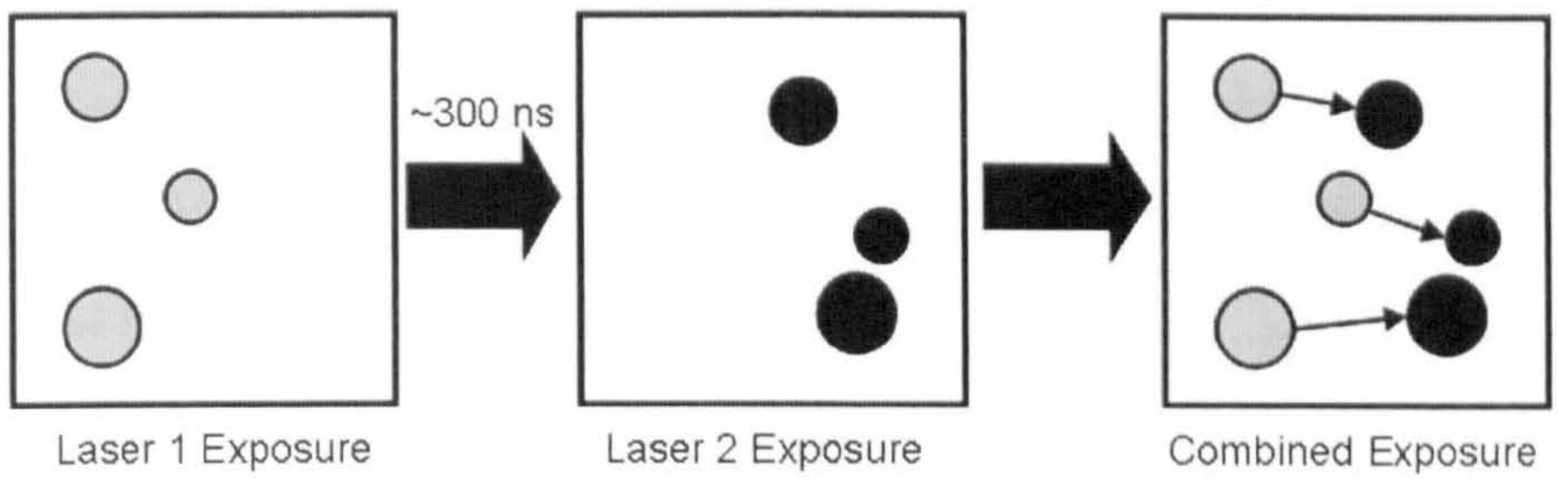

Figure 3.17 – The laser fires twice for every camera exposure resulting in a double exposed image of the particles as they pass through the spray plume.

Captured images are analysed by computer software, VisiSizer v2.093. The computer software detects particles within captured images by the change in contrast between the dark particle and the surrounding brighter background. Particles are paired together, if they are of similar size, and are also located relative to each other so that the particles velocity vector was at most +/- 22.5 ° of the direction of the spray plume itself. Before any further analysis is carried out by the computer software, particles are rejected that fail to meet shape or focus criteria. Shape criteria will reject particles that are not spherical in nature. This is important for rejecting particles that may appear to overlap in the captured images and would therefore skew any size distribution data. Images of out of focus particles arise due to the shallow depth of field of the focussing plane system, approximately equal to the FOV width. Particles that are out of focus are identified by the gradual change in contrast between the dark particle and bright background. Again, this would affect the measured size distribution data, due to particles appearing larger and would also influence the measured particle velocity due to a smaller distance between the pair of particles. With knowledge of the time delay between the laser pulses and the distance travelled by the particles between laser pulses, the computer software is able to calculate individual particle velocities and corresponding particle diameters. Particle diameter is calculated by measuring the area of the particle in pixels. Using equation 3.31 the particle diameter is then calculated for a particle of equivalent circular area.

$$D_a = C \cdot \sqrt{\frac{4A_{pixel}}{\pi}} \qquad \text{(Eq. 3.31)}$$

Where D_a is the particle diameter of equivalent circular area, C is the micron/pixel ratio, and A_{pixel} is the pixel area.

3.7.4.1. Calibration of PIV Equipment

The PIV system relies on knowing the time delay between the firing of the two lasers and accurate sizing of any particles captured within the images. Due to the short time delay between the two lasers firing, ~ 300 ns, it was not possible to check the accuracy of this piece of equipment. Accurate sizing of particles can be carried out if the microns per pixel ratio of the captured images are known. Prior to any experimental work the camera system was calibrated by capturing images of an optical microscope graticule and calculating the microns per pixel ratio. Images of a 1mm graticule, with a graded scale of 10 μm, were captured at each lens magnification used. The graticule length is measured by the supplied Oxford Lasers software and the microns per pixel ratio is calculated. Figure 3.18 shows the linear relationship measured between 1 / lens magnification and the microns per pixel ratio. The measured micron per pixel ratio was found to vary by less than 0.1 μm microns per pixel from the original calibration data supplied by Oxford Lasers. For all experimental work a magnification of 2x was employed, where approximately a 2 % variation between the measured micron per pixel ratio and the data supplied by Oxford Lasers was found.

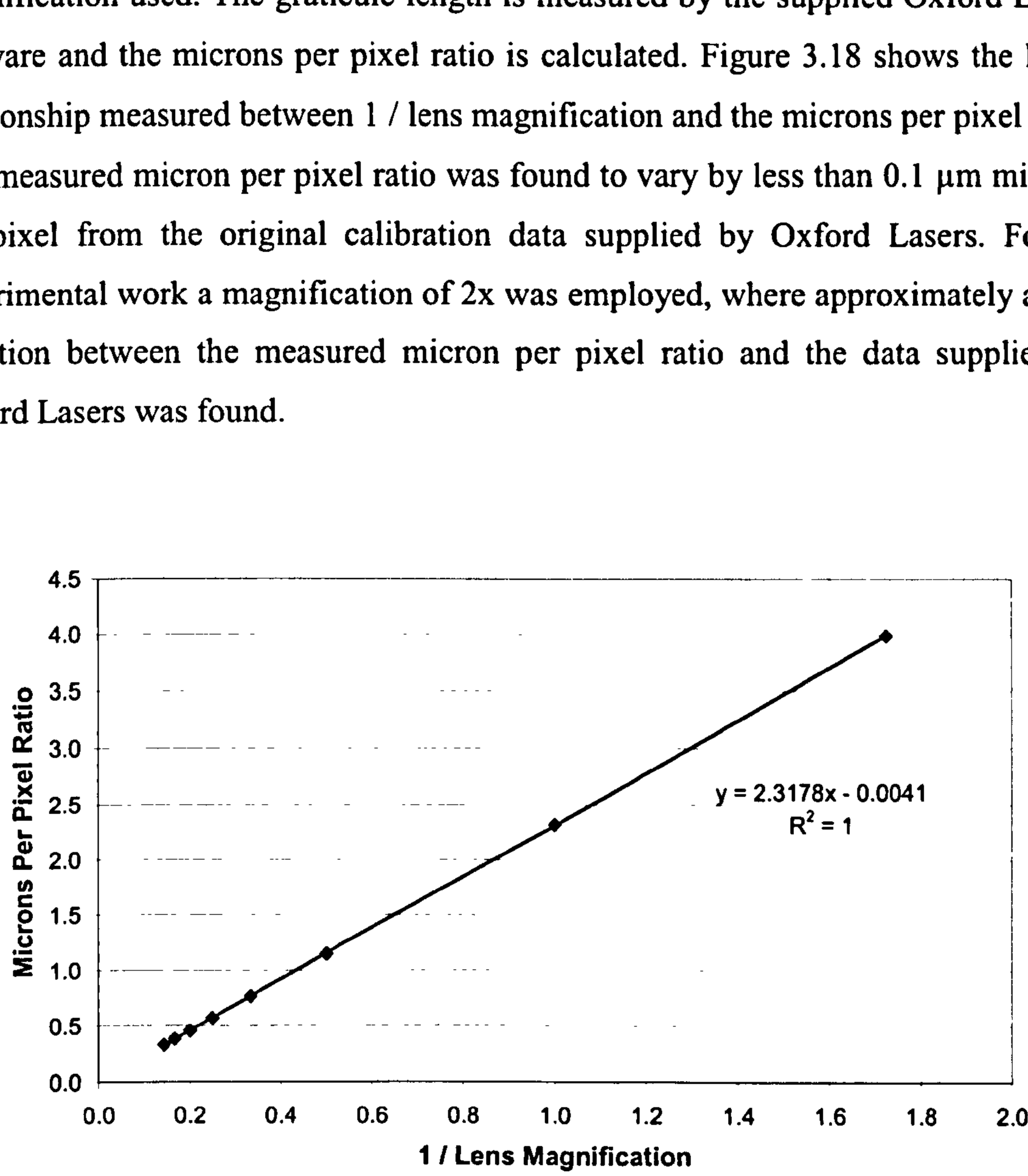

Figure 3.18 – Graph showing the relationship between the lens magnification and the calibrated microns per pixel ratio.

3.8. Experimental Results

This section describes the experimental results for powder characterisation and measurements of particle velocities. Section 3.8.1. compares the results from the methods available for measuring the copper and titanium powder size distributions. Section 3.8.2. describes the velocity measurements utilising the same copper and titanium powders. The influence of particle size, gas stagnation pressure and gas type on particle velocity were investigated and also measuring position and nozzle design.

3.8.1. Powder Size Distribution

There are many different methods for assessing a powder size distribution. These include commercially available size analysis solutions, manual measurements of particle sizes using the SEM and using the size analysis function of the Oxford Lasers PIV system. It would be difficult to compare and assess the results of these methods using the titanium powder due to it having an angular morphology. Powders of an angular morphology are more difficult to size, compared to a spherical powder due to the measurement techniques calculating the diameter of a spherical particle of equivalent area, and therefore the accuracy of each measuring system would be reduced. In an extreme case, a particle of high aspect ratio (i.e., tall and thin), the calculated particle diameter may not necessarily resemble any physical measurement of the particle. Aware of this limitation of the size analysis method measurements were first made with a spherical copper powder before measuring the angular titanium powder.

3.8.1.1. Copper Powder

Figure 3.19 is an SEM image showing the typical size distribution of the spherical copper powder. The majority of the particles are seen to be less than 12 μm diameter.

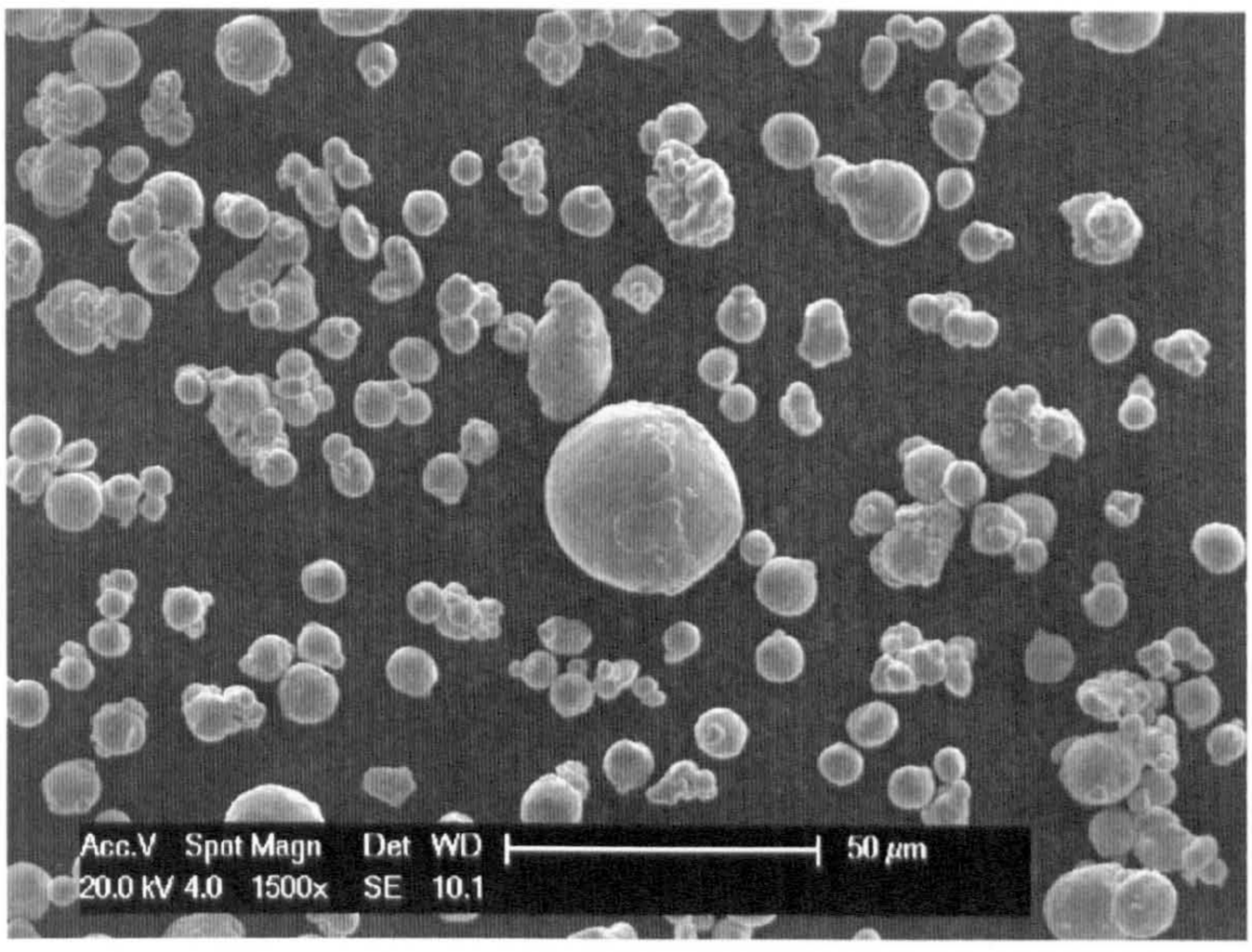

Figure 3.19 – SEM image of the spherical copper powder used for this study.

Figure 3.20(a) shows the size distribution of the copper powder measured by the four methods available; automated optical microscopy, laser diffractometry, PIV, and manual measurement of particles from SEM images. Figure 3.20(a) shows that at 50 % cumulative number% of particles the largest particle diameter was measured by the automated optical microscopy technique (9.5 µm) and the smallest particle diameter was measured by the laser diffractometry technique (6 µm). This 3.5 µm variation in particle size may be explained by errors of the different measuring techniques. The laser diffractometry technique does not measure individual particle sizes but instead calculates the volume percent of bins of particle diameters. Appendix 2 summarises the process to convert from the volumetric size distribution to a number size distribution.

To determine if the size distribution data may be approximated to a normal or log normal distribution the data is re-plotted using a probability axis. A probability axis is symmetrical about the cumulative number 50 % point and scaled in a manner that if a normal distribution is present a straight line is produced. Figure 3.20(b) shows that the data does not fit a normal distribution but may be approximated to a log-normal distribution as shown by Figure 3.20(c).

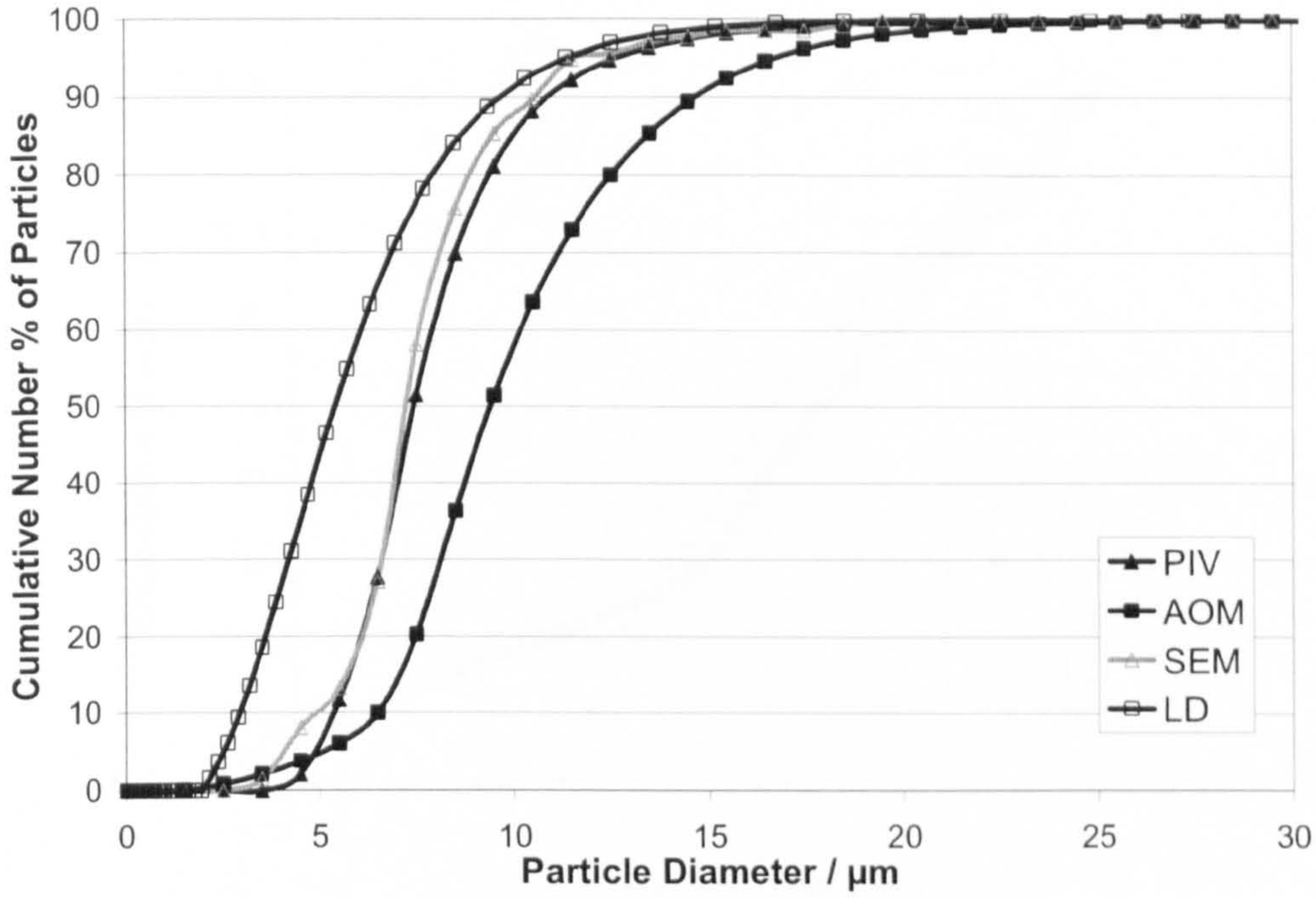
Cumulative Number % of Particles
100
90
80
70
60
50
40
30
20
10
0
0
5
10
15
20
25
30
Particle Diameter / µm
PIV
AOM
SEM
LD

(a)

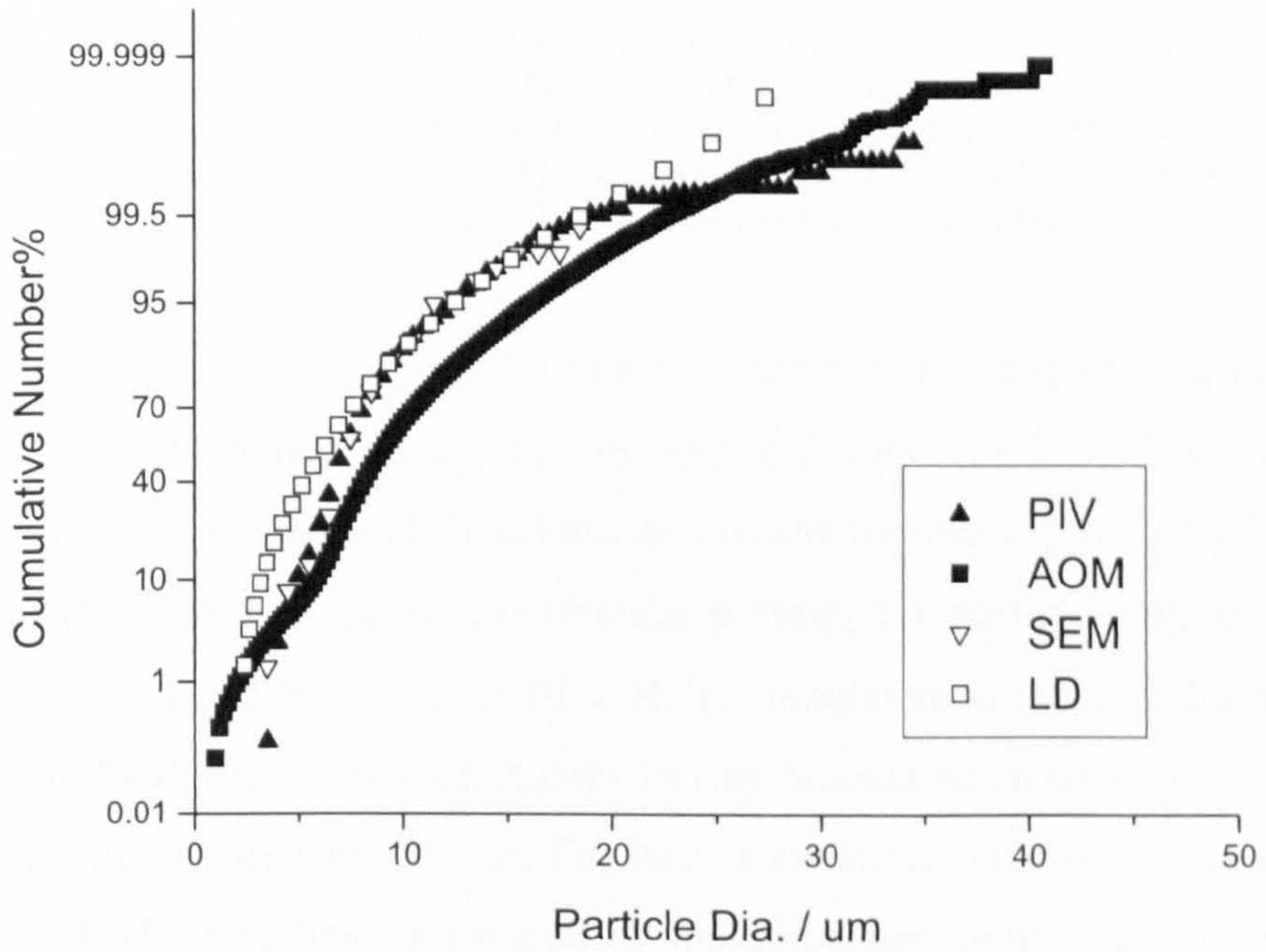
Cumulative Number%
99.999
99.5
95
70
40
10
1
0.01
0
10
20
30
40
50
Particle Dia. / um
PIV
AOM
SEM
LD

(b)

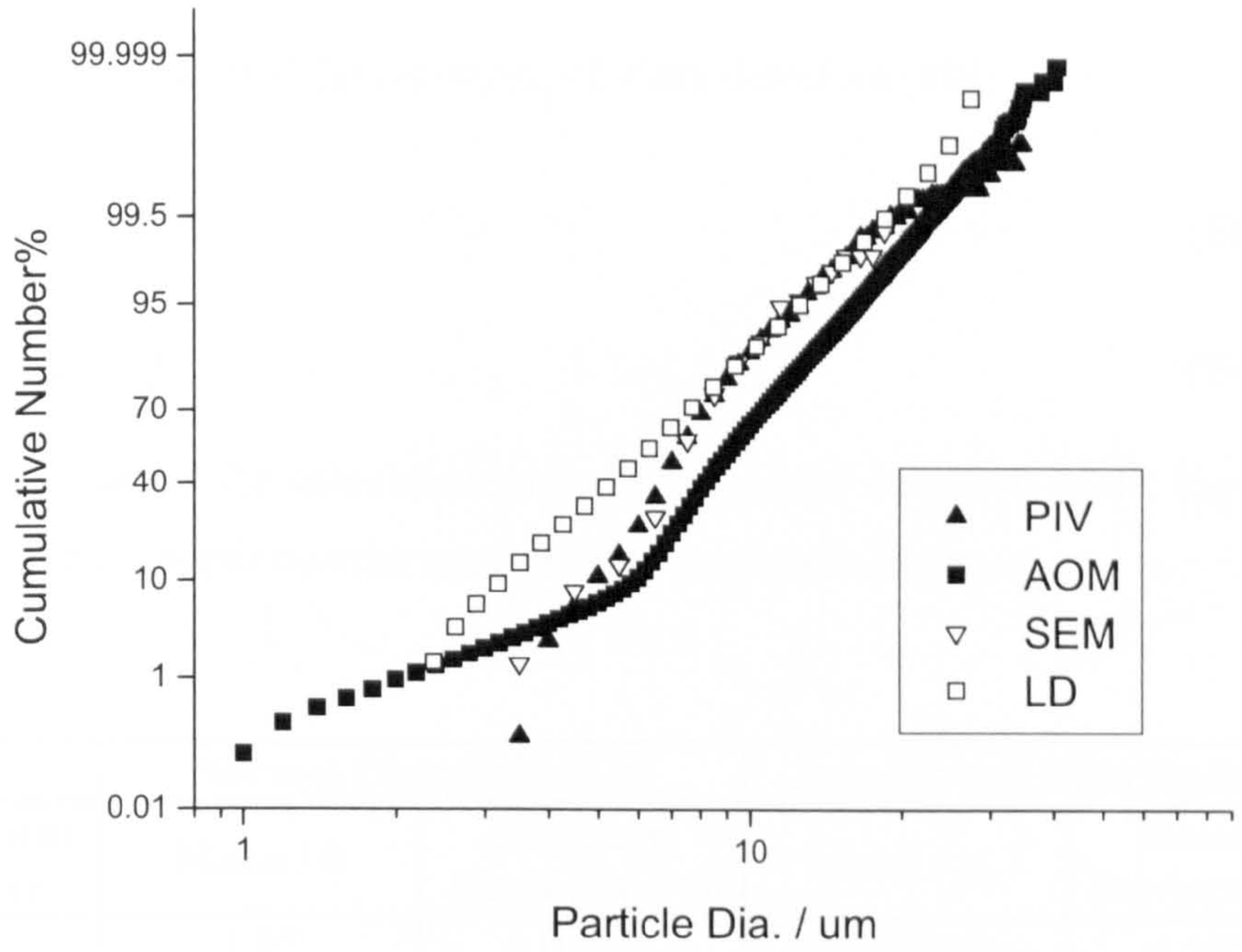

(c)

Figure 3.20 – Graph showing (a) cumulative number percent of particles, (b) normal distribution plot and (c) log-normal distribution plot for the copper powder. Measurements were made using four methods i) PIV – Particle Image Velocimetry, ii) Automated Optical Microscopy – AOM, iii) SEM analysis and iv) Laser Diffractometry – LD. PIV measurements were taken at a stand off distance of 20 mm within the centre of the gas plume.

Generally good agreement between the four measurement techniques is found. Data generated by the automated optical microscopy technique consists of two straight lines indicating two log-normal distributions present for the copper powders size distribution. The first log-normal distribution present, for particles approximately less than 6 μm, is found for less than 10% of the cumulative number % distribution. This is potentially due to the manufacturers sieving process when trying to produce a powder of size distribution +5 -25 μm. The largest variation in the size distribution is found for small sized particles measured by the automated optical microscopy and laser diffractometry techniques and this is due to the laser diffractometry technique originally measuring a volumetric size distribution and errors generated when converting this data to a number size distribution.

The mean and standard deviation of a log-normal distribution may be calculated using the following equations. Firstly, if a normal distribution, w, has a mean, θ, standard deviation, ω, and X is a log-normal random variable then [80]:

$$X = e^{w} \quad \text{(Eq. 3.32)}$$

The mean, μ_x, and standard deviation, σ_x, of X are therefore [80]:

$$\mu_x = e^{\theta + \frac{\omega^2}{2}} \quad \text{(Eq. 3.33)}$$

$$\sigma_x = \sqrt{e^{2\theta+\omega^2}\left(e^{\omega^2}-1\right)} \quad \text{(Eq. 3.34)}$$

Table 3.6 summarises the calculated mean and standard deviation of the log-normal distribution of the copper powder measured by the four techniques.

	Normal Distribution, w		Log-normal Distribution, X	
Measurement Technique	**Mean / θ**	**Standard Deviation / ω**	**Mean / μ_x**	**Standard Deviation / σ_x**
PIV	1.95	0.24	7.26 µm	4.53 µm
AOM	2.18	0.29	9.19 µm	5.81 µm
SEM	1.98	0.24	7.45 µm	4.65 µm
LD	1.79	0.49	6.72 µm	4.59 µm

Table 3.6 – The mean and standard deviation of the copper powder log-normal size distribution measured by the four available techniques.

Measurements made by the PIV system and shown in Figure 3.20 were all made at a stand off distance of 20 mm within a central position of the plume representing a small volume of the plume of approximately 1 mm^3. The total plume width is approximately 4mm and therefore it may be expected that not all particles were to pass through this portion of the plume. This may be due to selective powder feeding or non-uniform dispersion of powder within the plume. Further size analysis of the copper powder was made at different plume and stand off distance positions. Figure 3.21(a) and (b) show the effect of measuring the size distribution at a y-axis position of 0, 0.5 and 1.5 mm at a stand off distance of 20 mm and 1 mm respectively. Once again a log-normal distribution was identified. Table 3.7 summarises the mean and standard deviation of the log-normal size distribution of the copper powder measured at various positions within the plume. In both cases minimal variation in the size distribution was found when the y-axis position was changed. Furthermore in both cases no further large sized particles were found at the extremities of the spray plume.

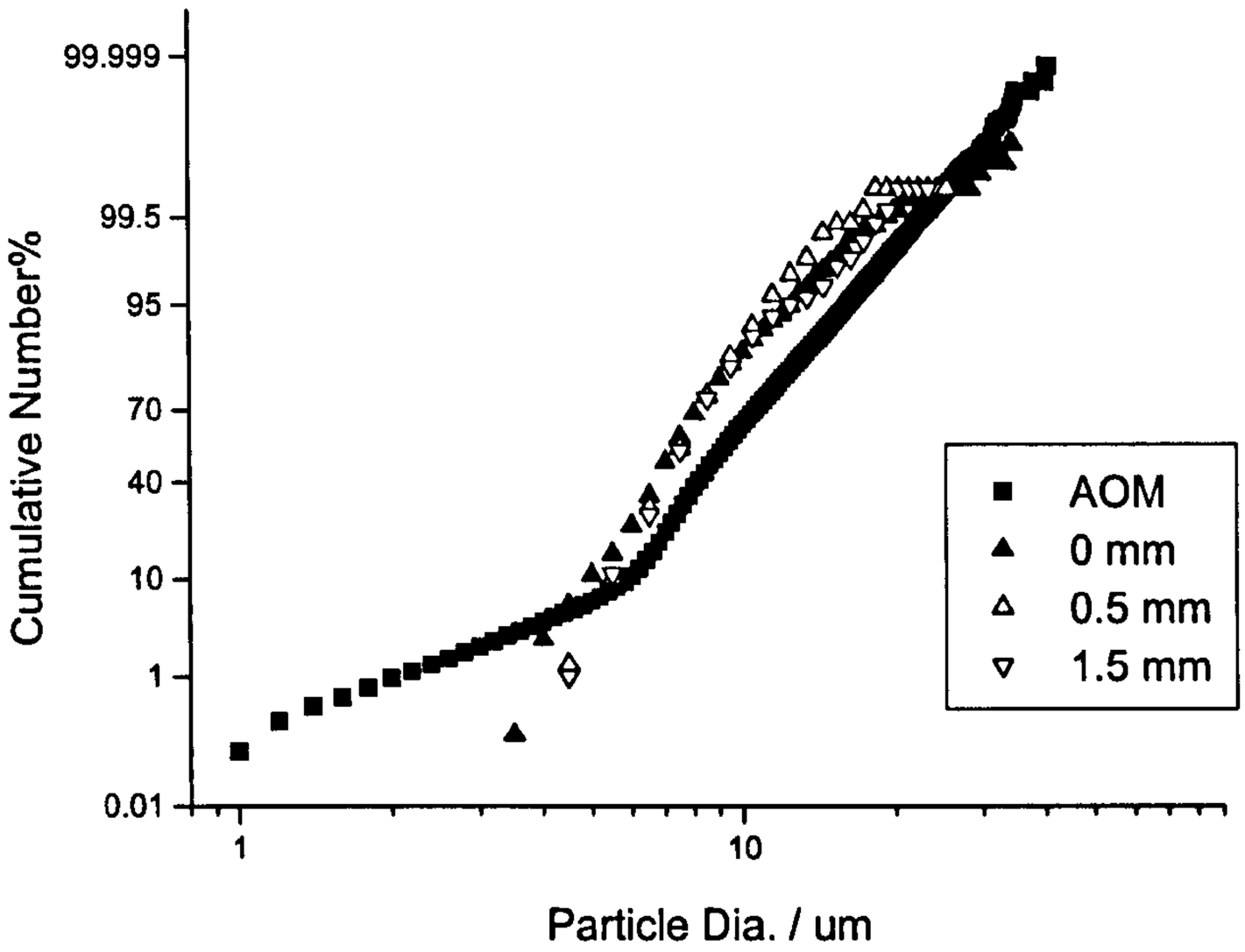

(a)

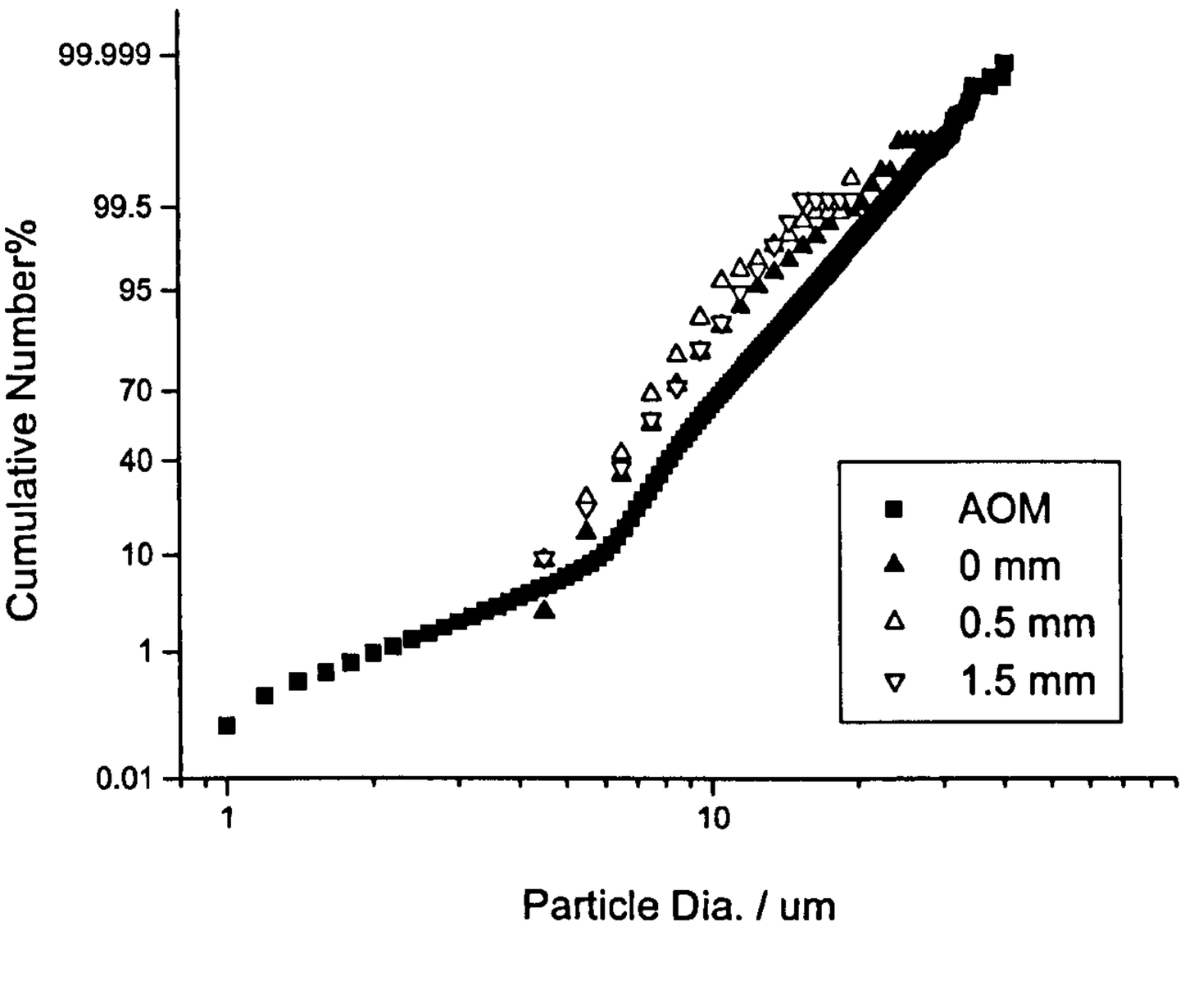

(b)

Figure 3.21 – Graph showing variation in size distribution of the spherical copper powder measured by the PIV system depending on y-axis position. Measurements were made at a stand off distance of (a) 20 mm and (b) 1 mm. For comparison data from the AOM measurement system is also presented.

		Normal Distribution, w		Log-normal Distribution, X	
Measurement Technique and Position		**Mean / θ**	**Standard Deviation / ω**	**Mean / μ_x**	**Standard Deviation / σ_x**
AOM	N/A	2.18	0.29	9.19 μm	5.81 μm
PIV	z = 20 mm y = 0.0 mm	1.95	0.24	7.26 μm	4.53 μm
PIV	z = 20 mm y = 0.5 mm	1.99	0.23	7.50 μm	4.67 μm
PIV	z = 20 mm y = 1.5 mm	2.00	0.24	7.58 μm	4.73 μm
PIV	z = 1.0 mm y = 0.0 mm	1.98	0.26	7.46 μm	4.68 μm
PIV	z = 1.0 mm y = 1.0 mm	1.91	0.32	7.11 μm	4.54 μm
PIV	z = 1.0 mm y = 1.5 mm	1.96	0.35	7.56 μm	4.88 μm

Table 3.7 – The mean and standard deviation of the copper powder log-normal size distribution measured by PIV at various z and y-axis positions. For comparison data from the AOM measurement system is also presented.

3.8.1.2. Titanium Powder

An SEM image of the titanium powder is shown in Figure 3.22. In comparison to the copper powder the angular morphology is clearly identified. There are a greater number of larger diameter particles compared to the copper powder due to the larger manufacturer's size distribution. Size distribution analysis of the titanium powder was carried out using the laser diffractometry and PIV techniques. Results are shown in Figure 3.23(a). In general there is good agreement between the two methods. There is some variation between the data outputted by the two methods. Mainly there are fewer particles greater than 15 μm shown with the data created from the PIV system compared to the laser diffractometry system.

Figure 3.23(b) shows the normal plot of the titanium powder size distribution data produced by the two methods. Similar to the copper powder size distribution a straight line is not produced and therefore the size distribution of powder may not be represented by a normal distribution. Figure 3.23(c) shows the log-normal plot of the titanium powder with data produced by the two sizing methods. A probability axis is used, and in both cases the data follows approximately a straight line indicating that

the size distribution can be approximated by a log-normal distribution. Measurements made by both measuring systems are in good agreement of each other. Table 3.8 summarises the calculated mean and standard deviation of the log-normal distribution of the titanium powder measured by the two techniques.

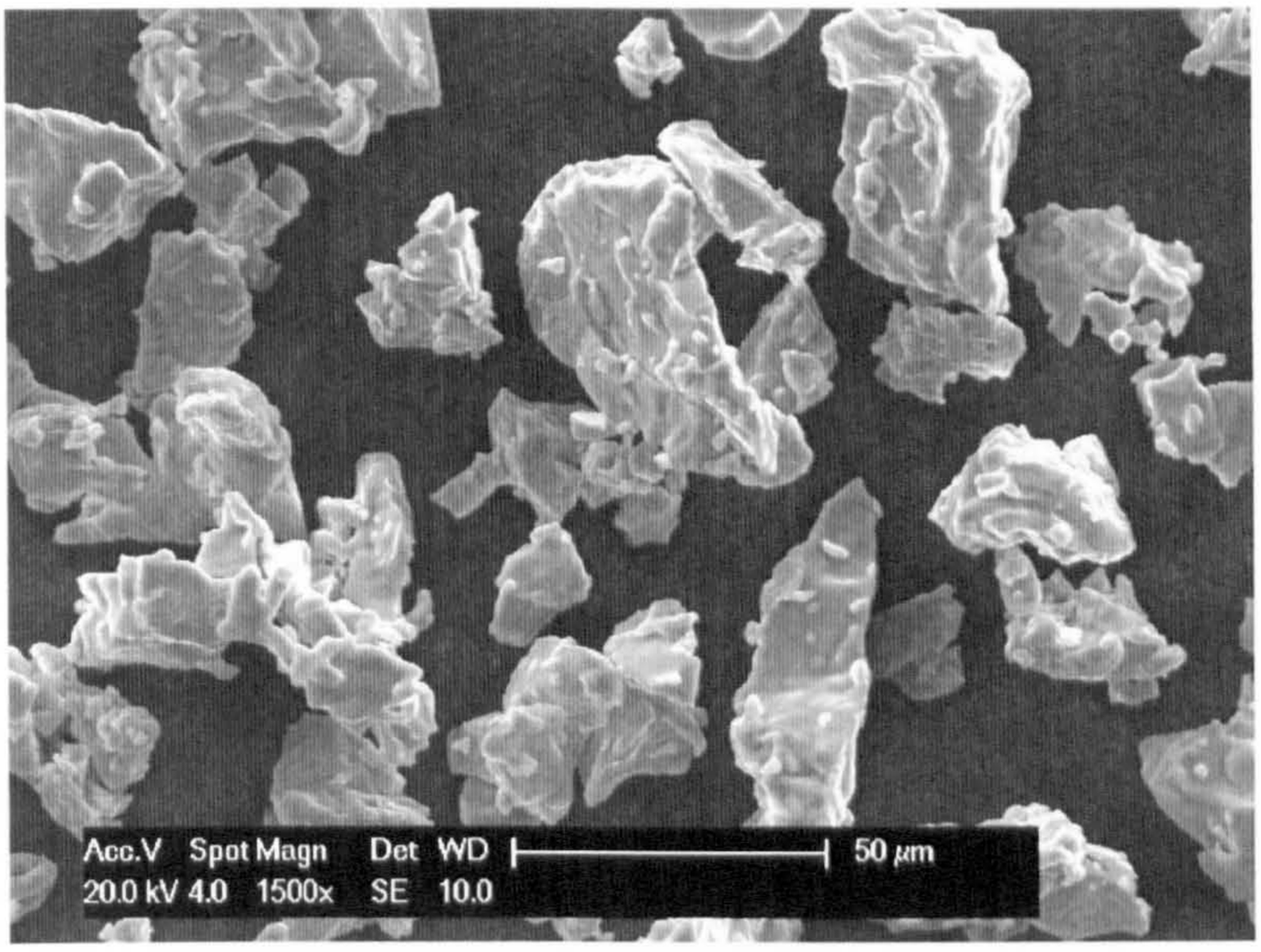

Figure 3.22 – SEM image of the angular titanium powder used for this study.

	Normal Distribution, w		Log-normal Distribution, X	
Measurement Technique	**Mean / θ**	**Standard Deviation / ω**	**Mean / μ_x**	**Standard Deviation / σ_x**
PIV	2.58	0.31	13.90 µm	8.85 µm
LD	2.72	0.50	17.26 µm	11.87 µm

Table 3.8 – The mean and standard deviation of the titanium powder log-normal size distribution measured by the PIV and LD techniques.

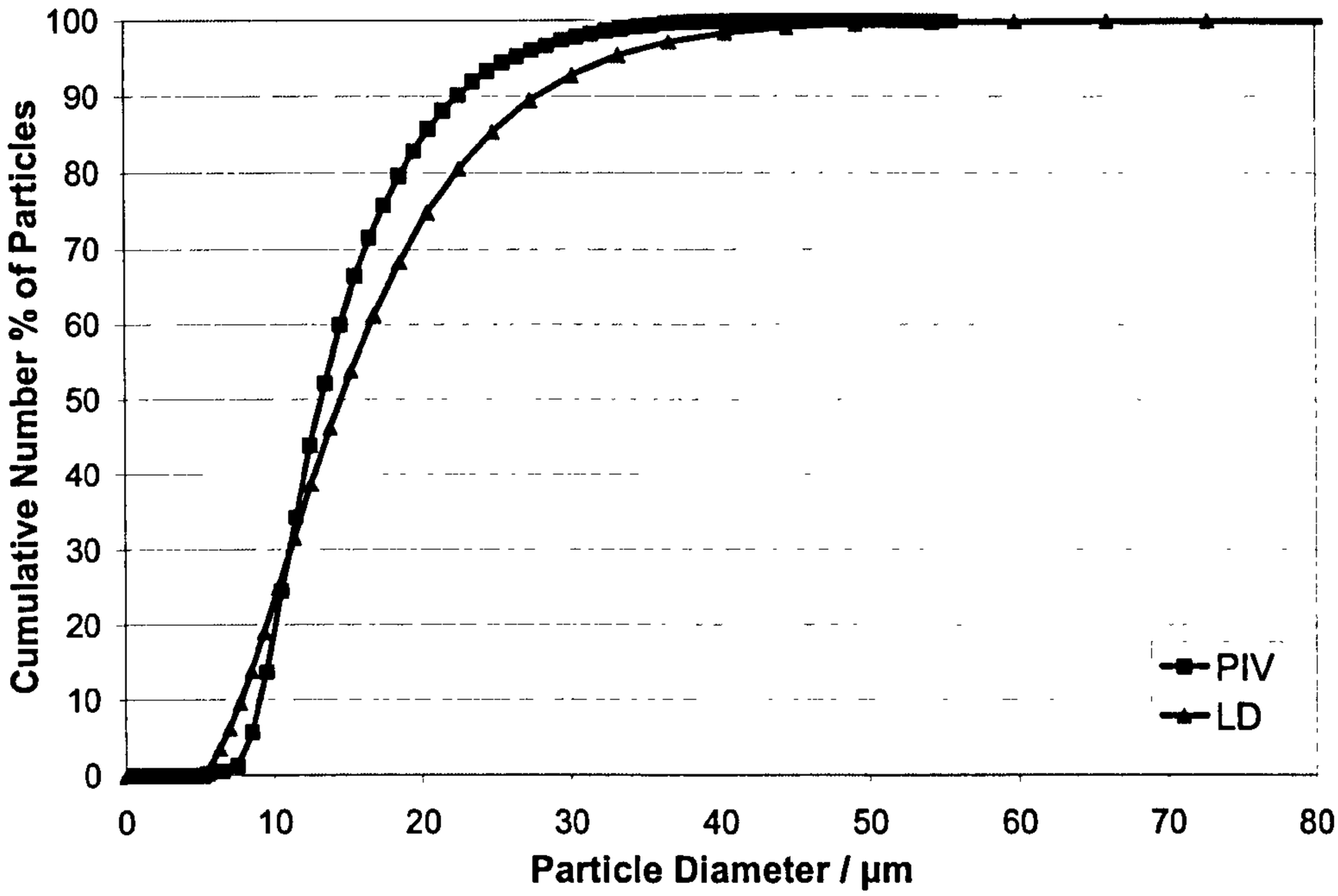
Cumulative Number % of Particles
100
90
80
70
60
50
40
30
20
10
0
0
10
20
30
40
50
60
70
80
Particle Diameter / µm
PIV
LD

(a)

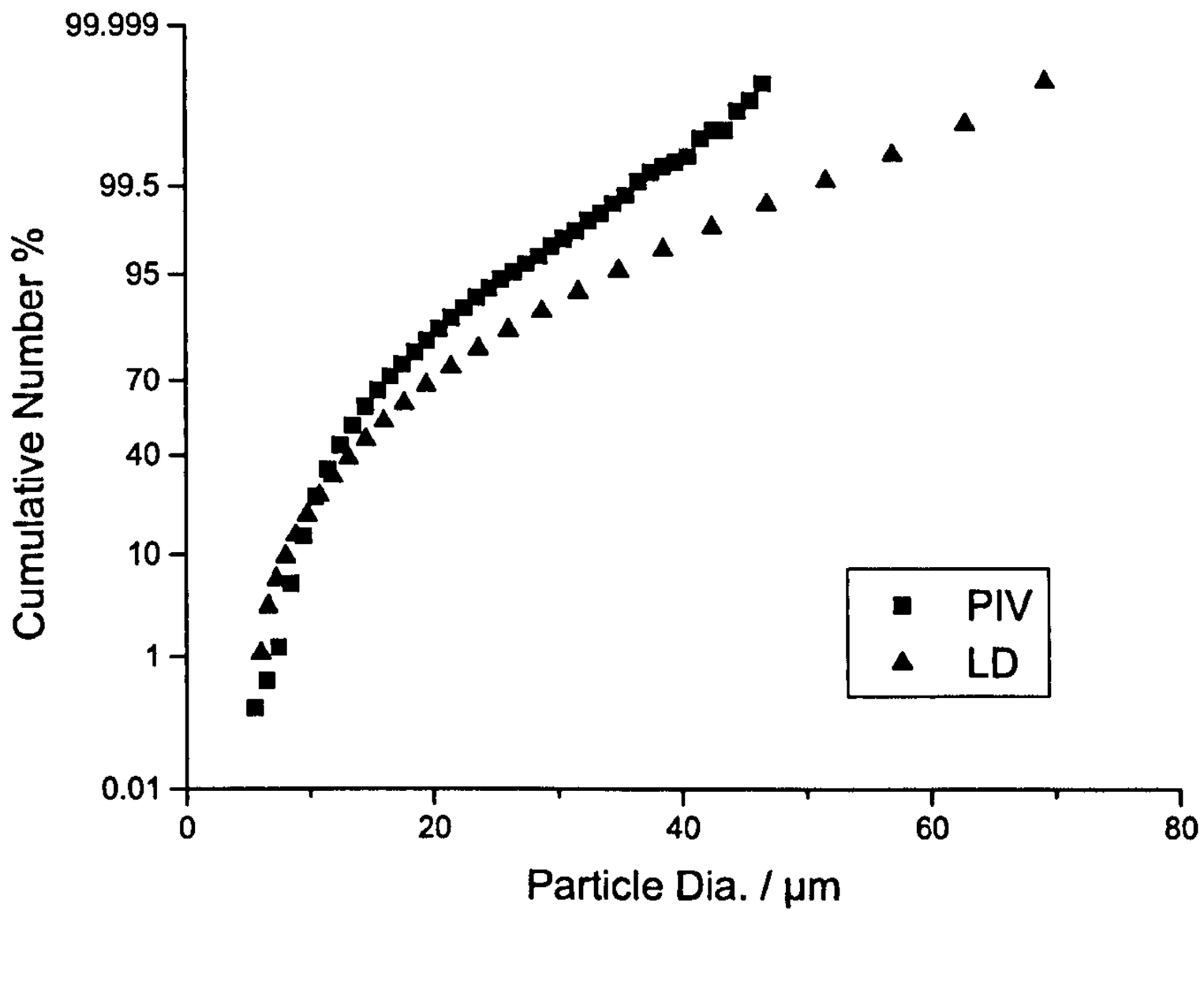
Cumulative Number %
99.999
99.5
95
70
40
10
1
0.01
0
20
40
60
80
Particle Dia. / µm
PIV
LD

(b)

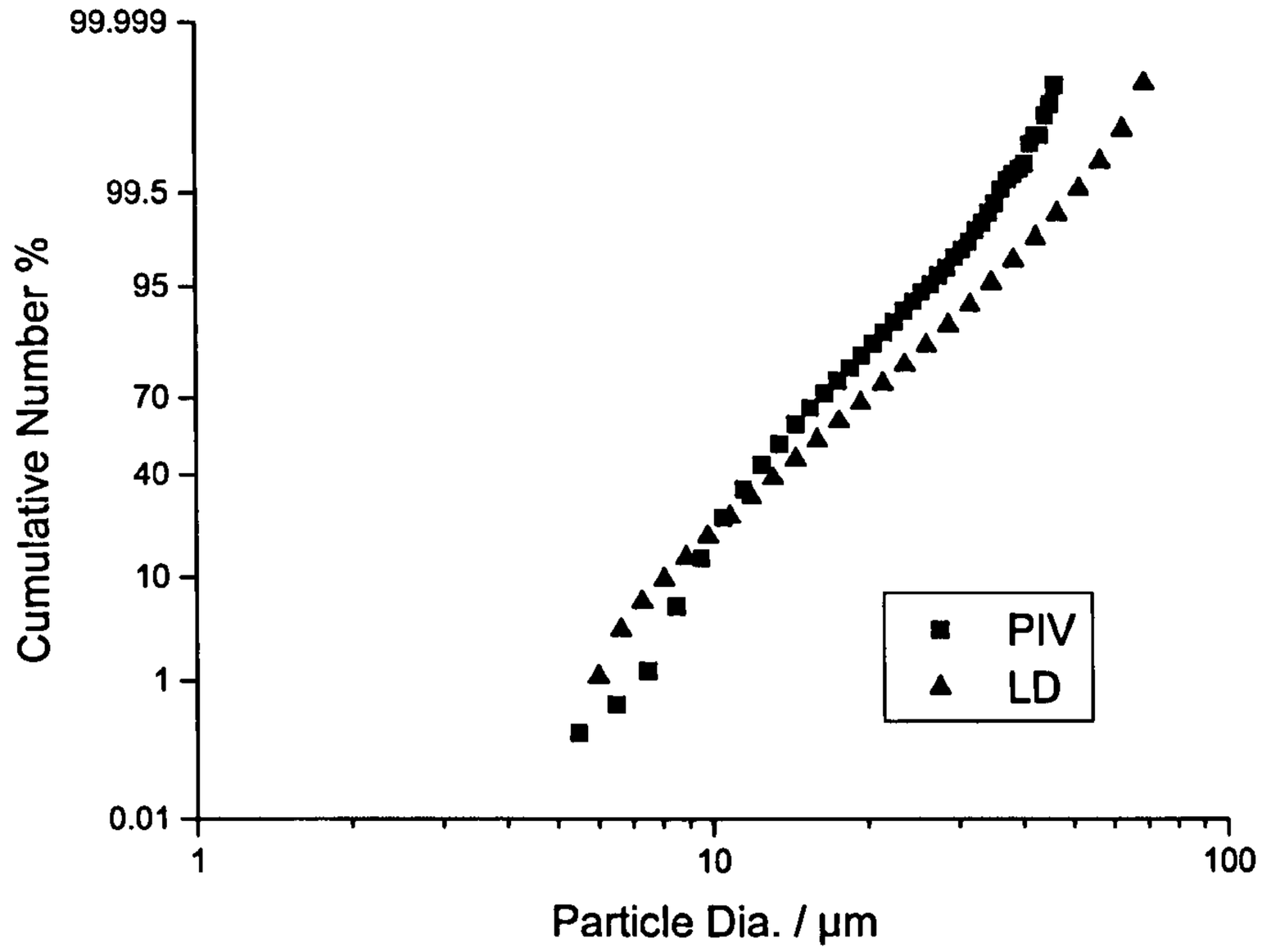

(c)

Figure 3.23 – Graph showing (a) cumulative number percent of particles, (b) normal distribution plot and (c) log-normal distribution plot for the titanium powder. Measurements were made using methods i) Particle Image Velocimetry - PIV and ii) Laser Diffractometry – LD. PIV measurements were taken at a stand off distance of 20 mm within the centre of the gas plume.

3.8.2. Velocity Measurements – Copper Powder

Initial velocity measurements were made using the spherical copper powder with helium and nitrogen as the main carrier gas. For each test 500 individual particles travelling with the gas plume had their velocity and diameter recorded. All measurements were made by a standard nozzle (Nozzle I) unless otherwise stated. The dimensions of the standard nozzle are found in Table 3.5. Results are shown in three main sections. First, Section 3.8.2.1. describes measurements made at a 20 mm stand off distance using room temperature helium and nitrogen gas. Measurements were predominantly made at the centre plume position but variation in particle velocity with varying plume position (y-axis) is measured using nitrogen gas. The next section, Section 3.8.2.2., comprises measurements made at a 1 mm stand off distance, this allows the influence of z-axis position to be determined and also allows comparison with the particle modelling carried out. Again measurements were predominantly made at the centre plume position but variation in particle velocity with varying plume position (y-axis) is measured using nitrogen gas. Finally, Section

3.8.2.3., shows results for a second nozzle design (Nozzle II), tested using the copper powder. The new nozzle uses the same area-expansion ratio but twice the throat area of the original nozzle. Reasons for this choice of nozzle design are discussed in further detail in Section 3.8.2.3.

3.8.2.1. 20 mm Stand Off Distance; Axial Position

Measurements were made using helium and nitrogen gas flows taken at a stand off distance of 20 mm at the centre of the plume. A stand off distance of 20 mm was chosen due to it being the same as regularly used for depositing coatings. Figure 3.24 shows a plot of particle diameter versus particle velocity for 500 individual particles of the copper powder travelling within a helium gas flow at a stagnation pressure of 29 bar. Figure 3.24 shows that far fewer particles are captured for size and velocity measurements once the particle diameter exceeds 15 μm.

Figure 3.24 shows that there is a large variation in particle velocity for particles of similar diameter and this makes it difficult to assess any trends between particle diameter and particle velocity that may be occurring. A method to allow for trends between particle diameter and particle velocity to be recognised is to calculate the average particle diameter and velocity for every 20 individual particle measurements. This was done by arranging the raw particle size and corresponding particle velocity data in order of increasing particle diameter. The data were then grouped into bins consisting of 20 particles and the average particle size and velocity of each bin was then calculated.

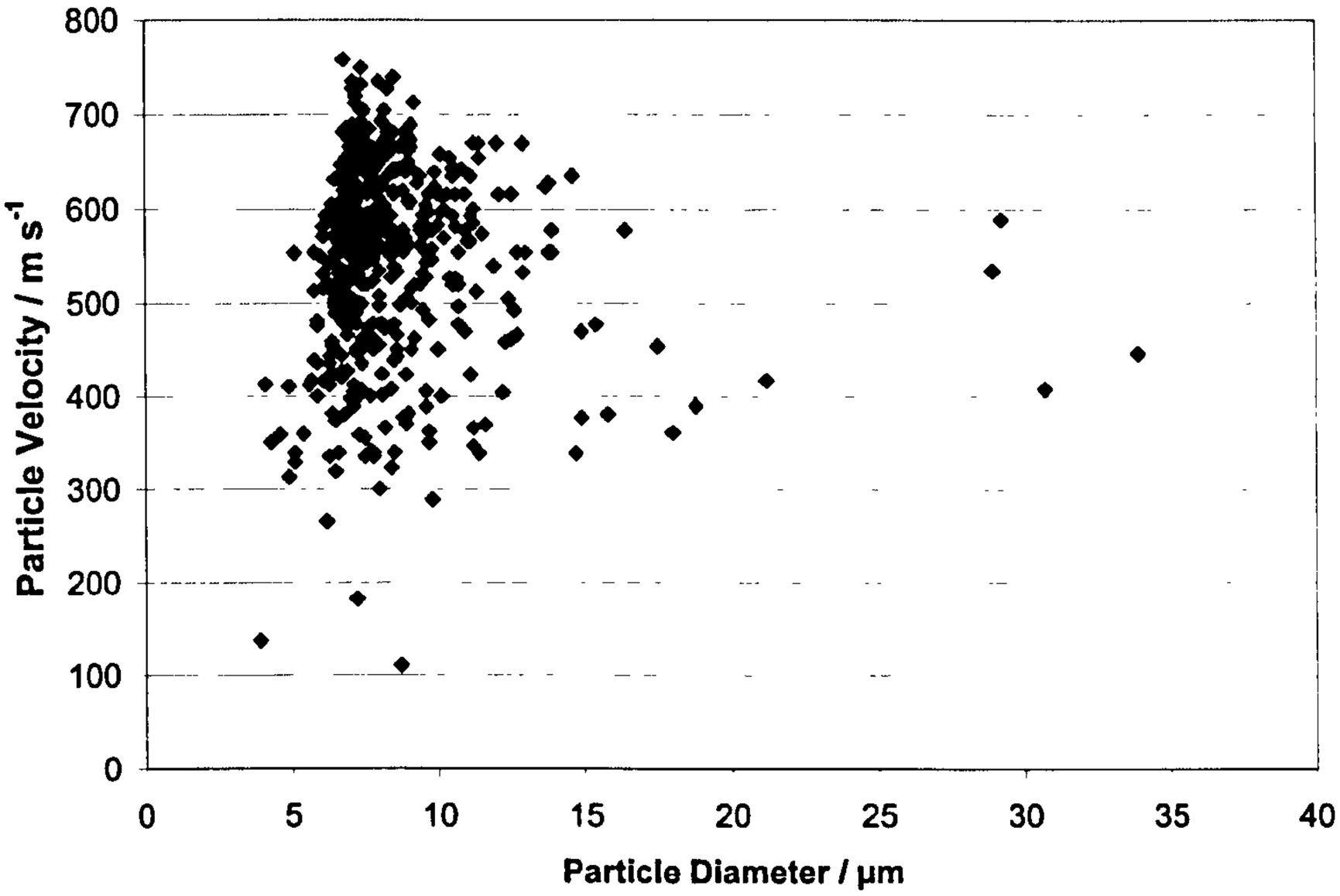

Figure 3.24 – Influence of particle diameter on particle velocity for the +5 -25 µm copper powder travelling with a helium gas flow at stagnation pressure 29 bar. Data for 500 individual particles was collected at a stand off distance of 20 mm and within the centre of the gas plume.

Results for stagnation pressures 10, 20, 25 and 29 bar for helium and nitrogen gas flows are shown in Figure 3.25(a) and (b) respectively. Each data point shown within the figures corresponds to the average particle diameter and velocity for 20 individual particles. Due to the smaller number of particles data captured for large particle diameters the data points become more sparsely populated as the particle diameter increases. The remainder of the particle velocity data for both copper and titanium powders will be displayed using this method. However, graphs of the raw particle velocity data from the main velocity measurements carried out are available in Appendix 3.

When using helium as the main carrier gas (Figure 3.25(a)) there is a gradual increase in particle velocity with increasing stagnation pressure. For an 11 µm particle the average velocity is found to increase from 252 m s^{-1} to 530 m s^{-1} when increasing the gas pressure from 10 bar to 29 bar.

At the lowest helium gas pressure, 10 bar, there appears to be little variation in the particle velocity for a particle diameter of 5 μm or 25 μm. As the gas pressure is increased the influence of particle diameter becomes more apparent and a decrease in particle velocity is found for particle diameters greater than 9 μm. Additionally for gas pressures of 20, 25 and 29 bar a reduction in particle velocity is found for particle sizes of approximately 7 μm or less. This trend did not occur when a helium gas pressure of 10 bar was used.

When nitrogen was used as the main carrier gas (Figure 3.25(b)) lower particle velocities compared to helium were found. This is expected because of the lower gas velocity of nitrogen compared to helium. An increase in particle velocity is found with increasing gas pressure but not to the same degree as found with helium. For example, for an 11 μm copper particle, approximately a 75 m s^{-1} increase in particle velocity is found when increasing the gas pressure from 10 bar to 29 bar compared to nearly a 300 m s^{-1} increase when helium gas is used. For nitrogen gas the effect of particle diameter on particle velocity is less well defined. For all gas pressures there are only minor decreases in particle velocities with increasing particle diameter. Additionally, there appears to be no decrease in particle velocity for the smallest particle diameters which was found with helium gas at all pressures except 10 bar. The velocities attained whilst using helium at 10 bar are similar to those that occur when using nitrogen at all the gas pressures tested.

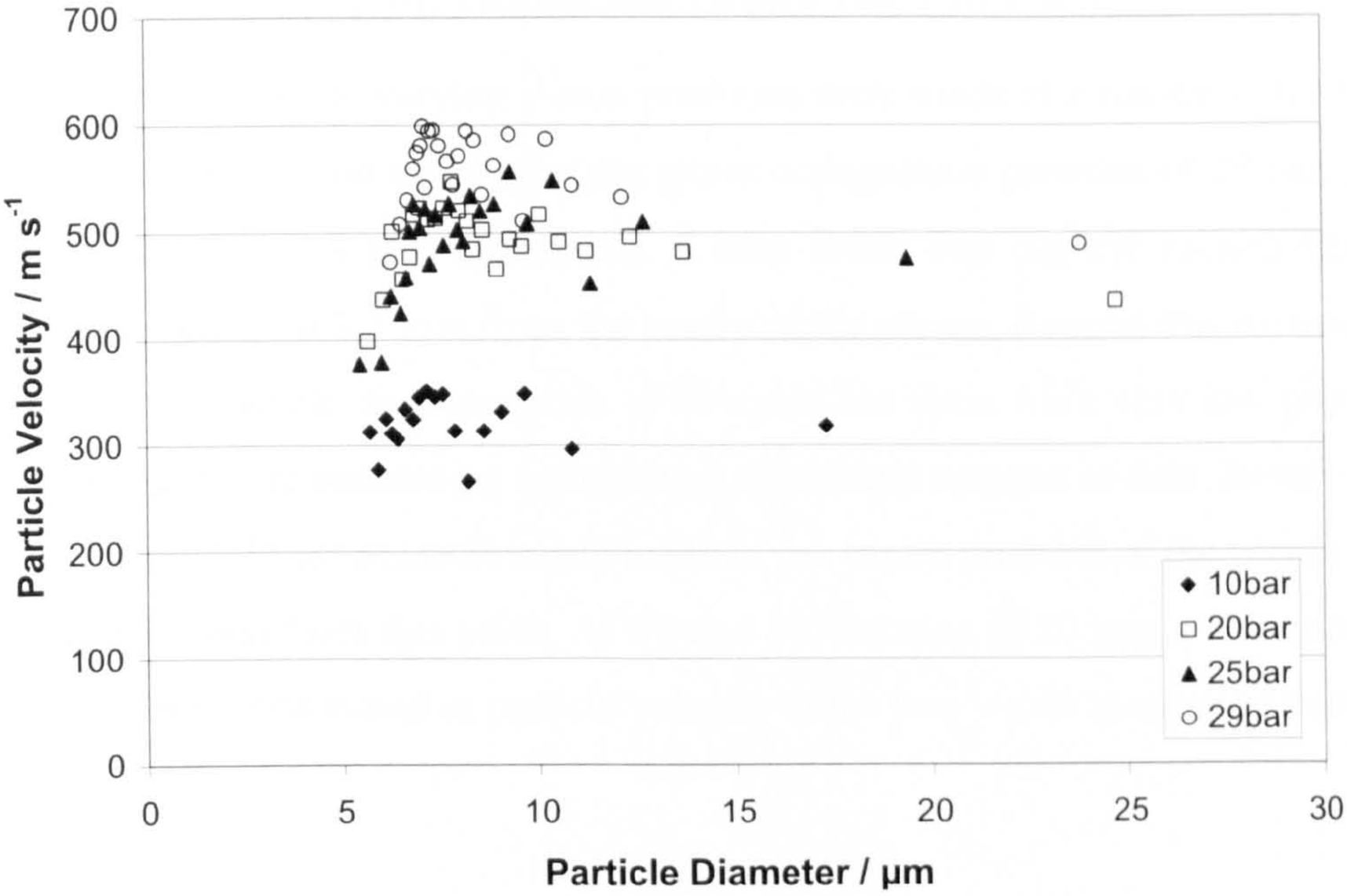

(a)

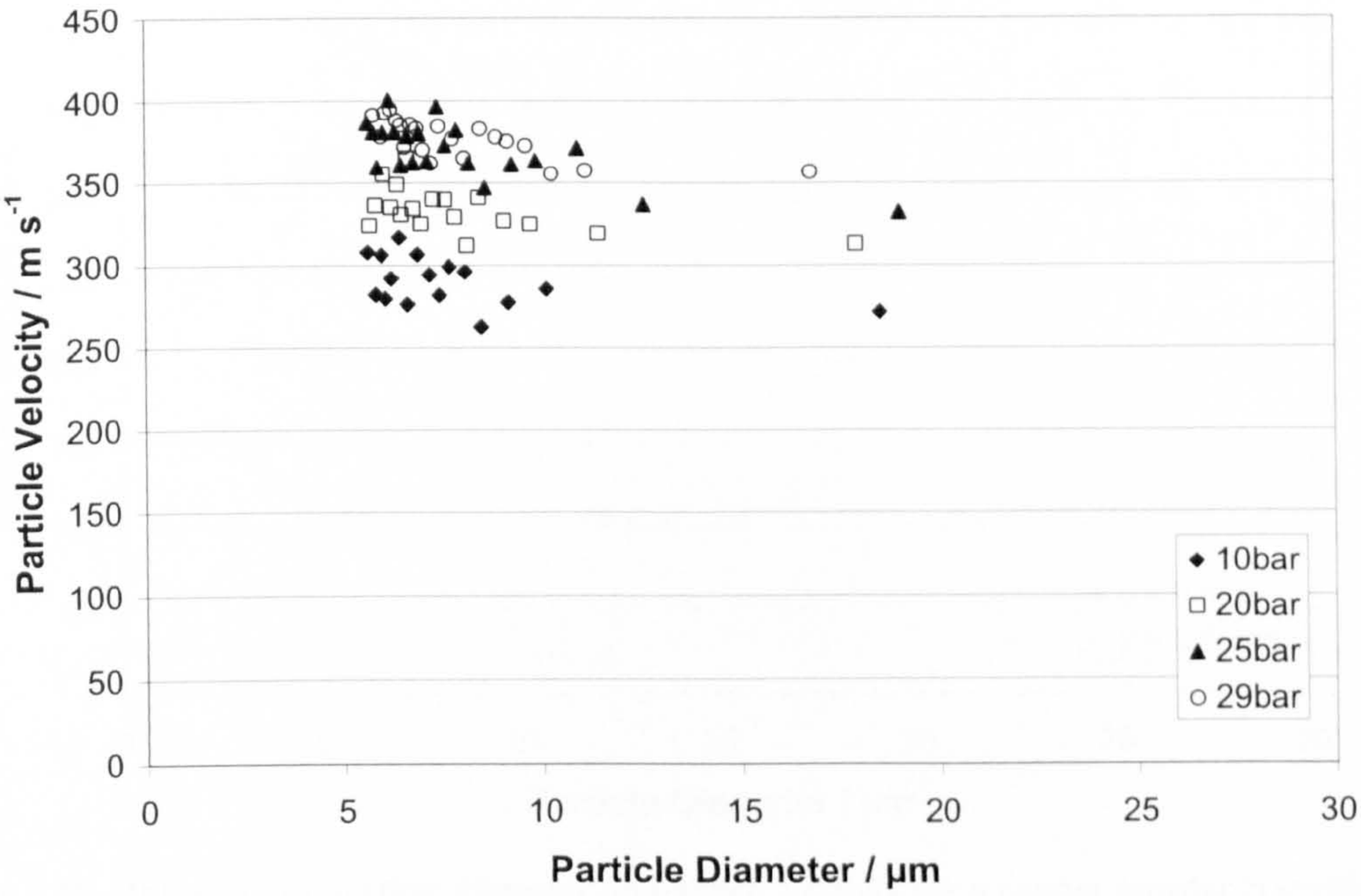

(b)

Figure 3.25 – Influence of particle diameter on particle velocity for a copper powder travelling within (a) a helium gas flow and (b) a nitrogen gas flow. Measurements were made at a stand off distance of 20 mm and results are shown for stagnation pressures 10, 20, 25, and 29 bar. Each data point corresponds to the average particle diameter and average velocity for 20 particles.

3.8.2.2. 20 mm Stand Off Distance; Off-Axis

Velocity measurements at varying y-axis positions were made at a constant stand off distance (z-axis) of 20 mm using nitrogen gas at a stagnation pressure of 29 bar. The y-axis was varied in 0.5 mm increments. It was found that particle measurements could be recorded up to 2.5 mm from the centre of the plume. Beyond this distance it was possible for particle measurements to be made but there were very low particle counts, making it time consuming to capture a significant amount of data. Results are shown in Figure 3.28 for measurements made at the centre position of the plume and at a distance 2.5 mm from this point. At a stand off distance of 20 mm a reduction of less than 100 m s^{-1} was found in particle velocity at the two y-axis measuring points.

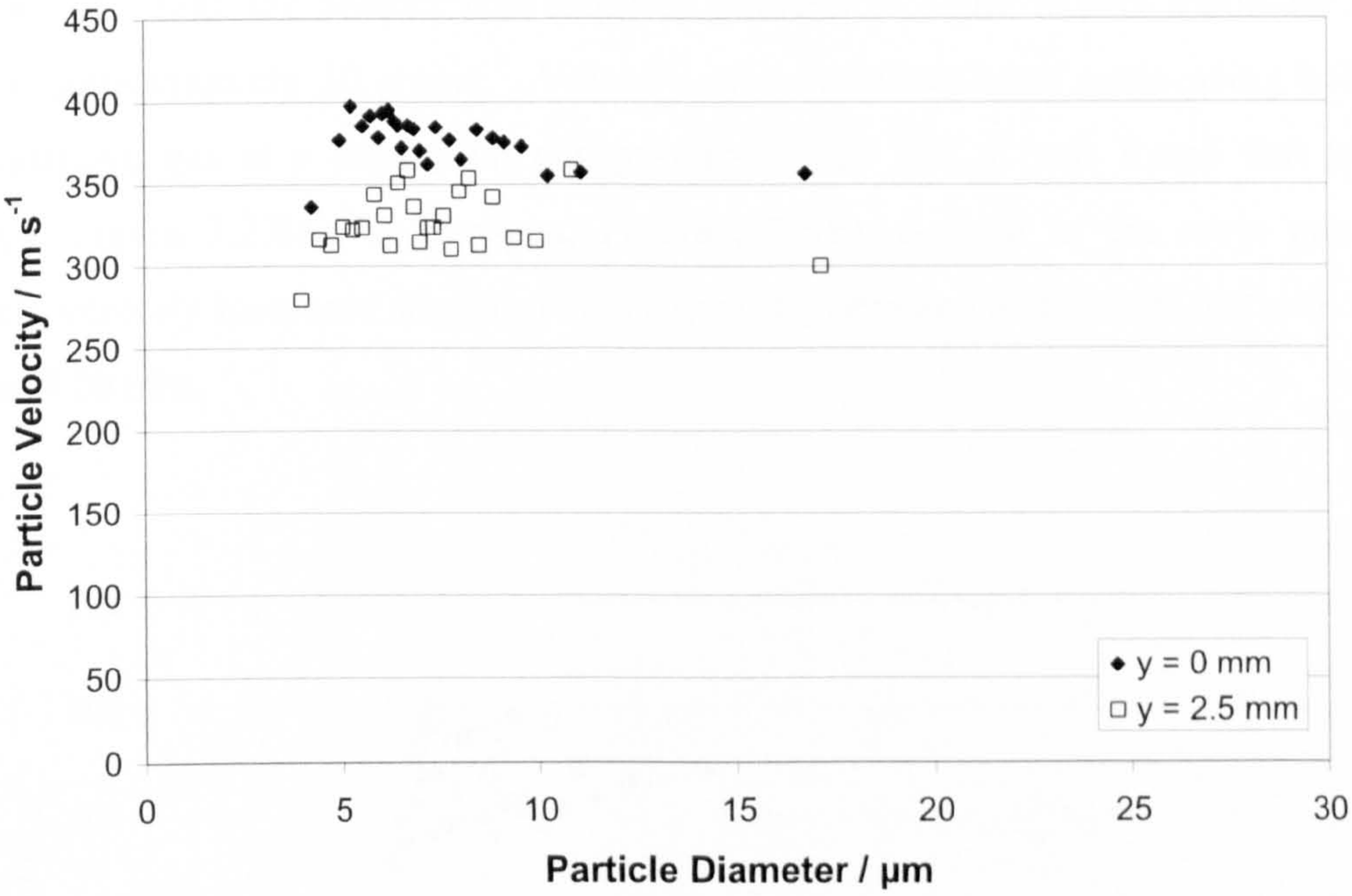

Figure 3.26 – Influence of particle diameter on particle velocity for a copper powder travelling within a nitrogen gas flow and a stagnation pressure of 29 bar at a stand off distance of 20 mm. Results are shown for y-axis positions 0 mm (centre of plume) and at the plume extremity, 2.5 mm. Each data point corresponds to the average particle diameter and average velocity for 20 particles.

3.8.2.3. 1 mm Stand Off Distance; Axial Position

Velocity measurements were made at a stand off distance of 1 mm to establish an understanding of the particle velocity upon leaving the nozzle. Additionally modelling output carried out in this project (Section 3.9.) only allows for particle

velocities to be predicted up to the nozzle exit; therefore to allow comparison between measured velocities and model output it was necessary to capture data as close to the nozzle exit as possible. A stand off distance of less than 1 mm could not be used due to a shadow of the nozzle occurring on the images captured by the PIV system. This meant that the background of the images captured had a varying contrast and therefore made it difficult for the computer software to detect particles accurately. A further complication was that when using a feed rate of 4 rpm, a powder feed rate of approximately 60 g min^{-1}, at a stand off distance of 1 mm (the feed rate used for velocity measurements at 20 mm and deposition of the copper powder) the spray plume was found to be too dense for the computer software to correctly pair particles together and also correctly size particles due to their overlapping in the images. Therefore, for these experiments carried out at a stand off distance of 1 mm, the powder feed rate was reduced to 2 rpm to give a powder feed rate of approximately 30 g min^{-1}. Velocity measurements were made using helium and nitrogen gas at a stagnation gas pressure of 29 bar. It was found that when helium, Figure 3.27(a), or nitrogen, Figure 3.27(b), is used as the main gas the particle velocity increases slightly when travelling between a stand off distance of 1 mm and 20 mm.

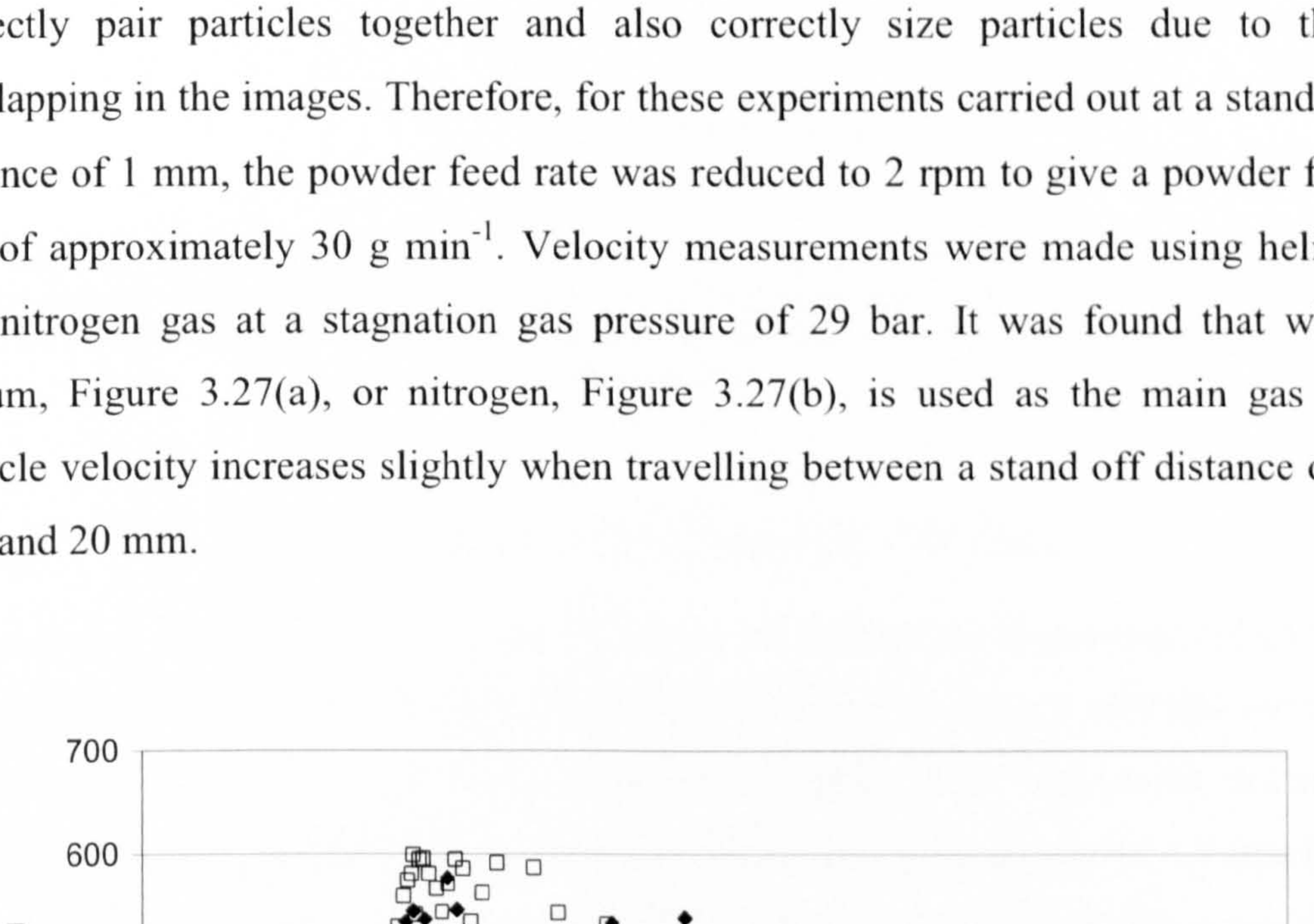

(a)

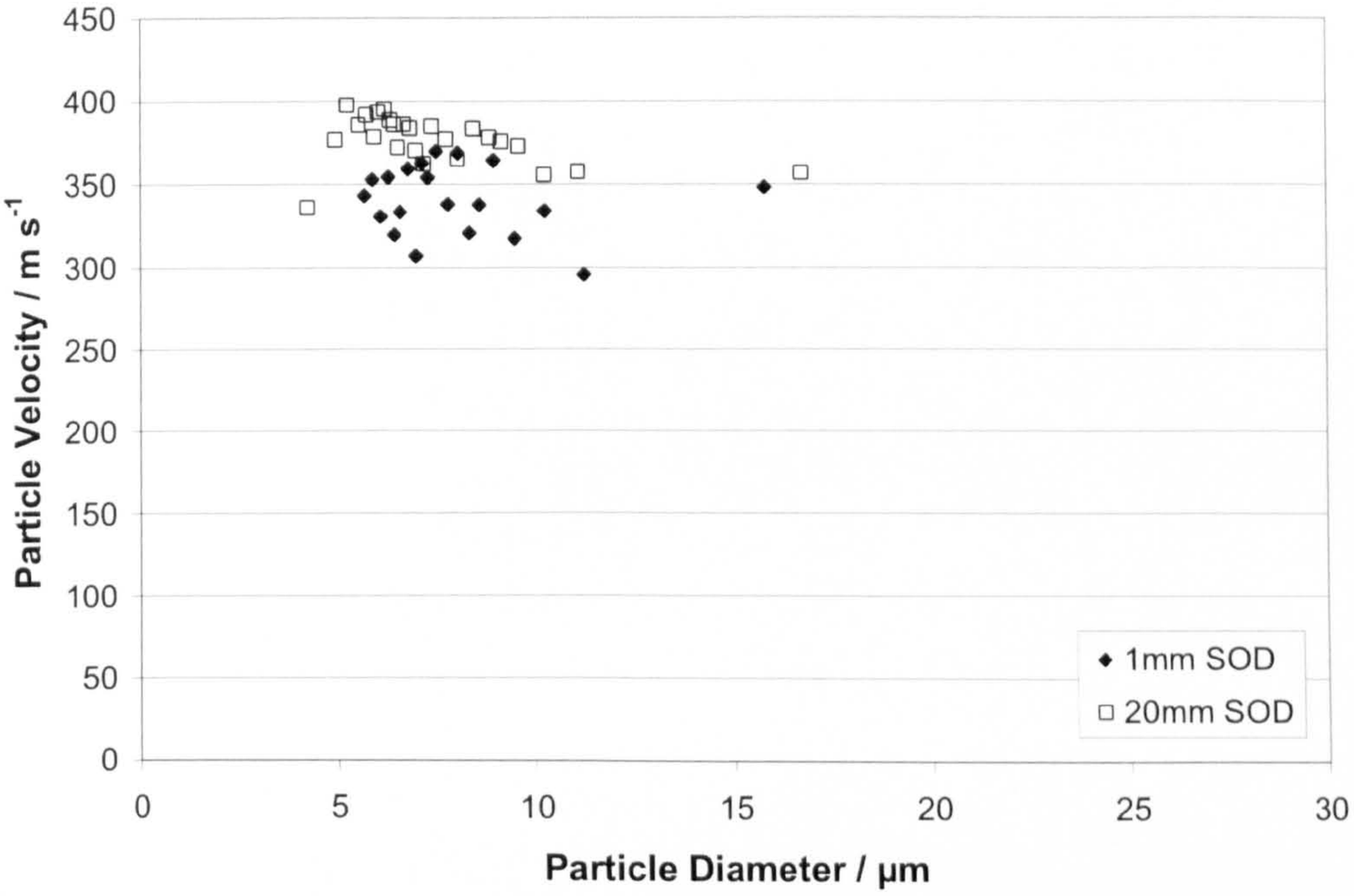

(b)

Figure 3.27 – The effect of stand off distance (SOD) on particle velocity for a copper powder travelling within (a) a helium gas flow and (b) a nitrogen gas flow with a stagnation pressure of 29 bar. Each data point corresponds to the average particle diameter and average velocity for 20 particles.

3.8.2.4. 1 mm Stand Off Distance; Off-Axis

Using a stand off distance of 1 mm the effect of varying the measuring position by changing the y-axis was repeated. Measurements were made at a constant nitrogen gas pressure of 29 bar and results are shown in Figure 3.28. Due to the diverging nature of the spray plume, particle velocities were only recorded up to 1.5 mm from the central portion of the plume compared to 2.5 mm at a stand off distance of 20 mm (Figure 3.26). Up to a 100 m s^{-1} reduction in particle velocity is found at a point 1.5 mm from the centre of the plume.

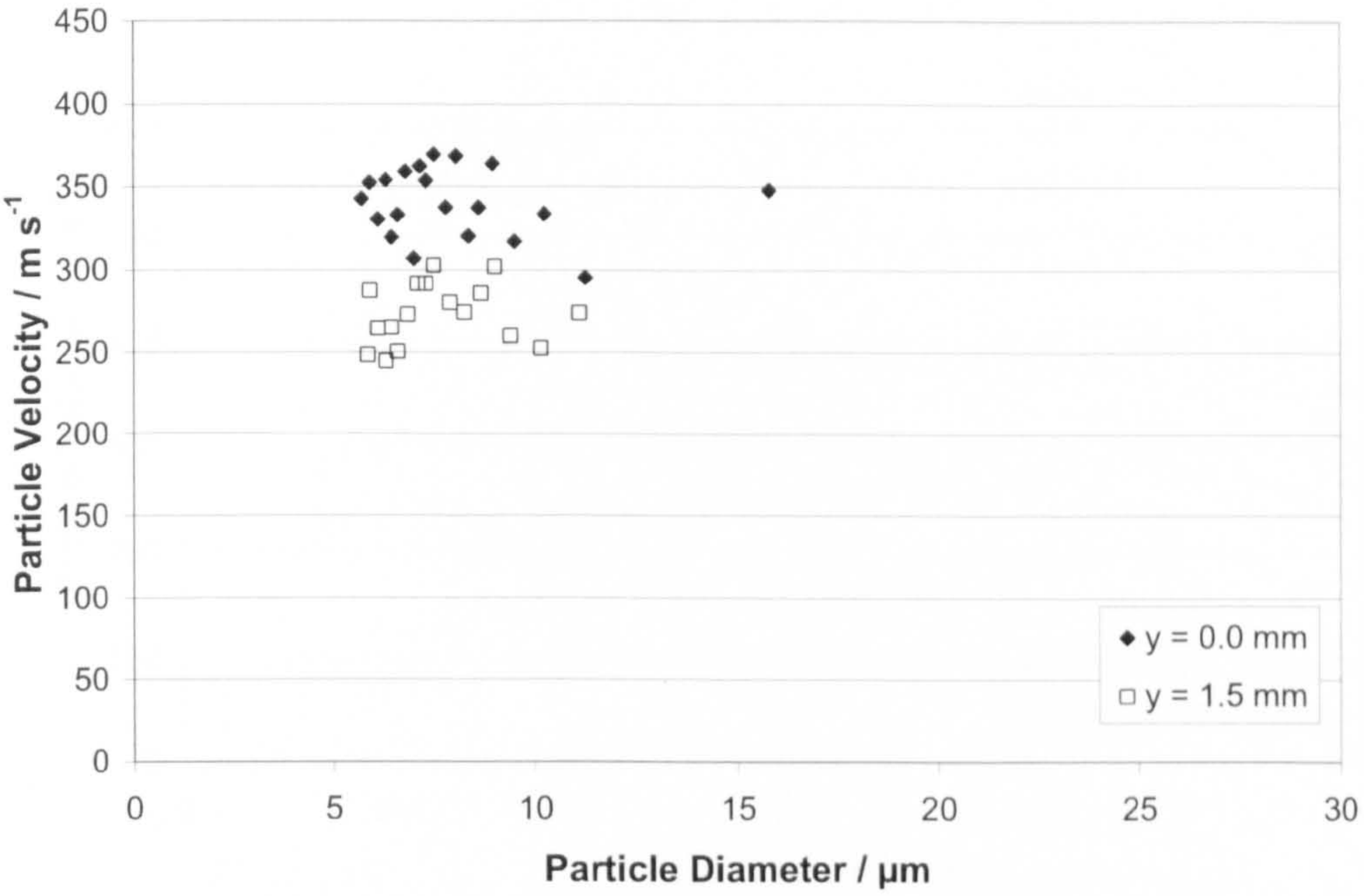

Figure 3.28 – Influence of particle diameter on particle velocity for a copper powder travelling within a nitrogen gas flow and a stagnation pressure of 29 bar at a stand off distance of 1 mm. Results are shown for y-axis positions 0 mm (centre of plume) and at the plume extremity, 1.5 mm. Each data point corresponds to the average particle diameter and average velocity for 20 particles.

3.8.2.5. Nozzle II

A new nozzle was designed so that the effect of nozzle diameter on particle velocity may be investigated. The cross-sectional throat area was doubled, with the aim of reducing the amount of gas flow that would be inhibited by frictional effects from the nozzle walls. The measurements of this nozzle are shown in Table 3.9. The nozzle exit cross-sectional area was also doubled and therefore the expansion ratio of the nozzle remained the same as the previous nozzle. This means that the same gas properties such as velocity and temperature within the nozzle are predicted and therefore further gas and particle modelling would not be required. Velocity measurements were made at a stand off distance of 20 mm at a stagnation gas pressure of 29 bar using helium and nitrogen gas. Results are shown in Figure 3.29(a) and (b) for helium and nitrogen gas respectively. Minimal variation in particle velocity was found between the two nozzle designs when employing the same spray parameters and using either helium or nitrogen gas. This indicates that frictional effects are minimal with both nozzle designs.

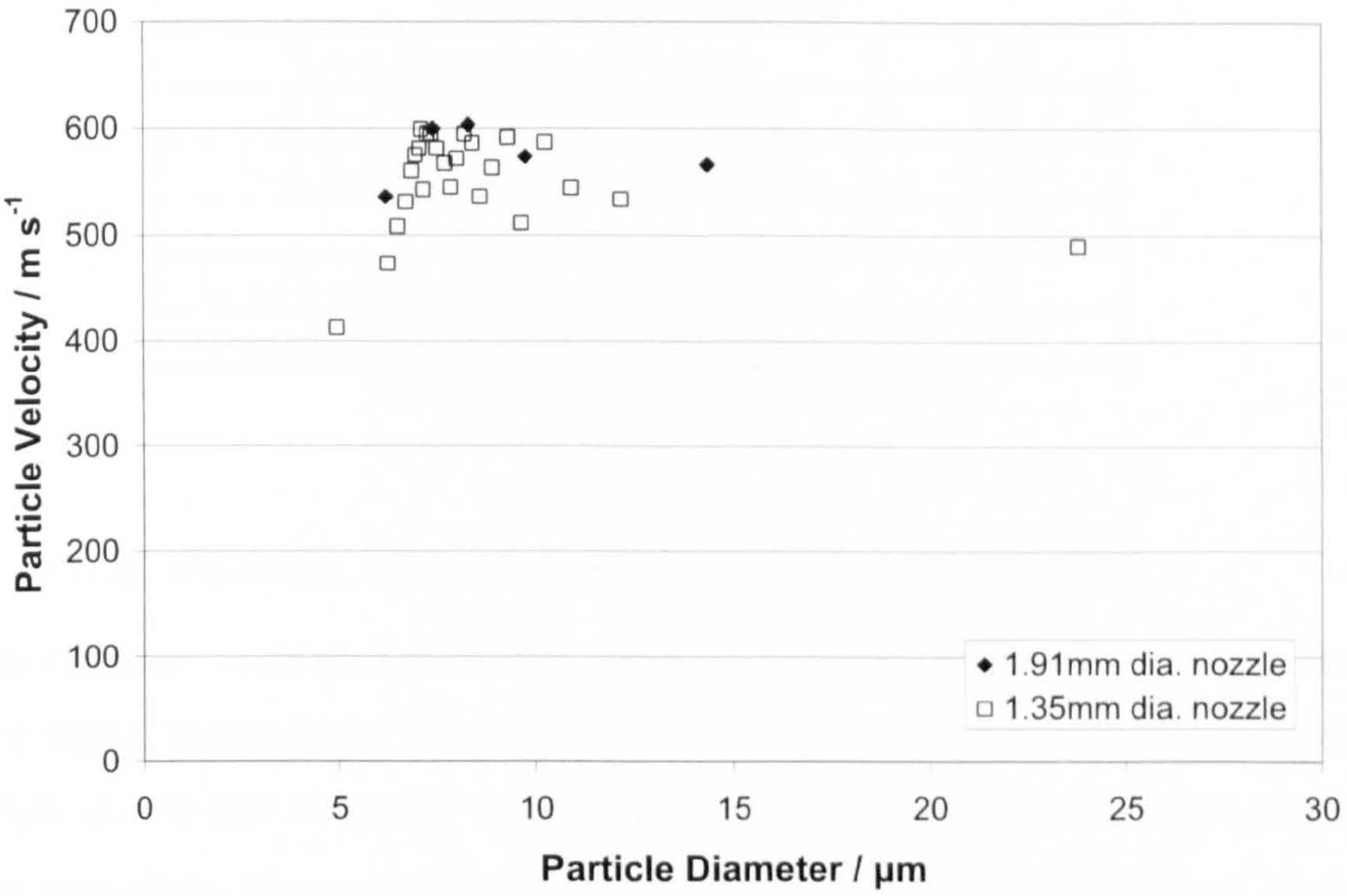

(a)

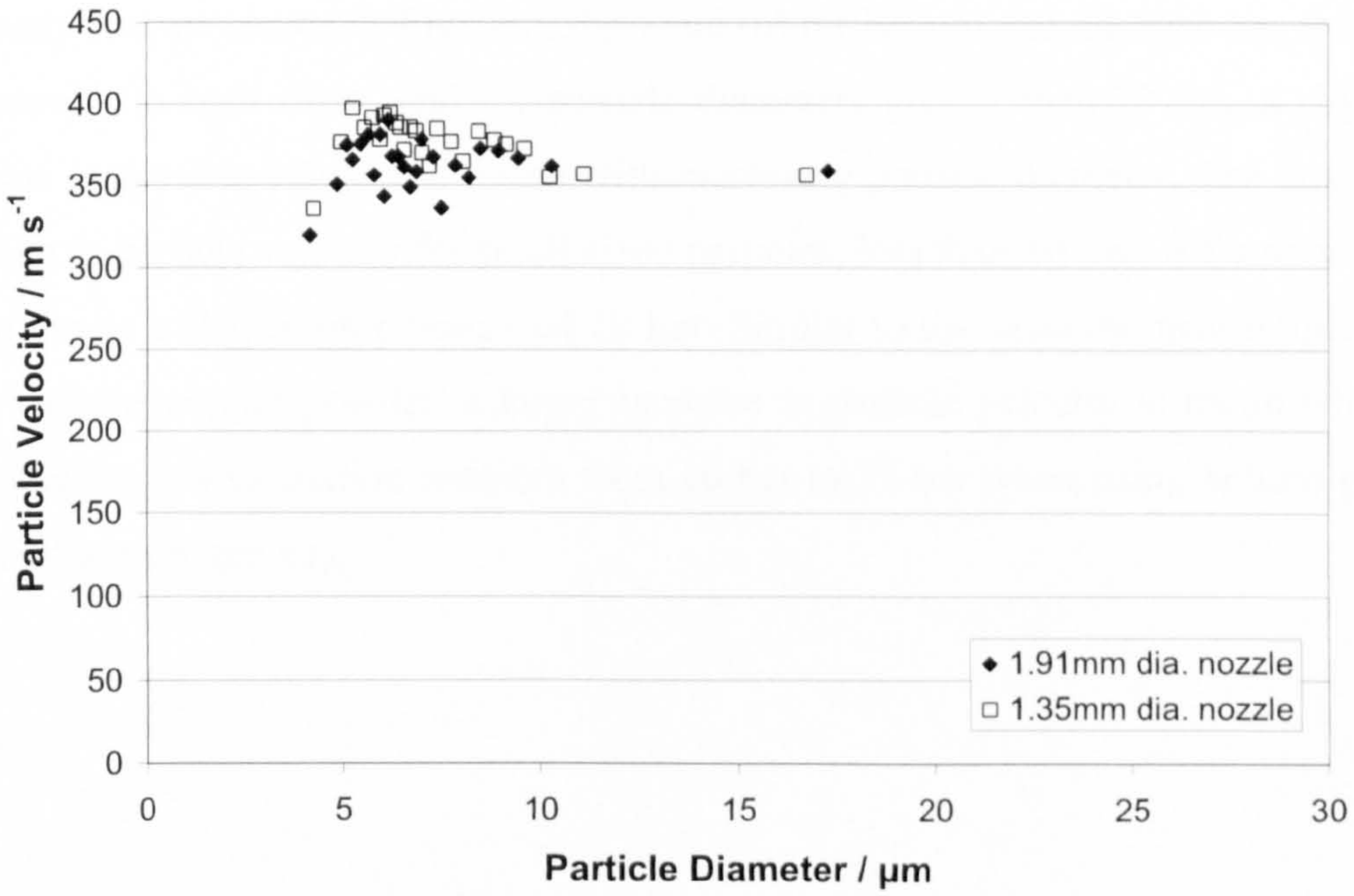

(b)

Figure 3.29 – Effect of particle velocity of a copper powder using nozzles with two different cross-sectional throat areas for (a) helium gas and (b) nitrogen gas. Measurements were made using a stagnation pressure of 29 bar and at a stand off distance of 20 mm. Each data point corresponds to the average particle diameter and average velocity for 20 particles.

Nozzle II Dimensions	
Throat Diameter / A* / mm	1.91
Entrance Nozzle Diameter / mm	13
Exit Nozzle Diameter / A_e / mm	5.66
A_e / A*	8.79
Length of Converging Section / mm	10
Length of Diverging Section / mm	100

Table 3.9 – Dimensions of Nozzle II.

3.8.3. Velocity Measurements – Titanium Powder

Particle velocities were also measured using the titanium powder. For this data there may be some assumptions when correlating the particle velocities to the particle diameters due to the difficulty of measuring the particle diameters of an angular powder accurately. Measurements were carried out at a stand off distance of 20 mm. Results were analysed using the same method as the copper powder described previously and are shown in Figure 3.30(a) and (b) for helium and nitrogen gas flows respectively. In both cases, and for particle diameters greater than 10 μm, a slight reduction in particle velocity is found with increasing particle diameter. The largest reduction in particle velocity for small sized particles, less than 10 μm, is found with helium gas at a stagnation pressure of 10 bar. Similar to the velocity measurements made with the copper powder, a larger increase in particle velocity is found when increasing the gas stagnation pressure from 10 bar to 29 bar when using helium gas compared to nitrogen gas.

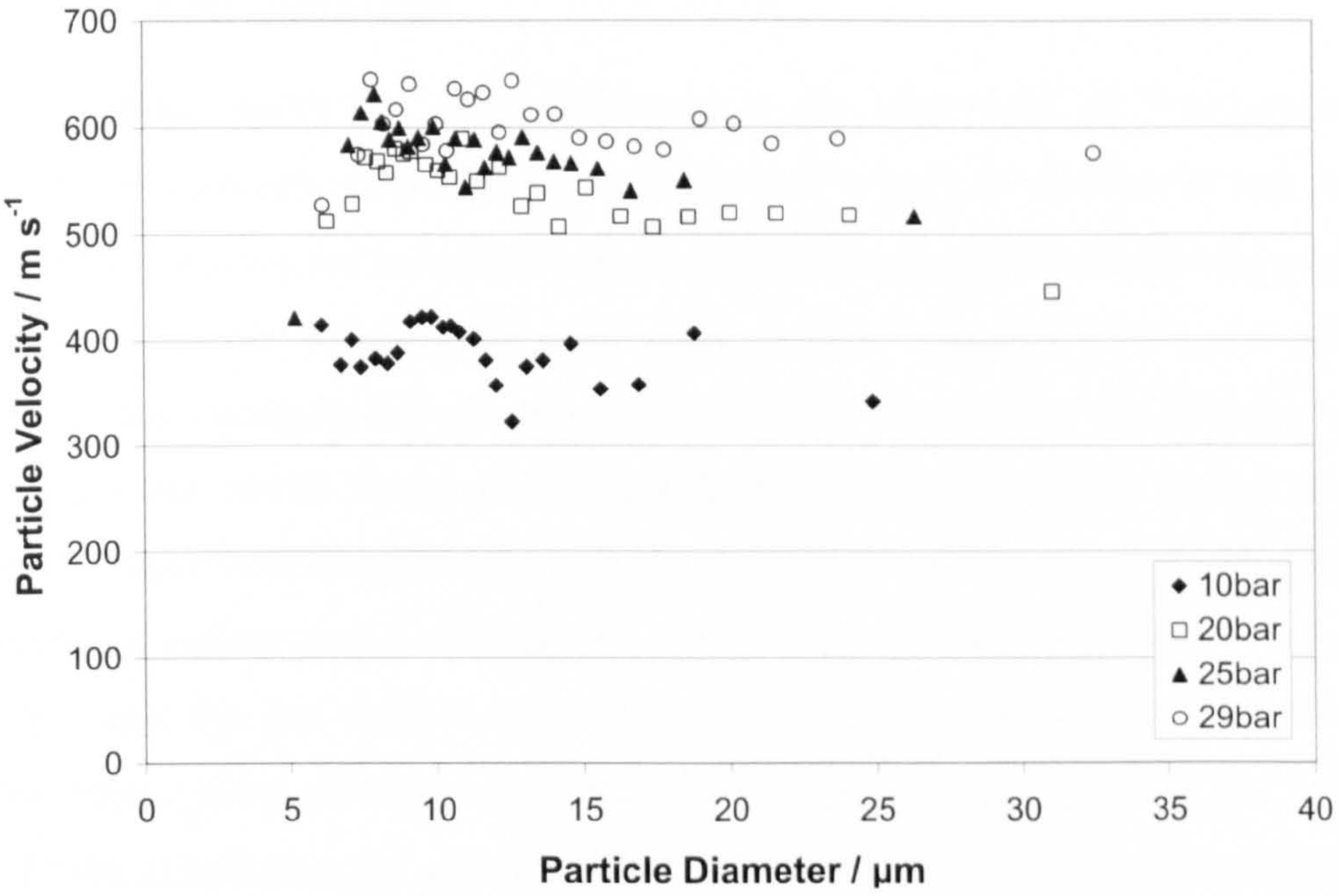

(a)

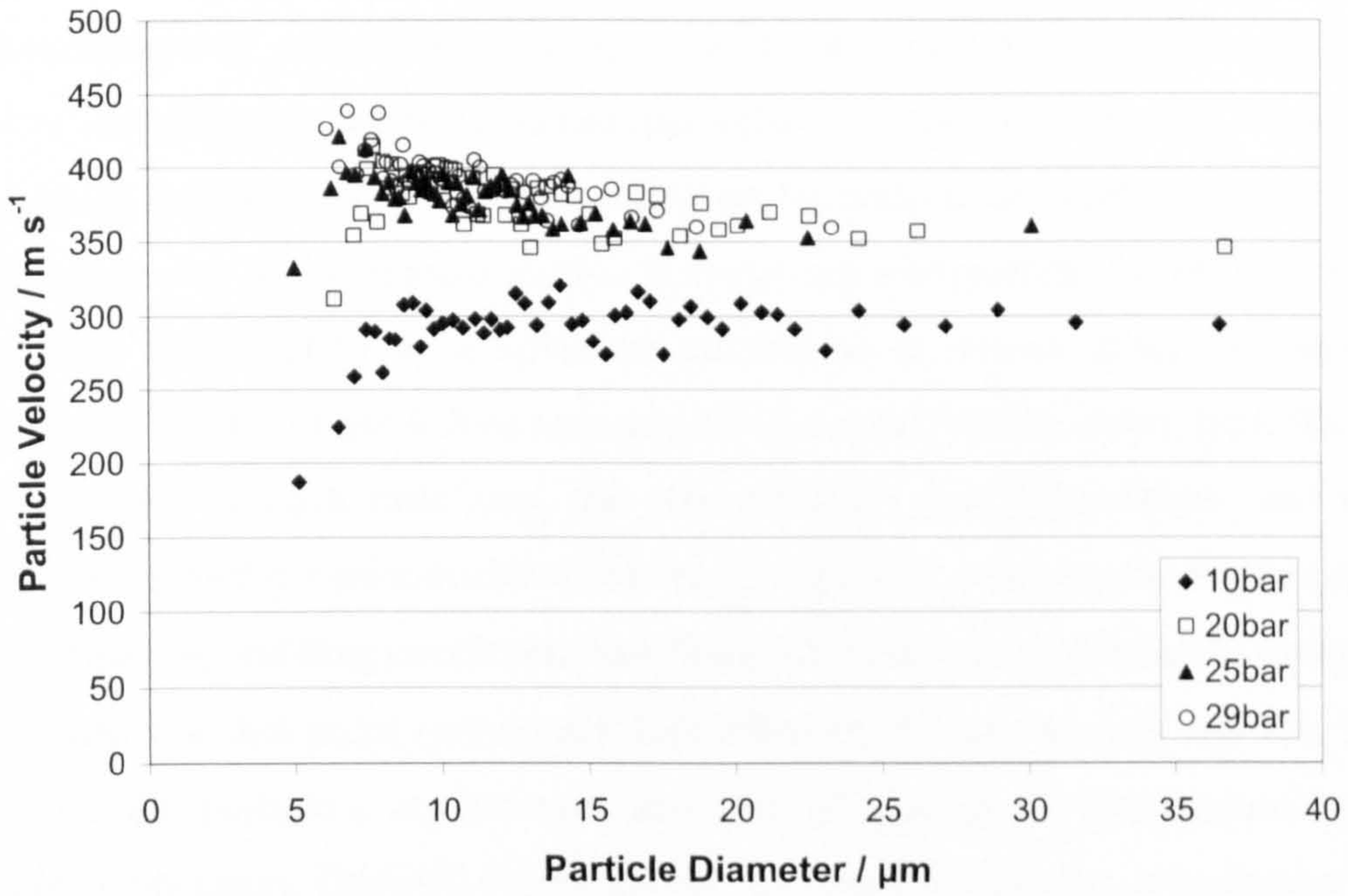

(b)

Figure 3.30 – Influence of particle diameter on particle velocity for a titanium powder travelling within (a) a helium gas flow and (b) a nitrogen gas flow at a stand off distance of 20 mm. Results are shown for a stagnation pressure of 10, 20, 25, and 29 bar. Each data point corresponds to the average particle diameter and average velocity for 20 particles.

3.9. Model Results

A mathematical model has been developed at the University of Nottingham to predict gas and particle velocities through the nozzle [65]. It consists of two parts, first the gas properties are calculated, and these are then used to calculate the particle velocity as it passes through the cold spray nozzle. The gas model, previously written in java, calculates the gas properties (density, temperature and velocity) as it passes from the nozzle throat to the nozzle exit. This part of the model uses a standard iterative procedure to calculate the gas mach number at any given point in the nozzle, of known cross sectional area, using the area-mach relationship, equation 3.7 [58]. Once the gas mach number is known, it is possible to calculate the gas velocity, temperature, density and pressure at that point using equations 3.8 to 3.11 [58]. Whilst calculating the gas properties within the nozzle it is assumed that no shockwaves occur. The variation in gas velocity, temperature and density along the length of the nozzle, calculated by the gas model, are used within the QBasic particle model to calculate particle temperature and velocities within the nozzle. Newton's second law is employed and all forces acting on the particle are neglected other than the drag force due to the relative motion between gas and particle. To determine the temperature and velocity of a spherical particle as it moves along the nozzle, equations 3.13 and 3.28 are solved numerically in a series of time steps, typically 0.1 μs. At the end of each time step, the new velocity, new temperature, and new position of the particle are calculated. At the new particle position and beginning of the next time step the drag coefficient and Nusselt number are recalculated, using the gas properties at that point (previously calculated by the gas model) and this then allows for the particle's acceleration and rate of change of temperature to be calculated once again. This will determine the next particle position, temperature and velocity and the calculation continues until the particle reaches the end of the nozzle [65].

The models require a number of parameters are required by the gas and particle models. The parameters required for each model are shown in Table 3.10 for a range of gas and powder types. Process parameters for the nozzle employed are also shown. Gas and particle parameters are taken from the literature [77]. The mean

particle diameter chosen for the particle modelling was the manufacturers measured 50% volume fraction of the powder. The table highlights the fact that some parameters that may be required by one model are not required by the other. For example, the gas model requires the nozzle dimensions to calculate the gas properties along the length of the nozzle but the particle model does not require any of this dimensional information.

Process Parameters	**Gas Model**	**Particle Model**
Throat Diameter (D*) / mm	1.35	-
Entrance Nozzle Diameter / mm	13	-
Exit Nozzle Diameter (D_e) / mm	4	-
Nozzle exit area (A_e) / Nozzle throat area (A*)	8.79	-
Length of Converging Section / mm	10	-
Length of Diverging Section / mm	100	-
Gas Stagnation Pressure / bar	10, 29	-
Initial Gas Temperature / K	293	-

Gas Parameters	**He**	**N_2**	**He**	**N_2**
Specific Gas Constant / J kg^{-1} K^{-1}	2079	296.8	2079	296.8
Adiabatic Index	1.667	1.404	1.667	1.404
Dynamic Viscosity / kg m^{-1} s^{-1}	-	-	1.86×10^{-5}	1.67×10^{-5}
Thermal Conductivity / W m^{-1} K^{-1}	-	-	0.1468	0.025
Specific Heat Capacity / J kg^{-1} K^{-1}	-	-	5193	1039

Particle Parameters	**-**	**Cu**	**Ti**
Particle Diameter / μm	-	+5 -25	+5 -45
Mean Particle Diameter / μm	-	11	15
Particle Density / kg m^{-3}	-	8960	4507
Specific Heat Capacity / J kg^{-1} K^{-1}	-	385	523
Melting Point / K	-	1356	1943
Porosity Fraction	-	0	0
Initial Particle Velocity / m s^{-1}	-	20	
Initial Particle Temperature / K	-	300	

Table 3.10 – The parameters used by the gas and particle models. Constants are taken from the Handbook of Chemistry and Physics [77]. Parameters are broadly defined as process parameters, gas parameters and particle parameters.

In summary the key issues with the current modelling process before this project begun were:

i) The gas model begins calculating gas properties from the throat of the nozzle and therefore does not consider the effect of the converging section of the nozzle.

ii) An incompressible fluid flow is assumed whilst calculating the particles drag coefficients through the gas flow to predict the interactions between gas flow and particles. For greater accuracy the particles drag coefficient needs to be calculated from equations that assume a compressible fluid flow (Section 3.3.)

iii) The model is only able to predict the velocity profile of a single sized particle. For multiple particle diameters the program must be repeated many times making the task time consuming and laborious.

iv) Currently the gas properties data output by the java model requires manual manipulation to be used by the particle model. The data output from the particle model then requires further manual manipulation for it to be recognised by Microsoft Excel. One again this is a time consuming and laborious operation.

3.9.1. Key Developments to the Model

This section highlights the main changes made to the gas and particle model during this study. To improve the gas models ease of use and to reduce the steps required to prepare the outputted data to be used within the particle model, the gas model was rewritten using Microsoft Excel. Additionally the variation in gas properties was calculated along the whole length of the nozzle incorporating the converging section of the nozzle. To solve the area-mach relationship (equation 3.7) within Excel an iterative bisection method was used [81]. To check the accuracy of the new gas model it was compared to the old java gas model and shown to behave in the same manner. By writing the model in Excel it was possible to use macros to create text

output of the gas properties that required no further manual manipulation to be used by the QBasic particle model.

The existing particle model assumes an incompressible gas flow to calculate the drag coefficient equations. The drag coefficient at any point within the gas flow is calculated depending on the Reynolds number of the particle at that point. The drag coefficient equations previously employed were replaced with those for a compressible flow as described previously in Section 3.3.

A final modification to the particle model allows the effect of varying the particle diameter on particle exit velocity to be assessed. The range of particle diameters to be assessed is inputted by the user before the program is executed. The properties (temperature, velocity etc.) of a single particle diameter as it passes along the nozzle are calculated, but only the properties of the particle at the nozzle exit are recorded to a data file. The process is then repeated automatically for the next particle diameter. The final data file consists of the particle properties at the nozzle exit for each particle diameter.

3.9.2. Copper Powder Modelling

Modelling was carried out for nitrogen and helium gas flows at gas pressures ranging from 10 bar to 29 bar and a gas stagnation temperature of 293 K. An initial particle velocity of 20 m s^{-1} and particle temperature of 300 K at the entrance to the converging section of the nozzle is assumed. Further nozzle dimensions, particle and gas parameters required for the modelling process are summarised in Table 3.10. A copper powder of size distribution +5-25 μm was chosen for the modelling process, the same as to be used for the experimental velocity measurements within this study. The variation in particle velocity along the nozzle length was carried out for a single 11 μm copper particle. An 11 μm particle was chosen due to it being the manufacturers (Sandvik Osprey Ltd, Neath, UK) measured 50% volume fraction of the spherical copper powder employed for the velocity measurements carried out within this study.

3.9.2.1. Influence of Compressible and Incompressible Drag Coefficient Equations

A typical comparison of the variation of drag coefficient with Mach number between the two methods used to calculate the drag coefficient is shown in Figure 3.31 for a 11 μm copper particle travelling with a helium gas flow at a stagnation pressure of 29 bar. As the particle accelerates within the subsonic region of the nozzle up to M_r = 0.5 both equations give similar drag coefficient values. Beyond this point the drag coefficient increases when using the compressible drag coefficient equation. Figure 3.31 highlights the variation in the calculation of drag coefficients by the two methods when supersonic flows are considered, and therefore will affect the final calculated particle velocities.

The large increase in drag coefficient at $M \approx 1$ is acknowledged to occur by Bailey and Hiatt [61] when comparing experimental data as shown previously by Figure 3.2. Figure 3.2 shows that for Reynolds numbers in the region of 100 to 1500, similar to those calculated for the cold spray system, the drag coefficient will increase abruptly from ~0.5 to ~1.2 as M_r increases for ~0.8 to ~1.5. This is a similar trend to the drag coefficients calculated by the mathematical model shown in Figure 3.31.

The influence of the compressible and incompressible drag coefficient equations on particle velocities were assessed by modelling spherical copper particles travelling within a helium gas flow along the length of the nozzle. Modelling was carried out at two different stagnation pressures; 10 bar and 29 bar. Results are shown in Figure 3.32(a). It can be seen in Figure 3.32(a) that relatively shortly after the throat region the particle velocities calculated by the compressible and incompressible drag coefficient equations vary. After 0.002 m from the throat, a variation of greater than 50 m s^{-1} of the particle velocity is found between the two techniques. Faster particle velocities along the length of the nozzle are found when using the compressible drag coefficient equations. For all further modelling the compressible drag coefficient equations are used.

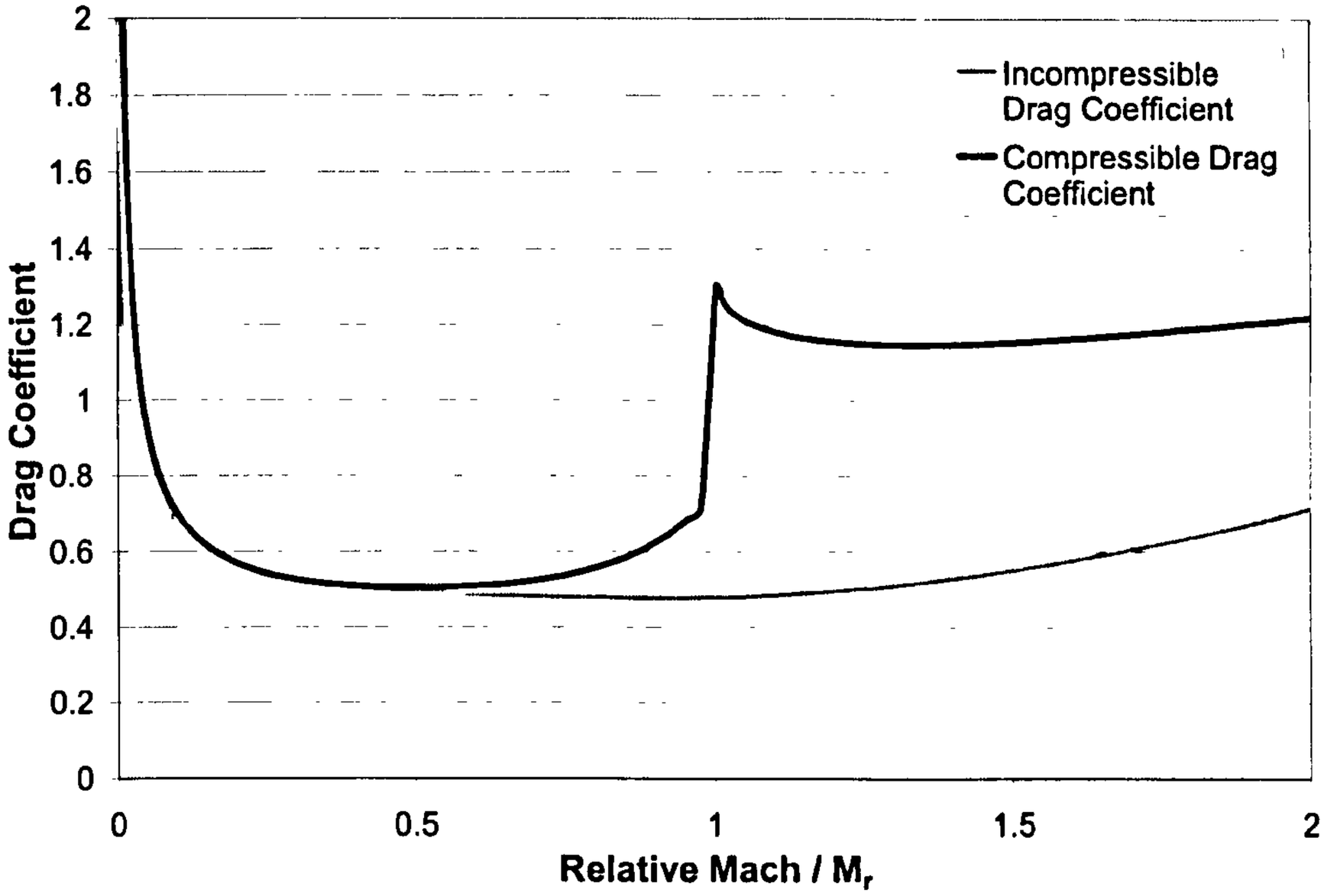

Figure 3.31 – Variation of drag coefficient with relative mach number for a 11µm copper particle. He, T_o = 293K, P_o = 29bar.

3.9.2.2. Helium Gas Flow

The velocity of a single 11 µm particle travelling along the length of the nozzle within a helium gas flow is shown in Figure 3.32(a). The helium gas velocity is also shown. Despite an increase in gas stagnation pressure having no effect on gas velocity, an increase in particle velocity is found. Higher particle velocities are predicted when using the compressible drag coefficient equations compared to the incompressible drag coefficient equations. The helium gas accelerates the most during the first third of the diverging section of the nozzle and as expected this is also when the largest amount of particle acceleration occurs for both gas pressures employed. Whilst it is interesting to know the particle velocities within the nozzle, the particle velocities at the nozzle exit are of greater interest, due to their influence on the mechanical properties of the coating, and how they are influenced by process parameters.

Figure 3.32(b) show the particle velocities at the nozzle exit for a spherical copper powder of size distribution 5 µm to 25 µm travelling within a helium gas flow. Figure 3.32(b) shows the influence of particle diameter and gas pressure on particle

exit velocity. The same gas stagnation conditions described previously are used and calculations are made using the compressible drag coefficient equations. The model predicts that the particle exit velocity increases with decreasing particle diameter. In the case of this one dimensional model this is due to the smaller particles being lighter and therefore easier to accelerate within the gas flow. Table 3.11 summarises the predicted particle exit velocities for a 5, 11 and 25 μm spherical copper particle travelling within a helium gas flow at 10 bar and 29 bar. The model predicts similar absolute increases in particle velocity due to increasing stagnation pressure across the size distribution of the copper powder. For comparison, maximum measured particle velocities at 10 bar (SOD = 20 mm) and 29 bar (SOD = 1 mm) are also included. The model output values are significantly higher than the measured values using a copper powder and described in Section 3.8.2.1. and Section 3.8.2.3. for a stand off distance of 20 mm and 1 mm. The largest variation between measured and predicted particle velocities is found for small sized particles. This is due to small sized particles decelerating to a greater extent compared to large size particles whilst travelling within the plume and interacting with other particles and the nozzle walls. The model used to predict particle velocities does not consider these interactions and deceleration of the particles occurring.

Gas Type	Cu Particle Size / μm	10 bar	29 bar	Velocity Increase / m s^{-1}
Helium	5	846	1059	+ 213
	11	647	870	+ 223
	25	469	667	+ 198
Nitrogen	5	500	545	+ 45
	11	413	478	+ 65
	25	335	422	+ 87

Table 3.11 – Predicted particle exit velocities (m s^{-1}) for a 5, 11 and 25 μm spherical copper particle travelling within helium and nitrogen gas flows calculated by modelling using the compressible drag coefficient equations. The increase in particle exit velocity by increasing the gas stagnation pressure from 10 bar to 29 bar is also shown.

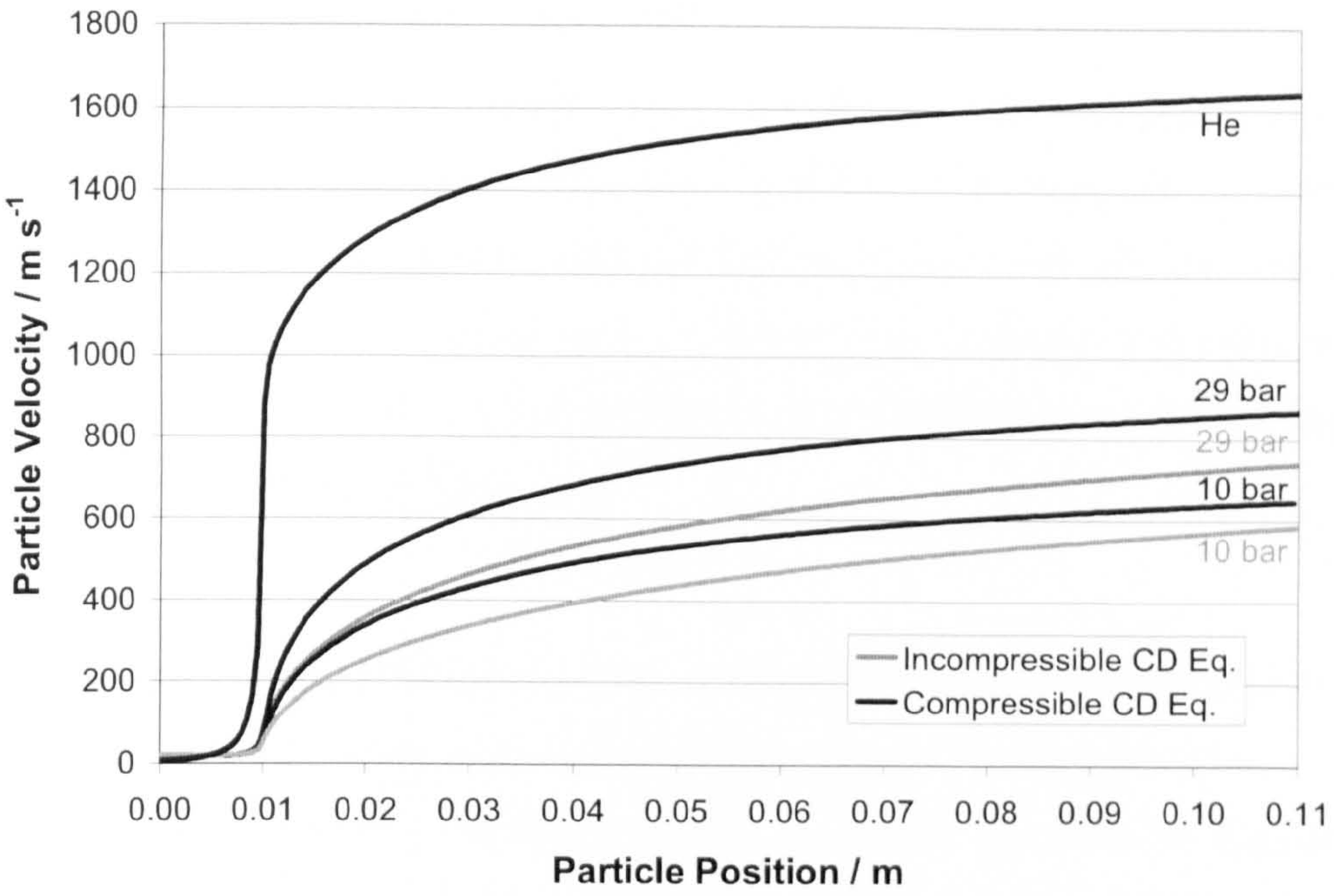

(a)

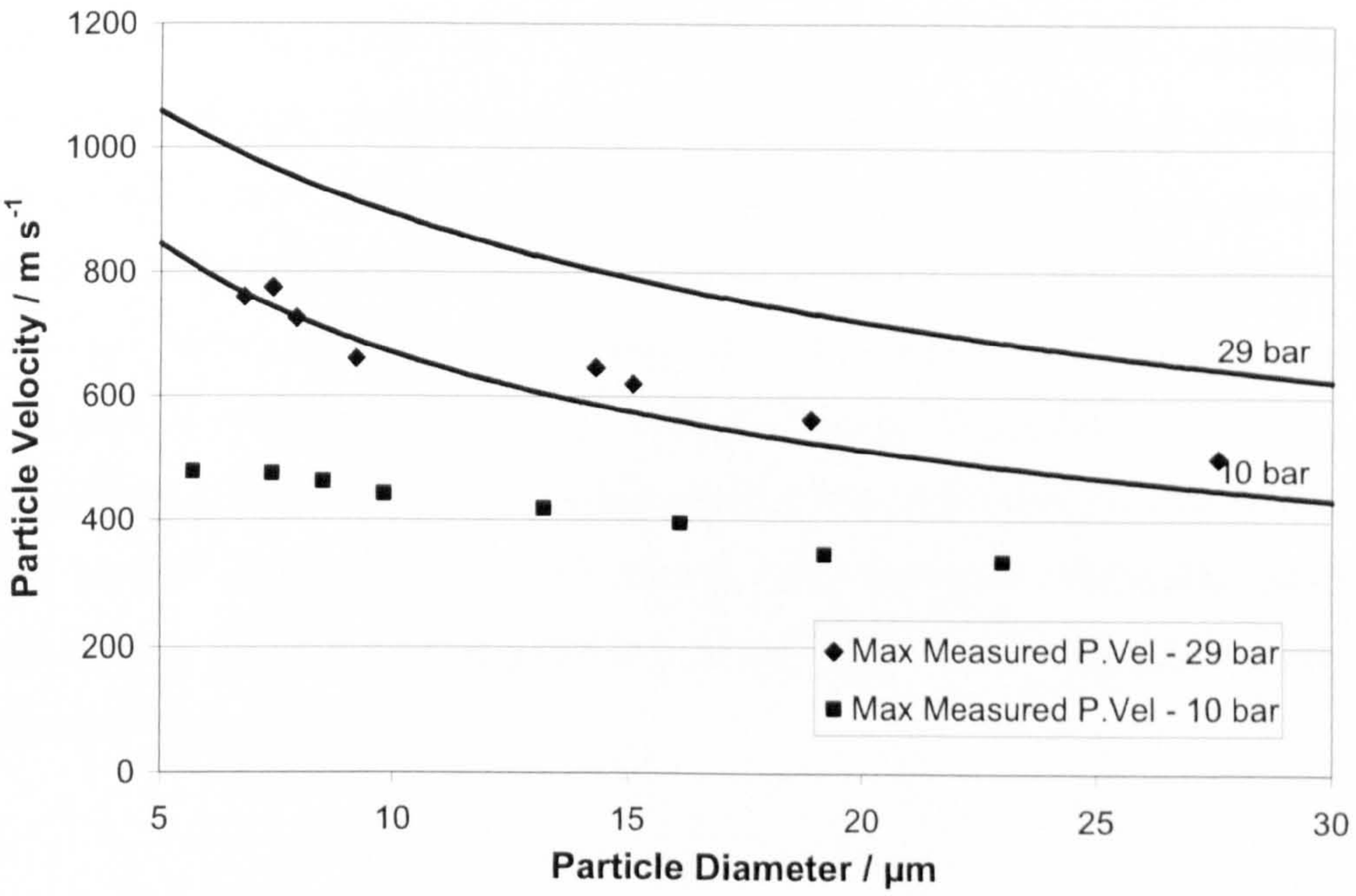

(b)

Figure 3.32 – Model output showing the variation in particle velocity with position for a copper powder travelling within a helium gas flow (a) along the length of the nozzle for an 11 µm particle calculated using the compressible and incompressible drag coefficient equations (the predicted helium gas velocity calculated by the model is also shown) and (b) particle exit velocity with varying particle diameter calculated using the compressible drag coefficient equations. P_0 = 10 – 29 bar; T_0 = 293 K. For comparison, maximum measured particle velocities at 10 bar (SOD = 20 mm) and 29 bar (SOD = 1 mm) are also included.

3.9.2.3. Nitrogen Gas Flow

Figure 3.33(a) shows an 11 μm copper particle travelling within a nitrogen gas flow. The nitrogen gas velocity is also shown. Smaller particle velocities along the length of the nozzle are found compared to when helium gas is used. Compared to helium a smaller variation in particle velocity between the two gas stagnation pressures of 10 bar and 29 bar is found. This is due to the lower gas velocities achieved by nitrogen whilst travelling within the nozzle.

Figure 3.33(b) shows the influence of particle diameter and gas pressure on particle exit velocity. Table 3.11 summarises the predicted particle exit velocities for a 5, 11 and 25 μm spherical particle travelling within a nitrogen gas flow at stagnation pressures of 10 bar and 29 bar. It is noticeable that in all cases the particle exit velocities are lower than those predicted for a helium gas flow. Figure 3.33(b) shows that substantially lower increases in particle velocity are found with nitrogen gas compared to helium gas but the increase in particle velocity is found to increase with increasing particle size. This indicates that an increase in nitrogen gas pressure is less influential in increasing particle velocity compared to a similar pressure increase for a helium gas flow. Similar particle velocities are predicted to the maximum measured particle velocities for particle diameters below 10 μm. This is in contrast to the modelling carried out for helium gas where it was found that the measured and predicted particle velocities were not similar. The maximum measured particle velocities show a larger reduction in particle velocity with increasing particle size to that predicted by the model.

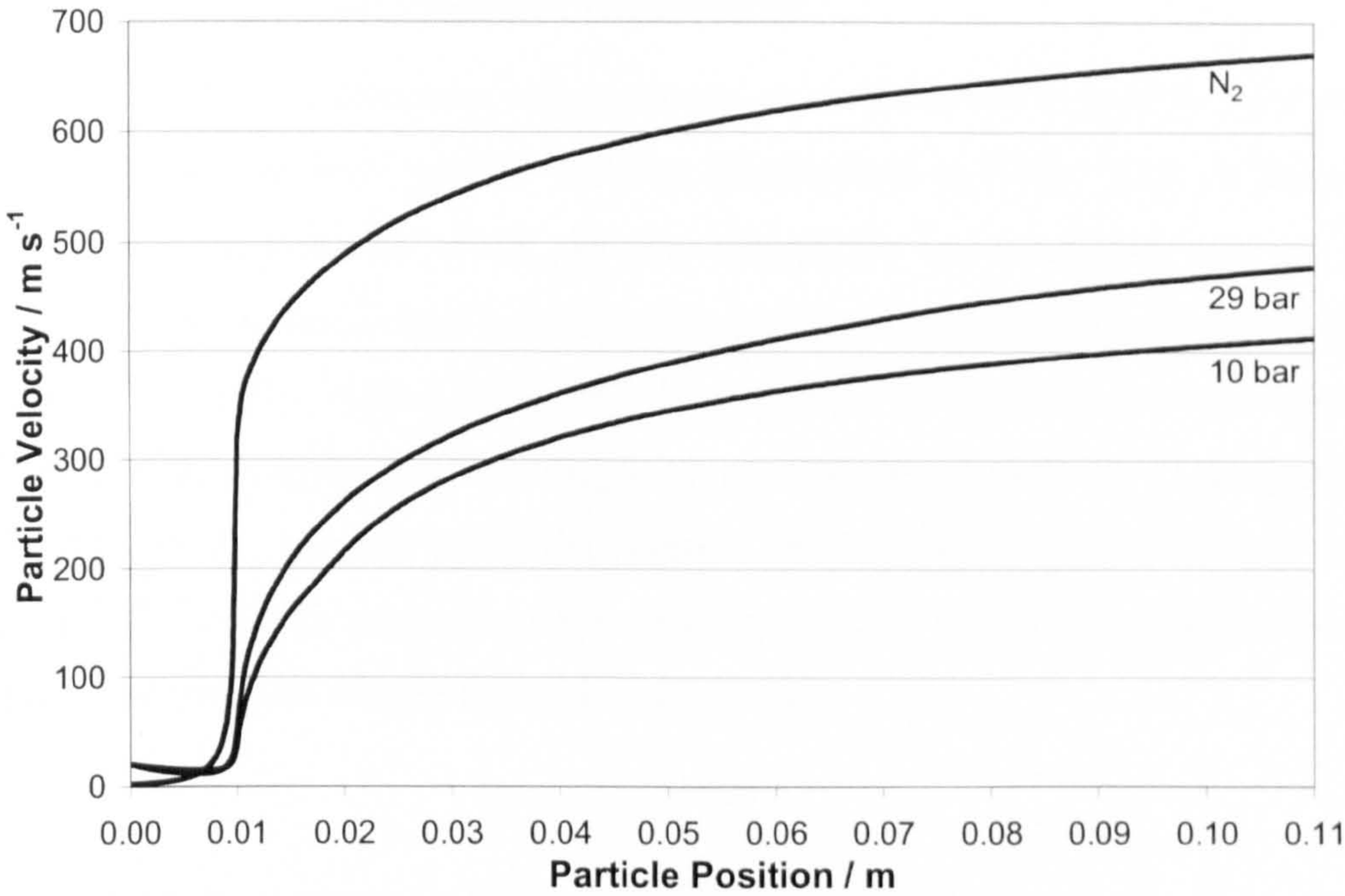

(a)

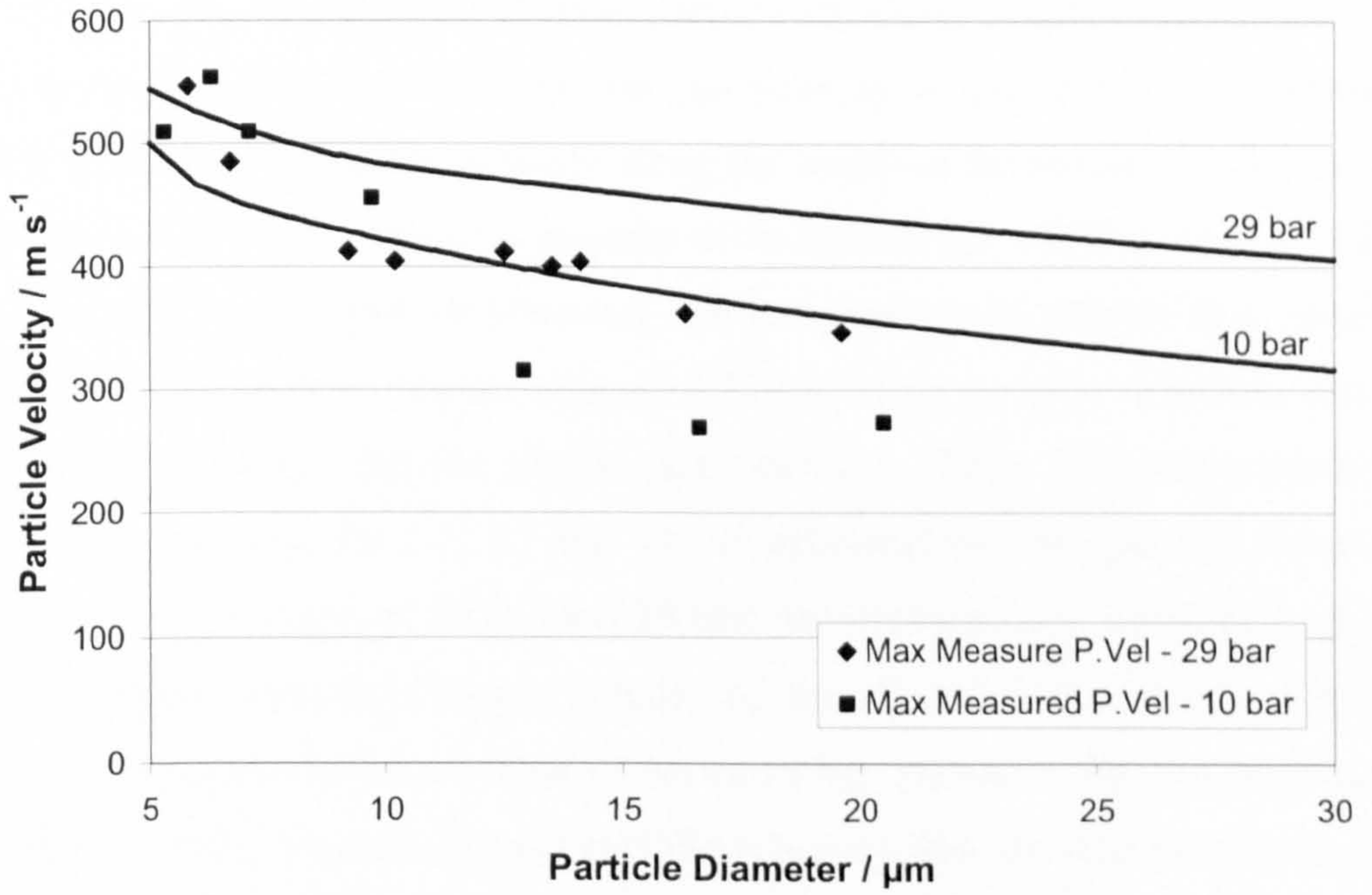

(b)

Figure 3.33 – Model output showing the variation in particle velocity with position for a copper powder travelling within a nitrogen gas flow (a) along the length of the nozzle for an 11 µm particle (the predicted nitrogen gas velocity calculated by the model is also shown) and (b) particle exit velocity with varying particle diameter. In both cases calculations were made using the compressible drag coefficient equations. P_0 = 10 – 29 bar; T_0 = 293 K. For comparison, maximum measured particle velocities at 10 bar (SOD = 1 mm) and 29 bar (SOD = 1 mm) are also included.

3.9.3. Titanium Powder Modelling

The same modelling parameters and constants as used for the copper powder were also used for the titanium powder and are summarised in Table 3.10. A titanium powder of size distribution +5-45 μm was chosen for the modelling process, the same used for the experimental velocity measurements, microstructural examination and mechanical testing within this study. The variation in particle velocity along the nozzle length was carried out for a single 15 μm titanium particle. A 15 μm particle was chosen due to it being the manufacturers (Active Metals Ltd, Sheffield, UK) measured 50% volume fraction of the spherical copper powder employed for the velocity measurements carried out within this study.

3.9.3.1. Helium Gas Flow

The velocity of a single 15 μm titanium particle travelling within a helium gas flow is shown in Figure 3.34(a). The helium gas velocity is also shown. As expected, there is an increase in particle velocity along the length of the nozzle with increasing gas stagnation pressure despite no increase in the helium gas velocity. Figure 3.34(b) shows the influence of particle diameter and gas pressure on particle exit velocity. Compared to the copper powder (Figure 3.32(b)) larger particle velocities can be expected at the nozzle exit for similar sized particles. Table 3.12 summarises the particle exit velocities for a 5, 15 and 45 μm spherical titanium particle travelling within a helium gas flow at 10 bar and 29 bar. Similar increases in particle velocity to the modelled output for a copper powder are found, irrelevant of the particle size as the gas pressure is increased from 10 bar to 29 bar. Similar to the copper powder, the modelled output produces higher particle velocities than the maximum measured particle velocities at 10 bar and 29 bar, shown in Figure 3.32(b). As the particle size increases the difference between the modelled particle velocities and maximum measured particle velocities reduces. It is noted that the maximum particle velocities shown in Figure 3.34(b) were made at a stand off distance of 20 mm and so some variation to the particle velocity upon leaving the nozzle exit may be expected. The variation between predicted particle velocities and the maximum measured particle velocities is expected to be most likely due to particles interacting with one another

and with the nozzle walls that will cause the particle velocity to decrease. The particle model used does not account for these factors occurring.

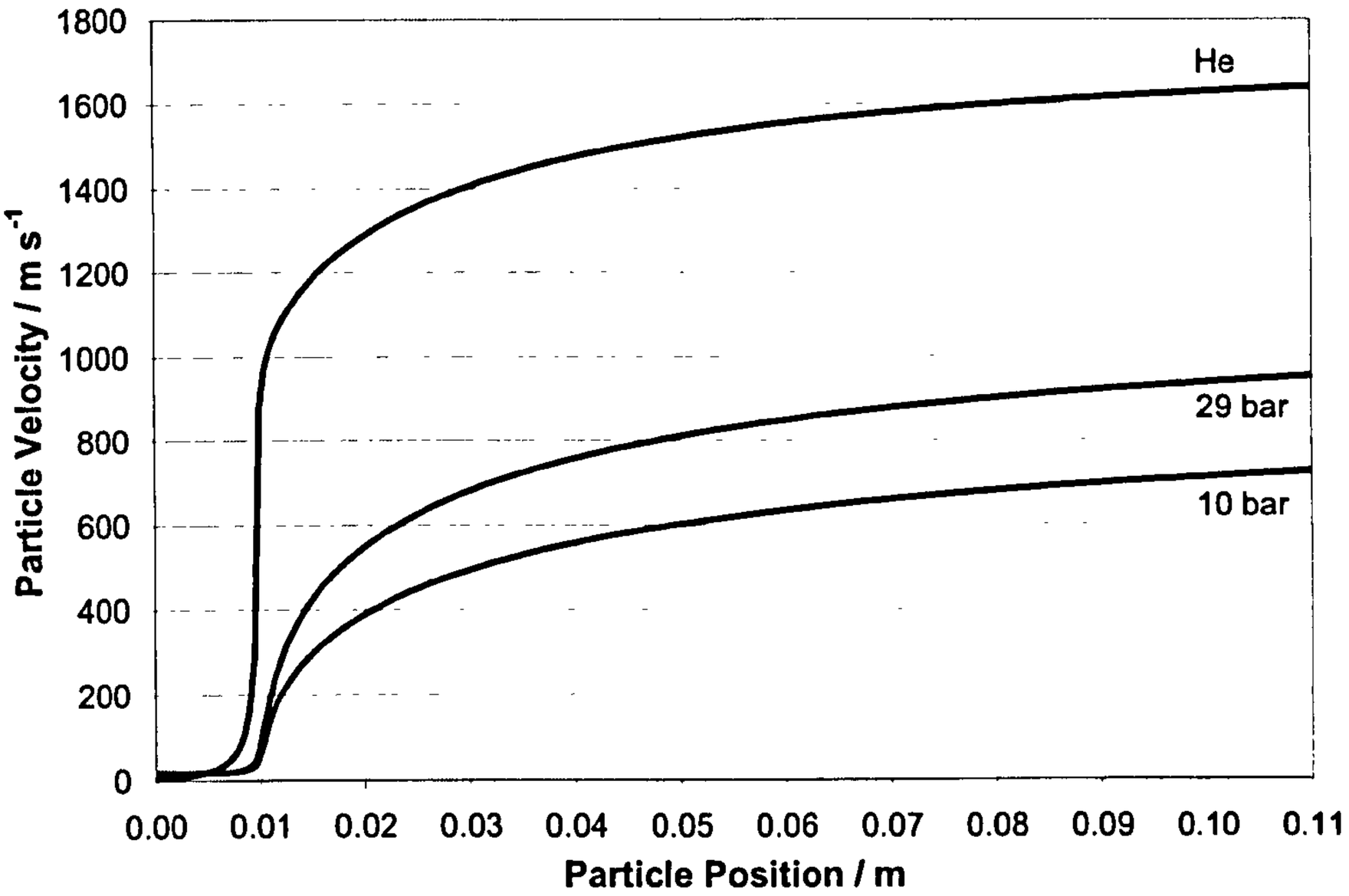

(a)

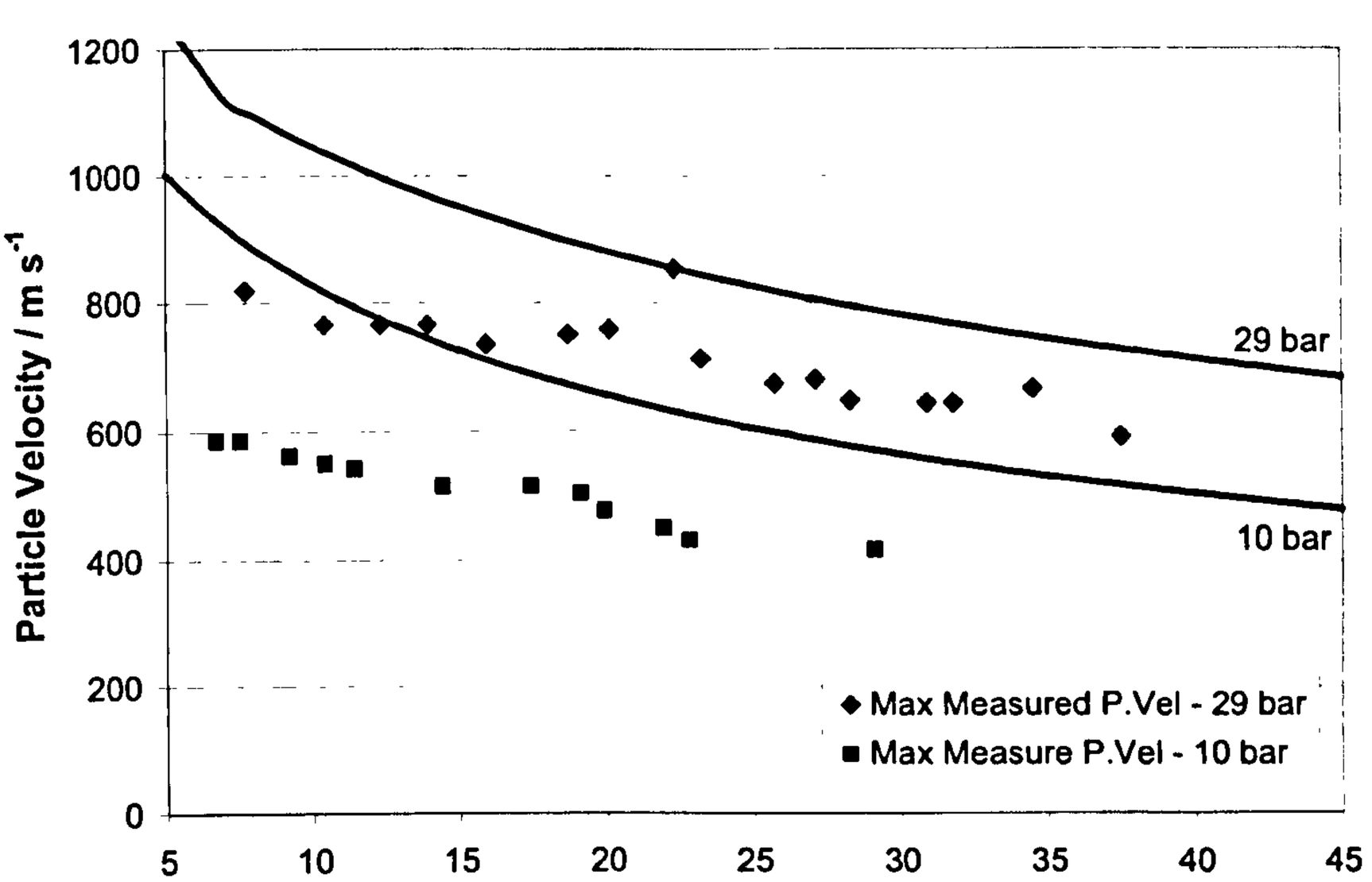

(b)

Figure 3.34 – Model output showing the variation in particle velocity with position for a titanium powder travelling within a helium gas flow (a) along the length of the nozzle for an 15 µm particle (the predicted helium gas velocity calculated by the model is also shown) and (b) particle exit velocity with varying particle diameter. In both cases calculations were made using the compressible drag coefficient equations. P_0 = 10 – 29 bar; T_0 = 293 K. For comparison, maximum measured particle velocities at 10 bar (SOD = 20 mm) and 29 bar (SOD = 20 mm) are also included.

Gas Type	Ti Particle Size / µm	10 bar	29 bar	Velocity Increase / m s^{-1}
Helium	5	1000	1200	+ 200
	15	726	952	+ 226
	45	479	683	+ 204
Nitrogen	5	554	589	+ 35
	15	440	494	+ 54
	45	341	427	+ 86

Table 3.12 – Predicted particle exit velocities (m s^{-1}) for a 5, 15 and 45 µm spherical titanium particle travelling within helium and nitrogen gas flows calculated by modelling using the compressible drag coefficient equations. The increase in particle exit velocity by increasing the gas stagnation pressure from 10 bar to 29 bar is also shown.

3.9.3.2. Nitrogen Gas Flow

The velocity of a single 15 µm copper particle travelling within a nitrogen gas flow is shown in Figure 3.35(a). The nitrogen gas velocity is also shown. As expected smaller particle velocities are predicted compared to when helium gas is used. This is due to the smaller gas velocity achieved by nitrogen gas compared to helium gas. Figure 3.35(b) shows the influence of particle diameter and gas pressure on particle exit velocity. Table 3.12 summarises the particle exit velocities for a 5, 15 and 45 µm spherical titanium particle travelling within a nitrogen gas flow at 10 bar and 29 bar. Similar trends to those identified for a copper powder travelling within nitrogen gas are found. There is some variation in the predicted particle velocities compared to the maximum measured particle velocities but not to the same degree as when helium gas is used.

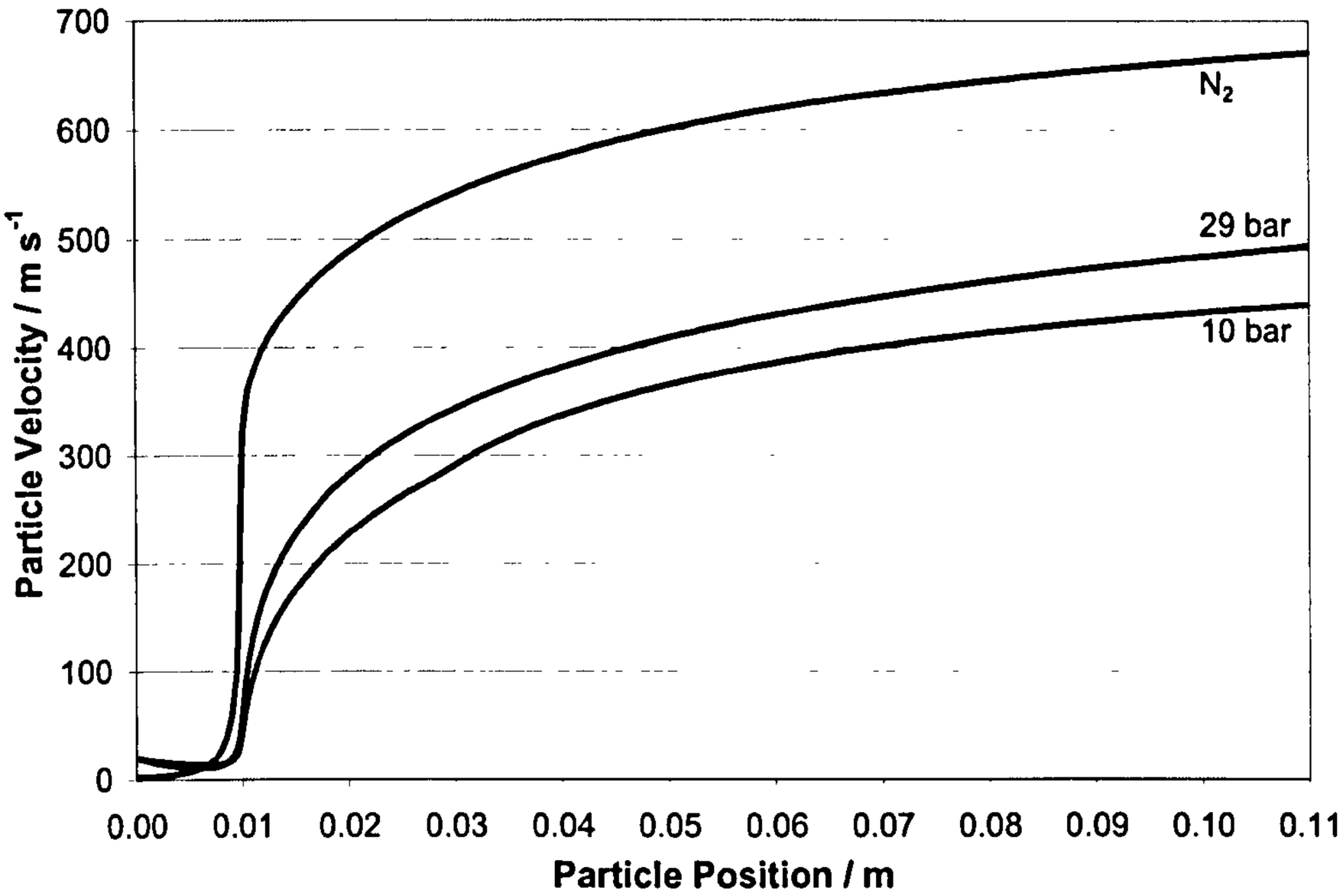

(a)

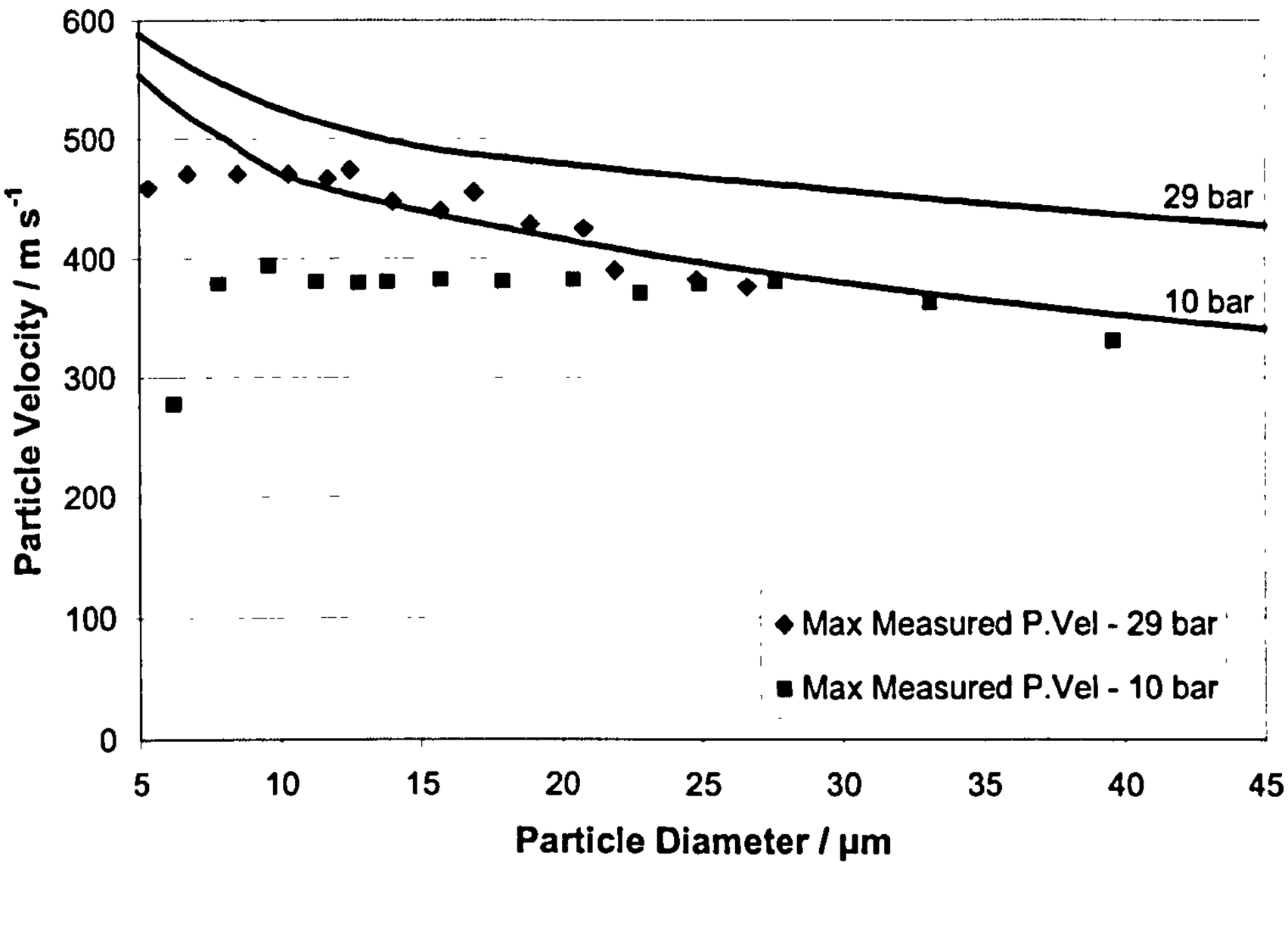

(b)

Figure 3.35 – Model output showing the variation in particle velocity with position for a titanium powder travelling within a nitrogen gas flow (a) along the length of the nozzle for an 15 µm particle (the predicted nitrogen gas velocity calculated by the model is also shown) and (b) particle exit velocity with varying particle diameter. In both cases calculations were made using the compressible drag coefficient equations. P_0 = 10 – 29 bar; T_0 = 293 K. For comparison, maximum measured particle velocities at 10 bar (SOD = 20 mm) and 29 bar (SOD = 20 mm) are also included.

3.10. Discussion

This section of the chapter will discuss the experimental results and model predictions made during this project. Firstly, the various methods employed to measure the powder size distributions are discussed. Then the particle velocity measurements made using the PIV equipment are considered. Finally the modelling results are discussed and comparisons between the modelling output and the actual velocity measurements for a copper and titanium powder are made.

3.10.1. Powder Size Distribution

The copper powder size distribution was measured by four techniques i) automated optical microscopy, ii) laser diffractometry, iii) particle image velocimetry and iv) manual measurement by analysis of SEM images. Due to the different methods of operation each system consists of different numbers of individual particles data. For example, the automated optical microscopy system is able to characterise the most number of particles, as many as 65,000. The data captured by the particle image velocimetry system consists of 2500 particles (7 individual runs), whilst manual measurement of particle sizes using the SEM has the lowest data yield of approximately 200 individual particle measurements due to being labour and time intensive to carry out the measurements. Figure 3.20(a) shows that the automated optical microscopy measuring system measures a size distribution consisting of a greater number of larger particles than the three other methods and there are a number of reasons for this. SEM was carried out by measuring particles from a small number of captured images. The total area of the captured images is a limiting factor in determining the number of particles that may be measured. Particles of larger diameter have a larger surface area and therefore there is a greater likelihood that fewer larger particles may be measured by this method.

The particle image velocimetry system is not a dedicated piece of equipment for measuring a particles size distribution, particles are travelling at velocities typically in excess of 500 m s^{-1} and therefore there is potential for error in the measurements. Additionally, measurements are made within a small volume portion of the spray

plume, typically 1 mm^3. Measurements shown in Figure 3.20(a) were made at a stand off distance (z-axis) of 20 mm within a central position of the plume. It may be possible that some particles may not pass through this small volume section of the plume, due to interactions with other particles or the possible turbulent nature of the gas flow, and this could influence the measured size distribution data. However, when measurements are taken at other positions within the plume, variation of the y-axis and z-axis shown in Figure 3.21, only minor change in the powder size distribution is found. As the y-axis position is changed, a greater number of smaller sized particles are found; however, the variation is found to be only up to 2 μm. Data measured at a y-axis position not at the central position of the plume only consists of 500 particles but the small variation in size distribution found is regarded as inconclusive evidence of whether a different size distribution of the powder may be measured at different positions within the plume. Selective powder feeding occurring during the cold spray process, upstream of the nozzle, would also influence the size of particles captured by the PIV system, regardless of plume measuring position.

The smallest size distribution was found when the copper powder was measured by the laser diffractometry technique. Up to a 3.5 μm variation in particle size was found compared to the automated optical microscopy measuring technique at the cumulative number 50% point. The laser diffractometer employed originally measures the volume distribution of the powder. Data is presented in bins of varying particle size and the volume% of each bin is measured. The method for determining the particle number size distribution from the volume size distribution is described in Appendix 2. Using the mid-point of each bin range for calculating the volume of each bin for a single particle, this method is particularly prone to error if large bin ranges are employed. Also, the assumption that every particle within a bin range will be of the same size, is not valid. This method is prone to error due to the fact that the size of each individual particle remains unknown.

In contrast, the automated optical microscopy equipment employed, measures the area of each individual particle and the diameter of a circle of equivalent area is calculated. A far greater number of particles are measured individually and therefore

there is a greater likelihood for large particles to be measured, and no errors are generated by converting the data from a volume to a number distribution. It is therefore regarded to be the most accurate size distribution of the different methods employed. By comparing the 50% cumulative number% of the copper powder measured by the automated optical microscopy technique and the particle image velocimetry technique (Table 3.7) the particle image velocimetry technique is found to consistently under size the copper powder compared to the size distribution measured by the automated optical microscopy technique by approximately 2 μm.

Further comparisons between the size distributions measured by the automated optical microscopy technique and the particle image velocimetry techniques were made by plotting the data onto a log-normal probability axis, shown in Figure 3.20(c). Data taken from the particle image velocimetry system and used in Figure 3.20(c) were taken at a stand off distance of 20 mm from the nozzle from the centre of the plume. A logarithmic axis is used for the x-axis and therefore, if the measured data creates a straight line, then a log-normal distribution is present for the powder size distribution. In the case of the data measured by the automated optical microscopy system two size distributions are identified. The first distribution covers particle sizes less than approximately 6 μm and account for approximately less than 10% of the cumulative number distribution. Due to the size of these particles, this small part of the size distribution will cover an even smaller percentage of the size distribution in terms of mass or volume. This size distribution is most likely an artefact of a sieving process used to create the desired size distribution of +5 -25 μm from an original copper powder of larger size range. The second log-normal distribution covers particle sizes of greater than 7 μm. A straight line is created indicating that the size distribution matches a log-normal distribution of mean 2.18 and standard deviation 0.29 as shown by Table 3.6. The data created by the particle image velocimetry system shows a relatively straight line up to particle sizes of 10 μm indicating a log-normal distribution. For particle sizes greater than 10 μm the size distribution deviates from the predicted log-normal distribution and the gradient of the line decreases. This indicates that insufficient numbers of large particles have been captured by the particle image velocimetry system for a true log-normal distribution to be recorded. Nevertheless, there is good agreement between the size

distributions measured by the two systems and therefore high confidence that the particle image velocimetry system is able to measure the size of particles, whilst travelling within the plume, accurately.

The copper powder was measured by the automated optical microscopy equipment using an external source. It was not possible for the titanium powder to be sized by this method. Despite the angular nature of the powder, making size analysis difficult, when comparing the size distribution of the titanium powder measured by the laser diffractometer and particle image velocimetry system, Figure 3.23, good agreement was found despite the laser diffractometer technique measuring the volume size distribution and not the number size distribution.

3.10.2. Particle Velocity Measurements – Copper Powder

When using nitrogen or helium as the main carrier gas, an increase in the measured particle velocity is found with increasing gas stagnation pressure. Larger particle velocities are found when using helium gas compared to nitrogen gas and additionally a larger increase in particle velocity is found with helium compared to nitrogen gas when increasing the gas pressure from 10 bar to 29 bar. Helium will have a higher gas velocity along the length of the nozzle due to a higher speed of sound, leading to greater particle velocities compared to nitrogen gas. This is despite the lower density of helium which may be expected to reduce the effectiveness of passing momentum from the gas flow to the individual particles.

3.10.2.1. Helium Gas

Figure 3.25(a) shows the effect of particle size on particle velocity at various helium gas stagnation pressures. For particles of diameter greater than 9 μm a slight decrease in particle velocity is measured with increasing particle size for all gas stagnation pressures considered. With a stagnation pressure of 29 bar, a decrease in particle velocity of approximately 100 m s^{-1} is found when increasing the particle size from 10 μm to 25 μm. It is proposed that this occurs because the larger sized particles are of greater mass and therefore experience much slower acceleration

compared to smaller sized particles whilst travelling within the nozzle and has been predicted previously by Grujicic et al. [68]. For a stagnation pressure of 10 bar the particle velocity is measured to remain fairly constant for all particle sizes measured. When the gas pressure exceeds 20 bar the particle velocity is found to reduce by up to 200 m s^{-1} for particles of less than approximately 9 μm or lower. Measurements were made at a stand off distance of 20 mm and therefore it is possible that particles of diameter less than 9 μm may be decelerating on leaving the nozzle exit or alternatively unable to be accelerated to the same degree as particles of larger size. For a stagnation pressure of 10 bar it is proposed that all particles are able to accelerate to similar values on leaving the nozzle exit.

Using Figure 3.7, originally created by Grujicic et al. [68], the greatest particle impact velocity for a copper particle travelling within a helium gas flow is predicted to be for a particle of approximately 2 μm in diameter. This particle size is far lower than the measured data from this study shown in Figure 3.25(a) where approximately a 10 μm particle was found to have the highest particle velocity. For the copper powder used for this study (+5-25 μm) Grujicic et al. [68] predict particle velocities of between approximately 800 m s^{-1} and 950 m s^{-1}. These values are higher than the measured velocities in this study because Grujicic et al. [68] carry out their calculation for a heated gas flow. However, the reduction in particle velocity for the size range +5-25 μm is in good agreement to that measured in this study. It is unclear whether a heated gas flow may affect the particle size that would provide the highest particle velocity. It may be suggested that on reducing the temperature of a gas flow, and therefore increasing the gas density, it would become easier for larger sized particles to be accelerated by the gas flow and therefore the optimum particle size offering the greatest particle velocity may increase.

To allow for a greater understanding as to why particles less than 9 μm have measured particle velocities lower than the remainder of the size distribution, tests were repeated at a stand off distance of 1 mm. A similar reduction in particle velocity is also found at a stand off distance of 1 mm when the particle size reduces below approximately 9 μm as shown by Figure 3.27(a). It may be concluded that the

smaller sized particles are not decelerating faster than larger sized particles on leaving the nozzle exit. Instead, it has been shown that, in the case of copper and a helium gas flow, particles of less than 9 μm do not attain as high a particle velocity whilst travelling within the nozzle. By removing particles of 9 μm or less from the powders size distribution, a greater proportion of the powder would attain the greater particle velocities. This would lead to greater deposition efficiency and less wastage of the powder when depositing material.

When carrying out velocity measurements at a stand off distance of 1 mm, the particle feed rate had to be reduced from 4 rpm (60 g min^{-1}) to 2 rpm (30 g min^{-1}). This was due to the spray plume consisting of too many particles and making it difficult for the computer software to pair particles together correctly and measure the particles velocity at a stand off distance of 1 mm (as discussed in Section 3.8.2.3.). The reduction in powder feed rate affects the ratio of gas mass flow rate to powder mass feed rate, termed the mass ratio. Using equation 3.30, the gas mass flow rate for helium is calculated as 386 g min^{-1} for a gas stagnation pressure of 29 bar. Therefore the mass ratio is calculated to reduce from 0.155 to 0.077, as the powder feed rate is reduced from 4 rpm to 2 rpm. The higher the mass ratio the higher the probability there is for particles to interact with one another and cause particle deceleration to occur. Figure 3.27(a) shows velocity measurements made at a stand off distance of 1 mm, a powder feed rate of 30 g min^{-1}, and 20 mm, a powder feed rate of 60 g min^{-1}, for a helium gas flow at a stagnation pressure of 29 bar. It could be argued that measurements made at a stand off distance of 1 mm show a slightly lower particle velocity, less than 50 m s^{-1}, and therefore particles continue to accelerate on leaving the nozzle exit. This is despite the higher mass ratio for the measurements made at a stand off distance of 20 mm, which may be expected to reduce the particle velocity. It is anticipated that the measured increase in particle velocity is too low to act as conclusive evidence. However, an even higher particle velocity may have been measured at a stand off distance of 20 mm if a feed rate of 2 rpm had been used, due to the lower mass ratio. Measurements were not made at a stand off distance of 20 mm and a powder feed rate of 2 rpm due to the cost involved in the increased time it would have taken to capture the particle velocities of sufficient particles. Measured data presented by Gilmore et al. [70] and shown in

Figure 3.13, found that when utilising helium gas, particle velocities were found to accelerate, by up to approximately 50 m s^{-1}, up to a stand off distance of approximately 30 mm. Whilst it is difficult to compare velocity measurements published from other authors, due to different nozzle designs and spray parameters employed, a similar trend has also been identified in this project. This indicates that for the nozzle design used that the maximum attainable particle velocity was not achieved whilst the particles were travelling within the nozzle and so were able to continue to accelerate on leaving the nozzle.

Some researchers calculate the largest sized particle to bond to the substrate with knowledge of the powder size distribution and its deposition efficiency as shown by Figure 3.36.

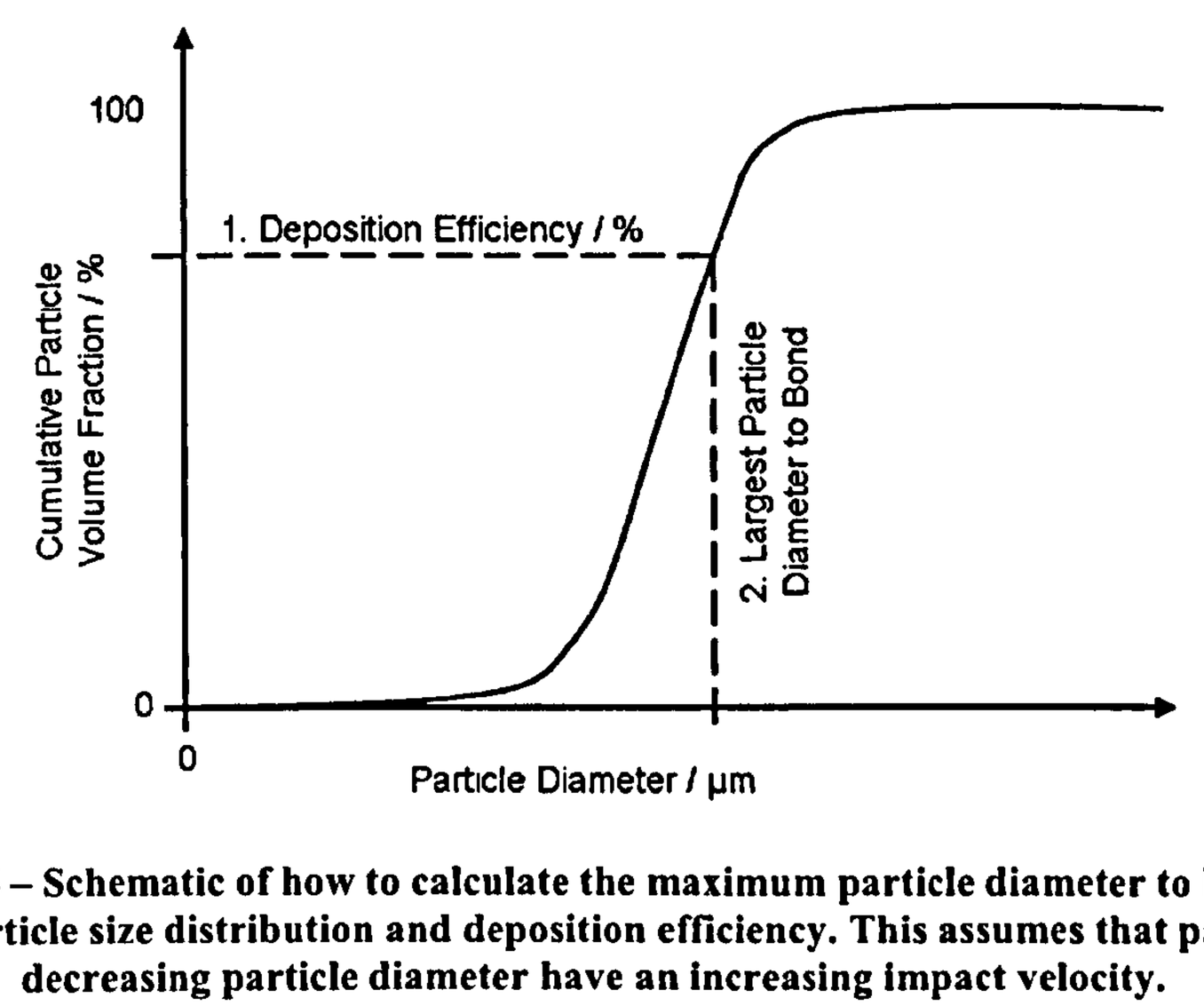

Figure 3.36 – Schematic of how to calculate the maximum particle diameter to bond for a known particle size distribution and deposition efficiency. This assumes that particles of decreasing particle diameter have an increasing impact velocity.

For this method to work it is assumed that for a powder of particular size distribution, the only particles that adhere are those that, because of their small size and therefore higher velocity (as shown by Figure 3.3(a), exceed the critical velocity. This technique was utilised by Stoltenhoff et al. [48] to find the maximum sized copper particle, from a +5 -25 µm powder, expected to deposit for various nozzles used to create coatings with different deposition efficiencies. For a deposition efficiency of greater than 70 %, particles of greater than 18 µm were not expected to

bond. However, from the results found by this study and as discussed previously in Section 3.3.2., it has been shown that for particles of small diameters a reduction in particle impact velocity may be expected and therefore this assumption may not be valid [47, 68]. It is in fact possible for similar sized particles to travel with a wide range of particle velocities due to the various interactions between other particles, nozzle walls and the surrounding atmosphere.

Previous studies found within the literature have often approximated particle velocity results to a normal distribution (Section 3.6.). A more accurate method of testing if this assumption is valid is to plot the data using a normal probability axis. Data collected within this study was plotted using a normal probability axis. Results are shown in Figure 3.37(a) for velocity data at 10 bar and 29 bar for a helium gas flow and theoretical normal distributions that approximately match the measured data. Table 3.13 summarises the mean and standard deviation of the theoretical normal distributions which are shown in Figure 3.37. Experimental velocities carried out with a helium gas pressure of 10 bar appear to match the straight line of the theoretical normal distribution much more closely than when using a helium gas pressure of 29 bar. The largest deviation from the theoretical normal distribution occurs with particles moving at low velocities (less than 300 m s^{-1}), where more than the expected number particles have been expected, and at higher velocities (greater than 650 m s^{-1}), where a lager than expected number of particles have been detected.

Gas Type	Gas Pressure	Mean / m s^{-1}	Standard Deviation / m s^{-1}
Helium	10 bar	308	92
	29 bar	551	103
Nitrogen	10 bar	289	60
	29 bar	376	42

Table 3.13 – Mean and standard deviation of the corresponding normal distributions shown in Figure 3.37 for the measured particle velocities of the copper particles.

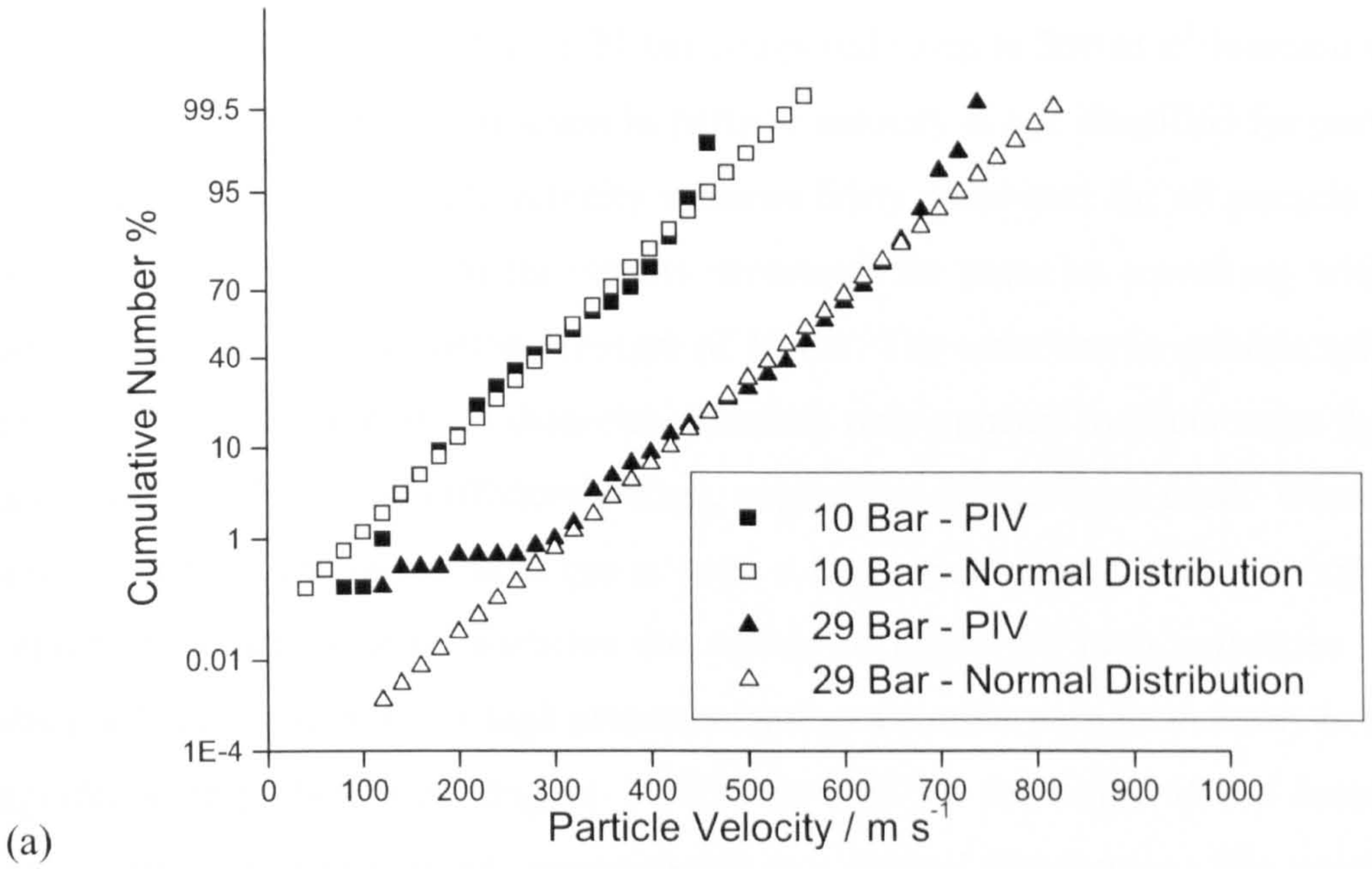

(a)

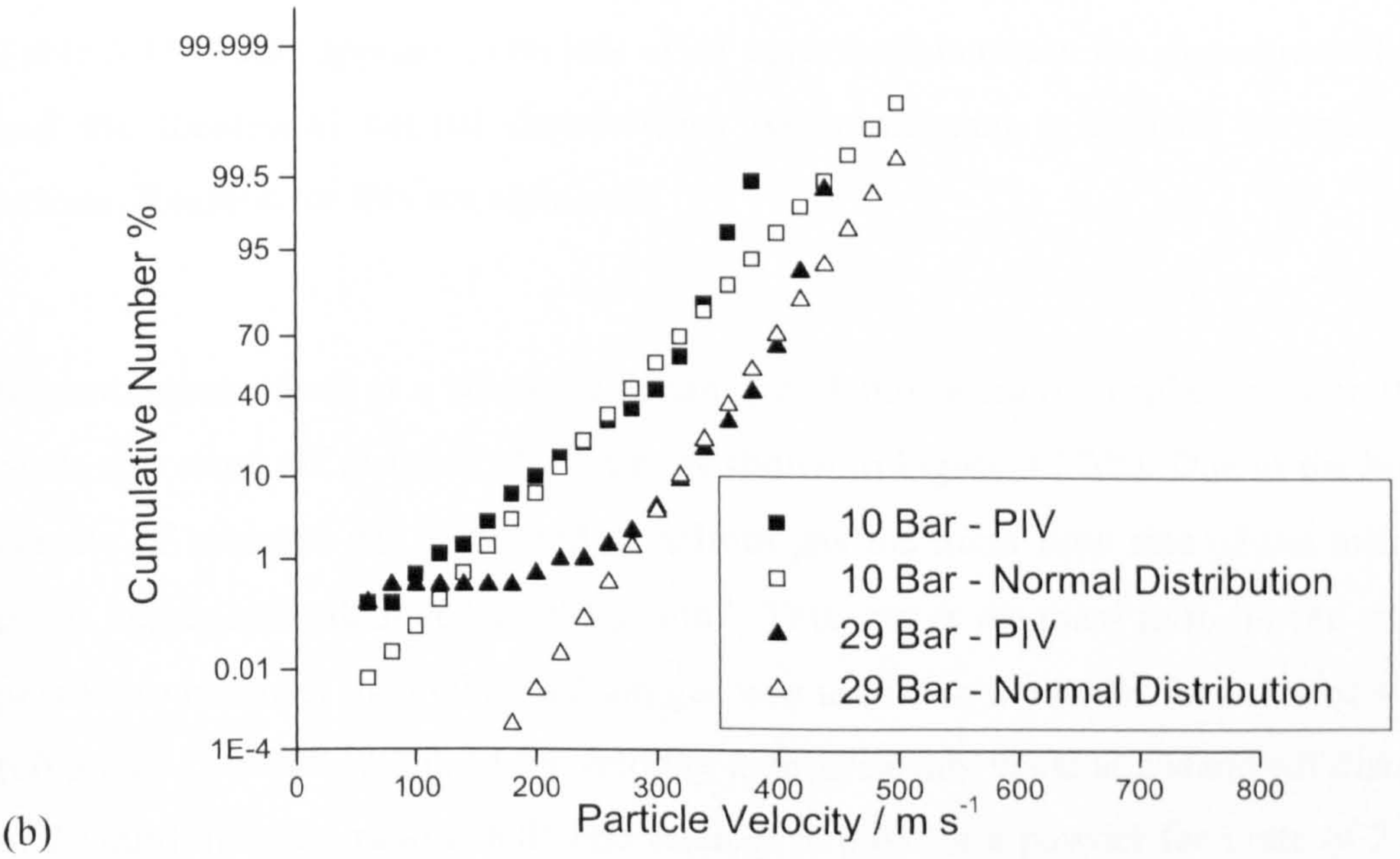

(b)

Figure 3.37 – Experimental velocity data for copper particles travelling within (a) a helium gas flow and (b) a nitrogen gas flow and plotted using a normal probability axis. The straight lines of corresponding standard normal distributions are also shown. Velocity measurements were made at a stand off distance of 20 mm.

3.10.2.2. Nitrogen Gas

When using nitrogen gas, lower particle velocities were found compared to when helium gas is used at a stand off distance of 20 mm. This is due to the lower gas velocity of nitrogen gas whilst travelling through the nozzle. Figure 3.25(b) shows

that only a 100 m s^{-1} increase in particle velocity is found by increasing the gas stagnation pressure from 10 bar to 29 bar compared to up to 300 m s^{-1} increase when helium gas is used. Also a reduction in particle velocity is not identified for particles of small size and the particle velocity remains fairly consistent for all particle sizes measured. This is similar to the results measured for particles travelling within a helium gas flow at a stagnation pressure of 10 bar. The reduction in particle velocity for particles of small particle diameter therefore only appears to occur once the gas and particle velocity is sufficiently high, regardless of gas type used. When low pressure helium gas or nitrogen gas is used a lower gas velocity may be expected. Therefore the larger sized particles are unable to attain the high velocities found when utilising helium gas at high pressures and so a similar particle velocity is found regardless of particle size. Figure 3.37(b) is used to determine if the measured particle velocity data may be approximated to a normal distribution. The mean and standard deviation that the particle velocity data is approximated to is shown in Table 3.13. There appears to be less of an agreement between the experimental data and the theoretical normal distributions when nitrogen is utilised compared to helium. Reasons for this are unknown.

Measurements made at a stand off distance of 1 mm were of similar value to those made at a stand off distance of 20 mm as shown in Figure 3.27(b). Due to the higher density of nitrogen gas compared to helium gas the mass flow rate of the nitrogen gas is higher and calculated as 964 g min^{-1}. This causes the mass ratio for the copper powder to be lower than when helium gas was used. For a powder feed rate of 4 rpm (60 g min-1) which was used for velocity measurements made at a stand off distance of 20 mm) the mass ratio is 0.06 and reduces to 0.03 for a powder feed rate of 2 rpm (30 g min^{-1}), used for velocity measurements made at a stand off distance of 1 mm. Similar to measurements made with a helium gas flow there is a small amount of evidence showing that particles accelerate between a stand off distance of 1 mm and 20 mm. In this case however, because the mass ratio is already significantly low for the measurements made at a stand off distance of 20 mm, no further increase in particle velocity is expected if the powder feed rate was reduced.

When considering the effect of measuring position within the plume it has been discussed previously, in Section 3.10.1., that no change in the measured size distribution was found. At a stand off distance of 20 mm a reduction in particle velocity was found at the extremities of the plume as shown in Figure 3.26. Similar results were found at a stand off distance of 1 mm (Figure 3.28). A reduction in particle velocity at the plume extremities may be expected due to particles interacting with the external environment leading to greater particle deceleration. Also some particles at the plume extremities may have originated from the nozzle at points close to the nozzle walls and therefore frictional effects may also lead to a reduction in their particle velocity. When carrying out measurements at a stand off distance of 1 mm it was found that particles were identified to be present up to 1.5 mm from the central plume position. At a stand off distance of 20 mm this distance increases to 2.5 mm and is due to the diverging nature of the spray plume on leaving the nozzle.

3.10.3. Particle Velocity Measurements – Titanium Powder

Velocity measurements were made using helium and nitrogen gas at a stand off distance of 20 mm at a central position within the plume. The reader is reminded that that the powder was of an angular morphology and therefore some inaccuracy in particle size measured by the Oxford Lasers system may be anticipated. First the velocity results made using helium gas are considered. All measurements were made with a powder feed rate of 4 rpm (20 g min^{-1}), giving a mass ratio of 0.05 and 0.02 when helium and nitrogen gas are used respectively.

3.10.3.1. Helium Gas

As expected, an increase in particle velocity is measured with increasing gas stagnation pressure despite a reduction in gas pressure. Velocities up to 650 m s^{-1} were measured with the titanium powder at a stagnation pressure of 29 bar as shown in Figure 3.30(a). Similar to the copper powder, a reduction in particle velocity is found for particles of approximately 10 μm or less. In the case of copper approximately a 200 m s^{-1} reduction was measured as the particle size reduced below

9 μm. This information may be used to improve the deposition efficiency of the titanium powder is these small sized particles are removed from the feedstock prior to spraying. With the titanium powder, the reduction in particle velocity due to reducing particle size is approximately 100 - 140 m s^{-1}. A higher particle velocity is measured for the titanium powder compared to the copper powder. This is primarily due to the titanium powder being of lower density and therefore easier for it to be accelerated by the gas flow. Secondly the angular nature of the powder may make it easier to be accelerated due to a higher drag coefficient. To assess if the data created can be approximated as a normal distribution the data was also plotted using a normal probability axis. Results are shown in Figure 3.38(a). Table 3.14 shows the mean and standard deviation of the normal distributions that approximately match the measured particle velocity data.

Gas Type	Gas Pressure	Mean / m s^{-1}	Standard Deviation / m s^{-1}
Helium	10 bar	382	105
	29 bar	601	102
Nitrogen	10 bar	292	64
	29 bar	391	56

Table 3.14 – Mean and standard deviation of the corresponding normal distributions shown in Figure 3.38 for the measured particle velocities of the titanium particles.

3.10.3.2. Nitrogen Gas

When using a nitrogen gas flow, the particle velocity was found to be lower than when using helium gas. A similar particle velocity was found when increasing the gas pressure from 20 to 29 bar. Overall a smaller increase in particle velocity was found when increasing the gas pressure from 10 bar and 29 bar and using nitrogen gas compared to when using helium gas. At a gas pressure of 10 bar a reduction in particle velocity was found for particles less than 10 μm in size. To assess if the data created can be approximated as a normal distribution the data was also plotted using a normal probability axis. Results are shown in Figure 3.38(b). The majority of the data closely matches a normal size distribution. The mean and standard deviation of

the normal distributions that approximately match the measured particle velocity data is shown in Table 3.14.

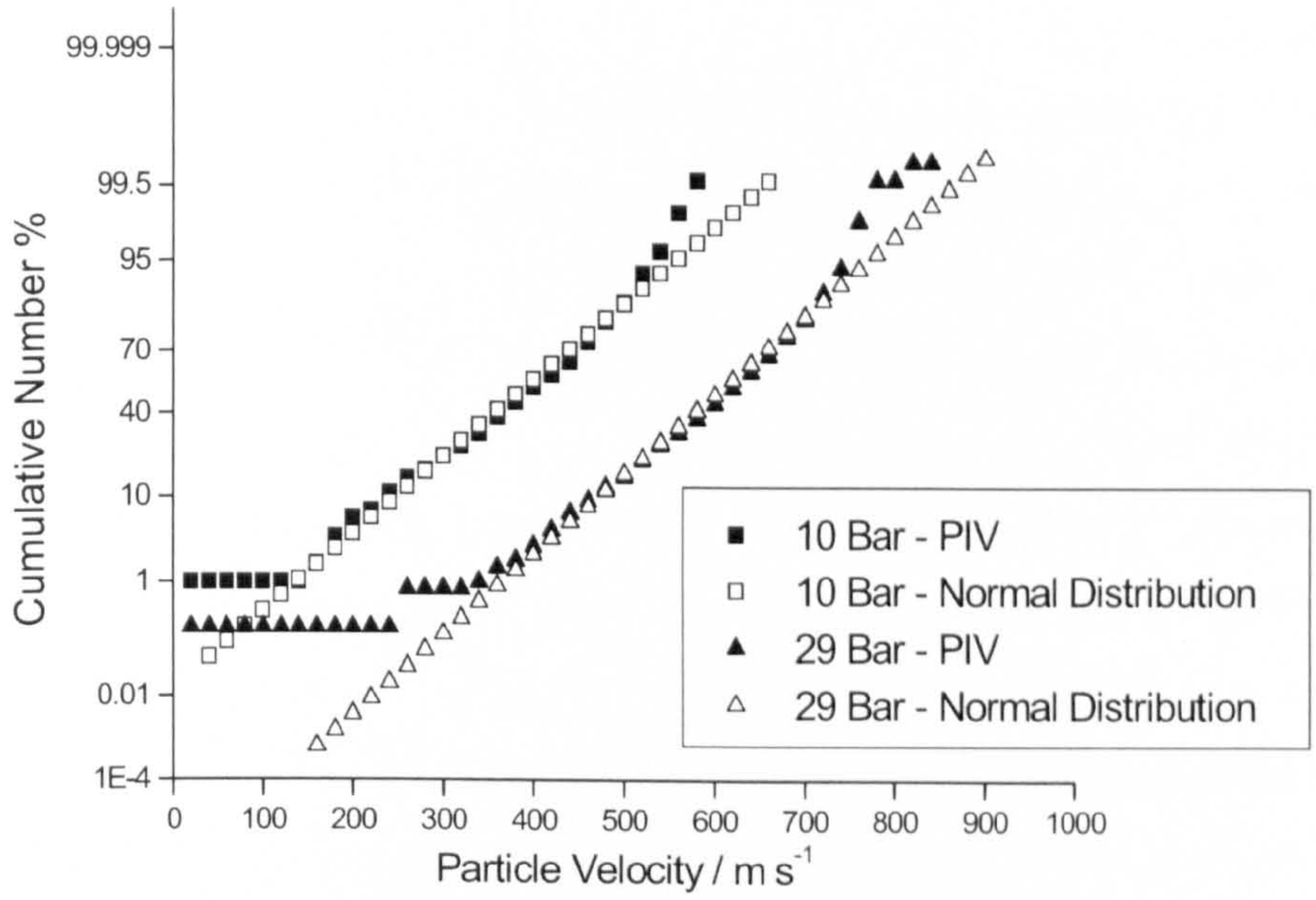

(a)

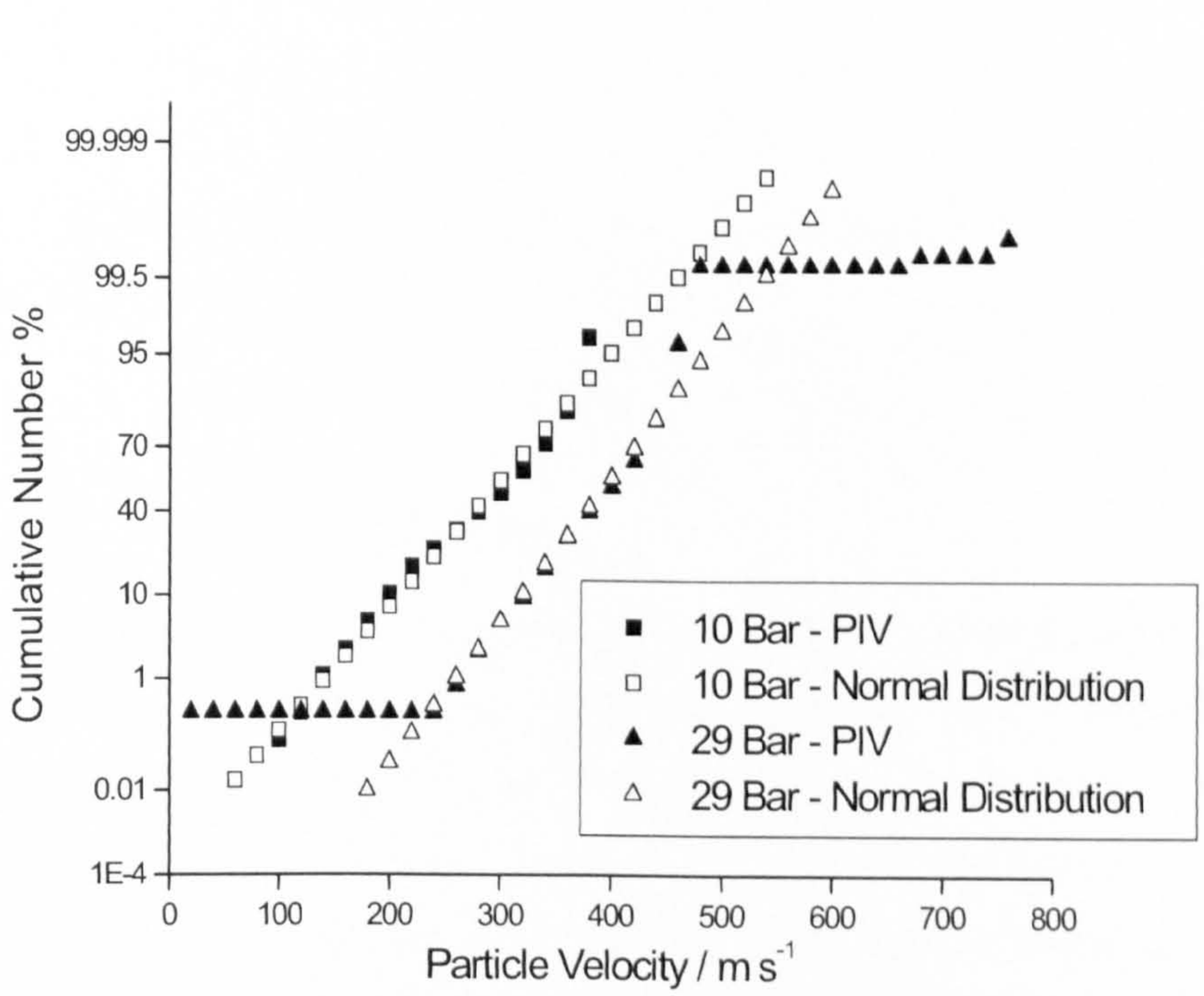

(b)

Figure 3.38 – Experimental velocity data for titanium particles travelling within (a) a helium gas flow and (b) a nitrogen gas flow and plotted using a normal probability axis. The straight lines of corresponding standard normal distributions are also shown.

3.10.4. Particle Velocity Measurements – Nozzle II

A final set of measurements was conducted using a larger diameter throat nozzle design as described in Section 3.8.2.5. In comparison to velocity measurements conducted with the nozzle regularly used for coating deposition, similar particle velocities were measured. The new nozzle was designed so that it maintained the same area-expansion ratio within the nozzle but twice the cross-sectional throat area. This means that the nozzle would theoretically attain the same gas velocity as the current nozzle but the mass flow rate will double. By increasing the cross-sectional throat area any frictional effects than may be present when using the current nozzle would be minimised due to a smaller proportion of the gas flow being influenced by the nozzle walls. Both nozzles were found to have similar particle velocities when using helium and nitrogen gas, as shown in Figure 3.29. It therefore is concluded that either frictional effects are not apparent in either nozzle design and do not prohibit particle velocity or the dimensions of the new nozzle were not large enough to cause a significant variation in any frictional effects present in the current nozzle. However, it should be noted that the measured particle velocities for the copper powder are of similar value to measurements made by other workers and identified in Table 3.2 and Table 3.3 previously. Therefore it is not expected that greater particle velocities would be attainable if further increases in the throat cross-sectional area were made.

3.10.5. Particle Modelling

Within this section comparison between output from the particle model and the measured particle velocities will be made. Figure 3.32(b) shows that the model predicts an increase in particle velocity of approximately 200 m s^{-1} when increasing the helium gas stagnation pressure from 10 to 29 bar. For nitrogen gas, shown in Figure 3.33(b), and the same pressure increase, only approximately a 60 m s^{-1} increase in particle velocity is predicted. The model therefore predicts that particles may be accelerated with greater efficiency using helium gas compared to nitrogen despite the lower gas density. Using the Oxford Lasers equipment an increase of particle velocity when increasing the gas stagnation pressure from 10 bar to 29 bar of approximately 280 m s^{-1} was measured when using helium gas compared to 150 m s^{-}

[1] when using nitrogen gas. Although the values predicted by the particle model are higher than the measured values the same trend has been identified.

The particle model may be regarded as calculating the maximum attainable particle velocity. The model calculates the particle velocity for a single particle travelling through the nozzle and therefore does not consider particle interactions with one another, the nozzle walls, frictional effects, or the effect of the external atmosphere on a particles velocity upon leaving the nozzle. A combination of all or some of these effects may be expected to reduce the particle velocity and cause it to decelerate. It is therefore not surprising that the model output predicts higher particle velocities compared to the maximum measured particle velocities, shown in Figure 3.32(b). When copper particles and helium gas are employed, it was found that as the particle diameter reduced, the difference between the maximum measured particle velocity and the modelled particle velocity increased. This may be explained by the smaller sized particles decelerating at a faster rate compared to the larger sized particles. Therefore a greater variation between the theoretical particle velocity, the model output, and the actual particle velocity may be expected for small sized particles. In the case of copper particles and nitrogen gas, shown in Figure 3.33(b) a much closer resemblance between the maximum measured particle velocities and the model output is found. This is due to the higher density of the nitrogen gas compared to the helium gas and so deceleration effects within a nitrogen gas plume are not as prominent as those found in a helium gas plume.

In the case of titanium similar trends were found to those identified with the copper powder. Higher particle velocities are predicted for the titanium powder compared to the copper powder. This is due to the lower density of titanium and therefore being easier to accelerate whilst travelling within the gas flow. When comparing the model output with the maximum measured particle velocities (Section 3.9.3.), higher velocities are predicted by the model. This is due to the same reasons as outlined above for the copper powder. A further consideration is the fact that the modelling was carried out assuming that the titanium particles were spherical. The titanium particles were in fact angular and this may allow for higher particle velocities, due to

a larger drag coefficient and therefore a greater likelihood of momentum being transferred from the gas flow to the particle, as discussed previously in Section 3.5.2.5.

For both a copper and titanium powder the model predicts reductions in particle velocity with increasing particle size. Whilst this trend was also identified when measuring particle velocities the model fails to predict a reduction in particle velocities for smaller sized particles, a trend first predicted by Grujicic et al [68] and Schmidt et al. [47].

3.11. Conclusions

Particle velocities of a copper and titanium powder have been successfully measured using a PIV technique and the influence of various spray parameters have been investigated. When helium gas and the highest stagnation pressure of 29 bar was used the highest particle velocities were measured for both copper and titanium powders. Whilst it is difficult to compare results with other workers, due to different nozzle designs and spray parameters, results for the spherical copper powder were found to be of similar magnitude to those measured by other workers.

Advantageously, the PIV equipment employed for this project allowed simultaneous measurement of particle size and particle velocity. Comparison of the size distribution measured by the PIV system has been found to be comparable to other particle size measuring techniques and has been successfully shown to be approximated by a log-normal distribution.

In the case of copper powder and using helium gas it was found that particle velocity generally decreased for particles of less than 9 μm in diameter at a stand off distance of 1 mm and 20 mm. Whilst this can not be explained by deceleration effects upon leaving the nozzle, it is attributed to particles of small diameter not attaining higher velocities than larger sized particles whilst travelling within the nozzle.

A nozzle of twice the throat area to that conventionally used for depositions was employed to investigate its effect on particle velocity. Whilst this nozzle would theoretically provide identical gas velocities and pressures, it would limit the influence of the nozzle walls and their subsequent interaction with the gas flow and particles such as boundary layers and frictional effects. Similar particle velocities were measured for both nozzle designs indicating that both nozzle designs do not suffer from frictional effects due to interaction between the gas flow and the nozzle walls. Alternatively both nozzles suffer from similar frictional effects and so an even larger nozzle throat diameter should be used to prove this theory.

When comparing the model output to the maximum measured particle velocities, higher particle velocities were consistently predicted by the particle model. This is not surprising as the model does not consider particles interacting with themselves and the external atmosphere that may lead to particle deceleration. The model failed to predict lower particle velocities for small sized particles that were measured with the copper powder and a helium gas flow. These discrepancies between the model and those measured may be explained by the simplistic nature of the model.

Chapter 4 – Substrate and Coating Characterisation

4.1. Introduction

The following chapter concentrates on the characterisation of the substrates used and the cold spray coatings produced during this project. Firstly, the process materials routinely used for cold spraying and the current state of cold spraying technology is described. The particle impact velocity is required to be greater than a critical velocity for coating build up to occur. This chapter describes the bonding mechanisms expected to occur within cold spray deposits, when particles exceed their critical velocity. It is found that spray parameters, nozzle design and powder types affect the mechanical properties of the coating due to variation in the particle impact velocities. An overview of the mechanical properties of cold spray coatings is made by discussing the mechanical properties of coatings produced from a range of materials, including titanium (the main scope of this project).

To gain a fuller understanding of cold spray coatings in general some work was also undertaken using aluminium and copper coatings. Also, when assessing titanium cold spray coatings it is useful to compare them to a competing spray process used to produce titanium coatings. Therefore some experimental work was repeated using titanium coatings produced by a shrouded arc process. Many experimental methods were used to mechanically test the coatings deposited and included hardness, stiffness, fatigue, bond and residual stress testing. Each of these methods employed are described within this chapter. Finally the experimental results are discussed and comparisons to results from previous workers are made.

4.2. Materials for Cold Spraying

The following section will highlight the characteristics of typical substrate and powder materials that have been used successfully in cold spraying by other workers.

4.2.1. Substrate Material

For cold spraying, many materials have been used as a substrate successfully including aluminium, steel, titanium and copper [45, 48, 53, 59, 65, 78, 82-88]. To aid coating formation it is preferential to choose substrate materials that do not have a tenacious oxide layer. Substrates are frequently ground or grit blasted immediately prior to spraying to increase the substrate surface area and to partially remove some of the unwanted oxide layers.

The current work primarily concentrates on spraying on to a titanium alloy (Ti6Al4V) as used for biomedical applications. Generally the surface is cleaned/degreased and either left in the as received state or grit blasted prior to spraying.

The Ti6Al4V microstructure is generally either lamellar or equiaxed and these are generated by differing thermomechanical treatments. The various microstructures have a strong influence on the mechanical behaviour of Ti6Al4V. Table 4.1 summarises qualitatively the effect of phase size and arrangement on selected mechanical properties of titanium alloys. For example, fine scale microstructures increase the strength and ductility of the material. Coarser microstructures are generally found to have increased fracture toughness and creep strength. Equiaxed microstructures are found to have high ductility and strength. In the case of fatigue properties, the resistance to fatigue crack initiation decreases with coarsening of the microstructure, i.e., a fine equiaxed microstructure will have the greatest effect of preventing fatigue crack initiation. However, for the second stage of fatigue damage, a coarse lamellar microstructure is found to show a more favourable rate of fatigue crack propagation. Therefore it is inherently difficult for both the fatigue crack initiation and crack propagation properties of a titanium alloy to be optimised at the same time [89].

Figure 4.1 is a schematic of the phase diagram for Ti6Al4V. It shows how, at room temperature Ti6Al4V, is a two-phase alloy and above temperatures of approximately 1000 °C changes to a single β phase alloy.

Fine	Coarse	Property	Lamellar	Equiaxed
-	-	Elastic Modulus	-	+/- (texture)
+	-	Strength	-	+
+	-	Ductility	-	+
-	+	Fracture Toughness	+	-
+	-	Fatigue Crack Initiation	-	+
-	+	Fatigue Crack Propagation	+	-
-	+	Creep Strength	+	-
+	-	Superplasticity	-	+
+	-	Oxidation Behaviour	+	-

Table 4.1 – Table shows qualitatively how the size of phases (comparison of fine and coarse microstructures) and arrangement of phases (comparison between lamellar and equiaxed microstructures) influence selected mechanical properties of titanium alloys [89].

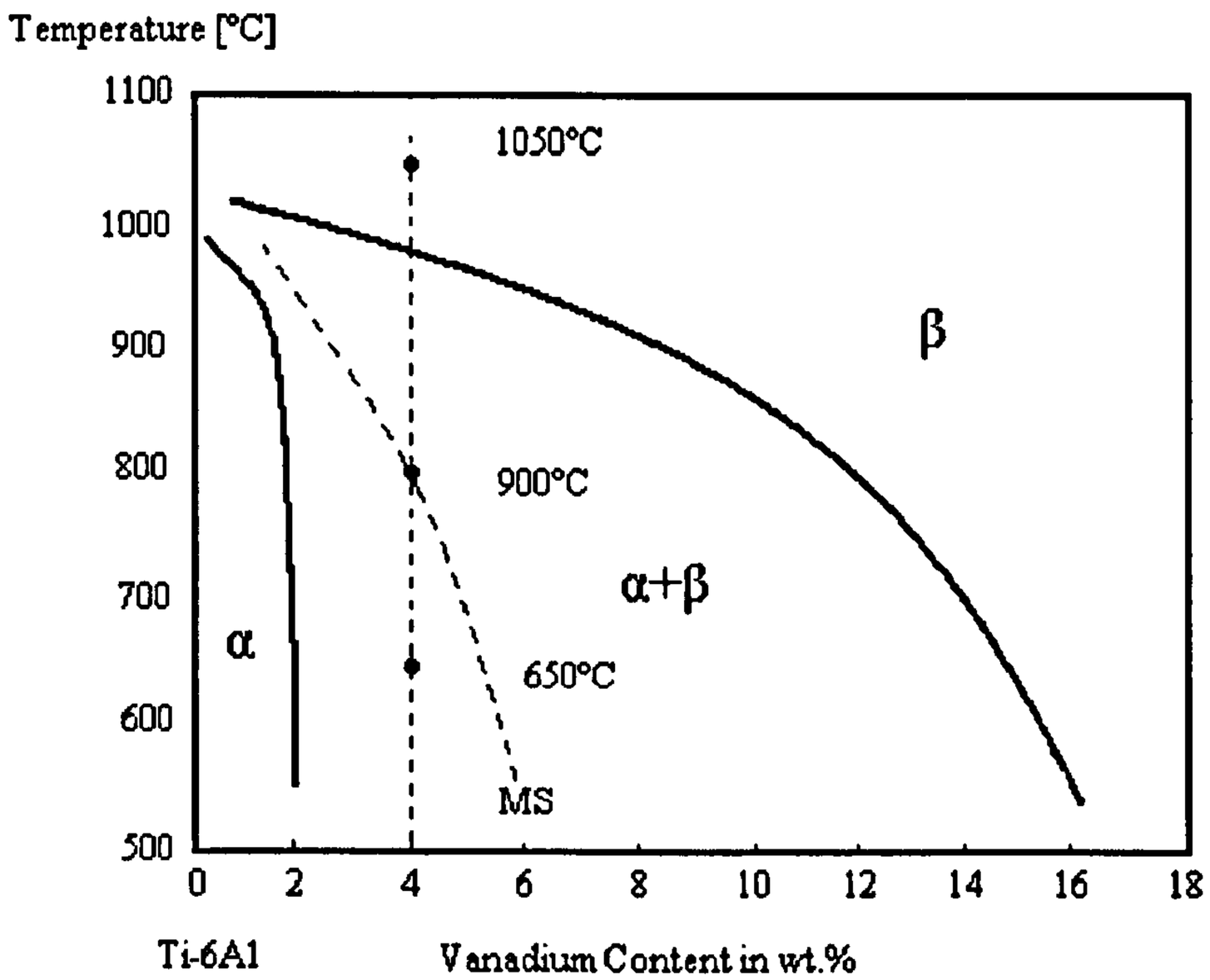

Figure 4.1 – Schematic of the Ti6Al4V phase diagram. MS – Marternsite start [89].

4.2.2. Deposited Material

The cold spraying process favours the successful deposition of metal powders as opposed to ceramics and polymers. This is due to the process relying on plastic deformation of the powder to create the build up of a coating onto the substrate. Aluminium, copper, nickel, titanium and steel have all been successfully sprayed using cold spraying [59].

The density of the particles is of importance. Particles of high density will accelerate more slowly when travelling along the nozzle compared to less dense materials. Therefore the cold spraying process is not suitable for very dense materials such as tungsten [42]. Modelling has been carried out previously to investigate the role of material properties, for example density and yield strength, on deposition efficiency and the reader is referred to Sections 4.3. and 4.4. for a greater explanation of findings.

4.2.3. Particle Size Distribution

Powders to be sprayed are generally of the region of 10μm to 60μm in diameter. Smaller particle sizes are more expensive to produce, and difficult to handle due to health and safety risks such as inhalation of the fine powder [87]. Smaller particle sizes in practice can be more difficult to feed and this often limits the minimum particle size that can be sprayed [70]. The velocity that the particle must exceed for bonding to occur, the critical velocity, is found to reduce also with increasing particle diameter and this is discussed in further detail in Section 4.5. Work by Schmidt et al. [47] shows that a reduction of approximately 200 m s^{-1} in the critical velocity is measured when a particle is increased in size from 25 μm to 2 mm in diameter. Tests were conducted using aluminium and copper.

4.3. Deposition Efficiency

The deposition efficiency refers to the ratio of the weight of the deposited coating (the weight gain of the substrate prior to spraying) and the powder feed rate [70]. The deposition efficiency is dependent on the particle impact velocity, particle material, size and shape, substrate material and surface finish. Deposition efficiencies of 65%-90% have been observed for CGDS for a range of gas types, spray materials and substrates [45, 47, 70]. Lower deposition efficiencies have been measured when using experimental materials or parameters not optimised for the cold spray process. For example, Shin et al. [90] found deposition efficiencies as low as 20 % for tungsten within a tungsten-copper blended powder. Pre-heating of the powder was found to increase the deposition efficiency of the tungsten to nearly 70 % and the author suggests that this is due to enhanced thermal softening, required to

improve bonding between particles. When spraying a thermoplastic powder by cold spraying, deposition efficiencies as low as 0.5 % have been measured [91]. The authors did not know why such low deposition efficiencies were measured but suggest that it is most likely due to either weak adhesion between particles or that erosion of the coating readily occurs due to further impinging particles at impact velocities greater than its critical velocity.

Particle impact velocities must exceed a particle critical velocity for deposition to occur and this is desribed in further detail in Section 4.5. The effect of critical velocity on the deposition efficiency has been successfully modelled by C.J. Li et al. [92] for a copper powder deposited by helium or nitrogen gas at a pressure of 2 MPa and a temperature of 340 °C. This is based on calculation of the particle deposition efficiency as a function of particle size distribution. Results are shown in Figure 4.2. Higher deposition efficiencies are predicted when helium gas is used rather than nitrogen because of the higher particle impact velocity associated with helium gas but in both cases a reduction in deposition efficiency is found for systems with higher particle critical velocities. For systems with higher critical velocities it will become increasingly harder for the particle impact velocity to exceed the critical velocity. As the particle impact velocity and critical velocity become similar, the deposition efficiency is expected to reduce as there is a greater likelihood of bonding between particles not occurring. One example of when this may occur is shown in Figure 3.6; as the particle diameter increases, its impact velocity will decrease and approach the critical velocity. Particle impact velocities can also be reduced to values close to or below the required critical velocity due to low gas pressure, sub-optimal stand off distance and/or incorrect powder size distribution. A low gas pressure will mean that there is insufficient kinetic energy within the gas flow to accelerate the particles. A sub-optimal stand off distance, usually too large, will allow the particles to decelerate whilst travelling between the nozzle and substrate. Finally an incorrect powder size distribution will either consist of particles that are too small and too light and therefore decelerate quickly upon leaving the nozzle or too large so that they weigh too much to be accelerated efficiently within the nozzle. These process variables have been discussed in more detail previously in Section 3.5.2.

Low deposition efficiencies can also be expected if the particle diameter is too small and therefore a fast rate of heat transfer over the particle volume prevents the localised particle temperature from being sufficiently high for shear instabilities to occur [47, 93]. Additionally, it may be expected that if a powder is chosen which has an oxide layer that is difficult to break down, there is greater likelihood of shear instabilities and bonding between particles not occurring and so the deposition efficiency will reduce.

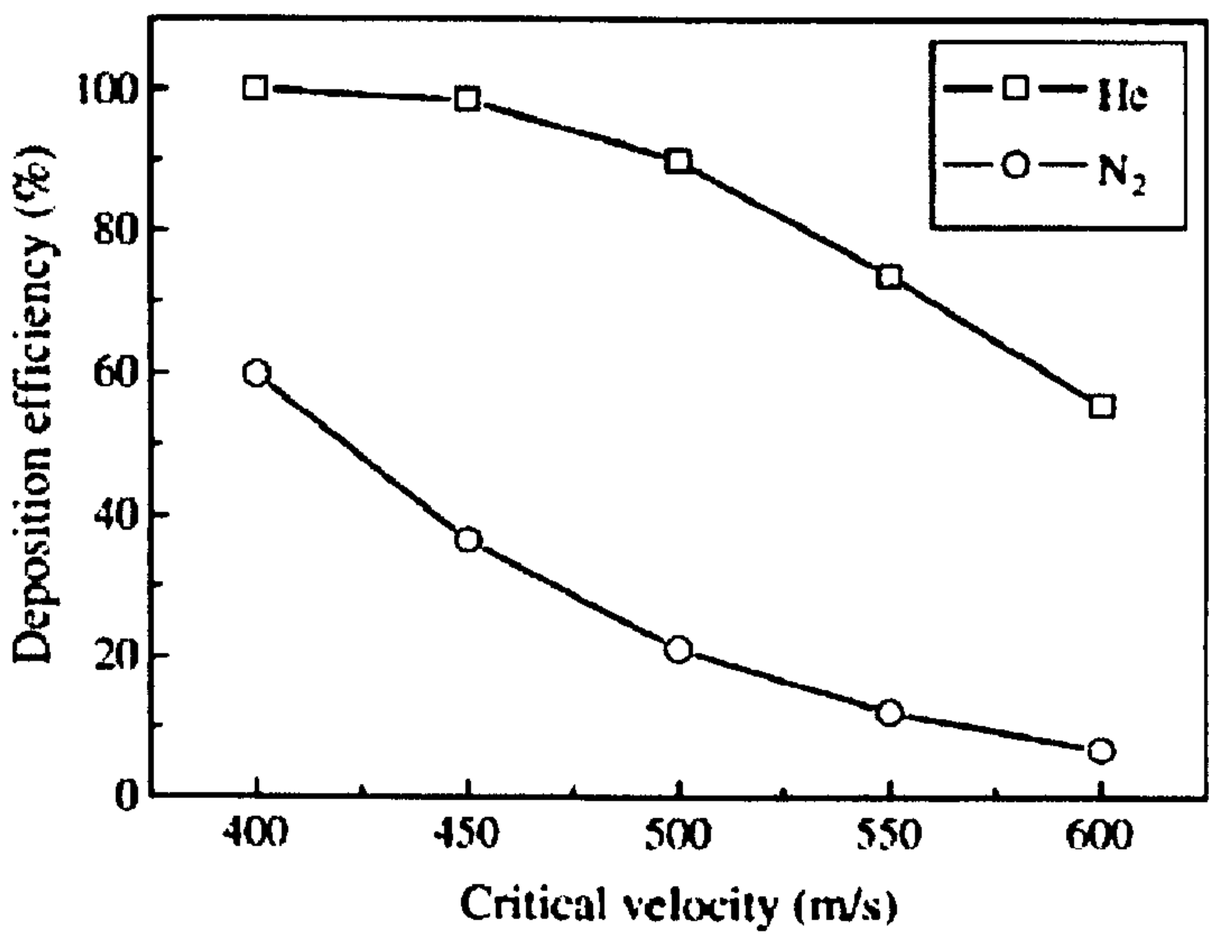

Figure 4.2 – Effect of critical velocity on the deposition efficiency of a copper powder when utilising helium or nitrogen gases operated at a run-time pressure of 2 MPa and temperature of 340 °C [92].

4.4. Bonding Mechanisms

For particles to adhere to the substrate in CGDS, it is widely recognised that they must have an impact velocity in excess of a critical velocity [47]. Particle velocity is a function of many spray parameters, for example; gas pressure, temperature, powder feed rate, nozzle dimensions, stand off distance and powder material. At low impact velocities, particles are unable to adhere to the substrate due to insufficient kinetic energy. Instead they will rebound from and possibly deform the substrate similar to a sand blasting process [43, 47, 49-52]. As the particle velocity increases, the amount of deformation and erosion to the substrate will increase leading to a breakdown of the oxide layers on the substrate; this has been observed by analysis of craters produced on the substrate surface after spraying [50, 85, 93]. Eventually particle velocities will exceed a critical velocity required for bonding between the substrate

and impinging particles to occur. Methods to estimate the particle critical velocity are described in Section 4.5.

There are various mechanisms suggested within the literature that explain the bonding mechanisms operating. These include mechanical interlocking between substrate and particles on impact and bonding due to the creation of Van der Waals forces between particles [50]. However, the adhesive strength of cold spray deposits is considerably higher than that expected of van der Waals forces. It is now widely agreed that for coating formation to occur there must be sufficient plastic deformation to the impinging particle themselves during substrate-coating bonding [47, 50-52, 55, 68, 83, 85, 87, 93] and, as such, the yield stress of the particle must be exceeded upon impact [93]. On impact, a strong pressure field propagates spherically into the particle and substrate from the point of contact as shown by Figure 4.3(a). This pressure wave is believed to deform the grain structure within the particle. Evidence of this phenomenon has been found by etching an aluminium deposit as shown in Figure 4.4 [84].

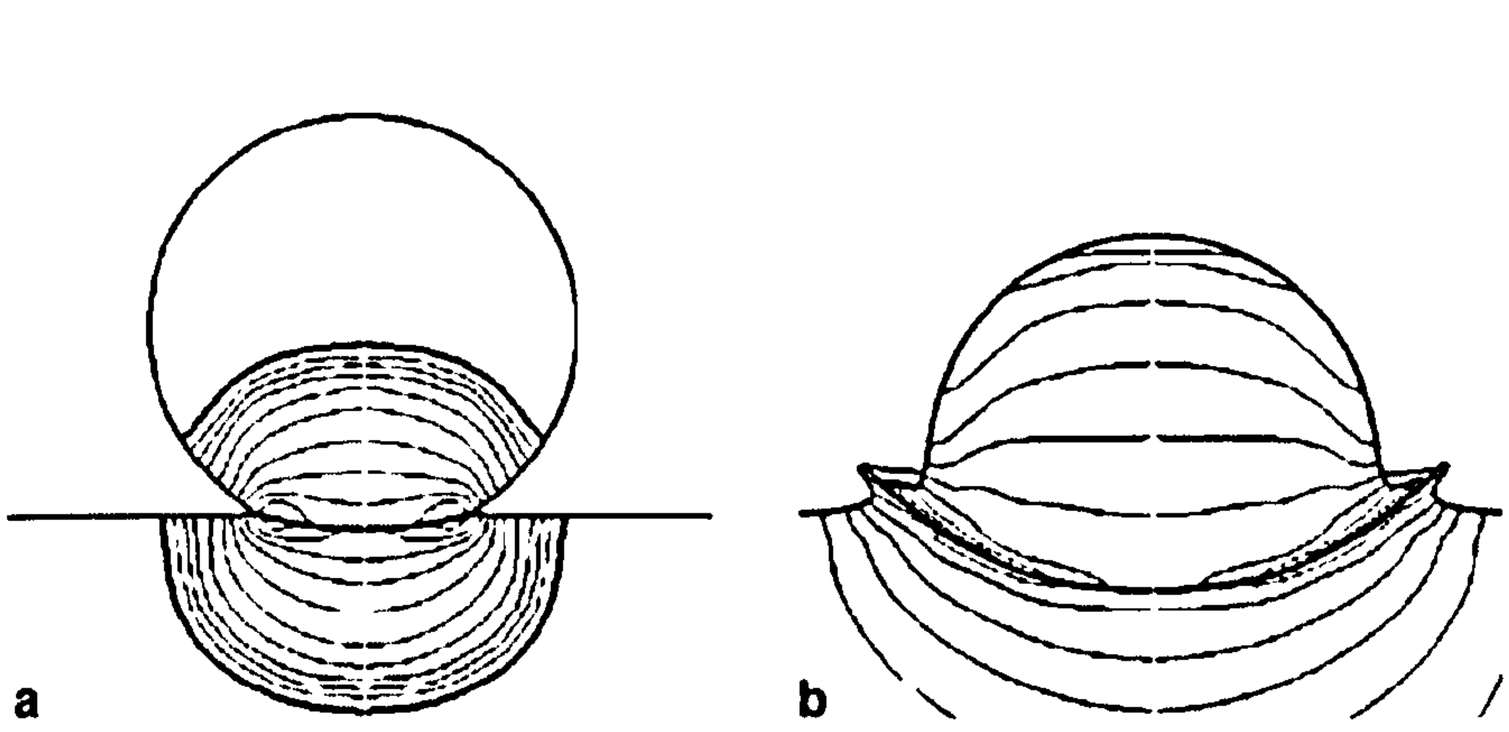

Figure 4.3 – Pressure field during impact (a), and jetting (b) [47].

The initial removal of oxide layers of the substrate allows further impinging particles to adhere to the newly-exposed metal surfaces [55]. On impact of further impinging particles, high plastic strain rates of the materials are observed which can result in shear instabilities and significant softening of the material surrounding the impact zone due to adiabatic heating [47, 48, 50-52, 54, 55, 85, 88, 93, 94]. This leads to lateral viscous flow of the particle and an increase in the local material temperature close to its melting point. Solid-state jets of metal are extruded from the interface between the particle and the material which is being impacted as shown

schematically by Figure 4.3(b) [47, 51, 93]. Topographical evidence of metal jetting occurring on impact has been found by Assadi et al. [93] when investigating copper particles impacting a copper substrate as shown in Figure 4.5. The bonding process results in removal of surface oxide layers, allowing true metal to metal contact and a bond to form between these surfaces [47, 51, 55, 68, 93-95]. Impinging particles will additionally cause consolidation of any already deposited material, thus reducing voids and porosity within the coating.

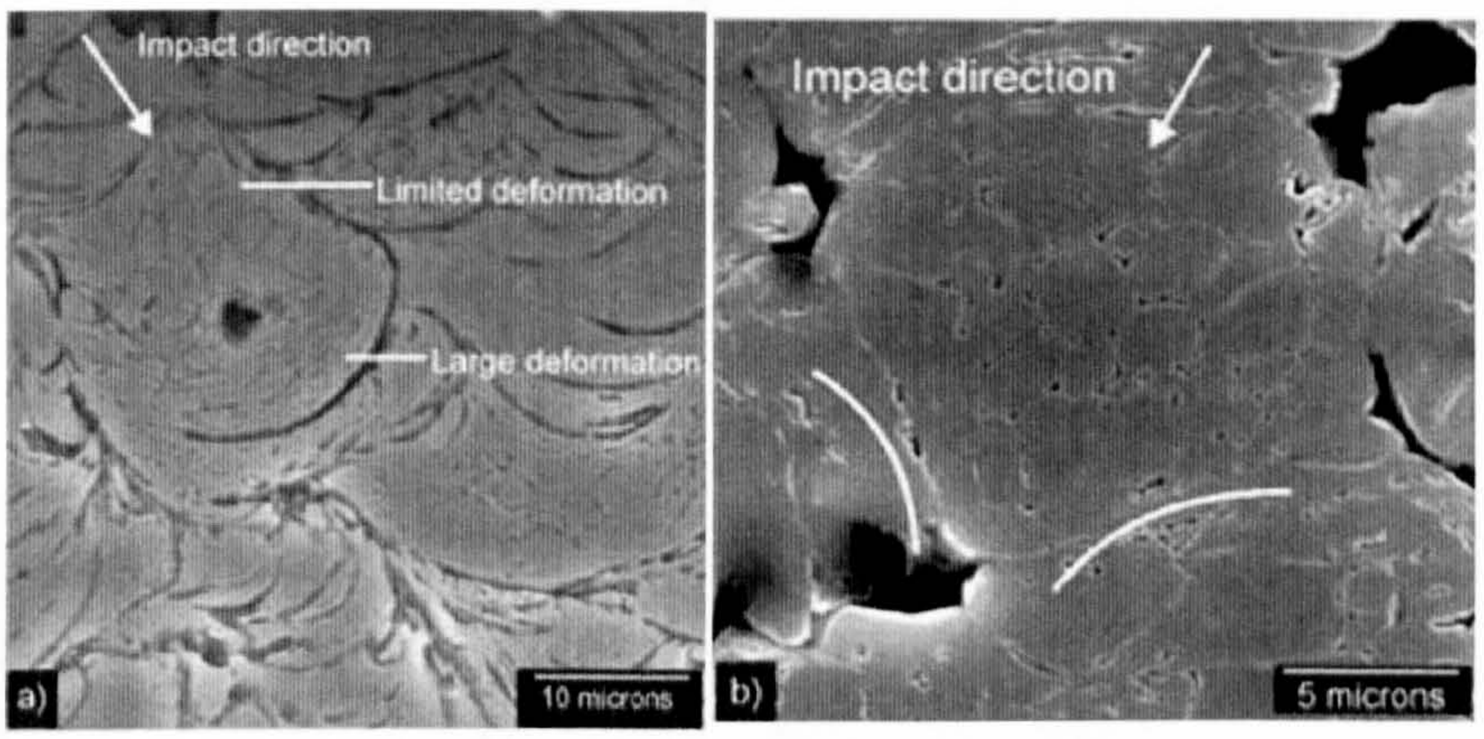

Figure 4.4 – (a) SE image showing aluminium particle impact. Deformation of grain structure within the particle perpendicular to impact direction at the leading edge may be identified. (b) Grain structure of particle is compressed between pre-deposited material on impact [84].

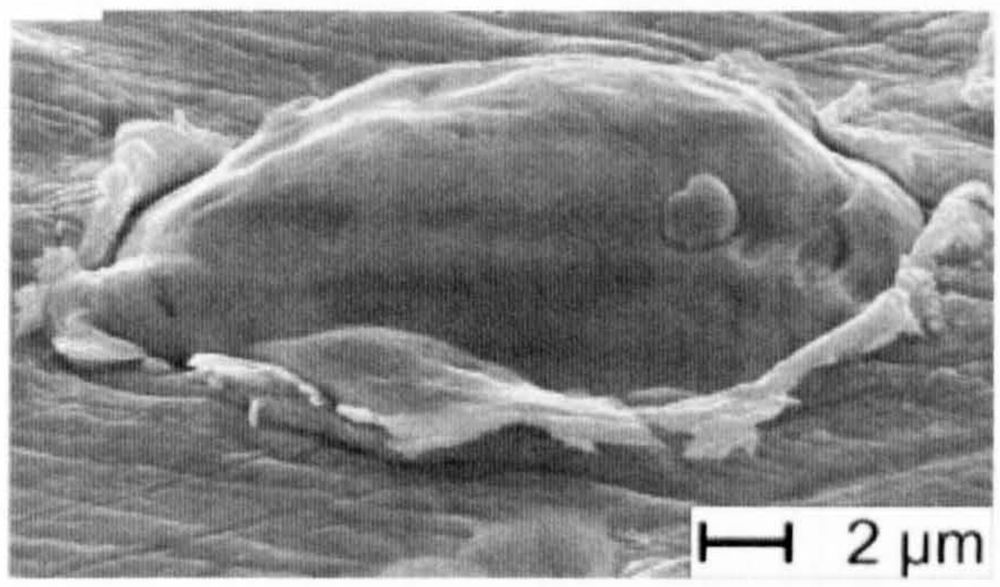

Figure 4.5 – Scanning electron micrograph of a copper particle impacting a copper substrate. Evidence of metal jetting can be seen [93].

Modelling of the bonding process has been carried out to further increase the understanding of the operative mechanisms. High strain rates and large temperature increases have been found for particles impacting at speeds in excess of the critical velocity [47, 52, 93]. It has been found that the particle size will affect the amount of localised deformation and temperature increase. Schmidt et al. [47] modelled local shear and temperature variations within particles on impact and allowed the

occurrence of shear instabilities to be analysed for typical particle diameters (5 – 50 μm) and impact velocities (400 – 600 m s^{-1}) as shown in Figure 4.6. A critical particle diameter required for shear instabilities to occur was found. Below this critical diameter (< 5 μm) the maximum local temperature is insufficient due to a fast rate of heat transfer over the particle volume and therefore shear instabilities are prevented from occurring. As the particle diameter increases, the cooling rate decreases and therefore an increase in the localised temperature can be expected. The interfaces are therefore exposed to higher temperatures for longer time periods and therefore a greater likelihood of bonding between the particles can be expected. Therefore for any given powder an increasingly stronger bond between splats is expected with increasing particle size for a given impact velocity.

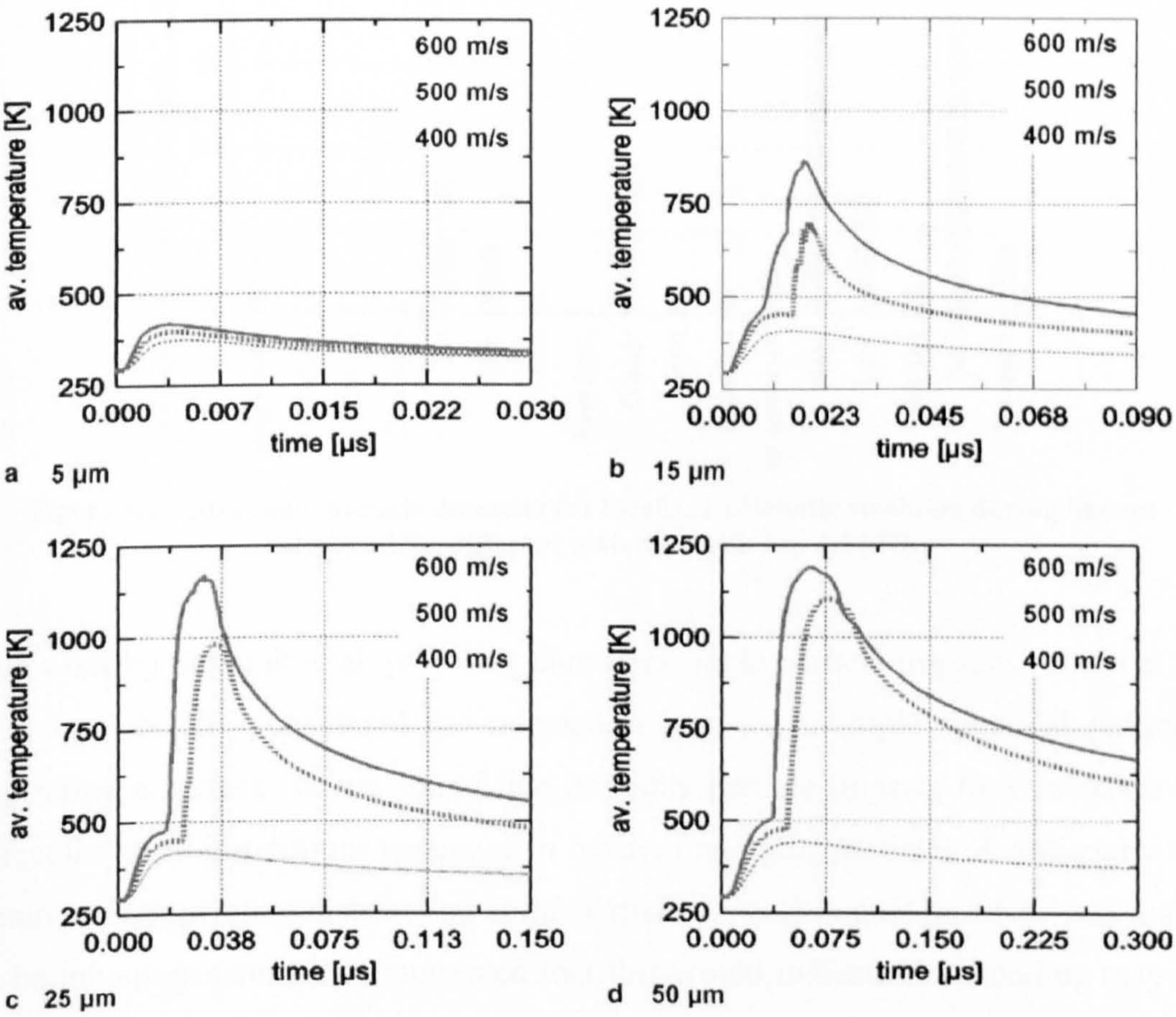

Figure 4.6 – Evolution of the local temperature for (a) 5 μm (b) 15 μm (c) 25 μm and (d) 50 μm copper particle for different impact velocities [47].

Schmidt et al. [47] generated the following equation for estimating the minimum particle diameter required for allowing shear instabilities to occur for a given particle impact velocity:

$$d_{crit} = 36\frac{\lambda_p}{c_p \cdot \rho_p \cdot u_p} \qquad \text{(Eq. 4.1)}$$

where d_{crit} is the critical particle diameter, λ_p is the thermal conductivity of the particles, c_p the specific heat of the particle, ρ_p the particle density and u_p the velocity of the particle. Figure 4.7 shows the minimum particle diameter for localised adiabatic straining to occur on impact for various materials using equation 4.1. Materials of high thermal conductivity require larger particle diameters to promote bonding between the particles.

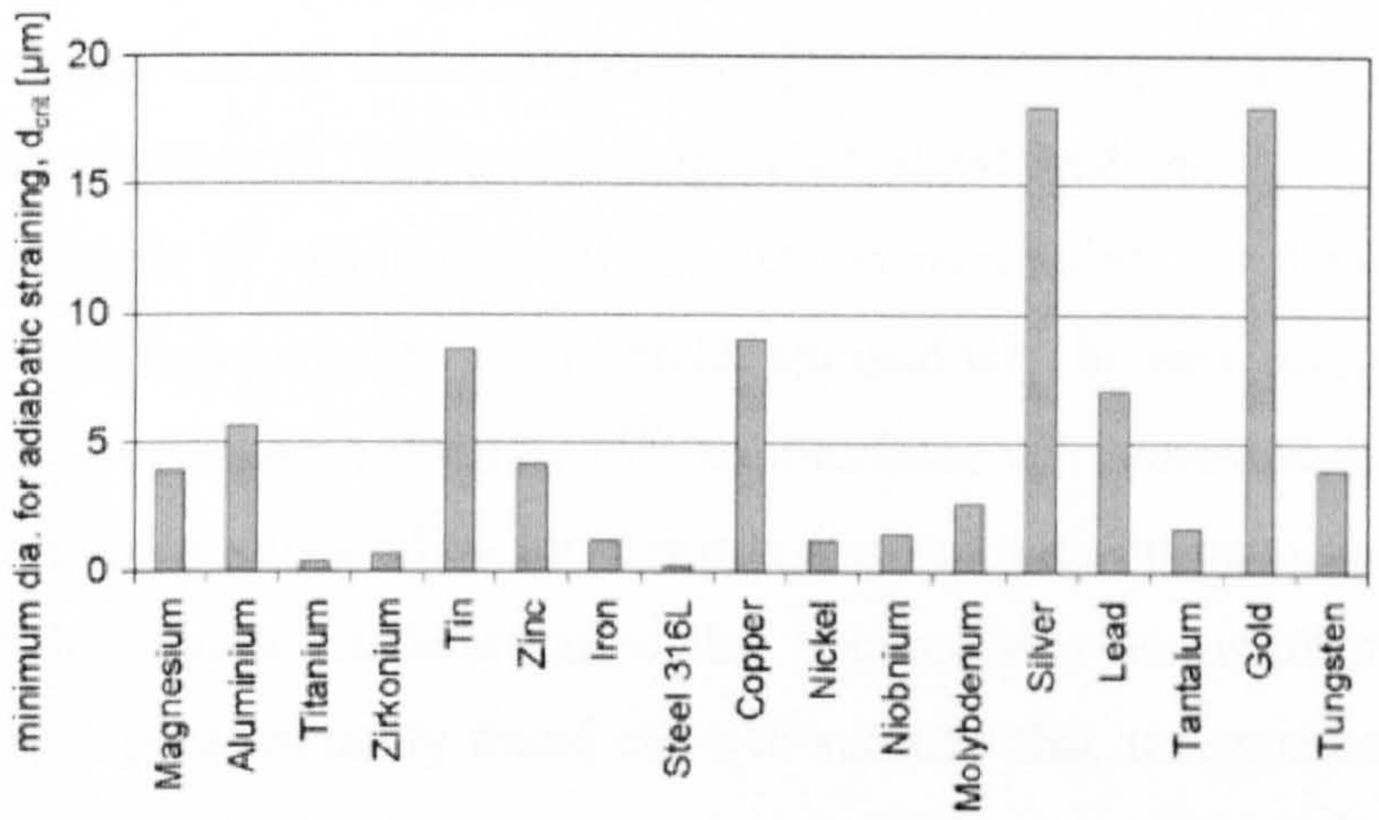

Figure 4.7 – Minimum particle diameter for localised adiabatic straining during impact calculated for different materials with Eq. 4.1 [47].

The work by Schmidt et al. [47] only considers single particle impacts. Assadi et al. [93] have briefly considered the interaction between multiple spherical particles impacting a surface. It was found that previous particle impacts to a substrate do affect the shear instabilities generated in further impinging particles. Additionally the strain and temperature distribution at the particle-particle impact interface was found to be inhomogeneous; they suggested that this would indicate that bonding may be confined to a fraction of the interacting surfaces. This could be potentially due to oxide layers not being removed on particle impact. When modelling particle impact, whilst shear and temperature effects can easily be considered, the role of surface

oxides in modifying interface interactions has not been addressed (even though its role is widely recognised) [47].

Examination of the bonding mechanisms operating during cold spraying has also been carried out by examination of the interfaces formed between splats. A range of techniques have been employed to determine whether oxide free boundaries do indeed exist [44, 53, 55, 84, 88, 96]. A number of authors have reported metallographic studies using scanning and transmission electron microscopy and have shown that, although particles appear well bonded, interparticle defects do exist in the form of voids, pores and sub-micron oxide layers. There has also been evidence presented for the presence of surface oxides ruptured during deposition. Etching of the coating microstructure, to highlight the defects surrounding individual particles, has been carried out on aluminium [55, 84] and copper [88] cold sprayed coatings. Stoltenhoff et al. [88] used this approach, combined with image analysis, to estimate the degree of metal-to-metal contact between splats for deposits sprayed with nitrogen and helium gases. For particles sprayed with helium gas (and therefore an expected higher impact velocity), 75% of interfaces were found to show metallic bonding compared to 30 to 35 % for deposits sprayed with nitrogen gas. They also showed that the amount of deformation that occured was non-uniform within the particle and was predominantly found close to surfaces that are impacted by further impinging particles. Whilst this etching technique provides useful insight, control of the etching behaviour to obtain reproducible results is very difficult.

The nature of the oxide layers between individual particles in aluminium, copper and nickel deposits has also been analysed using transmission electron microscopy [44, 53, 96]. It was found that at inter-particle boundaries, oxides were identified that appeared to have originated from the original powder. Although evidence of ruptured surface oxides was found, which allowed true metal-to-metal contact to occur at points along particle interfaces, true metal to metal bonding was incomplete [96]. For example, Figure 4.8, shows evidence of an oxide layer only forming at some points along the aluminium splat interfaces. No attempt was made to explain why surface oxides ruptured at some interfaces and not others. Further physical analysis of splat interfaces and modelling of the surface topography, particle interactions and their

effect on bonding mechanisms is required for a fuller understanding of the bonding mechanisms that occur within cold spray coatings.

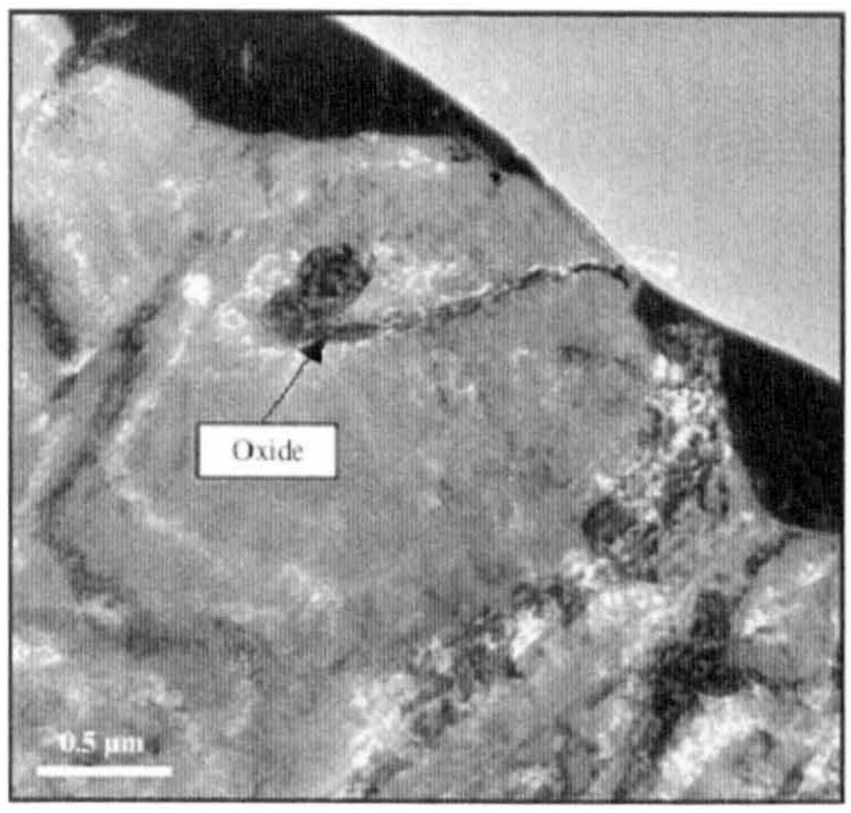

Figure 4.8 – Transmission electron microscopy image of an aluminium deposit showing evidence of oxide layers at a splat interface [96].

4.5. Particle Critical Velocity

The cold spray process relies on the correct process variables to ensure that the impact velocity of the particle is greater than the critical velocity. Knowledge of the particle impact velocities allow the critical particle velocity to be calculated if the particle impact velocity as a function of size and the deposition efficiency for a particular powder and substrate combination are known. It is assumed that only particles exceeding the critical velocity can deposit on the substrate and that the critical velocity is independent of particle size. Plotting the deposition efficiency on to a cumulative volume% plot of particle velocities allows the critical velocity to be found as shown schematically in Figure 4.9. A decrease in the critical velocity required for bonding to occur will lead to increased coating deposition efficiency.

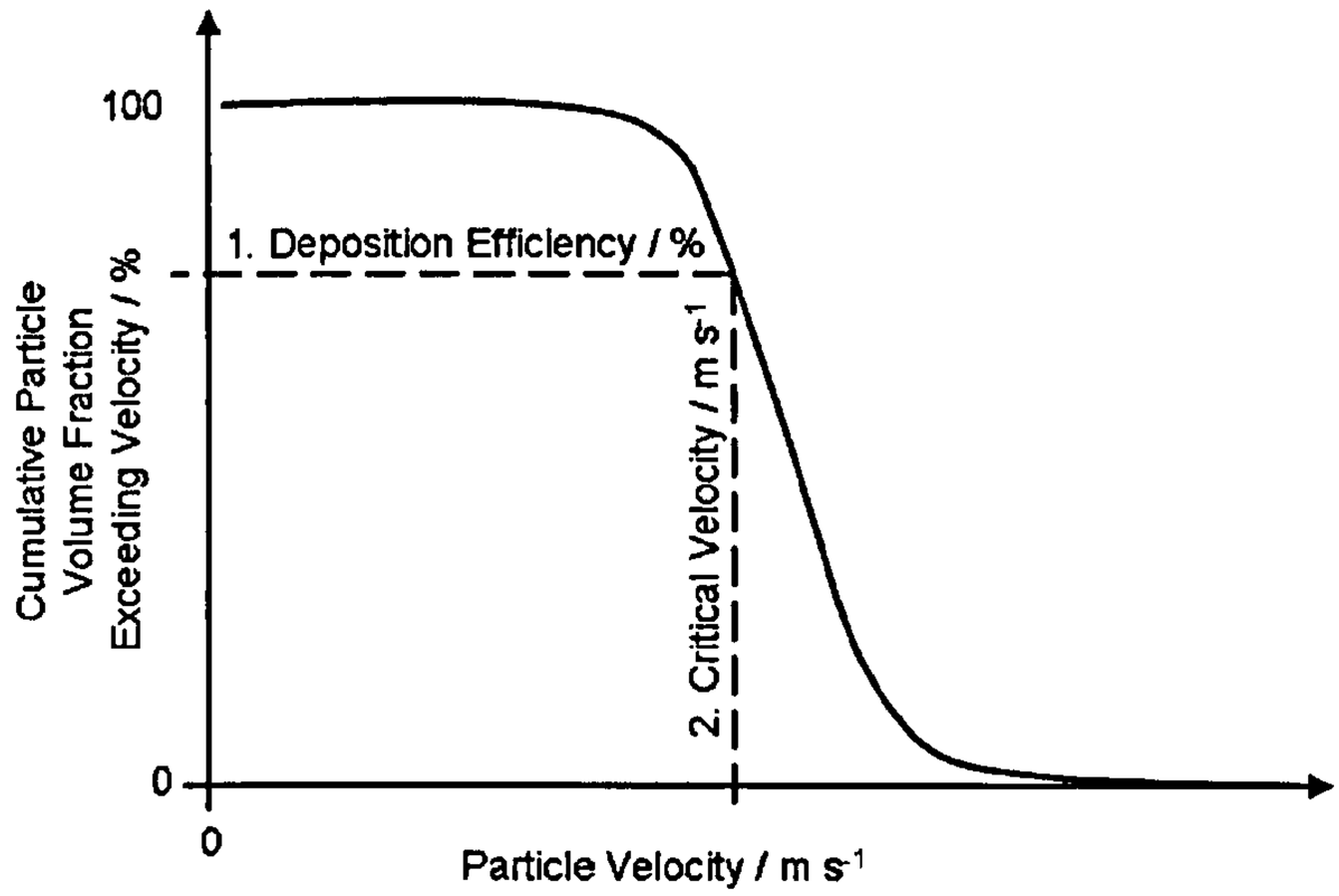

Figure 4.9 – Schematic of how to calculate the critical velocity for a known particle deposition efficiency and velocity distribution.

By using these derived critical velocities as reference conditions, it is possible by numerical analysis to predict the critical velocity for a range of powder materials and process parameters to develop equations that estimate the critical velocity for a powder [47, 93]. Work by Assadi et al. [93] used finite element analysis modelling to estimate the critical velocity for a copper powder. The following equation was derived for calculating a materials critical velocity:

$$u_c = 667 - 14\rho_p + 0.08T_m + 0.1\sigma_u - 0.4T_i \qquad \text{(Eq. 4.2)}$$

Where u_c is the critical velocity (m s^{-1}), ρ_p is the particle density (g cm^{-3}), σ_u is the particle ultimate strength (MPa) and T_m and T_i are the particle melting and impact temperatures (°C) respectively. Equation 4.2 allows the effect of changes of the particle properties (density, ultimate strength, melting temperature etc) on critical velocity to be predicted. It is shown that the ultimate strength and melting temperature of the particle has a smaller influence on the critical velocity than the particle density and impact temperature. Equation 4.2 was originally derived for copper; however it is also valid for calculating the critical velocity of other materials if there are only small changes in the particle properties. For large deviations from the copper reference condition, for example from copper to tin, less accuracy in the critical velocity can be expected. However the simplicity of equation 4.2 makes it easy to evaluate various materials and their applicability for cold spraying.

Schmidt et al. [47] worked to improve the accuracy of Assadi's equation (Equation 4.2). Their aim was to develop simple equations, which predict impact dynamic effects, such as particle bonding or erosion, based on available materials data. It is assumed that particle and substrate materials as well as initial temperatures are identical. Impact dynamic effects are determined by the relationships of the interaction between material strength and dynamic load [47]. The tensile strength of the particle and the Johnson-Cook equation for thermal softening are used to represent the temperature-dependent strength of the material and a ballistic expression is used for characterising the dynamic load. Comparisons between Assadi's equation, equation 4.2, and Schmidt's equation are shown in Figure 4.10. Figure 4.10 highlights the point that drastically different critical velocities are calculated by Assadi's equation when a material is analysed that has significantly different properties to the reference material copper; for example tin with a significantly lower melting temperature or tantalum with a significantly higher density.

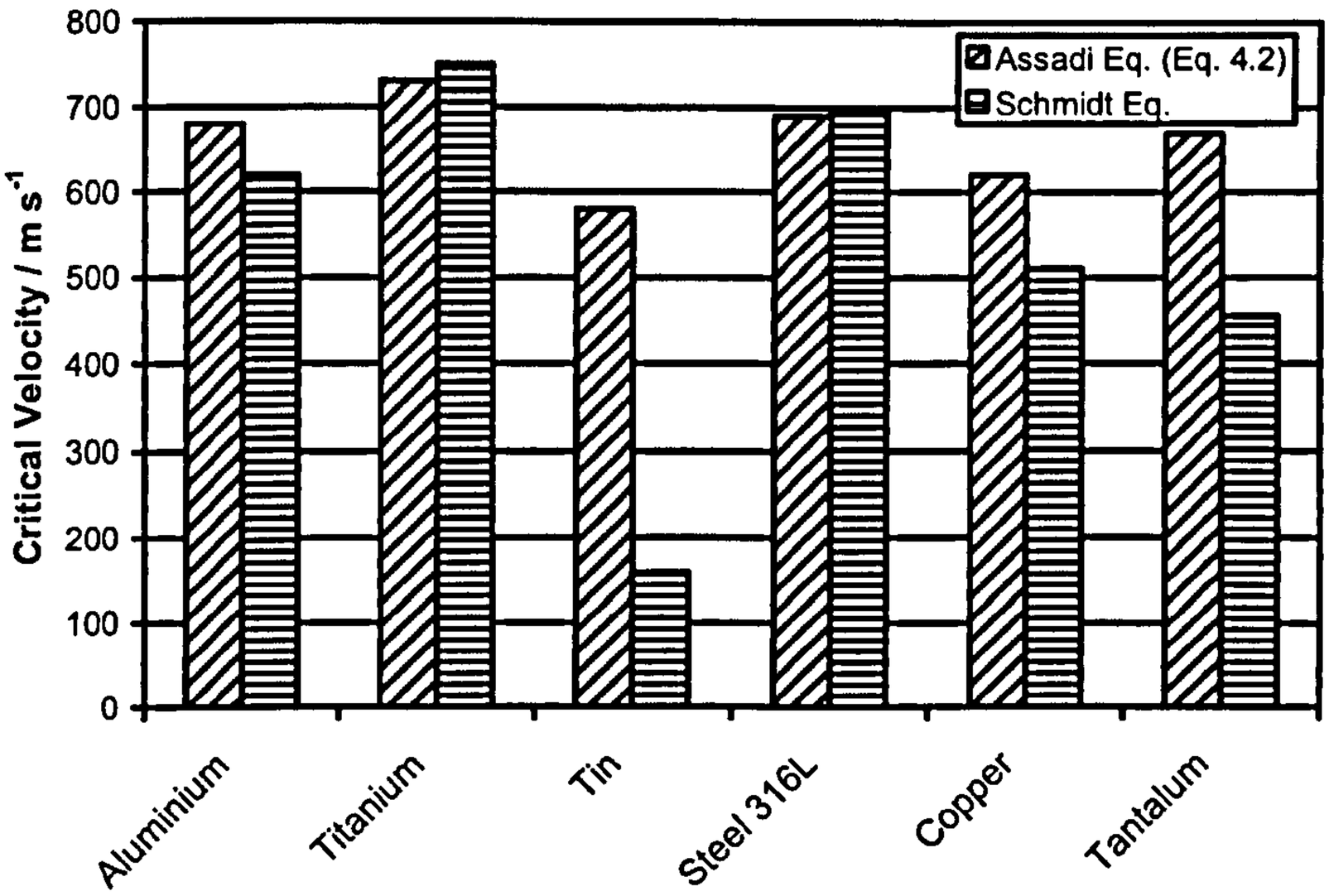

Figure 4.10 – Comparison of calculated critical velocities for 25 µm particles at room temperature by Assadi's equation (Eq. 4.2) and Schmidt's equation [47].

Figure 4.10 also only shows the respective critical velocities required for material deposition and not whether these velocities can be achieved by the powder and the cold spray process. For example tantalum is estimated to require a relatively low

critical velocity of less than 500 m s^{-1}. However, in practice due to the high particle density, it is often difficult to transfer the kinetic energy from the gas flow to the tantalum particle and accelerate it to a velocity greater than its critical velocity. Critical particle velocities of Cu, Fe, Ni, Al and Ti has been experimentally measured to be approximately 540-580, 620-640, 630-690, 660-700 and 680-750 m s^{-1} respectively [44-48]. Generally, the lower the materials particle critical velocity the more suitable the material is for deposition.

Both Assadi's and Schmidt's work does not take into consideration the particle diameter and it has been suggested that this may influence the critical and impact velocities [47, 55, 68, 87]. Schmidt et al. [47] developed new equations and these were analysed numerically; they allowed the effect of particle size on the critical and impact velocity of a copper particle to be shown schematically, shown by Figure 3.6. Figure 3.6 shows that the critical velocity increases as the particle diameter decreases. This is primarily due to greater levels of particle deformation and greater likelihood of oxide layers fracturing on impact occurring for larger sized particles and therefore less kinetic energy, and therefore a lower critical velocity, is required for a metallurgical bond to form between the deposit and impinging particles as described in the previous section [47, 55].

For deposition to occur, the impact velocity must be higher than the critical velocity. As shown by Figure 3.6 there is an optimum particle size range where the impact velocity is greater than the critical velocity and here particle deposition can be expected. A larger difference between the impact and critical velocity increases the likelihood of bond formation between particles. As the particle size increases the critical velocity approaches the impact velocity due to slower acceleration of the particle as its mass increases [68]. As the average impact velocity approaches the critical velocity, there is a greater likelihood of particles not bonding to form a coating and therefore coatings of increasing porosity and weaker bonding interfaces are expected to form.

4.6. Mechanical Properties

This section summarises the mechanical properties of cold spray coatings measured by previous workers. The section concentrates on mechanical properties that will also be measured during this study. To allow comparison between materials routinely deposited by cold spraying and corresponding bulk materials, Table 4.2 shows the mechanical properties of the bulk materials and the data for this is taken from the Metals Handbook [13]. Examples of typical physical and mechanical properties observed in cold spray deposits are given in Table 4.3. Available spray parameters have also been added so their influence on the deposits' mechanical properties may be observed. It must be noted that it is difficult to compare absolute values of mechanical properties between workers due to the variation in spray parameters, powder types, and nozzle designs. However it is anticipated that similar trends should be found by different workers and these will be identified.

Material	Modulus / GPa	Hardness / kgf mm^{-2}
Al	67	20 – 23
Cu	128	60
Fe	211	61
Ti	120	200 – 265

Table 4.2 – Mechanical properties of bulk materials typically cold sprayed supplied by the Metals Handbook [13]. Hardness values are given for the annealed state.

Powder			Cold Spray Conditions				Mechanical Properties					Ref.
Material	**Size / µm**	**Morphology**	**A_e/A^***	**Gas Type**	**Gas Temp / °C**	**Gas Pressure / MPa**	**Adhesive Strength / MPa**	**Coating Modulus / GPa**	**Residual Stress / MPa**	**Porosity / %**	**Hardness / kgf mm^{-2}**	
Al	< 45	Spherical	3.3	Air[a] He[b]	527	2.0	> 70 (Al, brass, Cu, steel)	-	-	0.5 – 12	48[a] 45[b]	[54]
Al	+63 - 106	Spherical	2.8	Air	288	2.4	49 (brass)	30.8	-	1.75	51	[55]
Al	+1-30	Spherical	-	He[a] He-20vol %N_2[b]	227 to 527	2.1	-	-	-	-	115-257[a] 84-128[b]	[97]
Cu	+9 -25	Spherical	-	Air	315	2.0 – 2.4	-	108 ± 9	-120	-	160 ± 8	[53]
Cu	+5 -25	Spherical	5.6[a] 2.3[b]	N_2[a] He[b]	305	3.0[a] 2.5[b]	10[a] (st. steel) 57[b] (st. steel) 44[a] (Al) 39[a] (Cu)	-	-	-	150	[88]
Cu	< 45	Angular	3.3	Air	527	2.0	~ 70 (Al, brass, Cu)	-	-	0 – 0.1	102	[54]
Cu	< 48	Spherical	9	N_2	150	2.0	-	-	-	-	135	[98]
Cu	+5 -22	Spherical	8.6	He	250	2.9	-	-	-	-	180	[99]
Fe	< 45	Angular	3.3	Air	430[a] 650[b]	2.0	~ 70 (Al, brass, Cu, steel)	-	-	0.1 – 1	122[a] 147[b]	[54]
Ta	+65 - 200	Sponge	3.3[a] 10.1[b]	He	204 to 427	1.4	51-62[a] (brass) 74-79[b] (brass)	-	-	8.8-9.6[a] 3.2-4.1[b]	155-167[a] 172-185[b]	[100]

Powder			Cold Spray Conditions				Mechanical Properties					Ref.
Material	Size / μm	Morphology	A_e/A^*	Gas Type	Gas Temp / °C	Gas Pressure / MPa	Adhesive Strength / MPa	Coating Modulus / GPa	Residual Stress / MPa	Porosity / %	Hardness / kgf mm^{-2}	
Ti	+5 -45[a] +5 -25[b]	Angular	7.6	He	RT	2.9	23[a] 24[b] (Ti6Al4V)	-	-	-	88 to 177	[65]
Ti	-	-	-	N_2	370	2.1	-	23	-	-	115	[82]
Ti	< 37	Angular	-	N_2	370[a] 480[b]	Up to 3.0 MPa	-	21[a] 26[b]	-	-	120[a] 130[b]	[78]
Ti6Al4V	< 45	-	-	He	500	2.4[a] 3.1[b]	-	-	-	4.6-7.8[a] 1.5-8.8[b]	-	[101]
Ni-5wt%Al	-	-	6.4	-	-	-	-	58 ± 7	- 40	-	27	[73]
Al-Si	+5 -30	Spherical	- (CGT)	0.3 to 3.0	400	-	20 to 70 (mild steel)	-	-	-	-	[102]
50Al -50Ti at%	+10-45^{Al} <45^{Ti}	Spherical ^{Al} Sponge ^{Ti}	-	He	200	1.6	-	-	-	14	24^{Al} 50^{Ti}	[83]
WC-Co	+10 -43	Spherical	-	N_2	540	2.1	-	-	-	-	1225 ± 282	[103]

Table 4.3 – Mechanical properties of various cold spray coatings available within the literature.

4.6.1. Coating Hardness

For aluminium [97], iron [54], copper [99] and titanium [78] coatings, an increase in coating hardness has been found with increasing particle impact velocity. This is expected as the higher impact velocity will lead to a greater amount of bonding between splats, compaction within the deposit and higher dislocation density throughout the microstructure [97, 99]. By comparing hardness values of cold spray deposits in Table 4.3 with hardness values of corresponding annealed bulk materials in Table 4.2, it can be seen that the hardness values of cold spray deposits are higher than those of the bulk material for aluminium, copper and iron. This is generally attributed to the fine grain size or high levels of dislocation density occurring on particle impact. For titanium, the hardness of the cold sprayed deposits is less than the bulk material and in this case is due to a greater level of porosity and defects within the coating. The significant cold working that occurs during cold spray coating deposition is expected to contribute greatly to the high hardness values routinely found within cold spray deposits.

4.6.2. Coating Porosity

Table 4.3 shows that cold spray deposits generally exhibit relatively low coating porosities, typically less than 10%. Low porosity values are found due to the high levels of particle deformation on impact. This allows the majority of voids and pores within the deposit to be filled or reduced. Particles of higher impact velocity will deform to a greater extent and therefore help to create a denser deposit with less voids and defects. This was shown by Van Steenkiste et al. [100] when measuring the porosity of tantalum coatings produced by two nozzle designs with different expansion ratios. The nozzle that was predicted to have the higher particle impact velocity, due to the higher expansion ratio (as shown in Table 4.3), had the lowest porosity volume fraction. The authors argue that a lower particle impact velocity translates into a reduction of the particle's kinetic energy with subsequently reduced deformation and void reduction, resulting in increased porosity. By heating the helium gas flow from 204 °C to 427 °C, further increases in the particle impact velocity were predicted, but only minimal variations in the coating porosity were measured that may be within the error of the measuring technique. This suggests that

either i) once the particle velocity is sufficiently high and greater than the critical velocity for bonding and void reduction to occur, further reduction in porosity by increasing the particle impact velocity does not occur, or ii), that the increase in gas temperature from 204 °C to 427 °C did not provide sufficient increase in particle impact velocity for void reduction to be observed.

Table 4.3 shows that coatings produced from a high density powder, for example copper or iron, generally exhibit lower porosities than those produced from a low density powder such as aluminium or titanium. Van Steenkiste et al. [54] found that the porosity levels of an aluminium deposit varied, depending on the position within the plume that the coating was created from. Porosity levels were found to be at their lowest at points where the deposit was created from the central part of the plume and increased when created from the extremities of the gas plume. Van Steenkiste et al. [54] suggest that this is due to the smaller and lighter aluminium particles being swept to the edges of the plume and where the particle impacts are smaller. Lower particle impact velocities are found at the plume extremities because of frictional effects from the nozzle walls and a greater amount of deceleration of the gas velocity due to its interaction with the surrounding atmosphere on leaving the nozzle. Particles of higher density, expected to be found in the centre of the plume, have greater momentum on impact and therefore consolidation of defects within the coating may occur leading to a reduction in coating porosity.

4.6.3. Coating Stiffness

It has been recognised that one of the important mechanical properties of deposits is the Young's modulus and a number of techniques have been employed previously to measure it. Table 4.4 summarises data available from the literature for cold sprayed and thermally sprayed coatings (along with the test method employed to measure the coating modulus) [53, 55, 73, 82, 104-108]. Alongside the actual measured coating modulus, E_c, the ratio of the coating modulus to a typically quoted Young's modulus of the equivalent bulk material, E_b, is also shown (termed the *modulus ratio*). If measured Young's modulus values for the bulk material are unavailable from the literature, then values obtained from the Metals Handbook have been used [13]. One

of the striking features is that the modulus ratio of cold spray deposits is usually much less than unity. This is found to be the case irrespective of whether measurements were made by a bulk measurement technique (e.g. beam bending) or a localised indentation method. In the work by Sampath et al. [73], in which the modulus of a single material was measured following deposition by different spray processes, cold spraying was found, surprisingly, to give the lowest modulus ratio despite the apparently low porosity and low oxide content of the deposit.

This difference between the modulus of a bulk material and that of a sprayed coating of the same material has generally been attributed, in qualitative terms, to defects within the coating [105, 106, 108]. These defects include pores, poorly bonded splats and a poorly bonded interface between the coating and the substrate (for measurements of the modulus which involve deformation of a coating-substrate system where interfacial shear is present). On application of a load, these pores have zero stiffness and will therefore lead to a reduction in the overall stiffness of the coating. Poor bonding between splats and between the coating and substrate will also allow easier deformation of the system under a given stress (either in shear or tension), resulting in a lower recorded value of Young's modulus.

Qualitatively the effect of inclusions or pores within composites, coatings and foamed metals has previously been modelled by Eshelby or modified-Eshelby model analysis [104, 109-115]. The Eshelby model was originally derived in the 1950's and allowed the elastic strain field of an ellipsoidal inclusion to be determined [114, 115]. The model is based upon the fact that an ellipsoid of any aspect ratio has a uniform stress at all points within it, and thus the variation of a uniform stress field in a material can be determined when it is disturbed by an ellipsoidal inclusion. This allows the stress due to the inclusion to be calculated without analysing the complicated form of the stress field matrix. To ease the calculation, the technique replaces the actual inclusion by one of the matrix material, which has an appropriate misfit strain such that the stress field is the same as that observed in the actual inclusion [116].

Coating Material	Spray Method	Test Method	Young's Modulus of Coating (E_c) / GPa	Young's Modulus of Bulk Material (E_b) / GPa	Modulus Ratio (E_c / E_b)	Ref.
Ti	CGDS	Indentation	~23	120 *	0.19	[82]
Ti	CGDS	4PB	20	107	0.19	[107]
Cu	CGDS	Composite Cantiliever	108 ± 9	126	0.84	[53]
Al	CGDS	Tensile	31	69 – 72	0.43 – 0.45	[55]
Al	APS	3PB	30	71	0.42	[104]
Al	WA	Indentation	24 ± 10	67 *	0.36	[105]
Ni	APS / VPS	3PB	55 – 80	200	0.28 – 0.40	[104]
IN625	APS	4PB	40 – 150	214	0.19 – 0.70	[108]
Ni-5 wt.% Al	APS	Indentation	83 ± 5	207 *	0.40	[73]
Ni-5 wt.% Al	TWA	Indentation	110 ± 23	207 *	0.53	[73]
Ni-5 wt.% Al	HVOF	Indentation	178 ± 10	207 *	0.86	[73]
Ni-5 wt.% Al	CGDS	Indentation	58 ± 7	207 *	0.28	[73]
Mo	APS / VPS	3PB	80 – 130	325	0.25 – 0.40	[104]
ZrO_2	APS	Indentation	35	190	0.18	[106]

Table 4.4 – Young's modulus values reported in the literature for cold and thermally sprayed coatings. Values for the Young's modulus of bulk materials used in the literature are shown (if not cited, values are taken from the Metals Handbook [13] and indicated by an asterisk). For Ni-5 wt.% Al, the Young's modulus of bulk nickel is used. (CGDS – cold gas dynamic spray; APS – atmospheric plasma spray; WA – Wire Arc; VPS – vacuum plasma spray; TWA – transferred wire arc; 4PB – four point bend technique; 3PB – three point bend technique).

The Eshelby equivalent homogeneous inclusion model has been used for thermally sprayed coatings to assess the effect of porosity content and aspect ratio on the coating stiffness [104]. The aspect ratio of a pore is defined as the width (x) divided by the length (y) as shown in Figure 4.11 where x is taken parallel to the coating-substrate interface and y is perpendicular to it. It was found that with an increasing content of spherical pores (an ellipse with an aspect ratio of 1), only a relatively small reduction in the coating modulus was observed. However, with a pore aspect ratio of approximately 0.01, a greater and more significant reduction of the coating modulus is predicted. This approach to modelling the elastic behaviour of a coating

was justified on the basis that through thickness cracks and weak intersplat bonds could be modelled as ellipses with low aspect ratio. Although the modulus ratios of several cold sprayed coatings have been determined (Table 4.4) the reasons for the low modulus values in these types of deposits have not yet been explored.

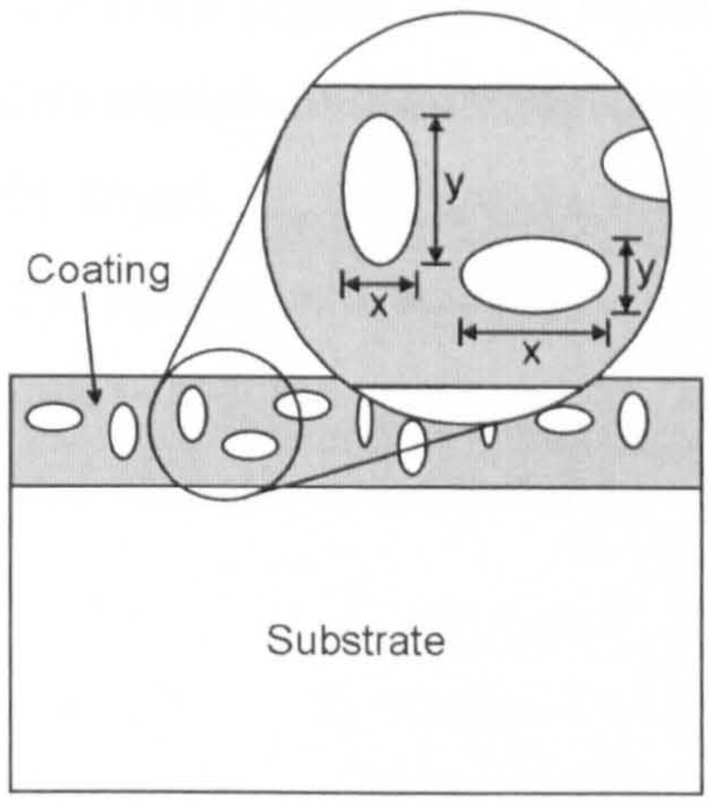

Figure 4.11 – The aspect ratio of a given pore is defined as the width (x) divided by the height (y) relative to the coating and substrate.

4.6.4. Coating Bond Strength

Typical cold spray coating bond strengths vary from between 5 MPa and 70 MPa and are heavily dependent on the spray parameters, powder material, substrate material and substrate surface finish as shown in Table 4.3. Bond strength is normally tested by using resin to attach a stud to the top surface of the coating and pulling the stud away from the coating-substrate interface as explained in Section 4.8.7.1. For some cold spray coatings there is some degree of uncertainty of bond strength because the coating bond strength is sometimes found to be in excess of that of the resin. For example Van Steenkiste et al. [54] tested the bond strength of aluminium, copper and iron deposits on a range of substrates including aluminium, brass, copper and steel. In the vast majority of cases the bond between coating and substrate remained and resin failure occurred at between 68 MPa and 82 MPa.

Spray parameters such as gas type and gas pressure are expected to influence the coating bond strength indirectly due to their influence on particle velocity. Stoltenhoff et al. [88] produced copper deposits using helium and nitrogen as the main gas type. When using steel as the substrate material, the bond strength

increased substantially from 10 MPa when using nitrogen to 57 MPa when using helium as the main gas type. Marrocco et al. [65] found an increase in bond strength from 20 MPa to 24 MPa for titanium deposits when increasing the gas stagnation pressure from 15 bar to 29 bar. Increase in bond strength due to variation in gas type and pressure can be attributed to the higher impact velocities expected and therefore greater levels of particle deformation and bonding on impact when using helium. Van Steenkiste et al. [100] found an increase in the bond strength of tantalum coatings on to brass when the particle exit velocity was increased by using a nozzle of higher area expansion ratio. In some cases epoxy failure at 79 MPa occurred, indicating that the actual bond strength of the tantalum coatings was higher than this measured value.

The effect of substrate surface finish on bond strength has been determined for titanium coatings deposited onto a Ti6Al4V substrate [65]. A significant reduction in bond strength from 22 MPa to 8 MPa was found for a grit blasted surface finish compared to a polished or ground surface finish. Similar results were found by Wu et al. [102] when depositing an Al-Si powder onto mild steel. The lower bond strength values observed for a grit blasted substrate surface finish were attributed to work hardening of the substrate during grit blasting, which decreases the level of deformation of the substrate on initial particle impact. Such a reduction in substrate deformation makes it harder for particles to adhere to the substrate.

In the case of titanium deposits, minimal variation in the bond strength was found when using two powders of different size distribution (+5 -25 μm and +5 -45 μm) and the same spray parameters [65].

4.6.5. Fatigue

High cycle fatigue can be tested in laboratory conditions using a rotating-beam fatigue machine. This method applies a cyclic load to the sample at a frequency of approximately 50 Hz as recommended by the relevant British Standard [117]. An idealised situation is created and a completely reversed cycle of stress of sinusoidal

form is created (ie. compressive and tensile forces exerted on the sample are equal and therefore the stress ratio, R, equals -1). Tensile stresses are considered positive, and compressive stresses are negative. Samples are tested until failure and the stress required for the sample to fail for a known number of cycles is recorded.

Ti6Al4V has been subjected to previous fatigue testing by many workers [14, 118-120]. Figure 4.12 shows the influence of the α grain size on fatigue endurance limit for a Ti6Al4V microstructure. It is found that with increasing grain size the fatigue endurance limit reduces. For equiaxed microstructures, fatigue cracks nucleate along slip bands within α grains and therefore the greater number of grain boundaries found when there is a small α grain size prevents crack initiation from occurring [12, 120]. Another important parameter is the surface finish and residual stress of the Ti6Al4V fatigue sample. Modifications of the surface finish will often modify the surface roughness, degree of cold work or dislocation density at the sample surface and the residual stresses of the sample. Compressive residual stresses at the sample surface are very favourable as they prevent fatigue microcrack propagation.

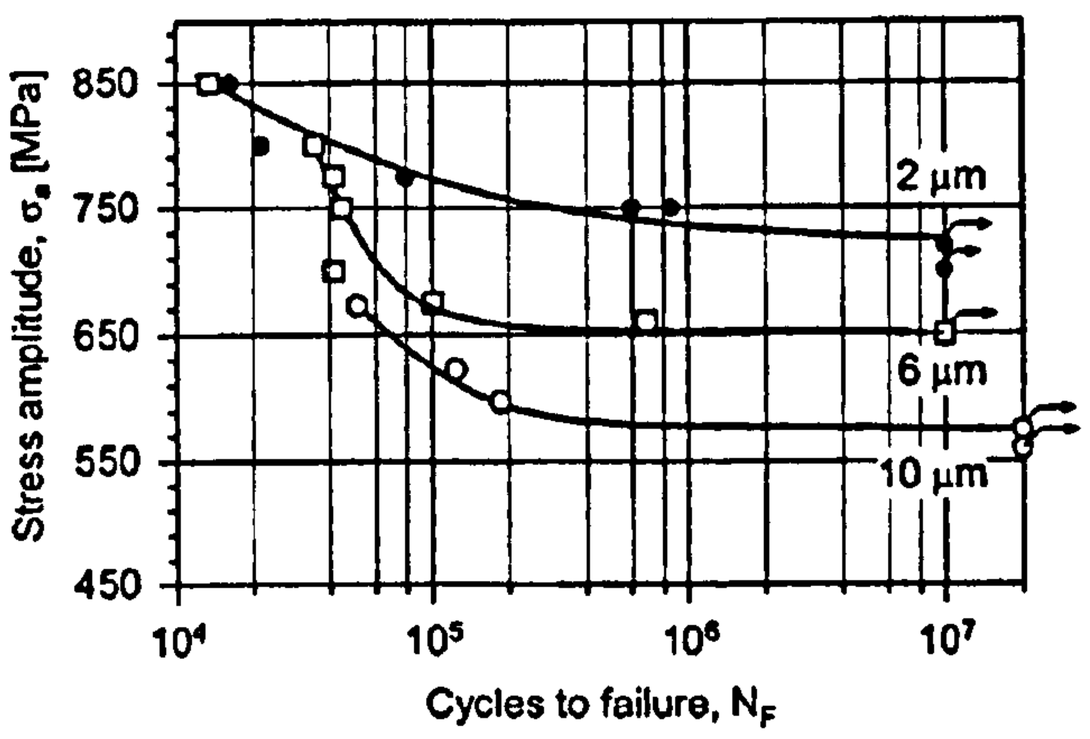

Figure 4.12 – Influence of α grain size (equiaxed microstructure) on the high cycle fatigue behaviour (R=-1) of Ti6Al4V [120].

Surface finish can also change the nature of surface stress raisers which could act as sites for fatigue cracks to initiate as shown in Figure 4.13. The shot peening (SP) process is shown to increase the fatigue endurance limit from that observed for an electro-polished (EP) surface finish. This is due to compressive residual stresses formed at the sample surface from the shot peening process. Shot peening and stress

relieving (SP + SR) at 600 °C for one hour causes further reductions in the fatigue endurance limit due to the removal of the compressive residual stresses and also the increased surface roughness increases the number of nucleation sites for fatigue cracks to develop.

Vacuum plasma sprayed titanium coatings have been shown to reduce the fatigue endurance limit of a Ti6Al4V substrate as shown in Figure 4.14. Depending on the spray parameters chosen, between a 20 % and 60 % reduction in the fatigue endurance limit was found compared to the uncoated samples [14].

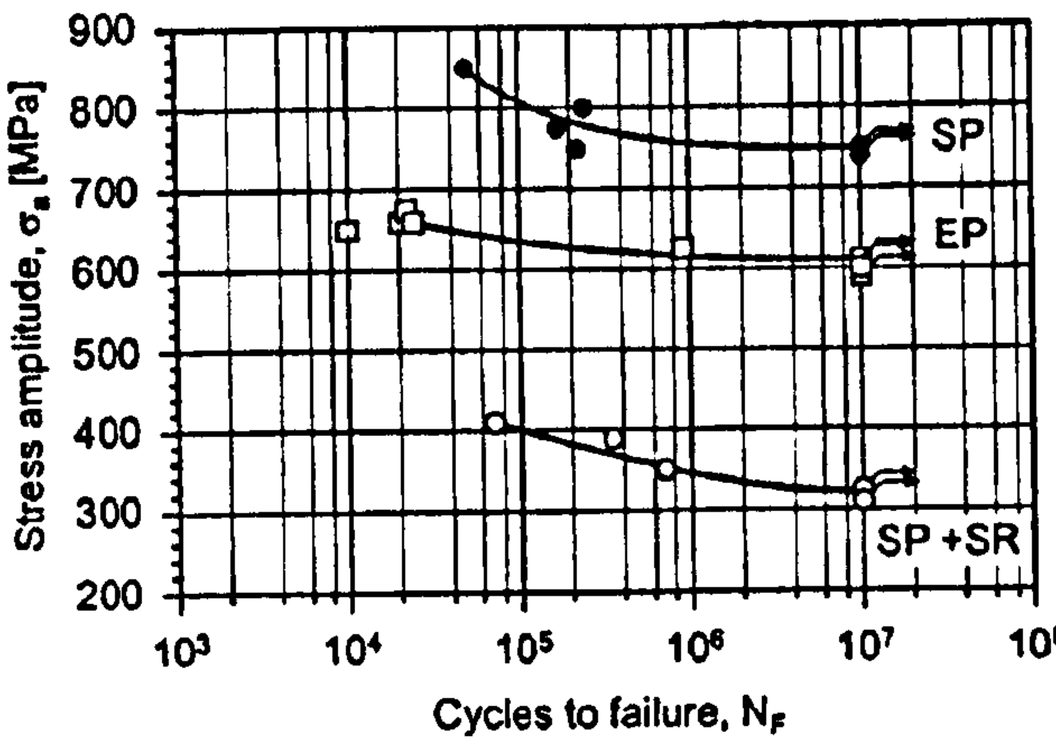

Figure 4.13 – Influence of Ti6Al4V surface finish on high cycle fatigue behaviour (R=–1) (SP = shot peening, EP = electro polishing, SR = stress relieving by heat treating at 600 °C for one hour) [120].

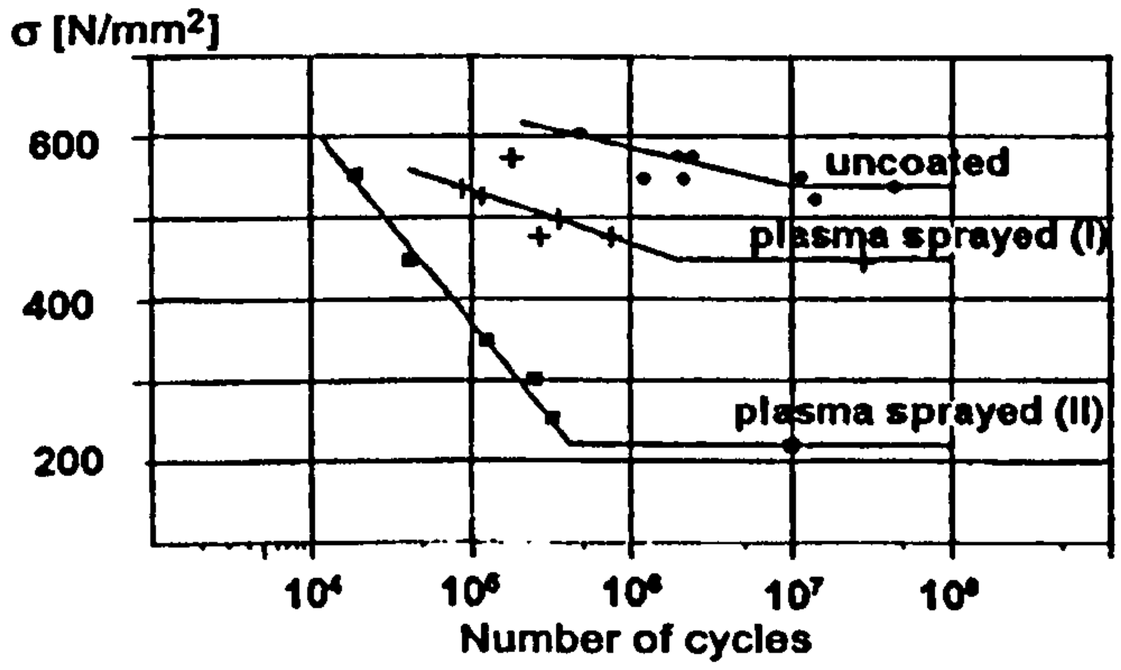

Figure 4.14 – Fatigue endurance limits of a forged TiAlV samples without and with vacuum sprayed titanium coatings, measured by rotating bending test. Two types of plasma spray parameters were tested [14].

4.6.6. Residual Stresses within Deposits

The residual stresses in CGDS coatings are generally found to be compressive and smaller in magnitude than those developed in thermally sprayed coatings, the latter which are predominantly formed as a result of the different cooling coefficients of the substrate and coating [53, 73, 121]. Work by Sampath et al. [73] compared the residual stresses in Ni-5wt%Al coatings deposited by thermal and cold spraying; results are shown in Figure 4.15. Figure 4.15 shows that for both plasma sprayed and wire arc sprayed deposits, a tensile residual stress is found at the coating top surface. This is a result of tensile quenching stresses due to rapid cooling and solidification of particles on impact. Additionally, stresses arise due to differences in the coefficients of thermal expansion between the coating and substrate on cooling after deposition and also due to the difference in operating temperature of the deposition methods. In the case of the plasma sprayed deposit, Sampath et al. [73] expected the thermal mismatch to be relatively small and therefore argued that the residual stress profile is dominated by quenching stresses. The stress gradient of the wire arc sprayed deposit is higher than the plasma sprayed deposit while in the substrate it is negligible. Sampath et al. [73] expected this to be due to higher quenching stresses that varied during deposit build-up, thus creating a larger and non-uniform stress deposit.

Whilst HVOF coatings will suffer from quenching and thermal mismatch stresses as described previously, the higher particle velocity impact also means that peening (compressive stresses) are also created. Compressive peening stresses are also expected within cold spray coatings and occur due to the plastic deformation of the surface layer of the coating by impact of impinging particles. Plastic deformation to under-lying layers of the coating causes compressive residual stresses to be generated. In the case of HVOF coatings, compressive residual stresses reduce as the top layer of the coating is approached as shown by Figure 4.15. This is due to a reduction in impacting particles that will induce peening stresses. Therefore as the top surface layer of the coating is approached, quenching stresses will have a greater overall impact on the residual stress levels, creating a trend towards tensile residual stress levels. In the case of a cold sprayed coating the compressive residual stress remains fairly constant throughout the thickness of the coating because quenching and thermal mismatch stresses are relatively minimal. Overall it was found that

compressive stresses are smaller in magnitude for cold spray than thermal spray coatings.

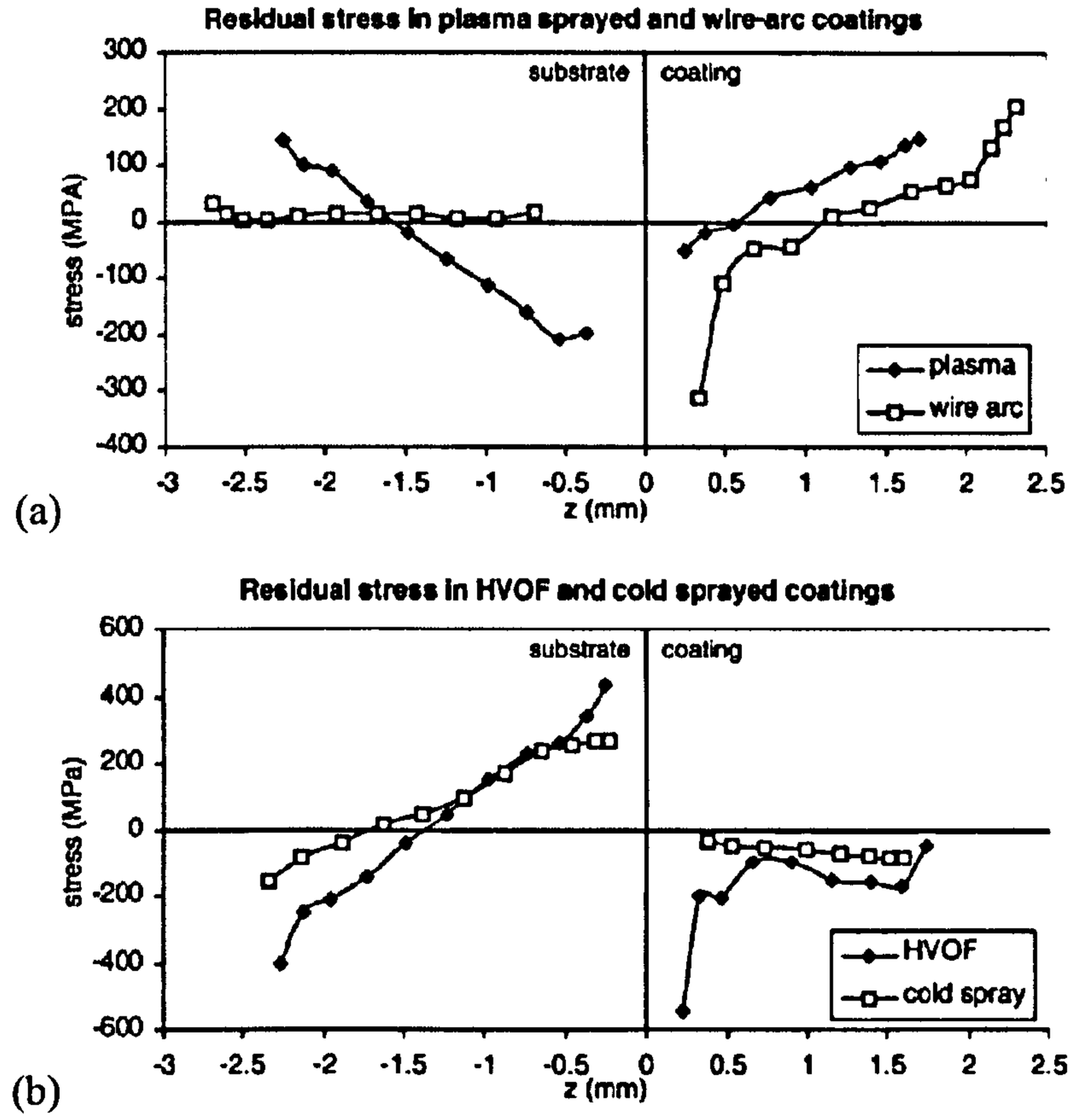

Figure 4.15 – Through thickness profiles of the residual stresses in (a) plasma sprayed and wire-arc sprayed and (b) HVOF sprayed and cold sprayed Ni-5%Al deposit and steel substrate [73].

4.6.7. Heat Treatments

Workers who investigate the influence the effect of heat treatments on the properties of cold sprayed coatings have predominantly focussed on the variation of coating hardness before and after heat treating [83, 88, 98, 99, 101]. Calla et al. [99], Stoltenhoff et al. [88] and Li et al. [98] investigated the effect of heat treating copper cold spray deposits. The as-sprayed coating hardness varied from 135-180 kgf mm^{-2} and was reduced to 50-80 kgf mm^{-2} depending on the heat treatment temperature and dwell time [88, 98, 99]. The high hardness values found in the as-sprayed copper cold spray coatings are commonly associated with either very fine grain size or high levels of dislocation density [99]. The authors suggested that a reduction in hardness due to heat treatment occurs because the number of dislocations within the deposit are reduced by recovery and recrystallisation [88, 99]. Recrystallisation was found to

occur predominantly at splat interfaces where the highest amount of particle deformation from deposition has previously occurred [98]. A further microstructural change was found due to heat treating; 'sphericization' of voids and pores within the cold spray deposits was observed. This occurs as new grains within the deposit grow and is also evident during diffusion bonding processes [98]. The lowest hardness values were observed for those deposits exposed to the highest temperatures and longest dwell times, and typical values found are shown in Figure 4.16.

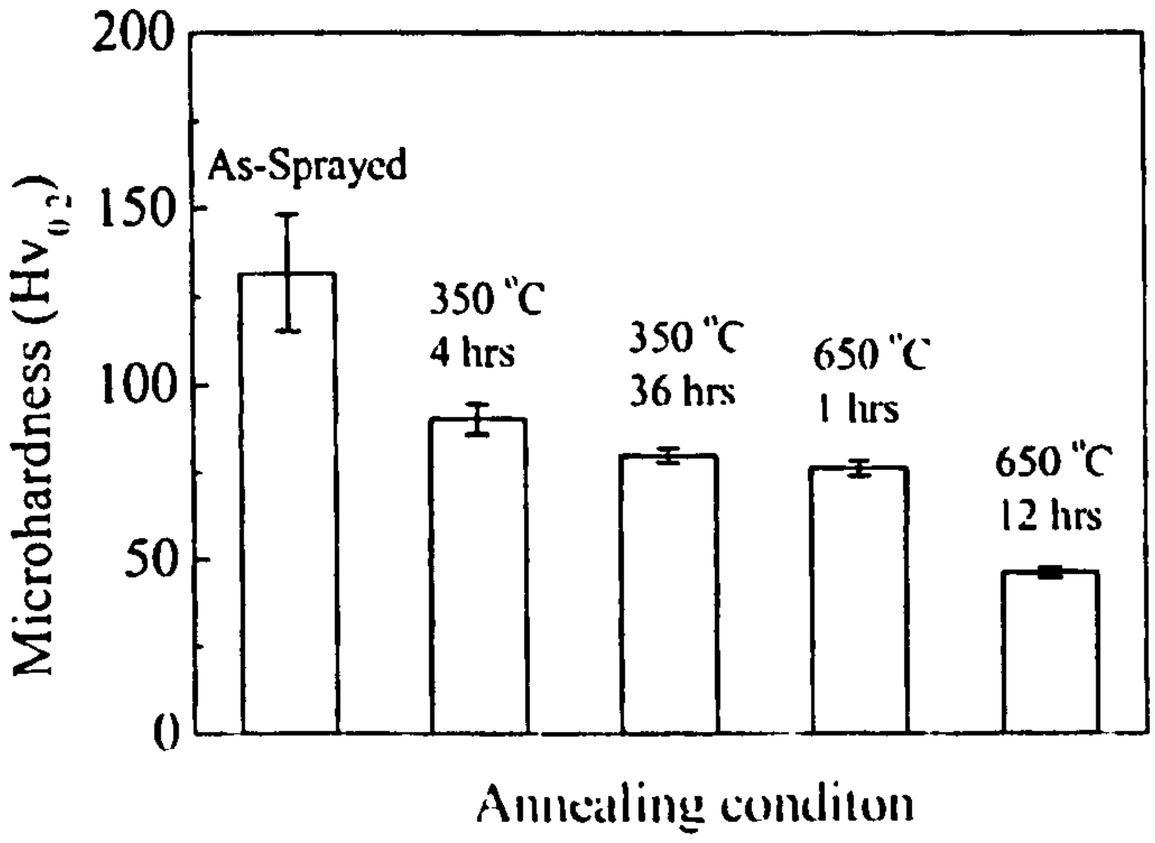

Figure 4.16 – Effect of annealing condition on the microhardnes of cold sprayed copper coating [98].

Whilst there is a large variation in hardness between heat treated and non-heat treated deposits, there is little variation in the hardness of deposits when heat treated at 350 °C for 4 hours or 36 hours. This is due to the majority of any recrystallisation effects occurring during the early stages of the heat treatment. Deposits showing the lowest hardness values, and therefore heat treated at the highest temperature and longest dwell time, were found to be similar to that of annealed bulk copper. The effect of recrystalisation meant that it was also found that deposits after heat treatment showed evidence of 'healing' occurring between splats at interfaces [98]. Due to this, experimentally, an increase in bond strength between splats may have been expected but was not shown. Stoltenhoff et al. [88] however did show an increase in bond strength between copper and aluminium substrates and copper coatings with increasing heat treatment temperature as shown by Figure 4.17. This is

predominantly expected to be due to diffusion bonding process and recrystallisation occurring at the coating-substrate interface.

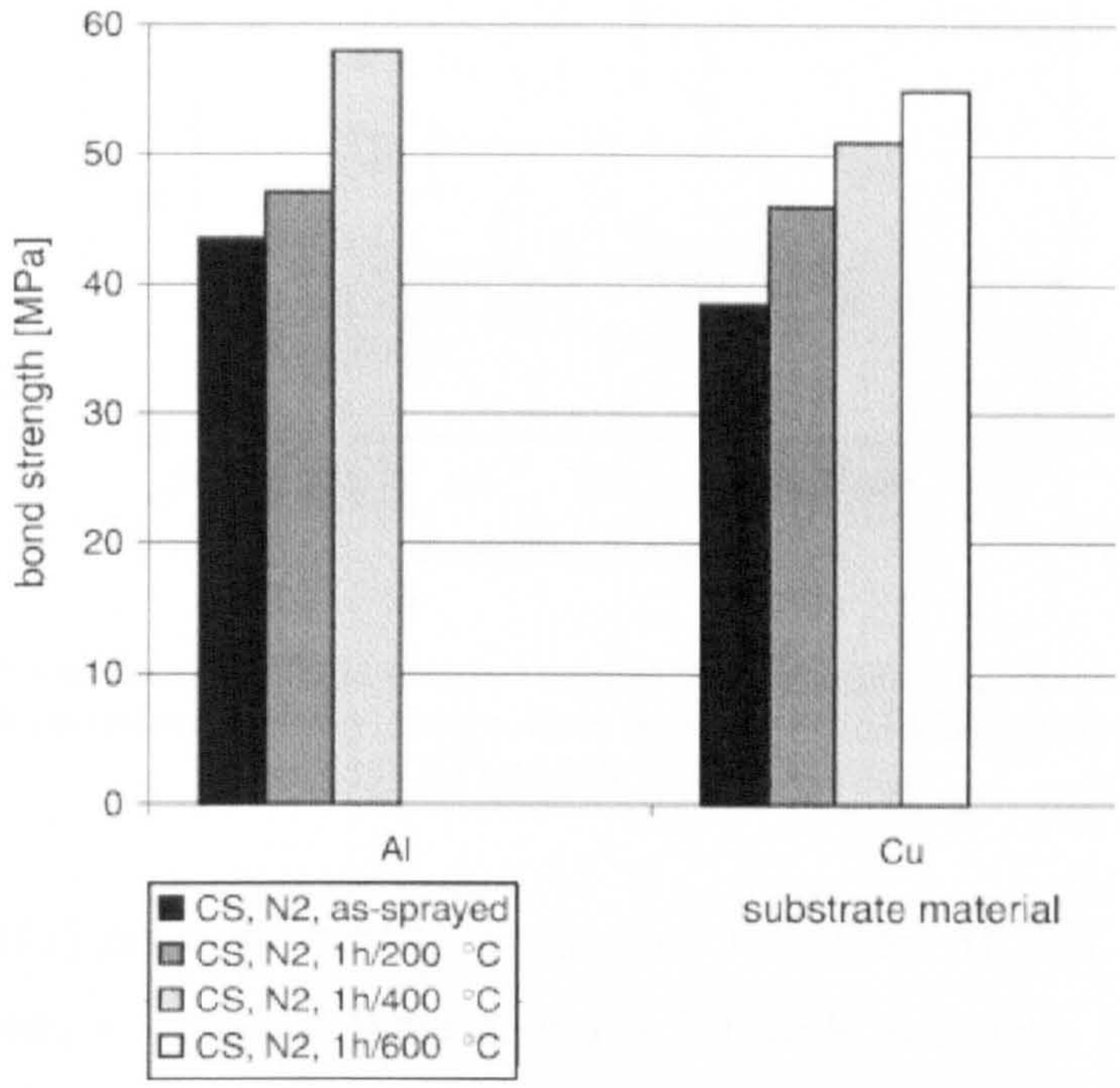

Figure 4.17 – Bond strength of cold sprayed copper coatings on two substrate materials (Al – aluminium, Cu – copper) as-sprayed and annealed [88].

Calla et al. [99] investigated the variation in hardness values of copper cold sprayed coatings after heat treating at temperatures ranging from 100 °C to 600 °C for 1 hour. Two copper coatings were used and were initially sprayed at different main carrier gas temperatures of 25 °C and 250 °C. Samples sprayed at the higher gas temperature have a higher hardness value due to the higher dislocation density because of the higher particle impact velocity as described in Section 4.4. It was found that a reduction in hardness values occurred at much lower heat treatment temperatures for deposits initially sprayed at the lower gas temperature of 25 °C as shown by Figure 4.18. This is due to an initial lower dislocation density compared to samples sprayed at a gas temperature of 250 °C; In this case the recrystallisation process is able to occur readily at lower heat treatment temperatures since the dislocation hindrance of recystallisation is lower.

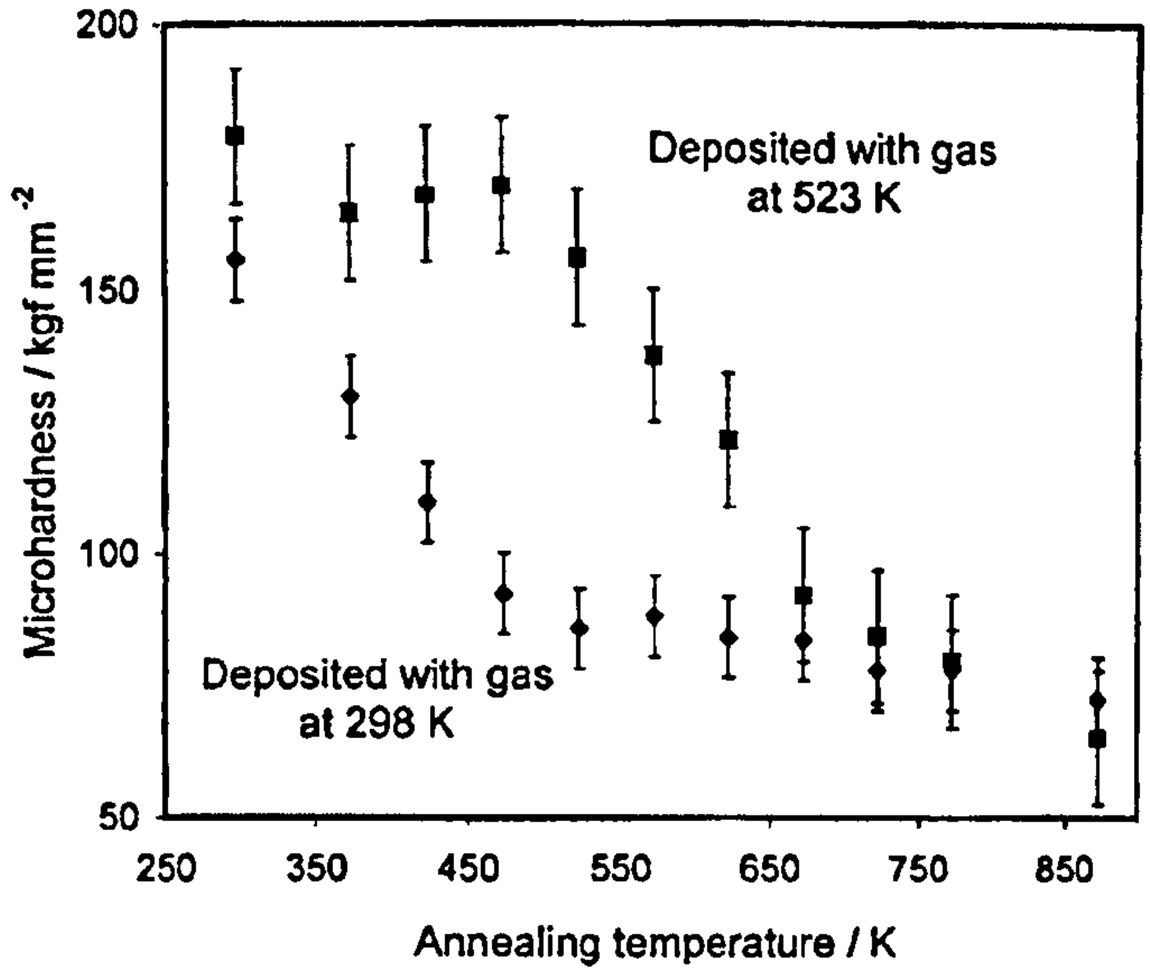

Figure 4.18 – Microhardness of cold sprayed copper deposits following heat treating at 1 hour as a function of heat treatment temperature. Data is shown for deposits sprayed with helium at 25 °C (298 K) and 250 °C (523 K) [99].

Blose et al. [101] microstructually investigated the effect of heat treating on the interface between a Ti6Al4V deposit and a Ti6Al4V substrate. Heat treatments carried out at 955 °C for 8 hours were found to show what appeared to be an improved metallurgical bond between coating and substrate compared to the non-heat treated deposit. No adhesion tests were carried out to confirm this theory.

4.6.7.1. Diffusion Bonding

Diffusion bonding is a process used within industry to form a bond between two materials. The two materials are locally heated at the point where bonding is required whilst a modest pressure is applied so that the two materials remain in contact. In the case of titanium or titanium alloys, the components are heated to temperatures in excess of 600 °C in a vacuum or inert atmosphere. At temperatures in excess of 600 °C, oxide surface layers dissolve, leaving pure titanium surfaces in contact. This results in the components bonding together by inter-diffusion, creating a bond that is imperceptible even during metallographic examination [12]. In the case of Ti6Al4V, the bond is formed due to the diffusion of interstitial and substitutional alloying elements across the interface.

Expected diffusion constants of interstitial and substitutional alloying elements within the alpha and beta phases of titanium alloys are shown in Figure 4.19 in the form of an Arrhenius plot [12]. It is shown that the diffusion of aluminium in the alpha phase is approximately five orders of magnitude lower when compared to the beta phase [12]. This is due to the densely packed atoms found in hcp α titanium preventing diffusion from occurring [89]. It is important to note the high oxygen diffusion rates within the titanium β phase shown in Figure 4.19. High levels of diffused oxygen within titanium will embrittle the metal causing a reduction in mechanical properties. Using the diffusion constant for the considered element and heat treatment temperature the diffusion distance may be estimated using the following equation:

$$w = \sqrt{D \cdot t} \qquad \text{(Eq 4.3)}$$

Where w is the diffusion distance, t is the dwell time of the heat treatment and D is the diffusion coefficient.

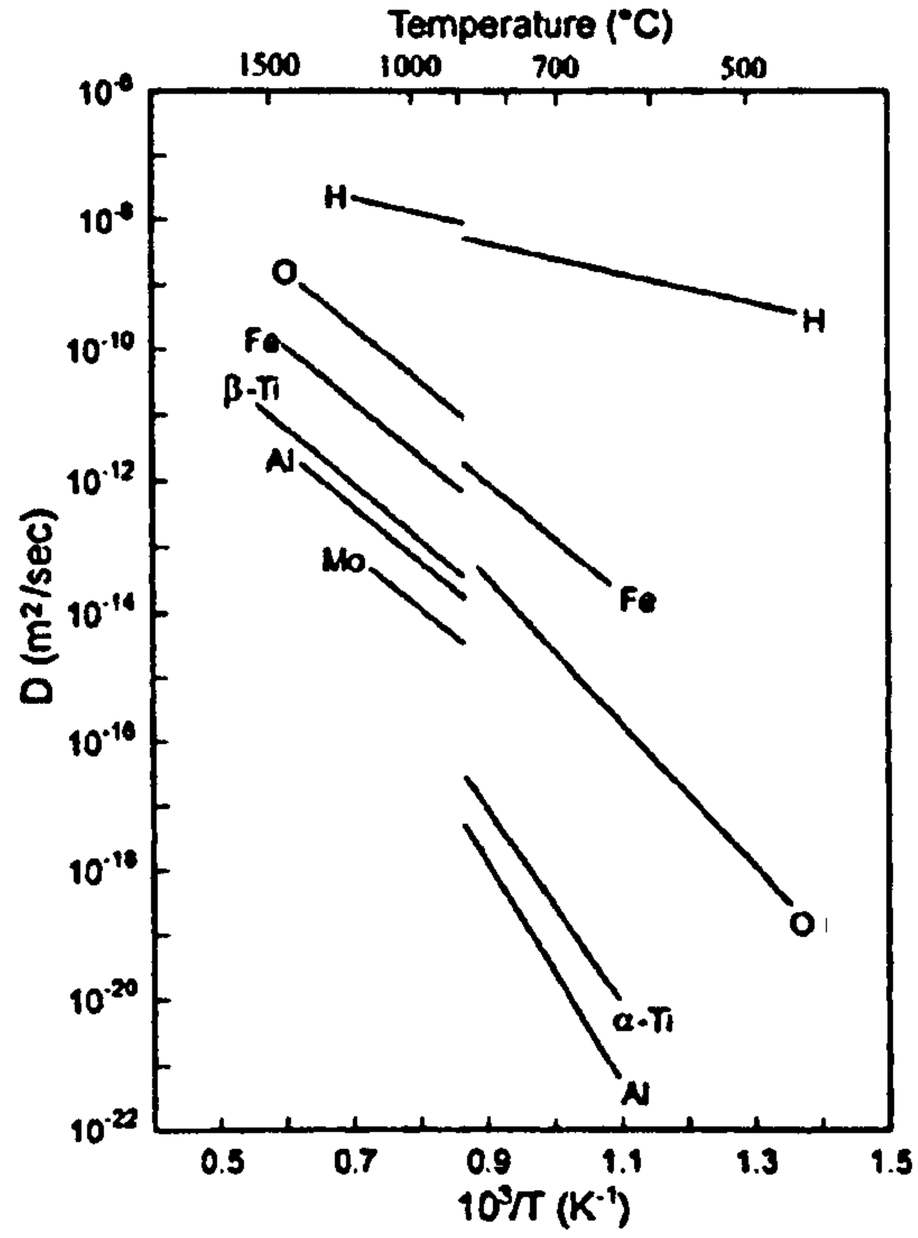

Figure 4.19 – Arrhenius plot for diffusion coefficients of interstitial and substitutional elements within titanium [12].

4.7. Conclusions of Literature Review

From the literature review carried out it may be concluded that:

i) Bonding within cold spay deposits is now widely recognised to occur due to shear instabilities occurring on particle impact and the breakdown of particle oxide layers. Modelling has identified localised temperature increases which in turn will cause the breakdown of oxide layers and allow shear instabilities to occur.

ii) SEM and TEM analysis has shown evidence of the breakdown of oxide layers occurring on particle impact but the true extent of this process remains unknown. For example, the inhomogeneous nature of inter-splat bonding has been identified but it remains unclear as to why inter-splat bonds are able to form at some particle-particle interfaces and not others.

iii) Coating bond strength, stiffness, porosity and hardness have all been characterised previously for cold spray coatings (although not necessarily for titanium deposits). Bond strengths have been previously directly attributed to the bonding mechanisms that occur between the cold spray coating and substrate.

iv) Similar to thermally sprayed coatings, low stiffness values have been typically found in cold spray coatings but reasons to explain these findings have not been fully explored.

v) Coating hardness has been used to previously quantify the effect of heat treating cold spray coatings. The effect of heat treating of titanium cold spray coatings on its mechanical properties has not been previously examined.

4.8. Experimental Methods

Within this chapter, the materials employed (Section 4.8.1.) and the coating deposition methods (Section 4.8.2.) are described. The majority of the work was carried out on cold spray deposits but some comparison work was also carried out

using titanium deposits produced by a shrouded arc process. Experimental techniques used to characterise the deposits are then explained and these include the microstructural (Section 4.8.3.) and mechanical characterisation techniques (Section 4.8.5. onwards) used. Section 4.8.4. explains the experimental methods used to visually indicate the distribution of true metal to metal bonding within cold spray coatings. Mechanical characterisation techniques were used to assess the mechanical integrity of the cold sprayed coatings. A range of techniques are employed including modulus testing, adhesion strength testing, fatigue testing and residual stress measurement. The final part of this section (Section 4.8.11.) describes the post-spray heat treatments used with the titanium cold sprayed deposits.

4.8.1. Materials Employed

Most of the work concentrated within this study utilises titanium as the feedstock. To increase general understanding of cold spray coating formation, some work was also carried out using aluminium, copper and a blended aluminium-copper powder as powders. The powder suppliers and nominal size distributions are summarised in Table 4.5. The blended aluminium-copper powder was mixed at a ratio of 1:1 by volume using a three-dimensional Turbula mixer (Glen Creston, Middlesex, UK) for 30 minutes.

Material	Nominal Size Range / µm	Supplier
Aluminium	+15 -45	The Aluminium Powder Co. Ltd. (Sutton Coldfield, UK)
Copper	+5 -25	Sandvik Osprey Ltd. (Neath, UK)
Titanium	+5 -45	Active Metals Ltd. (Sheffield, UK)

Table 4.5 – Powder materials employed in this study.

For the titanium deposits, Ti6Al4V was used as a substrate. When spraying copper, aluminium or the blended powder, copper substrates were used. Titanium coatings were deposited onto three substrate types; 1.6 mm thick sheet, 7 mm diameter rod and 5 mm thick sections from a 45 mm diameter bar. The 1.6 mm thick sheet substrate was used for modulus testing and microstructural examination of the

coatings, the 7 mm diameter rod was machined into cylindrical dog bones to be used for the fatigue testing and the 5 mm thick substrates cut from the 45 mm diameter bar were used for pull off tests.

Prior to coating deposition, the substrate surface was either left in the as-received state or prepared by grinding with P240 emery paper, or grit blasted with Al_2O_3 with an average particle diameter 250 μm. The different surface roughnesses obtained by these different preparation routes are summarised in Table 4.6. The as-received surface finish of the cylindrical dog bones is higher than that of the two other substrates due to machining marks left on the sample surface. Just prior to spraying, substrates were degreased using acetone and cleaned using a compressed air blower. The substrates used for depositing the titanium shrouded arc samples were not prepared at The University of Nottingham and therefore have a different surface roughness to the cylindrical dog bone samples prepared at The University of Nottingham for cold spray deposition.

Surface Preparation	1.6 mm thick sheet / μm	Cylindrical Dog Bones / μm	5 mm thick section
As-received	1.2	2.7	N/A
Ground	N/A	N/A	1.4
Grit Blasted (UofN)	3.5	3.5	3.5
Grit Blasted (Industrial Partner)	6.2	6.2	N/A

Table 4.6 – Surface roughness measurements (Ra) of the two substrate types employed for this study.

4.8.2. Method of Coating Deposition

Two deposition methods were used for this study. The vast majority of mechanical testing was carried out using material deposited produced by the cold spraying process. Comparisons of coating stiffness, fatigue and residual stress measurements were made between titanium coatings deposited by cold spraying and shrouded arc spraying.

4.8.2.1. Cold Gas Dynamic Spraying

Cold gas dynamic spraying (CGDS) was carried out at The University of Nottingham using an in-house designed system. A de Laval nozzle, 100 mm in length with a throat diameter of 1.35 mm and an area expansion ratio of ~8.8, was used. Table 4.7 summarises the critical nozzle dimensions.

Nozzle Dimensions	
Throat Diameter (D*) / mm	1.35
Entrance Nozzle Diameter / mm	13
Exit Nozzle Diameter (D_e) / mm	4
Nozzle exit area (A_e) / Nozzle throat area (A*)	8.79
Length of Converging Section / mm	10
Length of Diverging Section / mm	100

Table 4.7 – The nozzle dimensions.

Nitrogen was used as the carrier gas and helium for the main driving gas supply. Optimised carrier gas pressures were employed for the different powder types generally ranging from 25-30 bar and approximately 1 bar above that of the main driving gas. A constant stand-off distance of 20 mm was employed. A high pressure powder feeder (1264HP, Praxair, USA) was employed. For titanium deposits a '12-slot' feed wheel was used and for all other deposits a '120-hole' feed wheel was used. For the titanium powder a feed wheel speed of 2 rpm was used and for all other powder types was set to 4 rpm. The powder feed rate is the amount of powder fed to the nozzle and usually reported in grams per minute. For a titanium powder the powder feed rate is approximately 20 g min^{-1} and has been optimised previously to provide the greatest deposition efficiency. A schematic diagram of the cold spray system is shown in Figure 4.20.

Samples were mounted on an x-y traverse table that traverses typically at 100 mm s^{-1}. To allow deposits to be made over an area of the substrate, a number of individual tracks with a 2 mm separation between them was used. Samples used for microstructural examination and mechanical testing, except pull off and fatigue testing, were deposited onto Ti6Al4V sheet measuring 120 x 16 x 1.6 mm. The coating was approximately 700 μm thick, and was deposited centrally onto the largest face of the test strip, covering an area measuring 80 mm x 16 mm. Pull-off

test samples were deposited using a mask in order that a coating of 8.16 mm diameter and approximately 350 μm in thickness is created. For each sample, the coating thickness was measured at three locations using a vernier caliper and the average coating thickness was calculated.

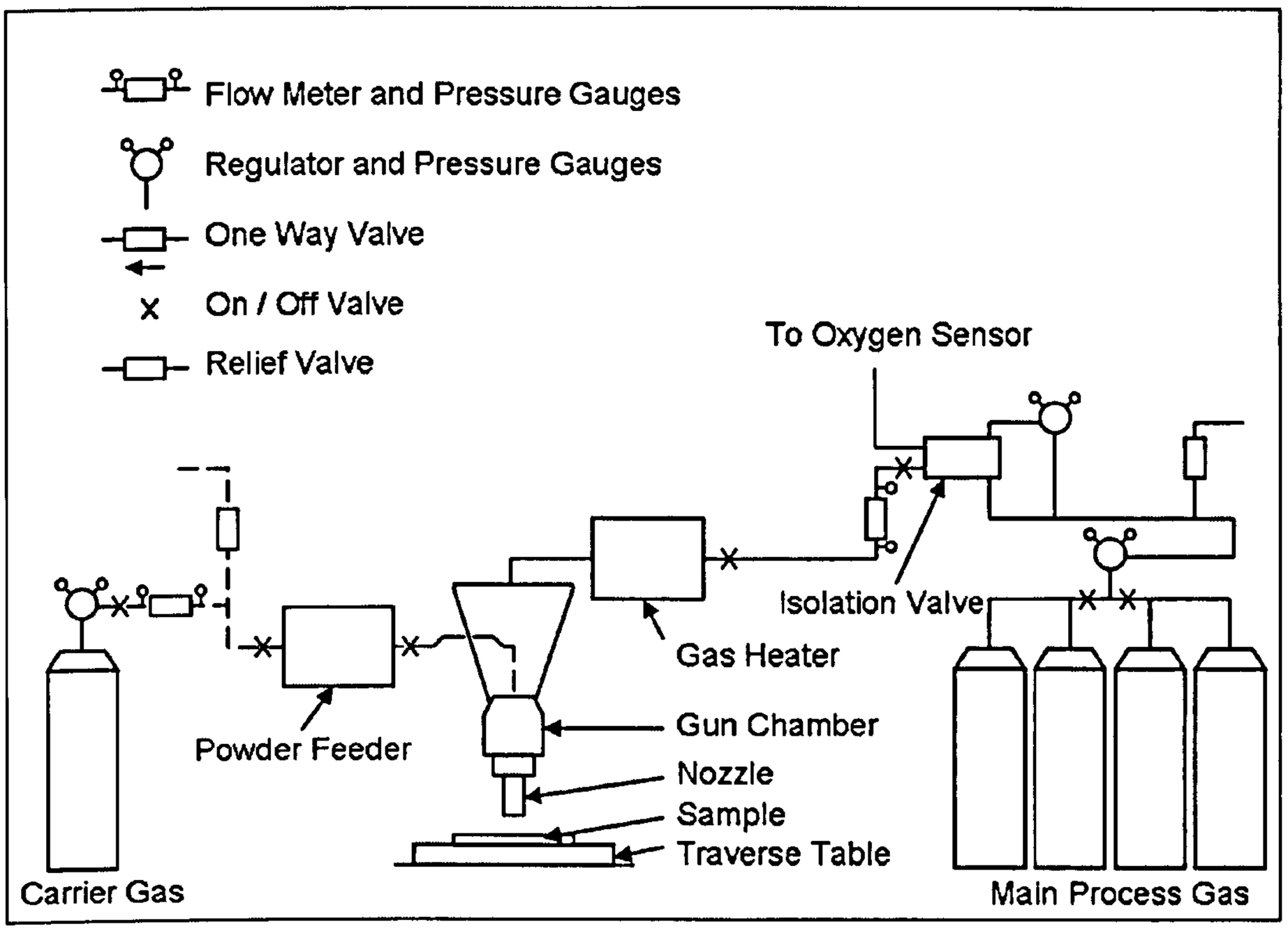

Figure 4.20 – Schematic of the cold spray system at the University of Nottingham.

When spraying fatigue samples a cylindrical dog bone substrate as shown in Figure 4.21 was used. When spraying, the substrate was rotated using a calibrated electric drill at a rotational speed of approximately 2800 rpm. A stand off distance of 20 mm was employed, measured from the central region of the substrate and a traverse speed of 100 mm s^{-1} was used. Coatings, ~120 μm thick, were applied to the central 21 mm of the substrate which covered the central test area and a small part of the shoulders.

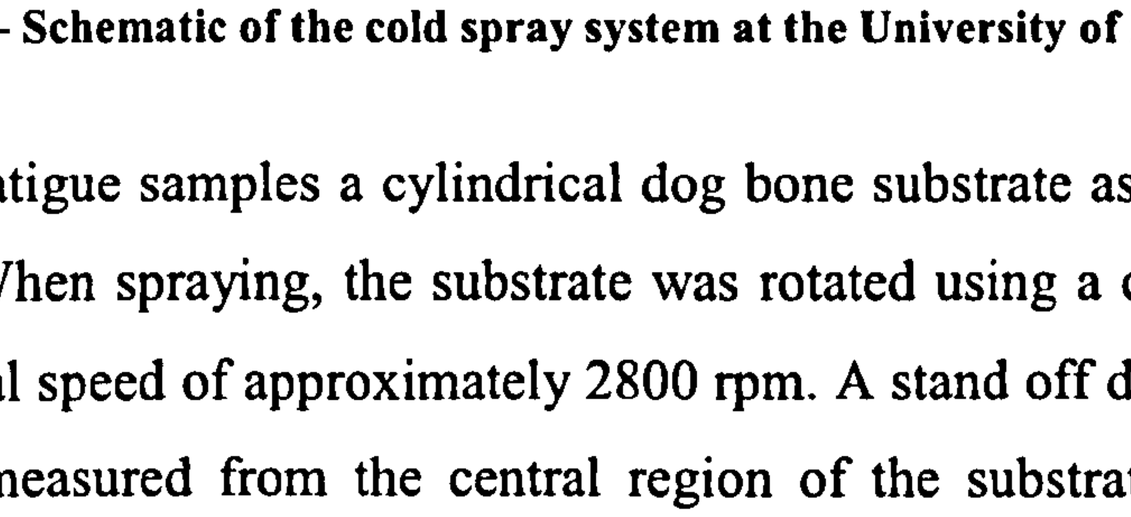

Figure 4.21 – Dimensions of the cylindrical dog bone Ti6Al4V substrates used for fatigue testing during this study.

4.8.2.2. Shrouded Arc Spraying

Shrouded arc samples were produced by an industrial partner and sprayed onto a Ti6Al4V substrate. The Ti6Al4V substrate was grit blasted by the industrial partner prior to spraying and an average surface roughness of the substrate was 6.2 μm as shown by Table 4.6. The coating was applied to the same portions of the fatigue and modulus substrates as the cold spray coatings as described in the previous section. Samples used for fatigue testing and modulus testing had coatings of approximately 100 μm and 900 μm in thickness respectively. Spray parameters for the shrouded arc process were unavailable due to the commercial sensitivity of this information.

4.8.3. Microstructural Characterisation of Coatings

This section describes the metallurgical preparation and microscopy techniques used to characterise the coatings created for this study.

4.8.3.1. Metallurgical Preparation

Coating deposit samples of a suitable size for OM and SEM analysis were cut cross-sectionally using a diamond saw and mounted in conductive resin. Samples were then ground and polished. The grinding and polishing were performed with emery papers starting with size 400 grit and progressively polishing with finer size paper up to 2400 grit. Water was used for sample cooling and lubrication. After this initial grinding stage, titanium deposits were subsequently polished with a solution of 1 part H_2O_2 (30 % by volume) with 9 parts water based colloidal silica solution. After the initial grinding stage, the copper and aluminium deposits were initially polished with diamond paste of 6 μm and 1 μm and final polishing was carried out using water based colloidal silica solution. Powders and deposits were observed in both the unetched and etched conditions to reveal the microstructure. Etching of titanium was performed using with a 10% hydrofluoric acid, 30% HNO_3 and 60% H_2O_2 solution.

4.8.3.2. Microscopy Techniques

Scanning electron microscopy, energy dispersive X-ray (EDX) analysis and optical microscopy were employed for coating characterisation.

4.8.3.3. Scanning Electron Microscopy

Scanning electron microscopy was performed using a Philips XL-30 (Philips, Eindhoven, The Netherlands) and JEOL 6400 (JEOL, Welwyn Garden City, UK). Examination of deposits was performed at 20 kV, utilising both secondary electron (SE) and backscattered electron (BSE) techniques. A working distance of 10 mm was used. EDX analysis was carried out on cross sectioned samples to measure chemical compositions of regions within the coating.

4.8.3.4. Optical Microscopy

Optical microscopy of the mounted coating cross-sections was carried out at a range of magnifications using a Nikon microscope fitted with a digital camera to record images (Nikon DXM 1200F, Kingston upon Thames, UK).

4.8.3.5. Measurement of Coating Porosity

Coating porosity measurements were taken by analysis of SEM BSE images. For each sample, a suitable magnification was selected so that a mosaic of nine BSE images covering the full coating thickness was obtained. The same contrast and brightness were used for each image so that, using analysis software, (Scandium, Olympus Soft Imaging Solutions GmbH, Münster, Germany) a set threshold grey value could be used to differentiate between the coating material and pores and measure its volume fraction. Analysis software, ImageJ (U.S. National Institutes of Health, Bethesda, Maryland, USA), was used to measure the aspect ratio of the pores. Firstly, the pores were approximated to ellipses. The aspect ratio was measured by dividing the minor and major lengths of each ellipse. This technique assumes that all pores are aligned with the major axis perpendicular to the substrate-coating interface. In reality pores of many orientations will exist and the effects of

any subsequent analysis is discussed in subsequent sections. It should also be noted that this technique is only suitable for measuring pores and defects that are large enough to be resolved by the SEM.

4.8.4. Method of Investigating Coating Bonding Mechanisms

A blended aluminium copper powder was deposited onto a copper substrate at gas stagnation pressures of 15 and 29 bar. Following spray deposition, samples (coating plus substrate) were heat treated in a tube furnace (Lenton Furnaces, Sheffield, UK). The furnace was evacuated using a rotary pump prior to heating and heat treatment was performed under a continuous flow of high purity argon gas. Samples were heated at 20 °C min^{-1} to the annealing temperature of 400 °C, held at this temperature for 15 minutes and then furnace cooled to room temperature. The furnace cooled at a rate of approximately 10 °C min^{-1} from the annealing temperature, 400 °C, to 350 °C. The heat treatment allowed intermetallics to form where there was sufficient metallic contact between the aluminium and copper particles.

Samples were prepared for cross-sectional examination in the SEM and using image analysis software, ImageJ (U.S. National Institutes of Health, Bethesda, Maryland, USA), the degree of intermetallic formation could be characterised. Two characteristic features were examined to quantify the extent of intermetallic phase formation at the interfaces between copper and aluminium particles. First, the fraction of the total Al-Cu interface length where an intermetallic phase had formed was measured and secondly, the average intermetallic layer thickness was determined. These measurements were made using the analysis software ImageJ. For each stagnation gas pressure, up to four BSE images at a magnification of 4000X, representative of the coating microstructure, were selected for quantitative analysis. All visible interface lengths and corresponding intermetallic lengths were measured. Lines were overlaid randomly across the microstructure, and the thickness of the intermetallic measured (perpendicular to the interface) at points where the lines intersected with any intermetallic region. Between 50 and 60 thickness measurements were made for each primary gas pressure.

4.8.5. Micro Hardness Testing

Micro hardness testing was carried out on coating cross sections. Samples were mounted and polished as described in Section 4.8.3.1. A 100 gf load was applied for 15 seconds using a Leco 400M micro hardness tester (LECO Instruments, Stockport, UK). To assess the variation in micro hardness with coating depth, measurements were made at various points on the coating cross section. After each indentation, the indentor was moved 150 μm in the x-direction and 50 μm in the y-direction as shown by Figure 4.22. The distance between indentations was sufficient enough that the indentations would not influence the measured hardness at other points.

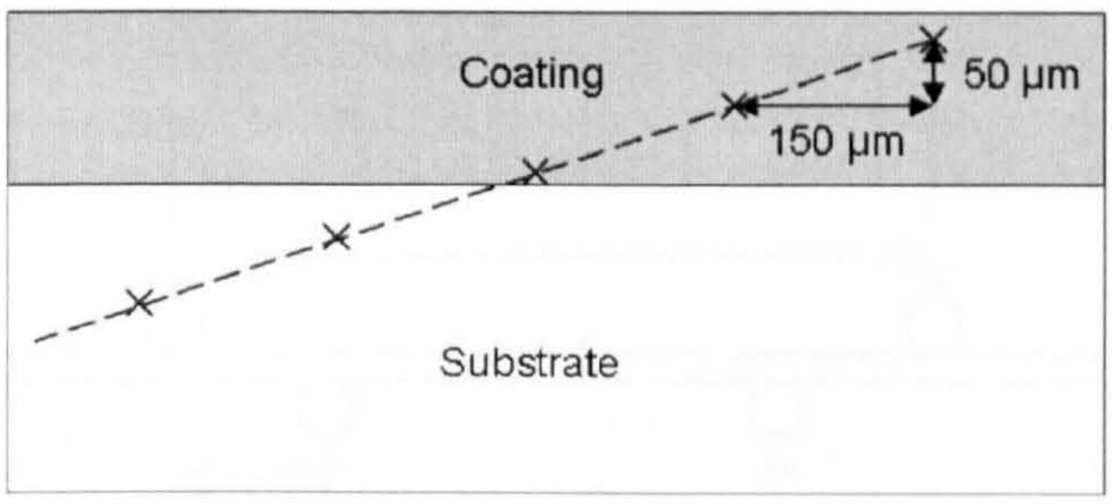

Figure 4.22 – Schematic diagram of micro hardness test indent placement.

4.8.6. Modulus Testing Methodology

The substrate and coating moduli were determined using a four point bend test methodology. Bend testing was carried out using a Mayes testing machine with a 2.5 kN load cell. During bend testing, samples were tested three times with the coatings in compression, from which an average elastic modulus was calculated. The mid-point displacement of the surface in tension was monitored using an external LVDT (Model 1000RA, RDP, UK) to an accuracy of ±1μm and a cross head loading rate of approximately 0.5 mm / minute was applied.

The modulus, E, of a uniform beam can be calculated from the slope of the load-displacement curve and is given by [122]:

$$E = \frac{P\,a}{24\,v\,I}\left(3L^2 - 4a^2\right) \qquad \text{(Eq. 4.4)}$$

where v is the mid-point displacement, L is the distance between outer support rollers (50 mm in this work), a is the distance between the loading and support rollers (15 mm in this work), and P is the applied load per loading point as shown by Figure 4.23. The rollers used had a diameter of 5.5 mm. I is the second moment of area, given by:

$$I = \frac{wd^3}{12} \qquad \text{(Eq. 4.5)}$$

where w is the width and d the sample thickness. However, if the beam is created from two dissimilar materials, (i.e. a substrate and coating) the method of equivalent sections must be employed to find the location of the neutral axis [123].

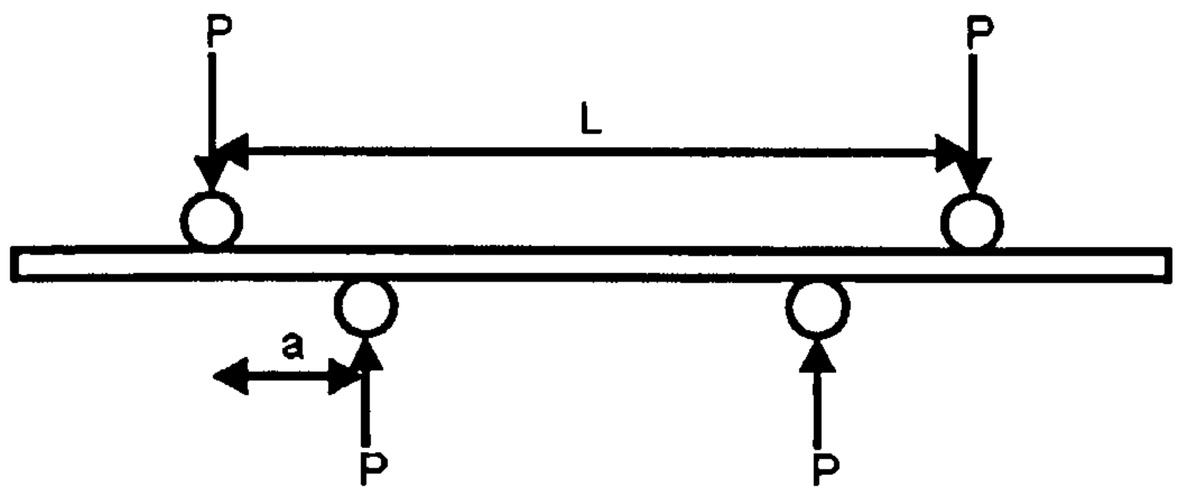

Figure 4.23 – Schematic of the four point bend rig employed.

4.8.6.1. Method of Equivalent Sections

This method replaces the actual section with a mechanically equivalent one, in which all the material has a common modulus. If the elastic moduli of the substrate and coating are E_s and E_c respectively, and w is the original width of the coating, then w' is the equivalent section width of the coating with an elastic modulus E_s as shown in Figure 4.24. H and h are the substrate and coating thicknesses respectively. It is anticipated that the coating must be approximately at least a third of the thickness of the substrate for this technique to be successful. w' is given by:

$$w' = w\left(\frac{E_c}{E_s}\right) \qquad \text{(Eq. 4.6)}$$

The distance between the neutral axis of the composite beam and the free coating surface, y_1, is given by:

$$y_1 = \frac{h^2 E_c + E_s H(H+2h)}{2(HE_s + hE_c)} \qquad \text{(Eq. 4.7)}$$

The second moment of area, I, of the composite beam can be shown to be equal to:

$$I = \left[\frac{wH^3}{12} + (wH)\left(\left(h + \frac{H}{2}\right) - y_1\right)^2\right] + \left[\frac{w'h^3}{12} + (wh)\left(y_1 - \left(\frac{h}{2}\right)\right)^2\right] \qquad \text{(Eq. 4.8)}$$

For unsprayed samples, equation 4.4 can be used to calculate the modulus of the substrate using the slope of the load-displacement curve generated from the four point bend test. To calculate the elastic modulus of the coating, the coated sample is treated as a composite beam. Using equation 4.4 and the slope of the load-displacement curve of the coated samples, it is possible to determine the value of the product $(E\ I)$ of the composite beam. Using equations 4.7 and 4.8, the known E_s values, and an estimate of E_c, an estimate of the $(E\ I)$ value can be made and compared with the experimentally derived value. E_c is then refined.

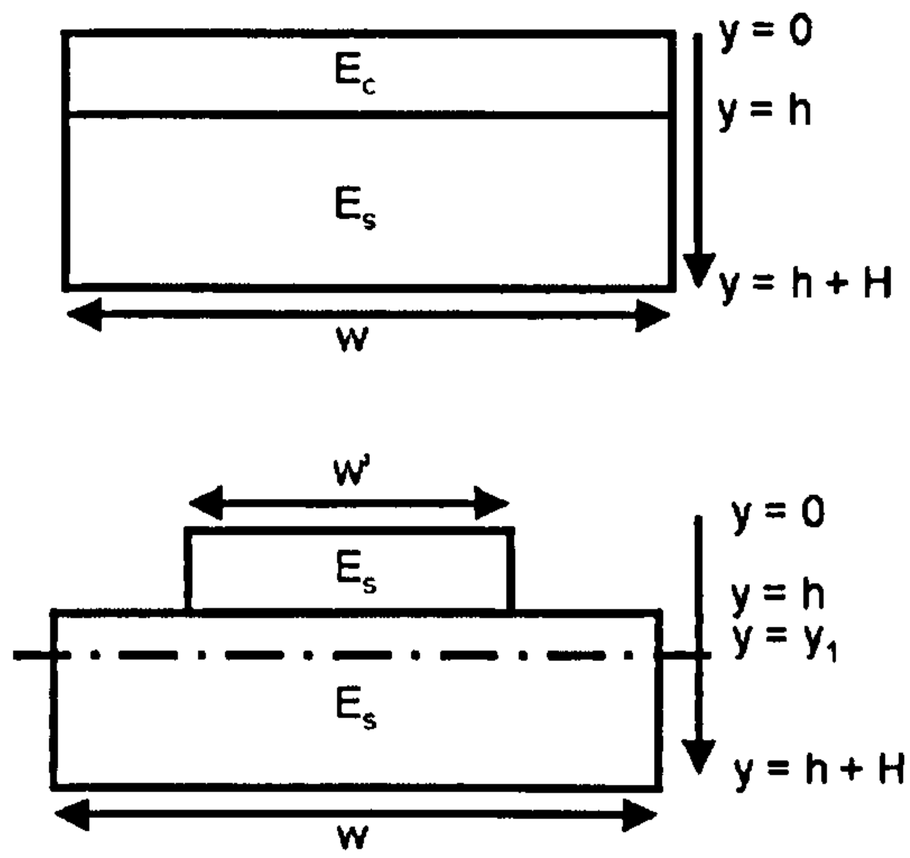

Figure 4.24 – Geometry of the actual and equivalent section.

4.8.6.2. Eshelby Equivalent Homogeneous Inclusion Model

The Eshelby equivalent homogeneous inclusion model allows the effect of ellipsoidal inclusions within a matrix material on its modulus to be calculated [114-116]. Eshelby visualised a series of cutting and joining exercises whereby an elliptical inclusion is cut from an elastically homogenous material, which then

undergoes a shape change (the transformation strain ε^T) free from the constraining matrix. A stress field is then applied to the ellipsoid in order to return it to its original shape and allow it to fit back into the original hole left within the matrix. The two regions are then assumed to be joined together and equilibrium is reached between the matrix and the inclusion with a constrained strain (ε^C) relative to its initial shape before removal [116].

The inclusion stress (σ_I) can be calculated using Hooke's Law in terms of the elastic strain (ε^C-ε^T) and the stiffness tensor of the material (C_M).

$$\sigma_I = C_M\left(\varepsilon^C - \varepsilon^T\right) \qquad \text{(Eq. 4.9)}$$

By using the Eshelby '*S*' tensor it is found that the final constrained strain (ε^C) can be obtained from a specified shape change (ε^T).

$$\varepsilon^C = S\varepsilon^T \qquad \text{(Eq. 4.10)}$$

The Eshelby '*S*' tensor is calculated in terms of the inclusion aspect ratio and the Poisson's ratio of the material. The aspect ratio of the pore is defined as the width (x) divided by the length (y) as shown in Figure 4.11.

Therefore:

$$\sigma_I = C_M\left(S\varepsilon^T - \varepsilon^T\right) \qquad \text{(Eq. 4.11)}$$

or:

$$\sigma_I = C_M\left(S - I\right)\varepsilon^T \qquad \text{(Eq. 4.12)}$$

where I is the identity matrix.

The case described above assumes the matrix and inclusion to be of the same material. In the case of sprayed coatings this is not the case as the defects or inclusions are considered to have zero stiffness. To ease the calculation, it is possible to replace the actual inclusion by an equivalent "ghost inclusion" of the same properties as the matrix material. For the ghost inclusion to have an identical

constrained shape of the real inclusion, the elastic strains within the inclusions will differ but the same uniform stress state of the composite will be attained. This allows the actual and equivalent inclusion to be freely interchanged whilst maintaining identical stress fields in the matrix [116].

To allow for external loading, the system is assumed to be elastically homogeneous, and therefore the strain arising from the applied stress is the same throughout. Consequently the stress (and strain) at each point is simply the sum of the applied stress or strain and the internal stress (Eq. 4.9) calculated previously.

Hitherto, it has been assumed that the system consists of a single inclusion embedded within an infinite matrix. To account for higher inclusion contents, the inclusion and its surrounding matrix is removed from the infinite matrix. This causes the matrix to deform due to the creation of a stress within the matrix to oppose the inclusion stress; previously the infinite matrix would have been able to successfully constrain the inclusion. This effect is modelled by superimposing a background stress (σ^b) upon the infinite matrix as if it was externally applied which satisfies the stress balance and causes the matrix and inclusion to relax uniformly. Finally, all inclusions within the matrix can be included by using the total volume fraction of all the inclusions and the mean internal stresses in the matrix and inclusions.

The composite stiffness tensor (C_C) is found to be [116]:

$$C_C = \left[C_M^{-1} - f\{(C_I - C_M)[S - f(S - I)] + C_M\}^{-1}(C_I - C_M)C_M^{-1}\right]^{-1} \qquad \text{(Eq. 4.13)}$$

where f is the porosity volume fraction and C_I is the inclusion stiffness. The engineering constants of the composite can be derived from this tensor. The axial and transverse Young's moduli are given by E_{3C} and E_{1C} respectively, which are defined as follows:

$$E_{3C} = \frac{1}{C_{3C}^{-1}} = \frac{\sigma^A}{\varepsilon_3^A + f\varepsilon_3^T} \qquad \text{(Eq. 4.14)}$$

and

$$E_{1C} = \frac{1}{C_{1C}^{-1}} = \frac{\sigma^A}{\varepsilon_1^A + f\varepsilon_1^T} \quad \text{(Eq. 4.15)}$$

σ^A and ε^A are the stresses and strains acting due to the applied load. These equations are best evaluated numetrically [116].

4.8.7. Adhesion Strength Test Methodologies

The surface of the substrate prior to spraying is a major factor in determining the bond strength between the substrate and coating. There are various methods available to measure the bond strength between coating and substrate. To validate results two separate analysis techniques have been derived.

4.8.7.1. Pull Off Test Method

Adhesion/tensile equipment supplied by DFD instruments (PAT, DFD Instruments, Kristiansand, Norway) uses a handheld hydraulic pump to generate force. After spraying, the top surface of the coating is attached with a heat curing resin (E1100S, DFD Instruments, Kristiansand, Norway) to the test element as shown in Figure 4.25.

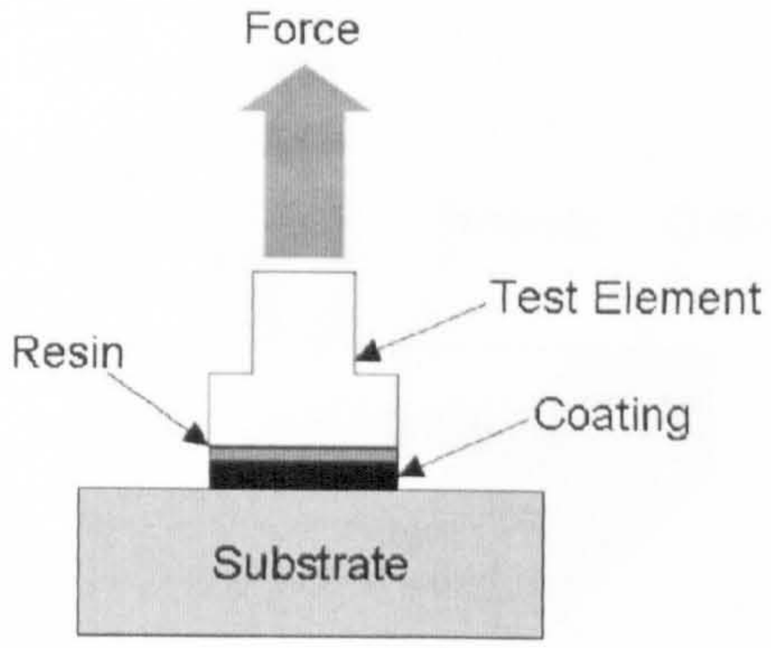

Figure 4.25 – Schematic of the pull off test procedure.

Once the resin is applied, the sample is placed in the furnace at 120 °C for 90 minutes. Once the resin is hardened, the test equipment is attached and pulls the test element away from the sample. Generally one of two failure mechanisms occurs, namely failure at the coating-substrate interface or failure at the coating-resin

interface. It is important to apply the resin carefully. The resin must be applied evenly, to a clean surface and not touch the substrate, ensuring that only a bond between the test element and coating is formed. Additionally, because the force is applied by hand it is difficult for the force to be applied linearly during the test. Results can be difficult to analyse if failure occurs between the resin and coating and not between the substrate and coating, as the former only provides a lower-boundary of the coating-substrate strength.

4.8.7.2. Transverse Scratch Test

The transverse scratch test method is a modified scratch test/indentation method [124-126]. Fixed load scratching is performed across the interface as shown in Figure 4.26. Loads up to 80 N are applied and the scratches created are evaluated by optical microscopy. Cracks generated along the interface can be analysed and used to qualitatively show the amount of delamination between the substrate and coating [126]. This method also allows investigation of bonding mechanisms between individual splats, by assessing qualitatively the amount of coating break up with increasing load.

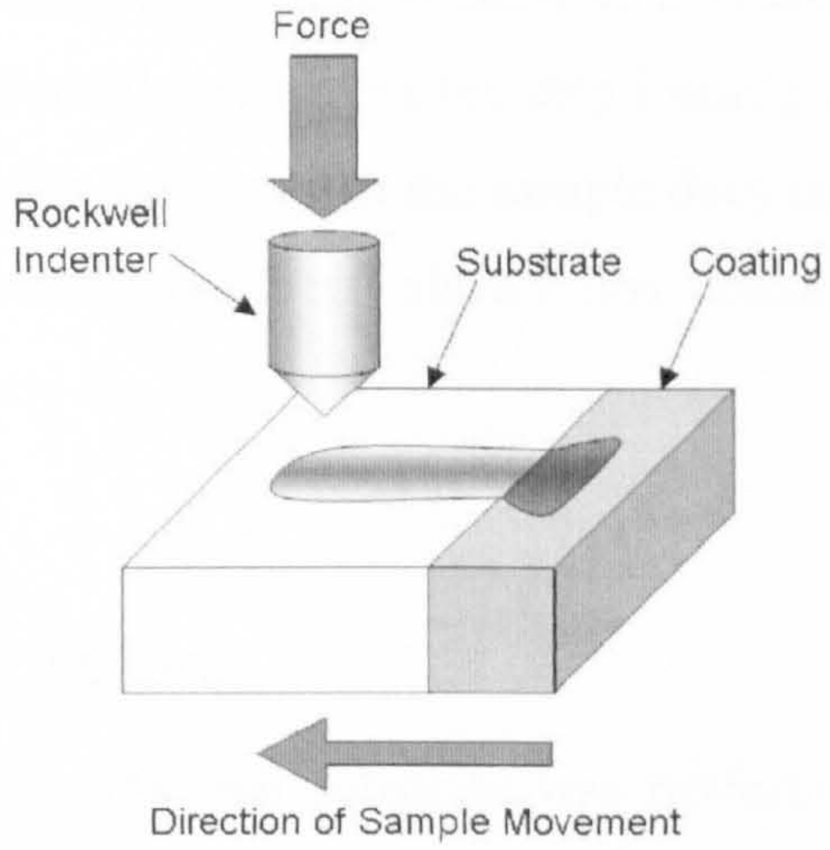

Figure 4.26 – Schematic of the transverse scratch test procedure.

4.8.8. Fatigue Testing Methodology

Samples were rotated by a Wöhler rotating bend fatigue testing machine at approximately 3000 rpm. A fatigue step loading method was employed. This method is widely employed [119, 127-130] since it addresses the statistical problems associated with fatigue testing [128]. Starting with an applied load known to not cause failure, the sample is rotated for blocks of 10^7 cycles. A countdown timer connected to the power supply was used to stop the sample rotating after 10^7 cycles had passed. The load applied was then increased by steps of 5% and the process repeated until failure occured [128]. The data is interpolated to calculate the applied stress required for failure to occur at 10^7 cycles using the following equation [128]:

$$\sigma_{10^7} = \sigma_{pr} + \frac{N_f}{10^7}\left(\sigma_f - \sigma_{pr}\right) \qquad \text{(Eq. 4.16)}$$

Where σ_{10^7} is the value of stress required for failure to occur after 10^7 cycles, σ_{pr} is the maximum stress level of the prior block of cycles where no failure occurred, σ_f is the maximum stress level of the final block of cycles where failure occurred and N_f is the number of cycles to failure within that block [128].

This constant life endurance stress is termed the endurance limit [15]. Up to five samples of each sample type were tested to allow an average fatigue endurance limit to be calculated. One potential problem of the step loading method is coaxing [119, 130], where fatigue at loads under which the sample does not fail do in fact alter its endurance limit. However, it has been shown that coaxing is not significant in Ti6Al4V [128, 130].

4.8.9. Tensile Testing

Tensile testing of the Ti6Al4V rod substrate was performed using tensile testing equipment manufactured by J.J. Lloyd (J.J.Lloyd, Southampton, UK). During testing the cross-head was moved at a rate of 1 mm per minute. Cylindrical dog bones samples were produced consisting of a central test section 30 mm in length and 4 mm in diameter.

4.8.10. Residual Stress Measurement

Two methods were evaluated for estimating the residual stresses developed in coatings during spraying, namely X-ray diffractometry (XRD) analysis and the variation of the induced bending of the sample pre- and post-spraying. Both types of analysis are non-destructive methods.

4.8.10.1. X-Ray Diffractometry

During x-ray diffractometry x-rays are diffracted by a sample surface. It is known that:

$$n\lambda = 2d'\sin\theta \qquad \text{(Eq. 4.17)}$$

where λ is the wavelength of x-rays, d' is the spacing between planes in the atomic lattice and θ is the angle between the incident ray and scattering plane. Equation 4.17 is known as Bragg's Law.

X-ray diffraction can be used to calculate macrostresses within the specimen being examined. Variations in the sample crystal lattice due to stress at its surface will affect the x-ray diffraction angle. The residual stress, stresses that persist in the absence of external forces, is determined from the elastic constants and assuming a linear elastic distortion of the appropriate crystal lattice plane. A full derivation of this method is available in Appendix 4 and with definitions of the various symbols used. Equation A97 (Appendix 4) allows the stress in any chosen direction to be calculated from the inter-planar spacings determined from two measurements, made in a plane normal to the surface and containing the direction of the stress to be measured.

The XRD process is regarded as a near surface measurement device. Strictly speaking the x-rays will penetrate into a small amount of the sample (<10μm), dependent on the anode material, and angle of incidence of the x-ray beam. Therefore the measured strain is in fact the average over a few microns depth under the surface of the specimen. To perform analysis at deeper depths into the specimen, material must be removed carefully to expose surfaces at varying depths through the sample. This turns the method into a destructive method. Abrasive or machining

removal methods, no matter how slow the removal rate, will deform the surface and introduce additional stresses. This will lead to alteration of the stress state and residual stress measurements must be corrected to take account of this. In this case it is recommended that electro polishing is used to remove material from the specimen since it will induce low residual stresses to the material [131].

X-ray diffractometry was carried out using a Bruker Diffractometer D8 Discover XRD (Bruker AXS, Coventry, UK) machine with Cu Kα radiation. A nickel filter was used to remove the Cu Kβ peak from subsequent analysis. Analysis was carried out using a spot focus of 1 mm in diameter on the sample surface and tube operating conditions of 40 kV and 30 mA. To assess the integrity of this method a four point bend rig was constructed for the X-ray diffractometer. A small piece of Ti6Al4V sheet, measuring 10 mm by 150 mm, was placed within the four point bend rig. Strain gauges were attached to the underside of the Ti6Al4V sheet. Residual stress measurements were made using the XRD and the strain gauges with the Ti6Al4V sheet with no applied strain and a known applied strain. By attaching the strain gauges to the underside of the Ti6Al4V sheet a compressive force is measured when the strain is applied. Stresses calculated by the strain gauges and the x-Ray diffractometer were compared.

4.8.10.2. Induced Specimen Bending

An alternative method to measure the amount of residual stress within a sprayed deposit, is to measure the amount of bending of the substrate, induced due to deposition of the coating. The induced bending of the sample was recorded by profiling the underside of the substrate pre- and post-spraying using a Talysurf CLI 1000 profilometer (Taylor Hobson, Leicester, UK) with a stylus having a resolution of 40 nm. This allowed the radius of curvature of the sample, R, associated with the residual stresses to be measured. The profile was measured for the central 80 mm portion of the sample.

The substrate and coating are considered to be a composite beam of two dissimilar materials. Due to the misfit strain between the coating and substrate, forces equal but

opposite in magnitude, occur. These forces act at the centre of the two sections to give a continuity of length [123] and cause the two sections to deflect by a radius of curvature R as shown by Figure 4.27 and Figure 4.28.

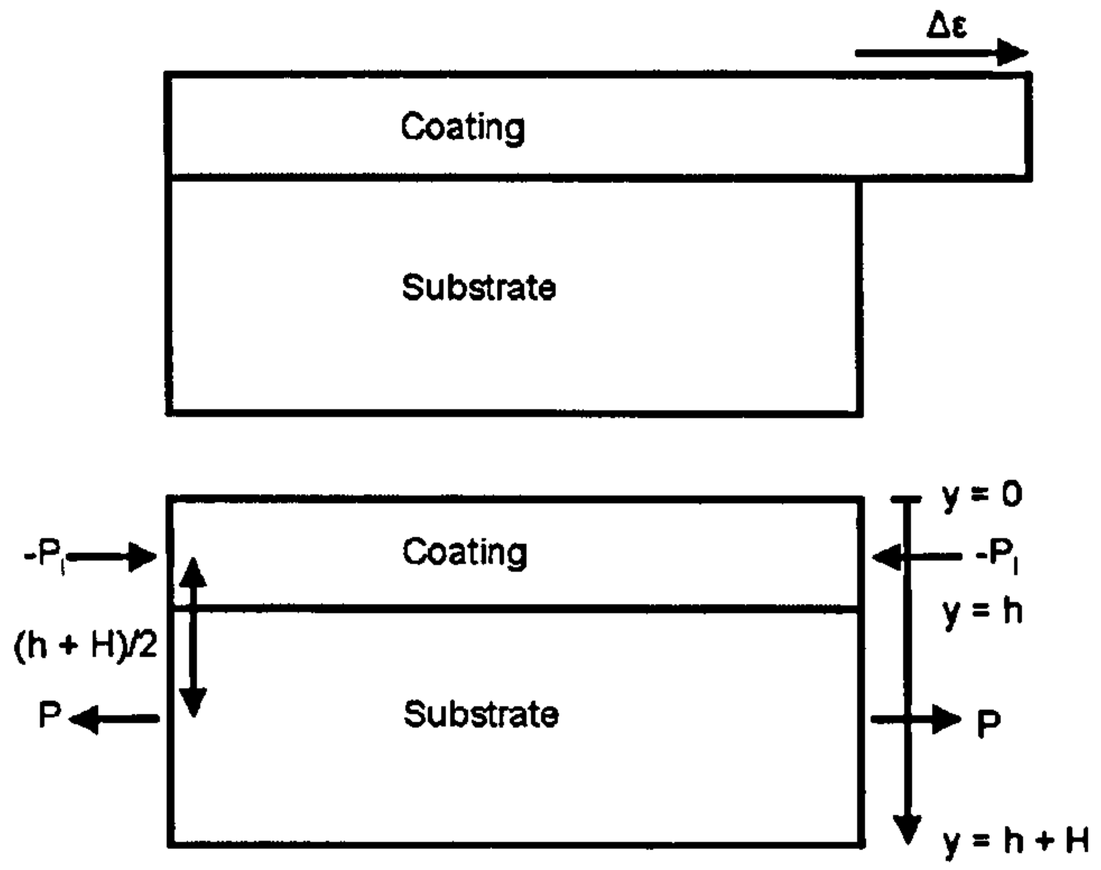

Figure 4.27 – Schematic of the misfit strain between the coating and the substrate.

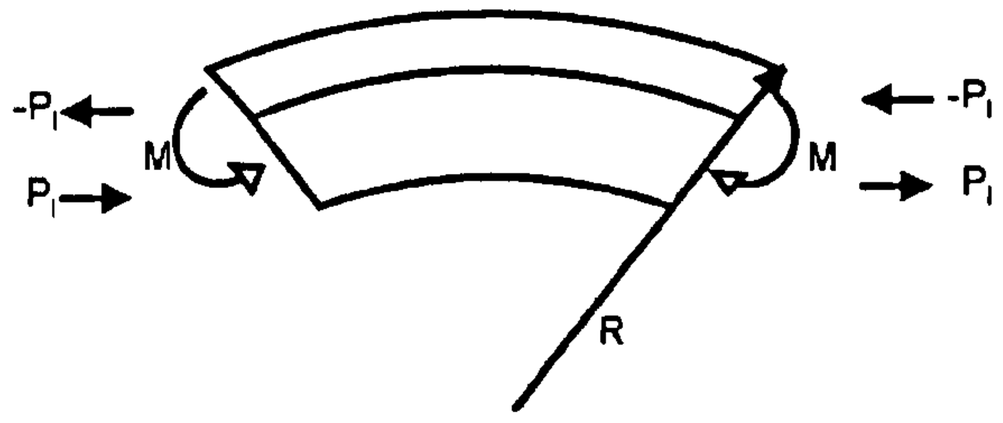

Figure 4.28 – After coating application, a misfit strain arises causing the sample to deflect by radius, R.

The moment associated with the forces is given by:

$$M = P_l\left(\frac{h+H}{2}\right) \qquad \text{(Eq. 4.18)}$$

Where P_l is the force applied to give continuity of length, h is the coating thickness and H is the substrate thickness. M is the resulting moment and balancing this moment will cause the beam to bend to give a radius of curvature, R, as shown by Figure 4.28. The stress, σ, in the beam is proportional to the distance, $(y_l - y)$, from its neutral axis where E_y is the beam modulus (a function of the position) [123].

$$\frac{\sigma}{(y_1 - y)} = \frac{E_y}{R} \qquad \text{(Eq. 4.19)}$$

Considering an element of cross sectional area dA at a distance $(y_1 - y)$ from the neutral axis and assuming that for pure bending the normal net force on the cross-section must be zero [123], then the bending moment is given by:

$$M = \frac{w}{R}\int_0^{h+H} E_y (y_1 - y)^2 dy \qquad \text{(Eq. 4.20)}$$

Solving equation 4.20 and inserting equation 4.18 gives:

$$P_l\left(\frac{h+H}{2}\right) = \frac{wE_c}{R}\left(y_1^2 h - h^2 y_1 + \frac{h^3}{3}\right) + \frac{wE_s}{R}\left(y_1\left(H^2 + 2hH - Hy_1\right) + \frac{h^3}{3} - \frac{(h+H)^3}{3}\right) \qquad \text{(Eq. 4.21)}$$

where y_1 is given by equation 4.7. Since $\varepsilon_s = \sigma / E_s$ and $\sigma = P_l / H w$, and similarly for ε_c, then if $\Delta\varepsilon = \varepsilon_s - \varepsilon_c$ then [123]:

$$\Delta\varepsilon = \frac{P_l}{HwE_s} + \frac{P_l}{hwE_c} \qquad \text{(Eq. 4.22)}$$

$$\therefore \frac{P_l}{w} = \Delta\varepsilon\left(\frac{hE_c HE_s}{hE_c + HE_s}\right) \qquad \text{(Eq. 4.23)}$$

The stress distributions within the coating and substrate can be determined by using the values of P_l and R from $\sigma / y = E / R$. Therefore, the stresses in the coating at the free surface ($y = 0$) and at the interface ($y = h$) are given by:

$$\sigma_c\Big|_{y=0} = -\Delta\varepsilon\left(\frac{E_c HE_s}{hE_c + HE_s}\right) + E_c\frac{y_1}{R} \qquad \text{(Eq. 4.24)}$$

and

$$\sigma_c\Big|_{y=h} = -\Delta\varepsilon\left(\frac{E_c HE_s}{hE_c + HE_s}\right) - E_c\frac{(h - y_1)}{R} \qquad \text{(Eq. 4.25)}$$

whilst the stresses in the substrate at the interface ($y = h$) are calculated by:

$$\sigma_s\Big|_{y=h} = \Delta\varepsilon\left(\frac{hE_c E_s}{hE_c + HE_s}\right) - E_s\frac{(h - y_1)}{R} \qquad \text{(Eq. 4.26)}$$

4.8.11. Post-Spray Heat Treatments

Deposits were cut using a diamond saw to approximately 6 mm in length prior to heat treatment. Heat treatments were carried out in a tube furnace (Lenton Furnaces, Sheffield, UK). A rotary pump was used to remove air from the chamber prior to the heat treatment and to prevent oxidation from occurring. Additionally during the heating, dwell and cooling stages of the heat treatment a flow of argon was used to prevent oxygen from entering the chamber. A range of temperatures up to 1150 °C and dwell times up to 60 minutes were employed for the titanium deposits. For the blended aluminium-copper deposits the samples were heat treated at a temperature of 400 °C for 15 minutes to allow formation of intermetallics between the aluminium and copper particles. In all cases a temperature increase rate of 20 °C min^{-1} was used. After the heat treatment, the deposits were cooled within the furnace.

4.9. Experimental Results

The effects of various spray parameters on the mechanical properties of the deposit are presented in the subsequent sections. First measured properties of the Ti6Al4V substrate are identified. Whilst this is not the main scope of this study, some substrate properties are required to be measured to allow calculation of the cold spray coating mechanical properties. Next the cold spray coating mechanical properties are shown. A range of mechanical tests were performed, predominantly to titanium coatings, to characterise the mechanical properties of cold spray coatings. The next section shows the effect of heat treatments on titanium cold spray coatings. Heat treatments at various temperatures from 400 °C to 1150 °C were carried out and their influence on the mechanical properties of the cold spray deposits was measured. Finally the mechanical properties of a competitors shrouded arc coating are displayed.

4.9.1. Ti6Al4V Substrate Properties

Titanium coatings were deposited onto a Ti6Al4V substrate. Figure 4.29(a) and (b) are optical microscopy images showing the etched microstructure of the Ti6Al4V rod and sheet used for fatigue and modulus testing respectively. The Ti6Al4V rod

(Figure 4.29(a)) has a coarse equiaxed microstructure. The light areas of the image are the α phase and the darker areas the β phase. The Ti6Al4V rod has an approximate grain size of 10 μm or less. In contrast the Ti6Al4V sheet (Figure 4.29(b)) has a much finer equiaxed microstructure, indicating that a recrystallization procedure was carried out after being rolled to sheet form. The fine equiaxed microstructure gives the substrate high strength and ductility [89]. All three substrate types were found to have similar hardness values of between 326 kgf mm^{-2} and 362 kgf mm^{-2} in the as received state.

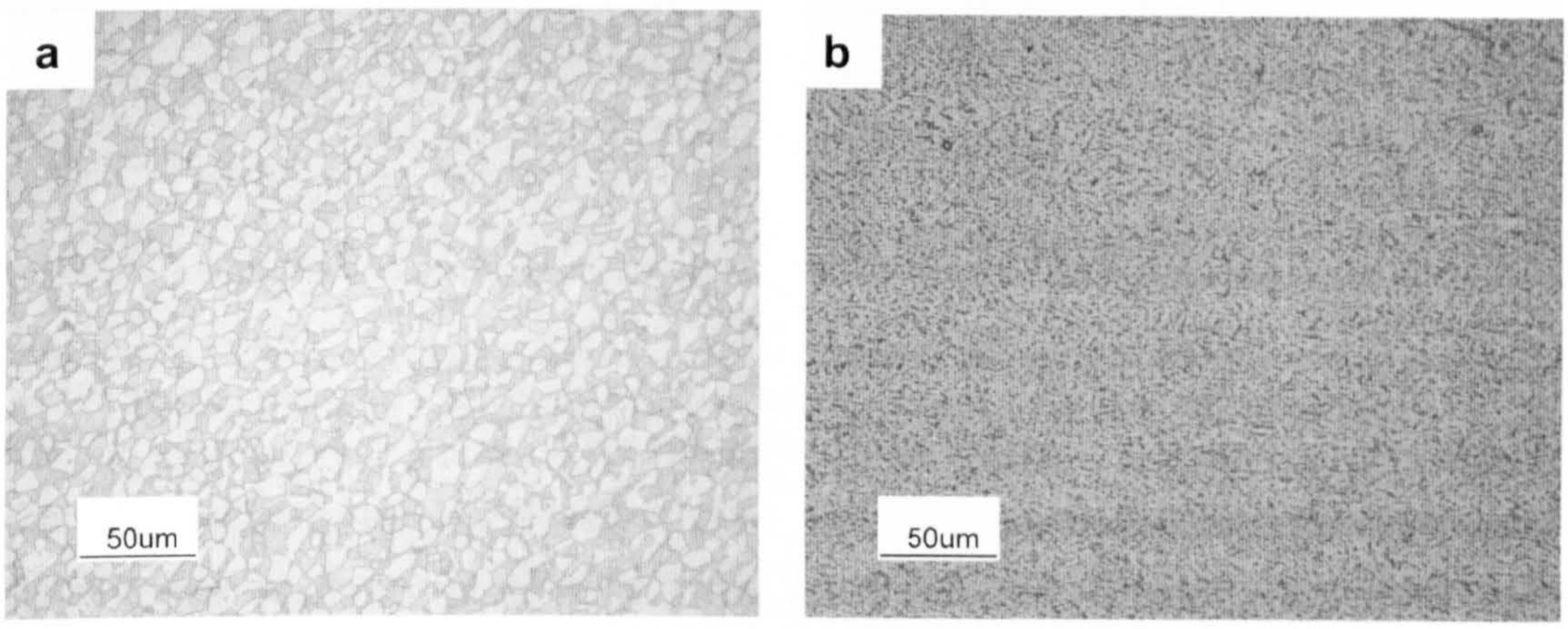

Figure 4.29 – OM images of the etched Ti6Al4V substrate microstructure; (a) Rod used for fatigue testing and (b) sheet used for modulus testing and microstructural analysis.

By four point bend testing, the 1.6mm thick Ti6Al4V substrate material was shown to have a modulus value of 107 GPa. The 0.2 % proof and yield stresses of the rod substrate to be used for fatigue testing by tensile testing was measured as 880 and 800 MPa, respectively. The Ti6Al4V substrate was found to have a rotating bend fatigue endurance limit for 10^7 cycles of 633 MPa. The fatigue endurance limit was found to reduce to 507 MPa or 418 MPa depending on the type of grit blasting surface finish employed.

4.9.1.1. Effect of Heat Treatment on Ti6Al4V Substrate Properties

Heat treatments were carried out at 400, 600, 800 and 1150 °C for 1 hour. Up to 800 °C there was minimal change in the substrate microstructure. In the case of the 7 mm

diameter rod, the coarse equiaxed microstructure previously identified in Figure 4.29(a) has been modified, due to growth of the lighter coloured alpha phase, and shown in Figure 4.30(a). For the 1.6 mm thick sheet, the fine equiaxed microstructure is still observed after the 800 °C heat treatment and shown in Figure 4.30(b).

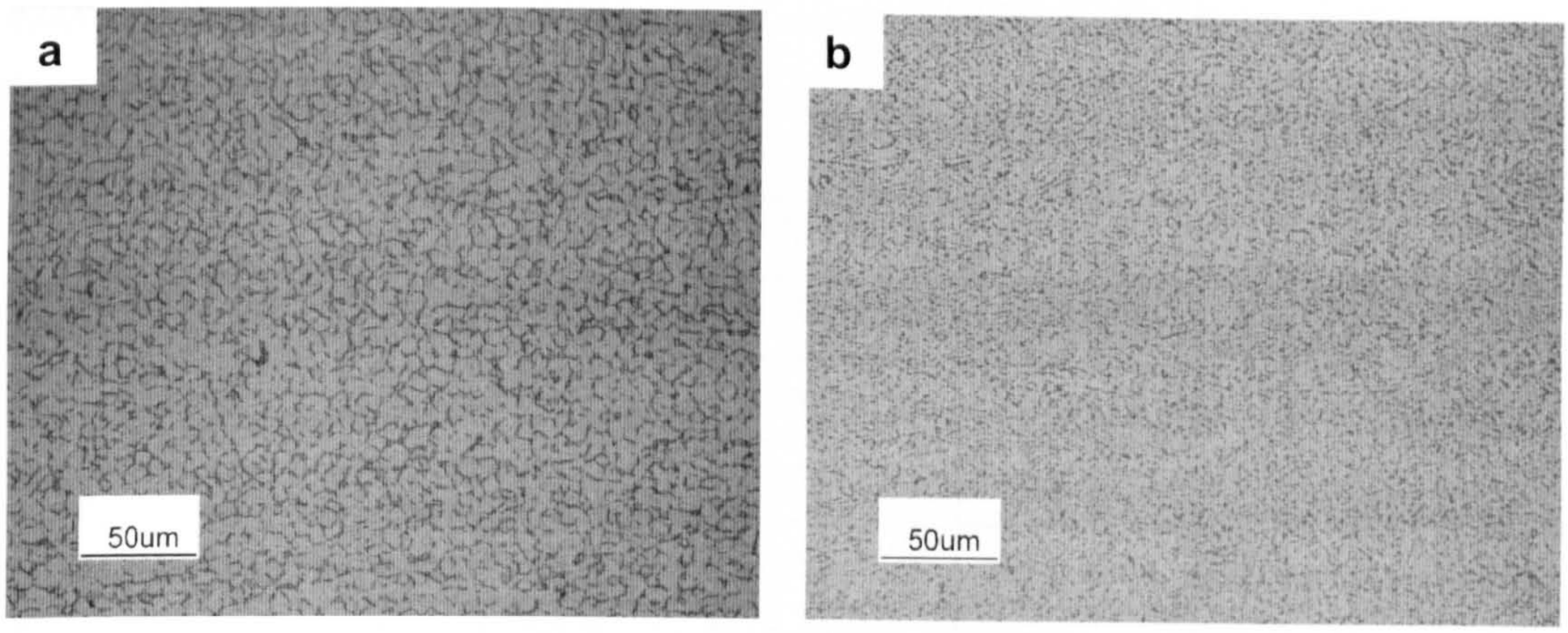

Figure 4.30 – OM images of the etched Ti6Al4V substrate microstructure after a heat treatment of 800 °C for 1 hour; (a) Rod used for fatigue testing and (b) sheet used for modulus testing and microstructural analysis.

After a heat treatment at 1150 °C there are significant variations in the substrate microstructure and these are due to the alpha / beta transus existing at approximately 1000 °C for this alloy. Figure 4.31(a) and (b) show lamellar microstructures of materials heated at 1150 °C with the beta phase as a small seam around the coarse and lighter coloured alpha [89].

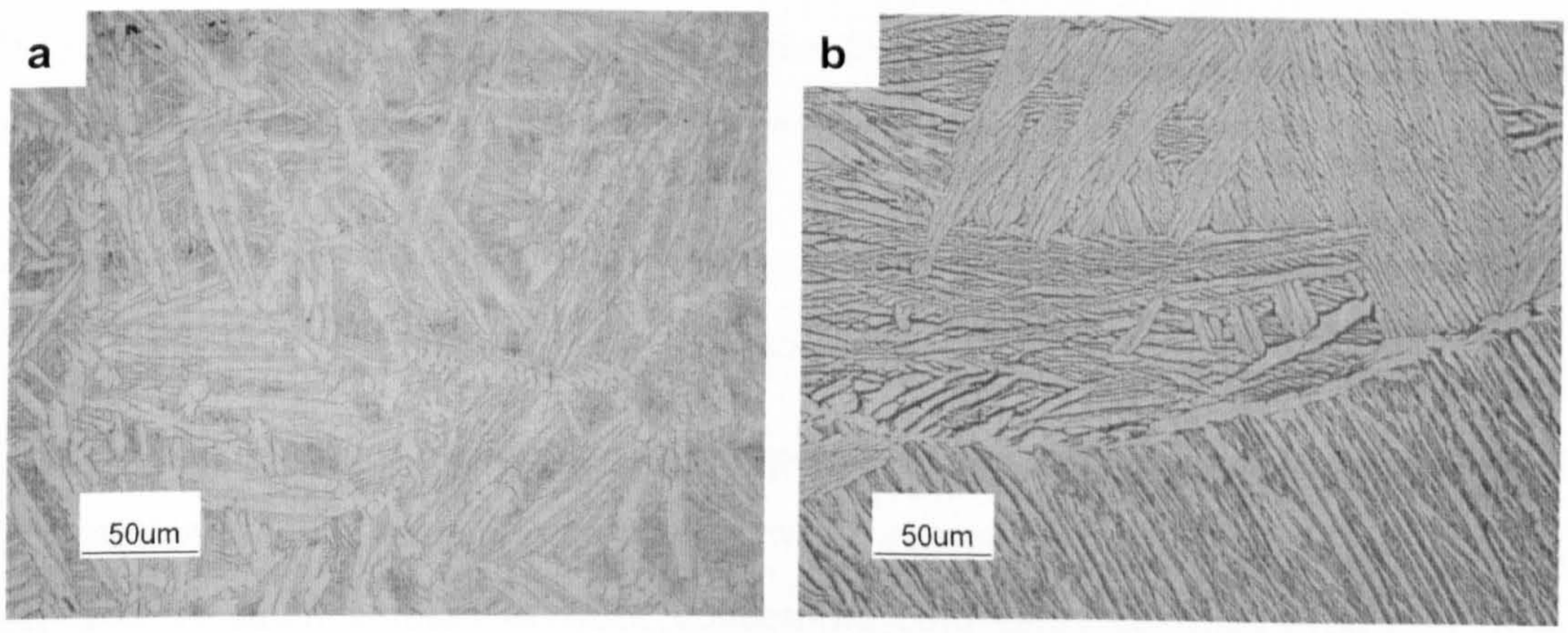

Figure 4.31 – OM images of the etched Ti6Al4V substrate microstructure after a heat treatment of 1150 °C for 1 hour; (a) Rod used for fatigue testing and (b) sheet used for modulus testing and microstructural analysis.

The variation in the average substrate hardness measured in this work with heat treatment temperature is summarised in Table 4.8. A reduction in substrate hardness was found with increasing heat treatment temperature. The 0.2% proof and yield stresses of the rod substrate to be used for fatigue testing were found to increase marginally from 880 and 800 MPa in the as-received condition to 945 and 824 MPa respectively after a heat treatment carried out at 1150 °C for one hour.

Heat Treatment	Hardness / kgf mm^{-2}	
	Substrate	Coating
400 °C	385 ± 5	90 ± 13
600 °C	375 ± 5	139 ± 27
800 °C	354 ± 9	130 ± 19
1150 °C	327 ± 6	157 ± 27

Table 4.8 – Average substrate and cold spray coating hardness values (kgf mm^{-2}) and the standard error of the mean after heat treating at various temperatures for one hour.

For most materials, the Young's modulus can be assumed to be independent of heat treatment; however, the Ti6Al4V alloy is known to behave differently in this respect. This is due to the modulus of the Ti6Al4V alloy being influenced by the specific moduli of the phases present and their volume fractions [12, 132]. The Young's modulus was 107 GPa in the as-received state, and increased approximately linearly with heat treatment temperature to a maximum of 123 GPa after a heat treatment at 1150 °C for one hour. It is also noted that some of the samples heat treated at 1150 °C suffered from brittle fracture during the four point bend testing due to oxygen embrittlement occurring during the heat treatment process.

4.9.2. Cold Spray Coating Properties

This section describes the mechanical properties of the cold spray coatings produced within this study. The majority of this work consists of examination of titanium deposits. A small amount of work concerning cold spray coatings produced from other materials (copper and aluminium) is also presented to give a more general overview of the mechanical properties expected from cold spray coatings. Firstly,

within Section 4.9.2.1. an assessment of the coating microstructure of the titanium cold spray coatings is made. Section 4.9.2.2. consists of results from utilising a blended aluminium and copper powder and subsequently heat treated to visually show the levels of bonding found within cold spray deposits; reasons for this choice of powder are discussed in further detail in the relevant section. The next sections assess the mechanical properties of the titanium deposits; coating porosity, stiffness, adhesion strength, rotating bend fatigue endurance limit and coating residual stress are all assessed. Coating stiffness measurements were also made with aluminium and copper cold spray deposits to give an overview of typical measured coating stiffness values for cold spray deposits. An Eshelby equivalent homogeneous inclusion model is also used to predict the effect of pores and defects on the coating stiffness for cold spray deposits.

4.9.2.1. Coating Microstructure

Figure 4.32(a) shows an overview of the microstructure of a cross-sectioned titanium coating deposited onto a Ti6Al4V substrate with an as-received surface finish. The coating consists of individual particles that are layered onto one another to form the bulk of the coating. Particles are surrounded by darker areas which are predominantly defects created during the coating process such as pores, voids or oxides where particles have not bonded together and are resolvable by the SEM. Figure 4.32(a) shows that approximately the top third of the coating appears to have a greater volume of voids and pores compared to the remaining two thirds. This is due to compaction of the underlying layers of the coating as further impinging particles impact the top surface of the deposit. Figure 4.32(b) is a higher magnification image of a densified region of the coating and it is possible to identify the light coloured individual particles more clearly that make up the coating and range in size up to approximately 40 μm. Figure 4.32(c) shows the coating-substrate interface. The interface is easily identifiable due to what appears to be incomplete bonding between the coating and substrate. Limited regions of the interface show no visible defects between the coating and substrate.

Etching the titanium coating allows individual grains within the particles to be identified more easily. The etching process also attacks defects within the coating and will therefore make these areas easier to identify. Figure 4.32(d) is an SE image of an etched titanium coating at the coating-substrate interface. The etch attacks the coating-substrate interface and large fractions of the particle boundaries are highlighted indicating that there are high levels of defects within the coating. There is a danger that over-etching the sample may attack areas within the deposit that have indeed formed a sufficient bond, leading to an over-estimation of areas where high levels of defects may be expected.

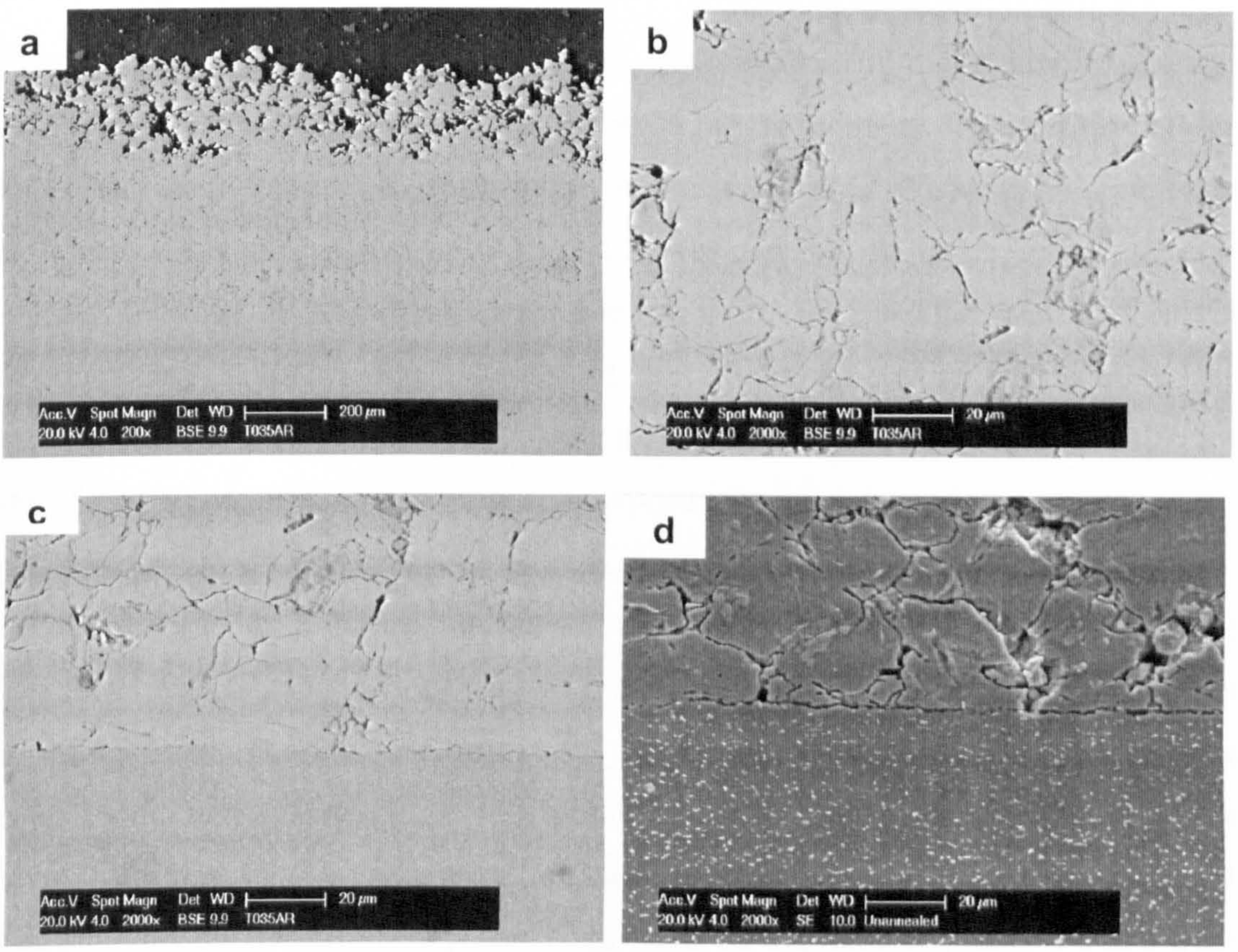

Figure 4.32 – BSE cross-sectional images of the titanium coating microstructure deposited onto a Ti6AL4V substrate with an as-received surface finish at (a) low magnification, (b) high magnification and (c) high magnification at the coating-substrate interface. (d) SE image of the etched titanium coating and Ti6Al4V substrate. Spray direction top to bottom utilising helium gas at room temperature and a stagnation pressure of 29 bar.

4.9.2.2. Visualisation of Coating Bonding

As discussed previously in Section 4.4. the bonding between individual particles is of great interest. Defects of any kind will affect the mechanical and physical

properties of a cold sprayed coating and it is important therefore to be able to characterise inter-particle bond formation and assess how it is affected by deposition conditions. The present study was therefore designed to investigate the interparticle bonding between aluminium and copper particles following deposition by cold spraying. The approach adopted was to spray a blended powder comprising elemental aluminium and copper particles and to subsequently anneal the deposit at 400 °C (Section 4.8.4.). If oxide free metal surfaces are in contact, intermetallic phases form rapidly for the aluminium-copper system by inter-diffusion at this temperature [133-135]. Therefore intermetallic phase formation can act as a marker for interfaces which were bonded together without oxide.

Figure 4.33(a) and Figure 4.33(b) show BSE images of the aluminium-copper microstructure after being sprayed at 15 and 29 bar respectively. In both figures there appears to be little porosity, with good interparticle contact. There is no significant difference observable between the 15 and 29 bar deposits. Following heat treatment of the deposits, it was found that one or more intermetallic phases form at interparticle boundaries, but coverage of the aluminium-copper interfaces by the intermetallics is incomplete. This is shown in Figure 4.34(a) and Figure 4.34(b) for the 15 and 29 bar primary gas pressures respectively.

It can be seen that although intermetallic layers are apparently absent from some interfacial regions, they had grown to a few microns in thickness in other areas. This is shown in more detail in Figure 4.35. Three different intermetallic phases have been found between a copper and aluminium splat, shown as intermediate grey levels (Figure 4.35). The intermetallic phases are numbered 1, 2 and 3, with phase 1 closest to the copper splat and phase 3 closest to the aluminium. Phases 1 and 3 were identified by EDX analysis as Cu_3Al_2 (δ – 60at% Cu) and $CuAl_2$ (Θ – 33at% Cu) respectively. Phase 2 was harder to accurately characterise due to its thickness being close to the spatial resolution of EDX analysis. However, both the BSE image and EDX analysis qualitatively indicate that this phase has a composition between that of phases 1 and 3. A previous interdiffusion study showed that up to five possible intermetallic phases may be expected for an aluminium-copper system ranging from Cu_9Al_4 (γ_2) to $CuAl_2$ (θ) [134]. Not all five intermetallic phases were identified

within the current samples; however, it may be postulated that phase 2 is CuAl (η_2 – 50at% Cu) or Cu_4Al_3 (ζ_2 – 57.1 at% Cu).

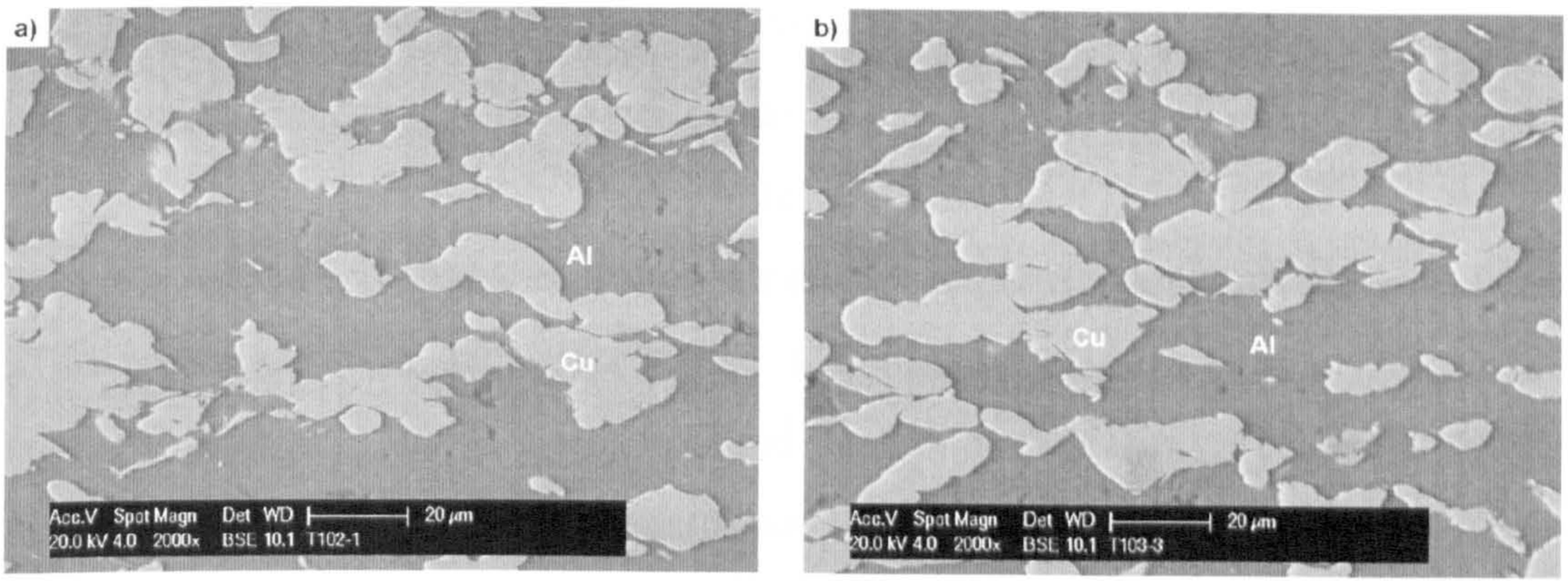

Figure 4.33 – BSE images of the as-sprayed Al-Cu deposits using helium gas at a pressure of (a) 15 bar and (b) 29 bar showing Cu, bright, Al dark and no evidence for intermetallic phase at the interface. Spray direction top to bottom.

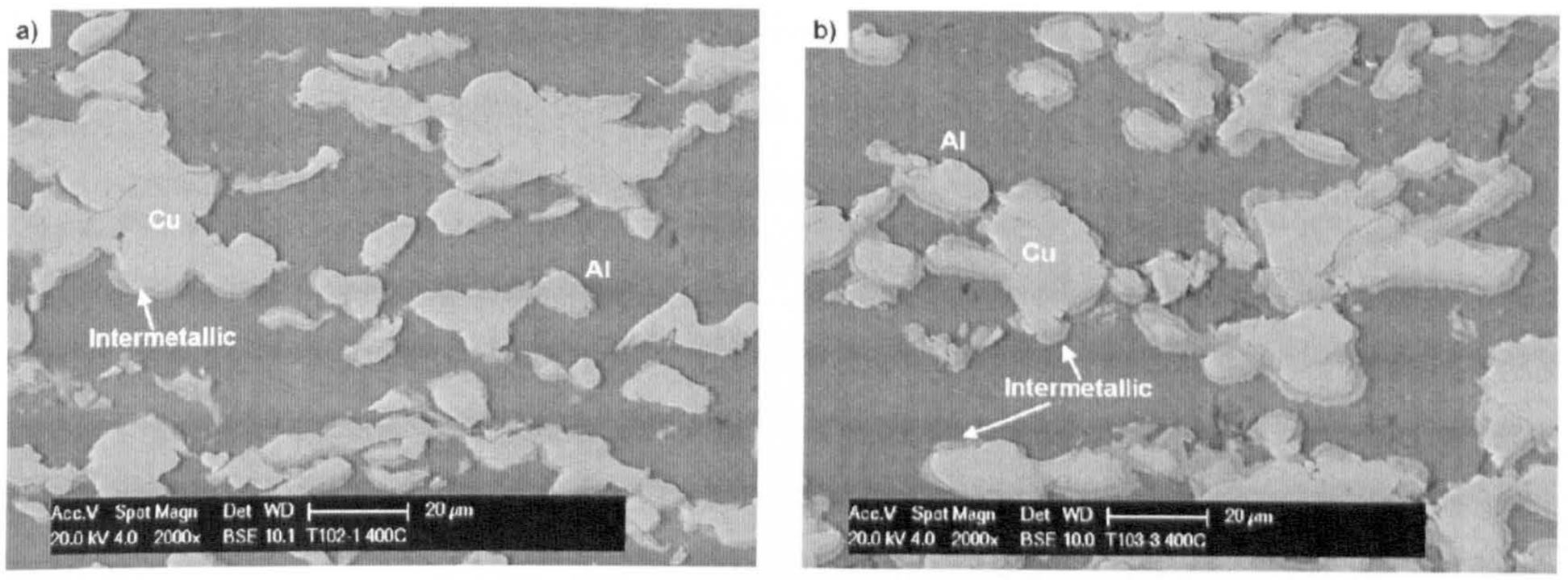

Figure 4.34 – BSE images of the heat treated Al-Cu deposits which were sprayed using helium gas at a pressure of (a) 15 bar and (b) 29 bar showing Cu, bright, Al, dark, and an intermetallic layer of grey contrast at the interface. Spray direction top to bottom.

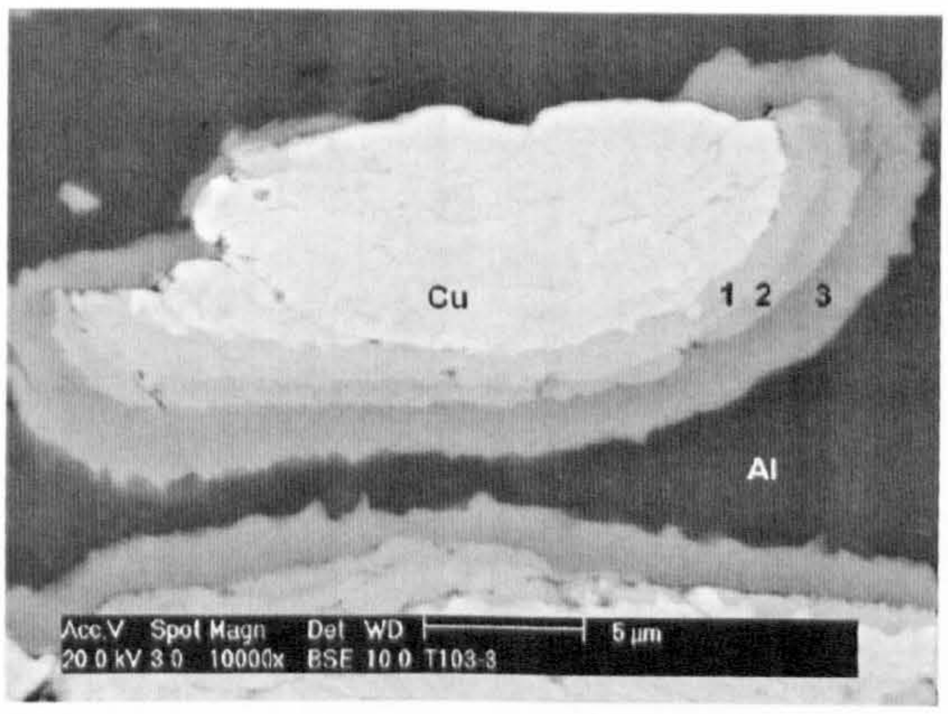

Figure 4.35 – BSE image of the heat treated Al-Cu deposit sprayed at 29 bar at high magnification showing Cu, bright, Al, dark, and three distinct intermetallic layers at the interface. Spray direction top to bottom.

Quantitative measurements with ImageJ, as described in Section 4.8.4., showed a significant difference between the deposits produced at the two different gas pressures following heat treatment. At 15 bar primary gas pressure, the average intermetallic layer thickness was found to be 1.1 ± 0.1 μm and the fraction of the interface length covered with intermetallic was 0.44 ± 0.05. For the 29 bar primary gas pressure, the corresponding values for thickness and fractional coverage were 2.0 ± 0.1 μm and 0.74 ± 0.05 respectively; a significant increase compared with the deposits made at 15 bar. It was also found that the development of the intermetallic layer did not depend on interface orientation with respect to the impact direction.

4.9.2.3. Porosity Measurements

Porosity in cold spray deposits of aluminium, copper and titanium was identified by SEM; image analysis of the porosity was carried out to yield the porosity volume fractions and aspect ratios. Porosity measurements were made on these three deposit types as this information was required for subsequent Eshelby analysis relating to modelling of the coating stiffness. Typical microstructures, polished and unetched, for titanium deposits are shown in Figure 4.32(b) and for aluminium and copper deposits in Figure 4.36(a) and (b) respectively. Pores, shown as dark areas, are randomly distributed within the coatings. The copper coating appears to have significantly lower levels of porosity and other defects than the other two coating types.

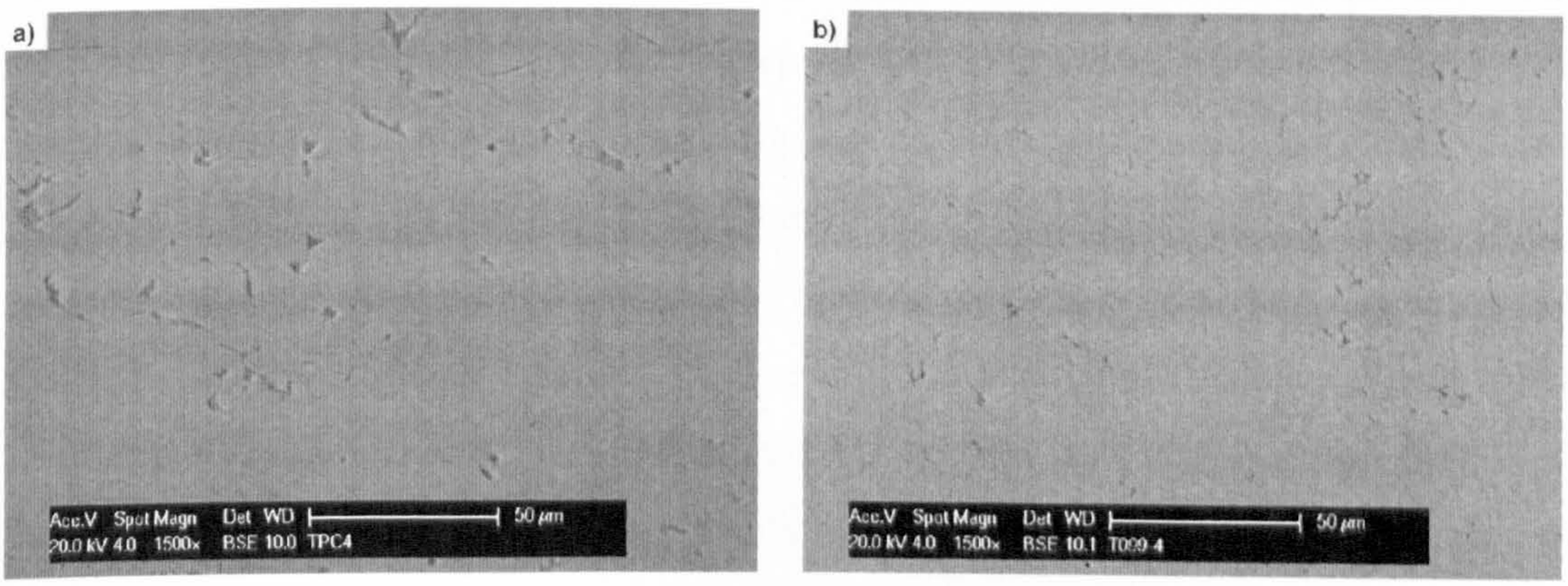

Figure 4.36 – BSE images showing typical (a) aluminium and (b) copper microstructures. Spray direction top to bottom utilising helium gas at room temperature and a stagnation pressure of 29 bar.

Measurements of porosity were made and the mean porosity measured over the nine images, along with the standard error in the mean for the three coating types is shown in Table 4.9. Also shown in Table 4.9 are measurements of the coatings modulus, described in the next section, and the effect of post-spray heat treatment on the titanium coatings porosity and modulus, described in Section 4.9.3.

Coating	Heat Treatment	Young's Modulus of Coating (E_c) / GPa	Young's Modulus of Bulk Material (E_b) / GPa	Modulus Ratio (E_c / E_b)	Pore Volume Fraction
Aluminium	-	11 ± 1.0	67	0.16	0.031 ± 0.0016
Copper	-	52 ± 1.0	128	0.41	0.060 ± 0.0004
Titanium	-	20 ± 0.7	120	0.17	0.045 ± 0.0046
Titanium	400 °C	18 ± 1.0	120	0.15	0.033 ± 0.0048
Titanium	600 °C	16 ± 1.0	120	0.13	0.037 ± 0.0030
Titanium	800 °C	17 ± 1.1	120	0.14	0.036 ± 0.0026
Titanium	1150 °C	43 ± 0.9	120	0.36	0.056 ± 0.0084

Table 4.9 – Modulus and porosity measurements of the various cold spray coatings and the corresponding error of the mean are shown. Bulk modulus values are given from the metals handbook for titanium in a non-heat treated state [13].

The normalised volume fraction of pores as a function of their aspect ratio for each of the coatings deposited is shown in Figure 4.37(a) with the standard error of the mean. Finally, the cumulative normalised volume fraction of pores with different aspect ratios measured within the three coatings deposited in this study is shown in Figure 4.37(b). It is shown that pores of aspect ratio 0.1 or less were only detected as minimal volume fractions using this analysis method, and pores of aspect ratio 0.2 or less account for only 5% or less of the total pore volume found within the deposits. The majority of pores are found to have an aspect ratio of approximately 0.3 or greater. Unlike the aluminium and copper coating microstructures, boundaries between individual powder particles within the titanium coating can be clearly seen. Defects and individual particles are not as readily apparent within the aluminium and copper coatings. Defects surrounding the individual titanium splats indicate poor bonding within the coating and suggest that, on impact, there was a smaller degree of particle deformation in the titanium deposits when compared to the aluminium and copper deposits.

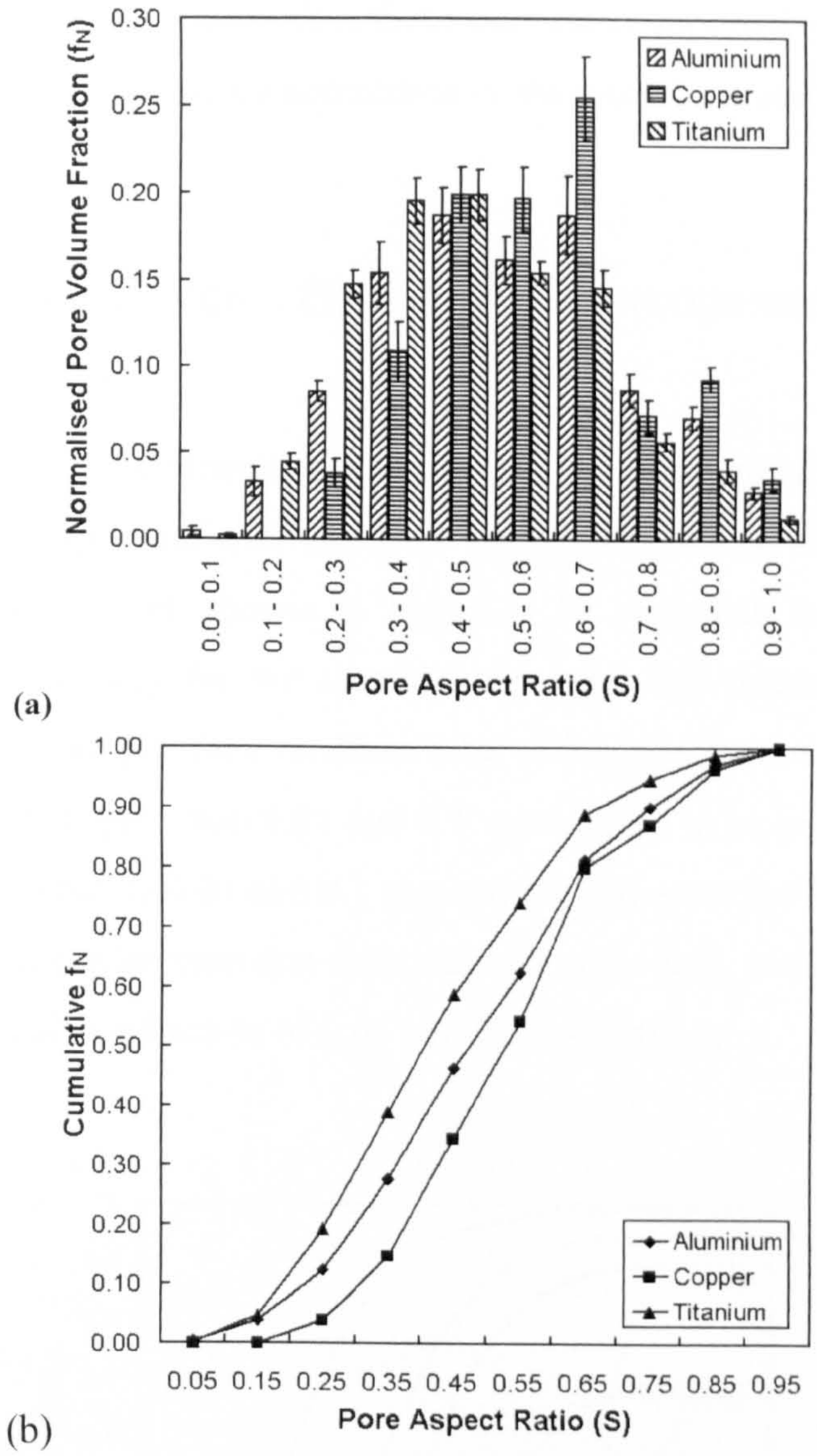

Figure 4.37 - (a) Normalised pore volume fraction (f_N) (calculated as the volume fraction of a specific volume fraction divided by the total volume fraction) as a function of pore aspect ratio and (b) cumulative normalised pore volume fraction as a function of pore aspect ratio.

4.9.2.4. Coating Stiffness

Modulus testing was carried out on the cold spray coatings and results are shown in Table 4.9 with the standard error of the mean. The bulk modulus values for the materials [13] and the corresponding modulus ratios are also reported. A significantly higher modulus ratio (0.41) was found for the copper coatings than for the aluminium and titanium coatings (0.16 and 0.17 respectively). Table 4.9 shows that the measured titanium modulus ratio is in close agreement with results from previous literature. The aluminium and copper coatings modulus ratios, measured in

this study, exhibited lower values than those previously reported in the literature for cold spraying; reasons for this are considered in the discussion section.

4.9.2.5. Eshelby Equivalent Homogeneous Inclusion Model

Using equation 4.14, the elastic modulus ratio of a porous material was calculated as a function of pore aspect ratio, *S*, and pore volume fraction, *f*, as shown in Figure 4.38. The horizontal lines shown in Figure 4.38 represent the modulus ratios determined experimentally for the aluminium, copper and titanium deposits. This illustrates that, for example, for a modulus ratio of 0.4, (i.e. that measured for copper deposits), defects of aspect ratio 0.01 and 0.1 would have to be present with volume fractions of approximately 0.01 and 0.1 respectively, whereas for the aluminium and titanium deposits it can be seen that defect aspect ratios 0.01 and 0.1 would have to be present with a volume fraction of 0.05 and 0.3 respectively.

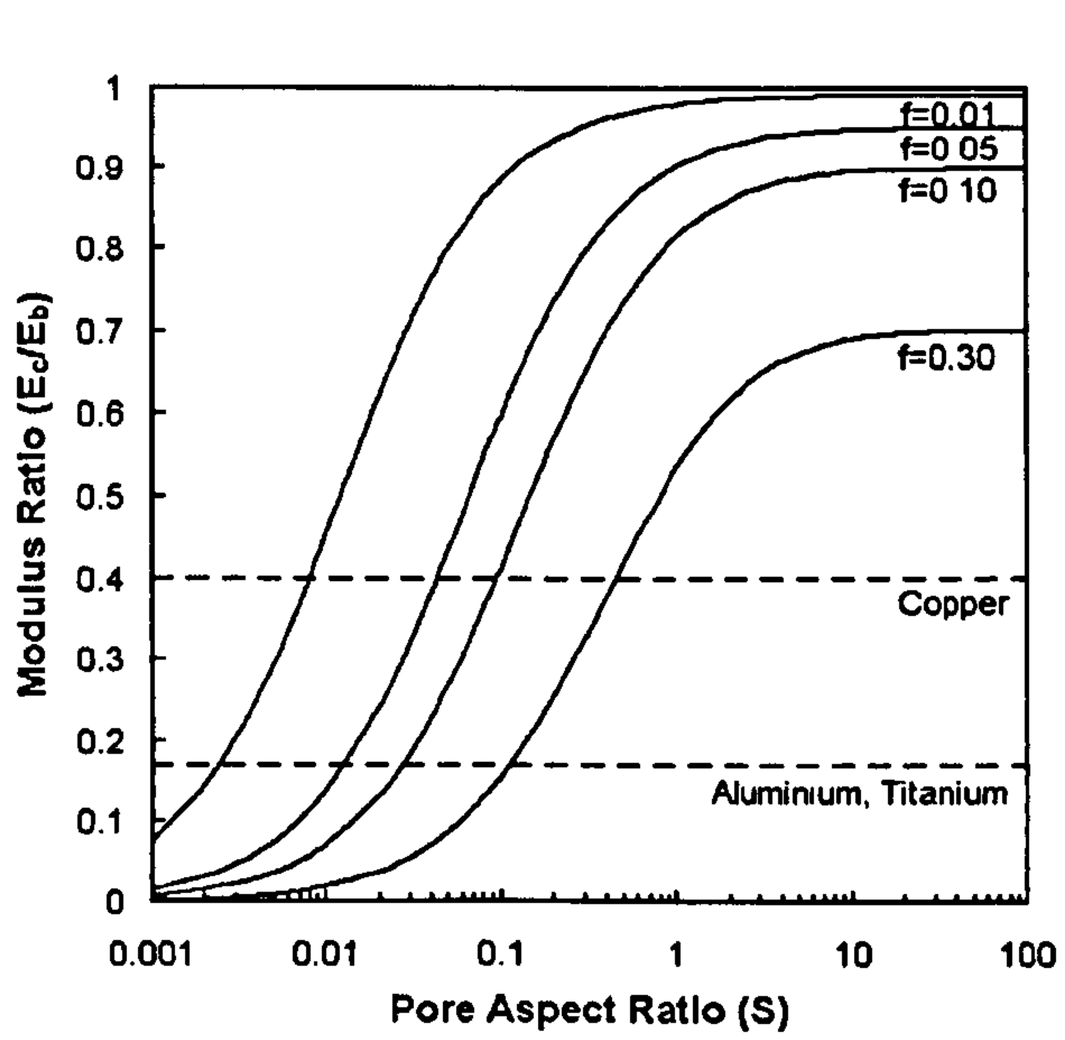

Figure 4.38 – Effect of defect aspect ratio, S, on modulus ratio for defect volume fractions, f, of 0.01, 0.05 and 0.10. Horizontal lines indicate the experimentally measured modulus ratios for the aluminium, copper and titanium deposits.

In both cases this is significantly greater than the measured porosity in the respective aspect ratio ranges, as shown in Table 4.9 and Figure 4.37. Note that in this model, all defects are assumed to be orientated with the *x*-axis parallel to the substrate-

coating interface and the aspect ratio is defined as x/y as shown in Figure 4.11; the most detrimental defect orientation in terms of the predicted Young's modulus reduction. In reality defects of many orientations would exist. As the defect aspect ratio falls below unity, the defect more closely resembles a through-thickness crack and as the aspect ratio increases above unity, the defect more closely resembles a crack in the plane of the coating.

4.9.2.6. Coating Bond Strength

The coating bond strength was assessed by two main methods; i) hand operated pull-off test and ii) transverse scratch testing (Section 4.8.7.). For the pull-off test method a significant number of samples were found to show resin failure, as opposed to coating failure, at applied tensile strengths of up to 80 MPa. This indicates that the coating bond strength is expected to be greater than this measured value. This value exceeds the required tensile strength of HA coatings, 50.8 MPa [9, 21].

An alternative method, transverse scratch testing, allows a qualitative understanding of the bonding process to be obtained. Figure 4.39 shows OM images of scratches made on a cross section sample of a titanium coating deposited onto a Ti6Al4V substrate with as-received and grit blasted surface finishes with applied loads of 10 N and 70 N. For both surface finishes some cracking within the coating has been observed when a load of 10 N is applied and shown in Figure 4.39(a) and Figure 4.39(c). At the higher load of 70 N, cracks formed within the coating are larger and longer. Furthermore, delamination at the coating substrate interface is found for both substrate surface finishes. The amount of delamination found for the grit blasted substrate (Figure 4.39(d)) is less than that observed for a substrate with an as-received surface finish (Figure 4.39(b)). This indicates that bonding between the substrate and coating is greater when a grit blasted substrate is used. Delamination between the substrate and coating is first observed to have occurred after a load of 20 N was applied for both substrate surface finishes. In contrast, for copper deposits, application of normal loads of both 10 N and 70 N in the transverse scratch test caused minimal cracking and debonding to occur at the interface and within the

coating itself (Figure 4.40(a) and (b)), indicating a high level of bonding within the coating and at the substrate-coating interface.

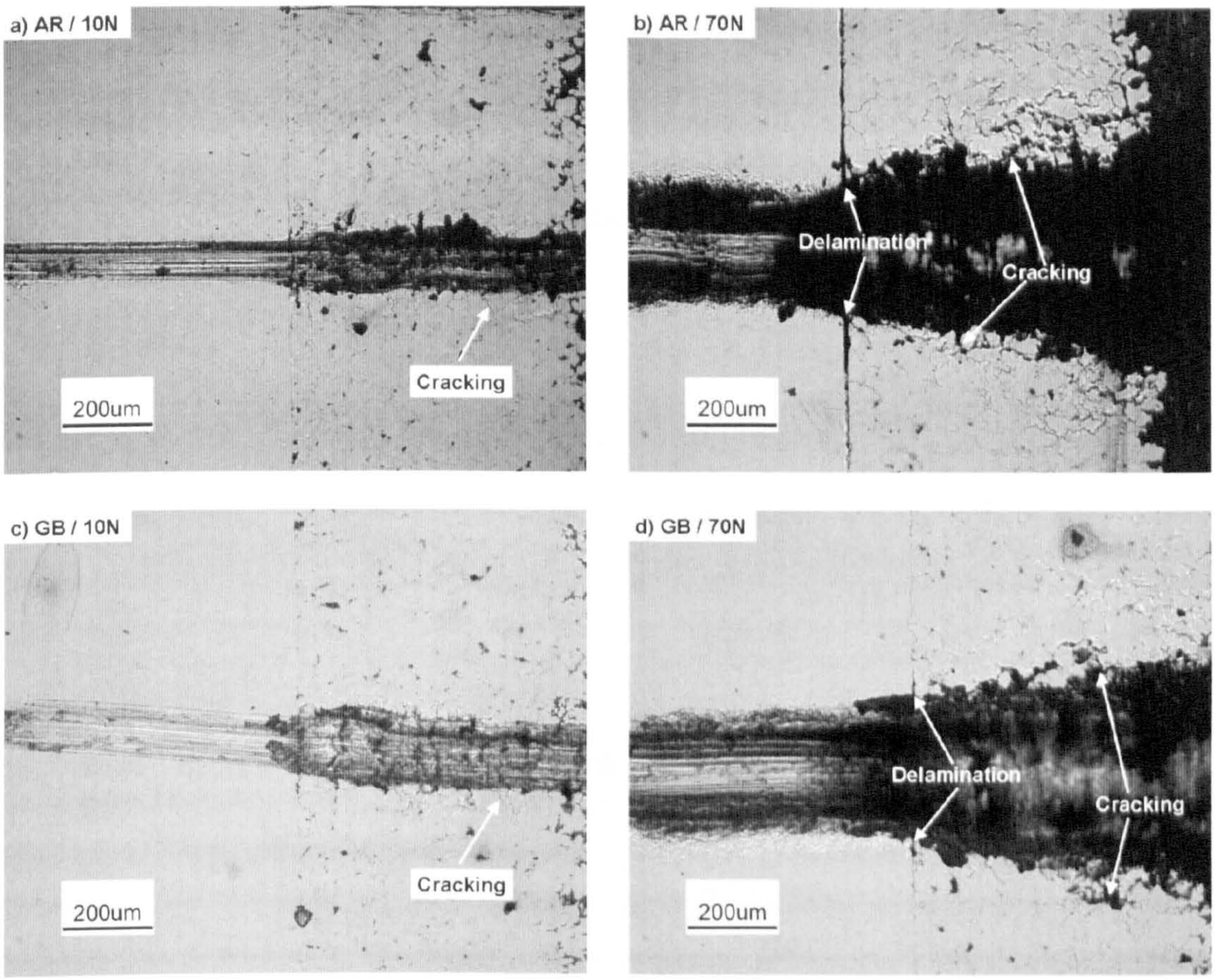

Figure 4.39 – OM images showing transverse scratches for titanium deposits onto a Ti6Al4V substrate with, (a) and (b), an as-received (AR) surface finish and, (c) and (d), a grit blasted (GB) surface finish generated by applied loads of 10 N and 70 N as indicated by each image. Scratch direction is from substrate into the coating (left to right). The coating was deposited using helium as the primary gas at room temperature and a stagnation pressure of 29 bar.

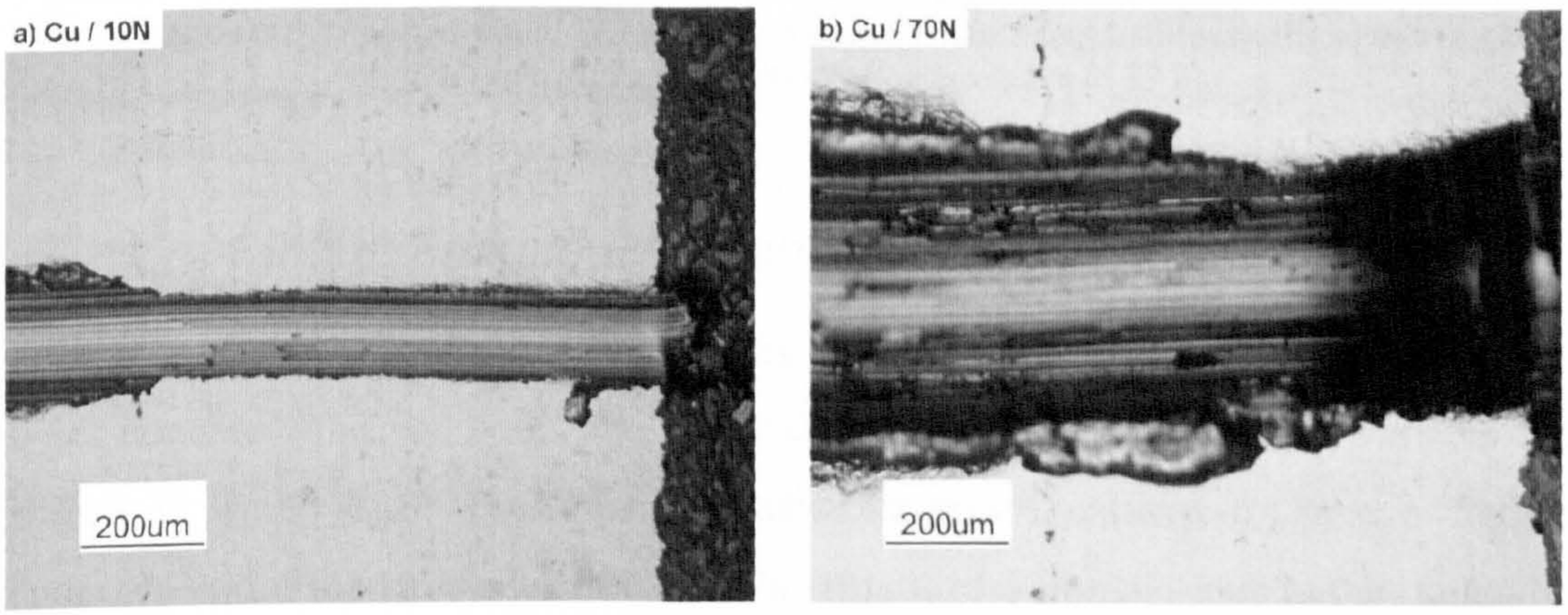

Figure 4.40 – OM images showing transverse scratches for copper deposits onto a copper substrate with an applied load of (a) 10 N and (b) 70 N. Scratch direction is from substrate into the coating (left to right). The coating was deposited using helium as the primary gas at room temperature and a stagnation pressure of 29 bar.

4.9.2.7. Coating Hardness

The micro-hardness of the titanium coating was found to increase as the distance from the coating-substrate interface decreased. Results are shown in Figure 4.41. At the top surface of the coating, the hardness of the coating is measured as 80 kgf mm^{-2} and increases to 340 kgf mm^{-2} close to the coating-substrate interface. This is higher than the hardness value of bulk pure titanium generally quoted as 200 – 265 kgf mm^{-2} as shown in Table 4.2.

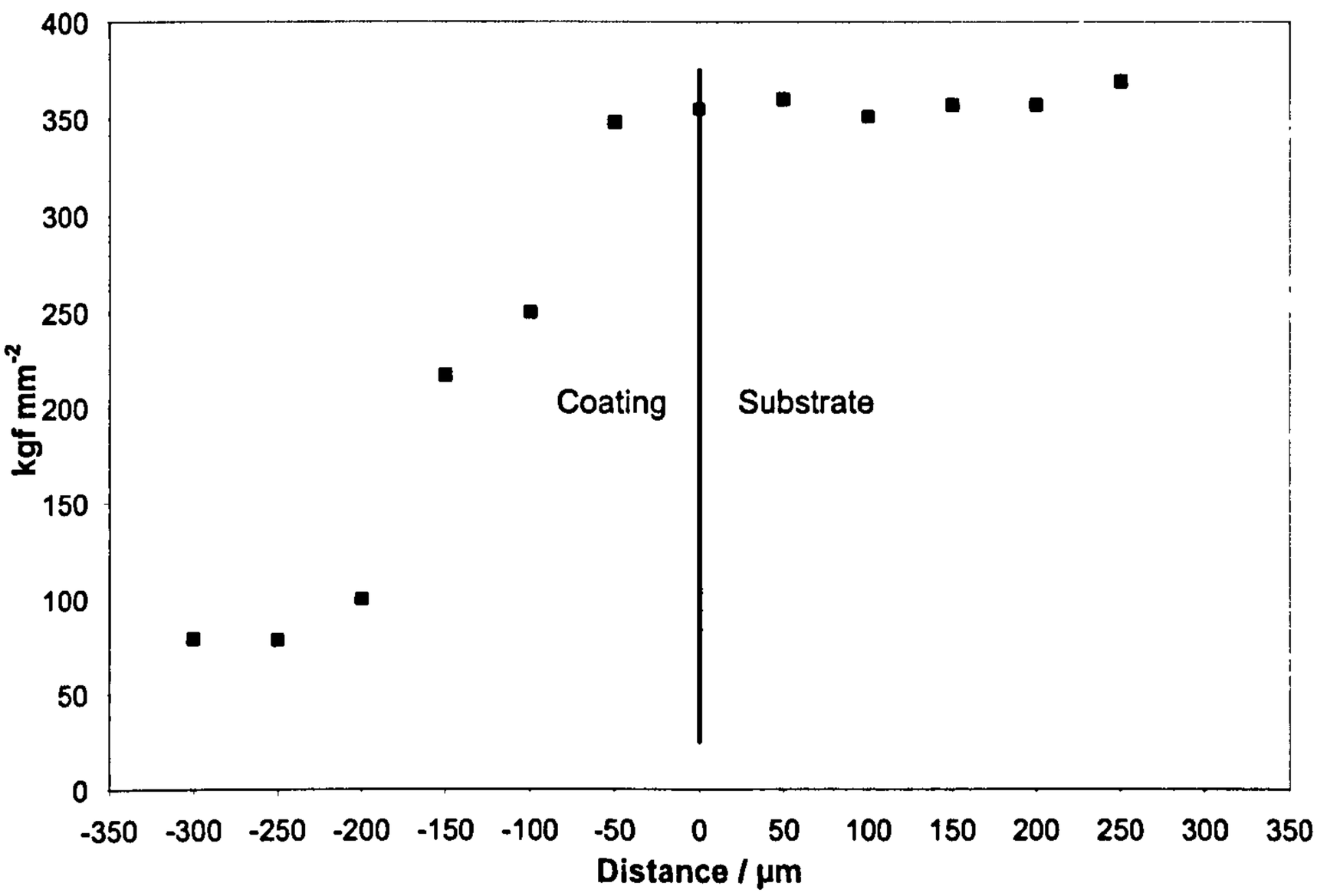

Figure 4.41 – Titanium coating hardness deposited onto a Ti6Al4V substrate as a function of distance from the coating-substrate interface. The coating hardness increases as the coating-substrate interface is approached. The coating was deposited using helium as the primary gas at room temperature and a stagnation pressure of 29 bar.

4.9.2.8. Fatigue Endurance Limit

Fatigue endurance limits after 10^7 cycles as a function of substrate surface finish type, uncoated and for both cold sprayed and shrouded arc sprayed samples are shown in Table 4.10. The Ti6Al4V substrate was measured to have a fatigue endurance limit for 10^7 cycles of 633 MPa. This is of a similar value to that found by previous workers for a Ti6Al4V substrate with an approximate grain size of 10 µm (Figure 4.12). Table 4.10 shows that both grit blasting and cold spraying have a significant effect on the fatigue endurance limit. A 15 % reduction in the fatigue

endurance limit was observed after application of the coating to the as-received substrate. A 20 % reduction was observed after grit blasting an as-received substrate; this is attributed to the grit blasting process producing surface stress raisers. It is clearly shown that both grit blasting and cold spraying has a significant effect on the fatigue endurance limit. However, when applying a cold sprayed coating to a grit blasted substrate surface, it is found that the fatigue endurance limit does not reduce further. Also shown in Table 4.10 are fatigue endurance limit results relating to cold sprayed coating subsequently heat treated and titanium coatings created by the shrouded arc spray process. These results are described in Sections 4.9.3. and 4.9.4. respectively.

Coating Type	Heat Treatment	Surface Finish	Fatigue Endurance Limit at 10^7 cycles / MPa
Substrate Only	-	AR	633 ± 20
Substrate Only	-	GB	507 ± 28
Substrate Only	-	GB (Industrial Partner)	418 ± 1
Cold Sprayed	-	AR	537 ± 8
Cold Sprayed	-	GB	512 ± 13
Shrouded Arc	-	GB (Industrial Partner)	< 182
Substrate Only	800 °C	AR	345 ± 9
Substrate Only	1150 °C	AR	262 ± 5
Cold Sprayed	800 °C	AR	217 ± 5
Cold Sprayed	1150 °C	AR	200 ± 5

Table 4.10 – Fatigue endurance limits after 10^7 cycles for as-received (AR) and grit blasted (GB). Results for as-received samples are shown for the non-heat treated and heat treated state. The standard error of the mean is also shown.

4.9.2.9. Analysis of Fracture Surfaces

Figure 4.42(a) shows the fracture surface of an as-received sample. It is possible to identify the structural features commonly observed in fatigue fractures; these are, slip band formation, stage I and stage II crack growth [136]. Fatigue fractures normally originate at the surface and it is possible for multiple initiation sites of fractigue fractures to be present. Cracks generated proceed along grain boundaries and this is known as stage I crack growth. Stage I crack growth generally occurs within the first few thousand cycles of stress. Successive cycles produce additional

slip bands, but the number of slip bands is not directly proportional to the number of cycles of stress. Stage I crack growth normally only extends over a few grain diameters before crack propagation changes to Stage II. The rate of crack propagation in Stage I is generally very low, (angstroms per cycle), compared to the rate of propagation in Stage II crack growth, usually microns per cycle [136]. Therefore the surface of Stage I fractures are practically featureless as shown in Figure 4.42(b). In Stage II crack growth, a pattern of ripples or fatigue fracture striations is produced as shown in Figure 4.42(c). Each striation represents one complete cycle and the advancement of a crack normal to the greatest tensile stress [136]. Eventually the crack will become so long that the remainder of the cross sectional area of the specimen is unable to support the cyclic load and will also fail.

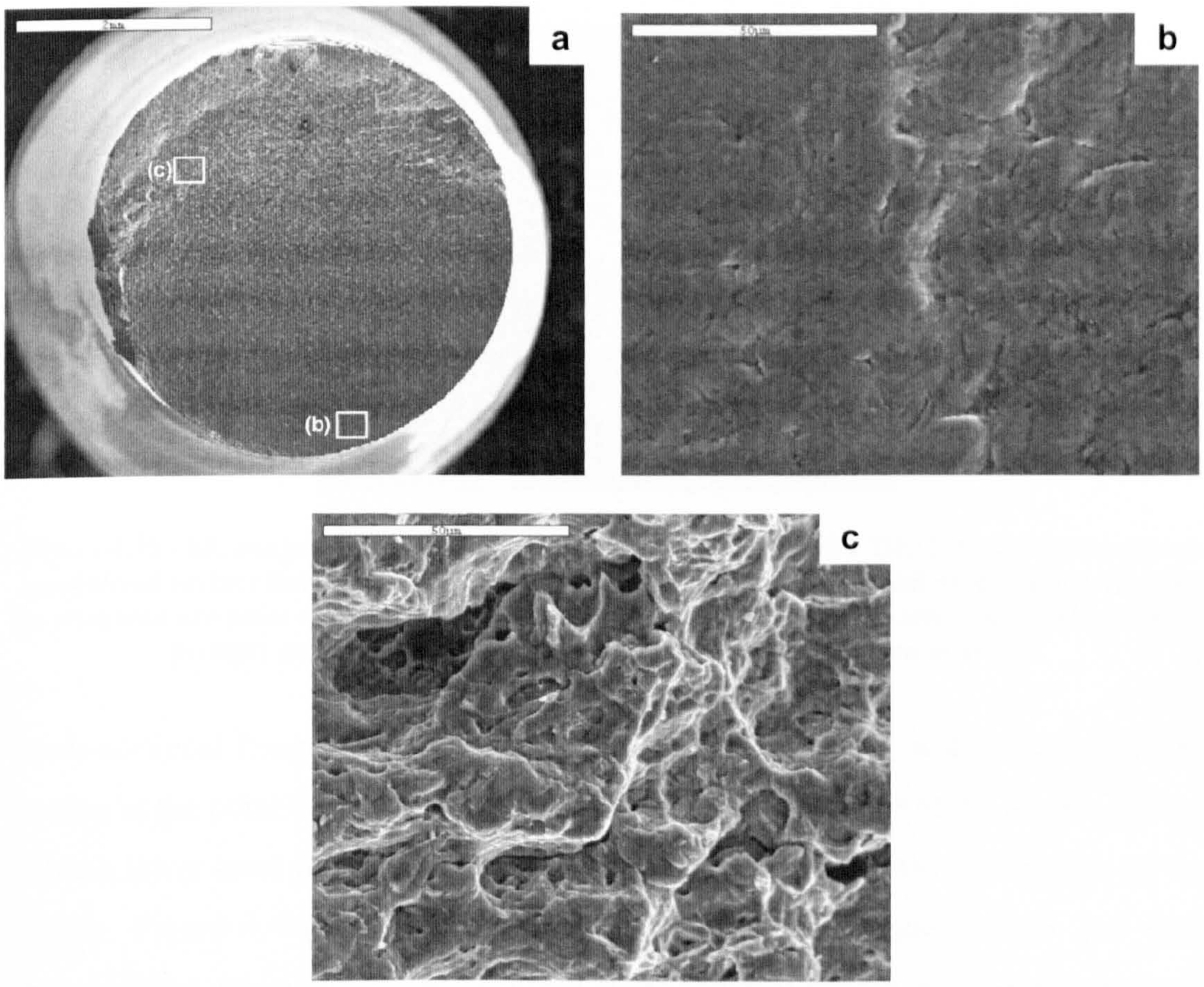

Figure 4.42 – SE image showing the (a) fatigue fracture surface of the Ti6Al4V substrate with an as-received surface finish and; (b) higher magnification of Stage I crack growth and (c) Stage II crack growth. The coating was deposited using helium as the primary gas at room temperature and a stagnation pressure of 29 bar.

Figure 4.43(a) shows the fatigue fracture of an as received and cold sprayed sample. There appears to be little deformation to the coating itself at the point of initial

fracture, shown in Figure 4.43(b), and the coating appears well bonded to the substrate. In contrast, in the regions associated with final the final fracture, the coating was seen to have debonded from the substrate as shown in Figure 4.43(c).

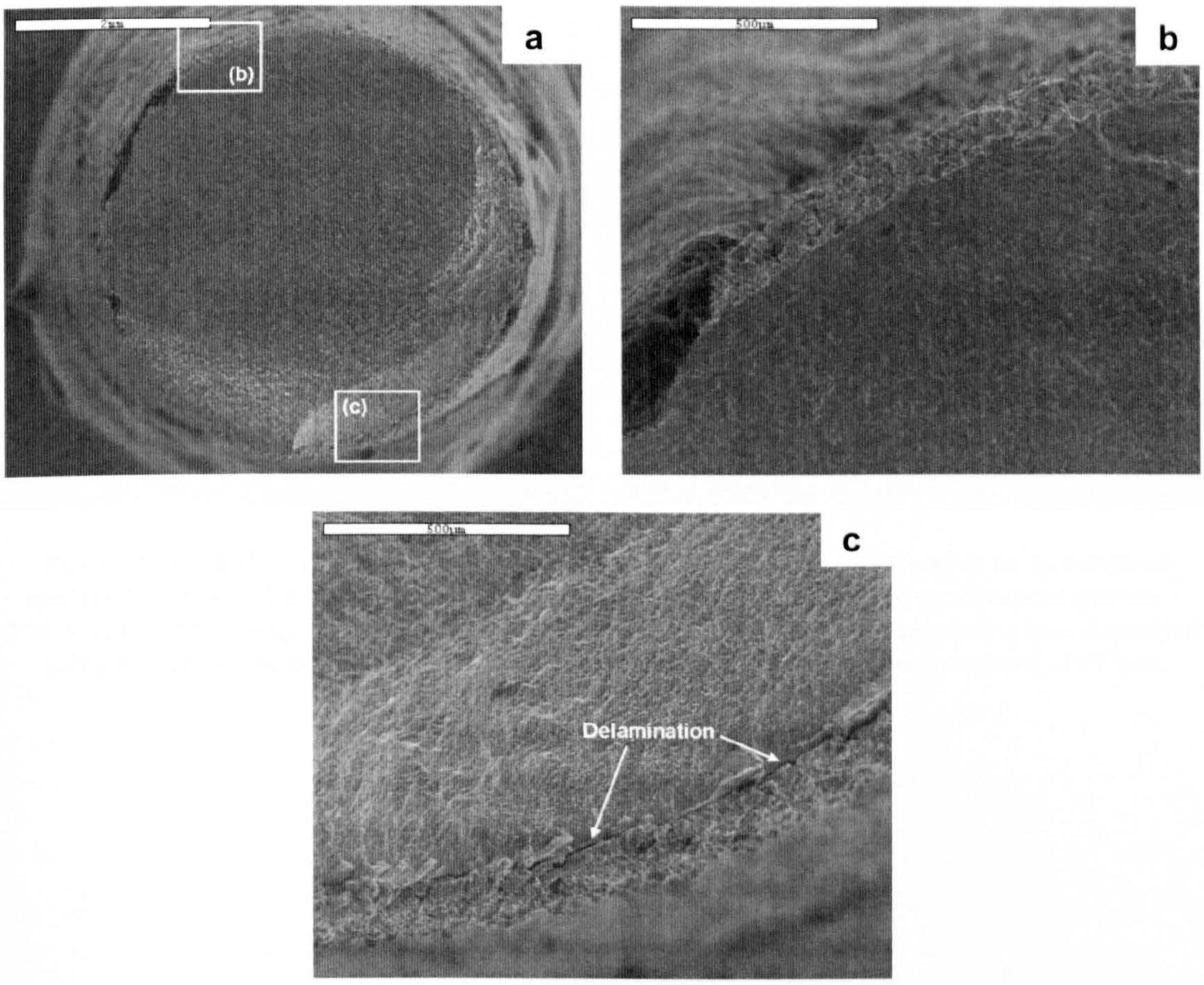

Figure 4.43 – SE image showing the (a) fatigue fracture surface of a Ti6Al4V substrate with an as-received surface finish and cold sprayed titanium coating and; (b) initial fracture point and (c) final fracture point and coating delamination. The coating was deposited using helium as the primary gas at room temperature and a stagnation pressure of 29 bar.

Cross-sectional images of these samples show the difference in degradation of the coating at the point of fatigue fracture and close to the shoulder of the sample, where a much lower level of alternating stress is experienced due to the dimensions of the sample. Figure 4.44(a) is an image taken close to the fatigue fracture and it is observed that delamination has occurred along the coating-substrate interface, along with cracking within the coating itself. In contrast Figure 4.44(b) is an image taken close to the shoulder where significantly less coating degradation has occurred.

Grit blasted and cold sprayed samples showed similar structural features to the as-received and cold sprayed samples. However, coating delamination was found close

to the initial point of fracture and shown in Figure 4.45. This is in contrast to the coating sprayed onto the as-received substrate (Figure 4.43(b)) and may be due to the stress raisers at the substrate surface, which increase the likelihood of crack formation and coating delamination.

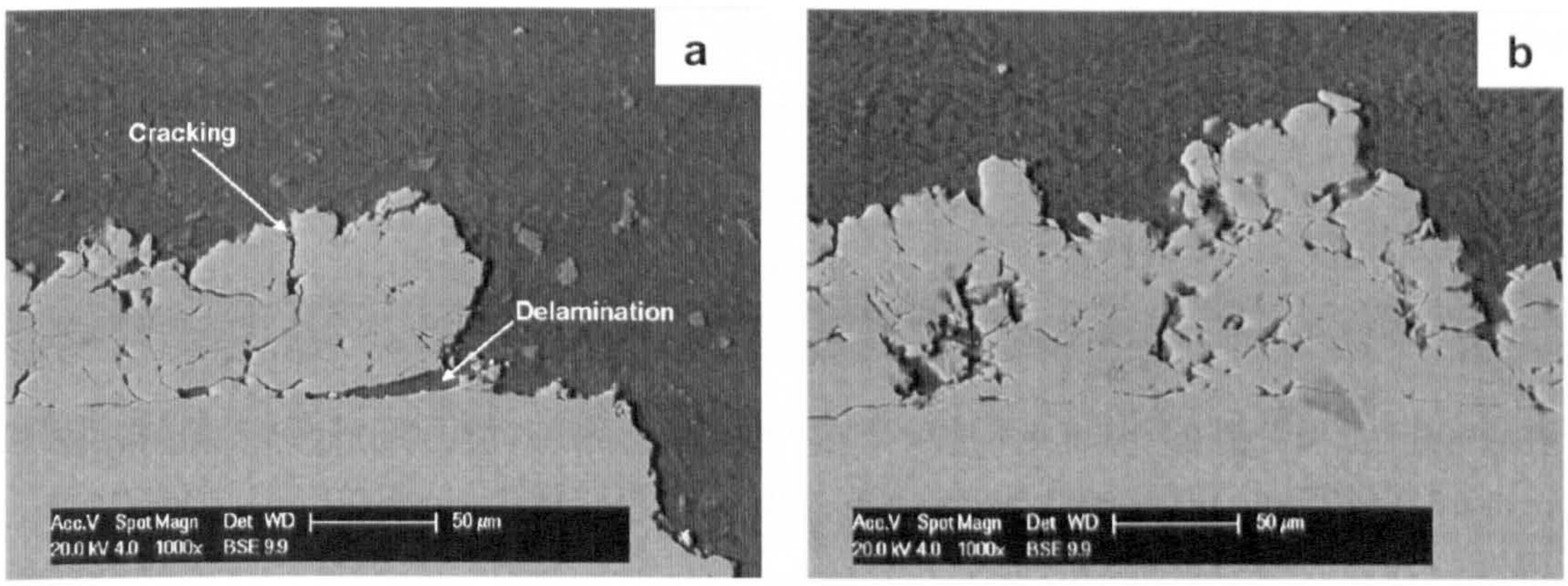

Figure 4.44 – BSE images of the cross-section of the Ti6Al4V substrate with an as-received surface finish and the titanium cold sprayed coating (a) close to the fatigue fracture (Stress = 570 MPa) and (b) away from the fatigue fracture (stress = 190 MPa). The coating was deposited using helium as the primary gas at room temperature and a stagnation pressure of 29 bar.

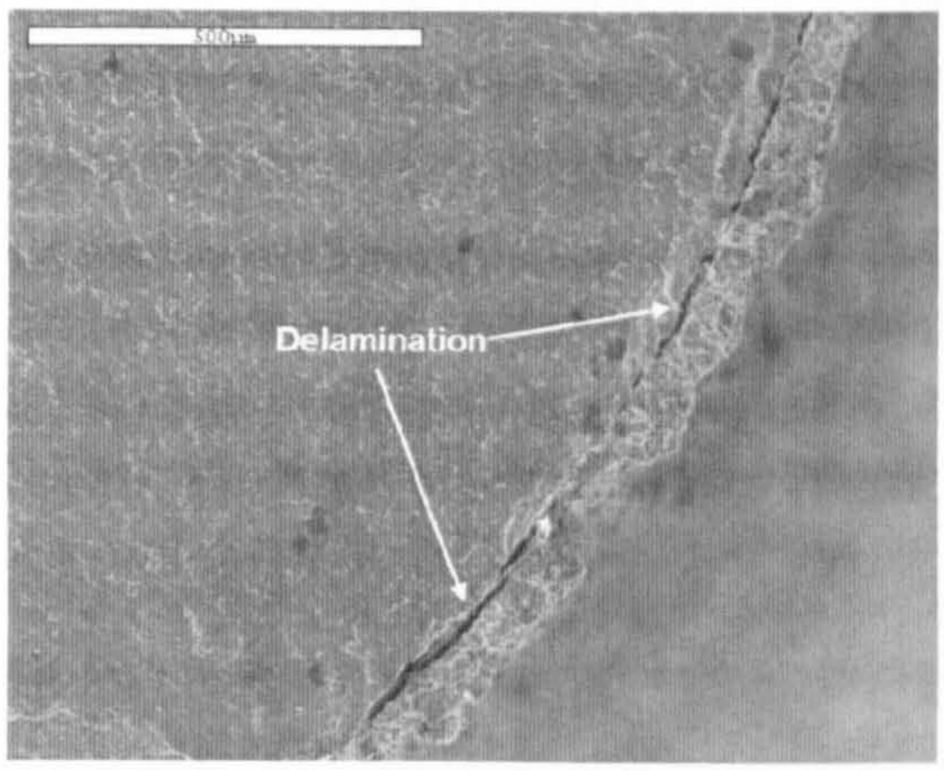

Figure 4.45 – SE image showing initial fracture surface of the grit-blasted Ti6Al4V substrate and the titanium coating. The coating was deposited using helium as the primary gas at room temperature and a stagnation pressure of 29 bar.

4.9.2.10. Residual Stresses within Deposits

From previous literature, Section 4.6.6., it has been shown that residual stresses within cold spray deposits are expected to be low in magnitude, which tends to result in low accuracy in measurement of such stresses. The suitability of XRD testing was evaluated for the measuring of residual stresses within cold spray deposits using a

small four point bend test rig (Section 4.8.10.1.). The XRD recorded an applied stress (between the strained and no known strain applied positions) of 115 MPa compared to 100 MPa measured by strain gauges. The variation between the measured induced stress between the XRD and strain gauges is believed to be within the error of the measuring process. However, when carrying out XRD stress analysis on the top surface of titanium cold sprayed deposit and Ti6Al4V substrates, the residual stress values measured were lower than the errors generated by the analysis equipment. Furthermore, this technique only allowed the top surface of the deposit, which tends to have high levels of porosity, to be analysed. To measure residual stresses within the coating, part of the coating would require removal until the area where analysis was to be carried out was left exposed. Electro polishing is typically used for this as it is known to induce minimal stresses within the sample. However, on attempting to electro polish the titanium cold spray deposits, inhomogeneous removal of the coating material occurred due to the polishing process preferentially removing material at particle boundaries.

The induced specimen bending method (Section 4.8.10.2.) is a simpler method by which to measure the residual stresses and allows average residual stresses within the coating to be evaluated without the need for machining or polishing of the sample. The form of the underside of the substrate surface (i.e. the face not being coated) is measured before and after spraying, which allows the deflection of the substrate due to spraying to be calculated. Measured results can then be fitted to a circle of known radius and an example of this is shown in Figure 4.46. Using the known radius of curvature, the residual stresses within the deposits are calculated (Section 4.8.10.2.). Residual stress measurements for titanium coatings deposited onto a Ti6Al4V substrate with an as-received and grit blasted surface finish are summarised in Table 4.11. Stresses within the cold spray coatings are found to be small and compressive; accordingly, tensile stresses are expected in the substrate close to the coating substrate interface. Also shown in Table 4.11 are measured residual stress values for cold sprayed coating subsequently heat treated and titanium coatings created by the shrouded arc spray process. These results are described in Sections 4.9.3. and 4.9.4. respectively.

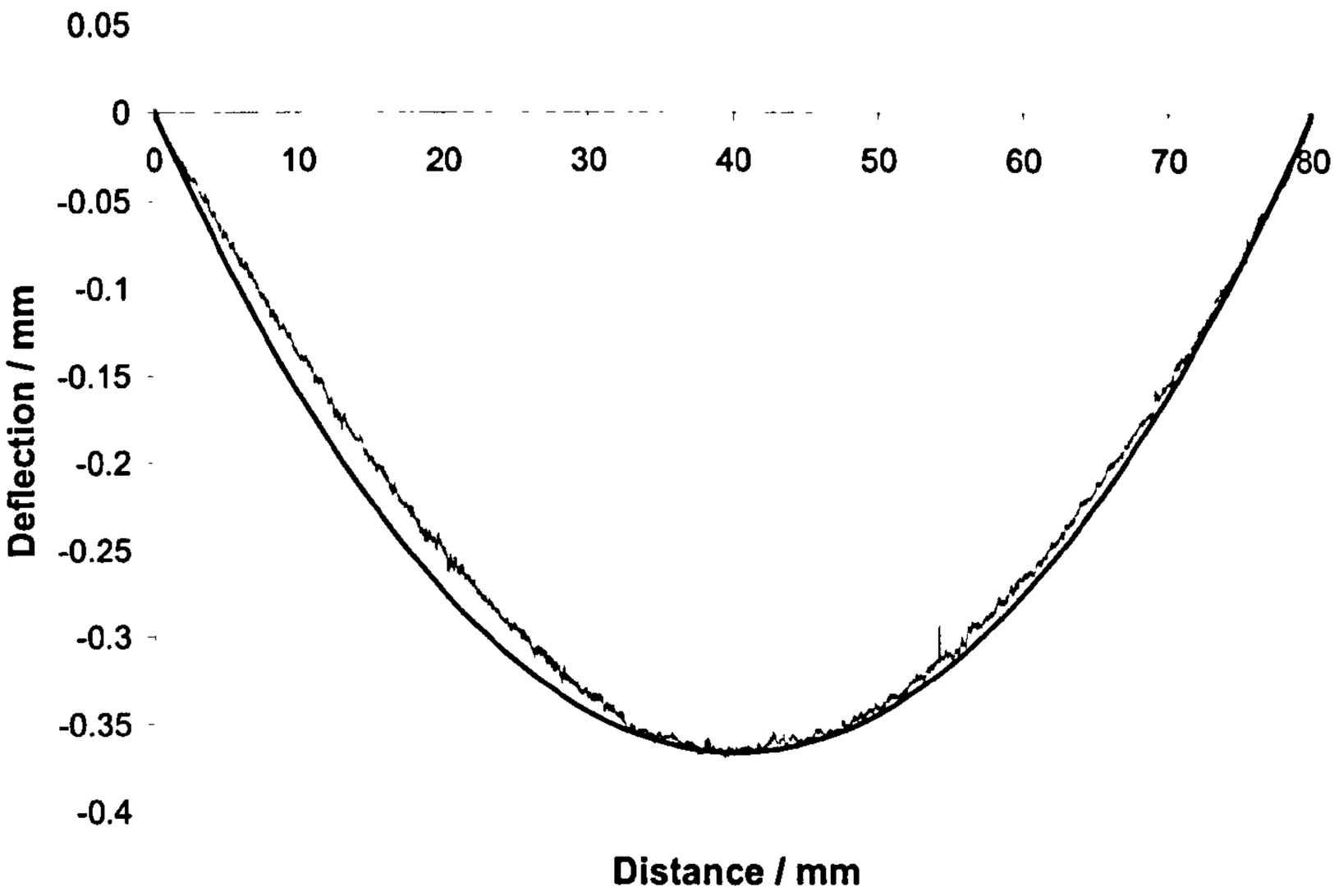

Figure 4.46 – A typical measured amount of Ti6Al4V substrate deflection due to a titanium cold spray deposit (grey line) and fitted to a curve of radius R (black line).

Coating Type	Heat Treatment	Surface Finish	σ_c at y = 0	σ_c at y = h	σ_s at y = h
CS	-	GB	-10	-13	+21
CS	-	AR	-25	-32	+52
CS	400 °C	AR	-10	-12	+17
CS	600 °C	AR	-7	-8	+11
CS	800 °C	AR	-5	-6	+9
CS	1150 °C	AR	-5	-6	+9
SA	-	GB (Industrial Partner)	+45	+65	-84

Table 4.11 – Measured residual stresses within the titanium cold sprayed coating (CS) and shrouded arc coatings (SA). Residual stresses are calculated for the coating (σ_c) and Ti6Al4V substrate (σ_s) for a grit blasted (GB) and as-received (AR) surface finishes. Samples with an AR surface finish were also heat treated at 400 °C, 600 °C, 800 °C and 1150 °C for one hour respectively. Measurements are calculated at y = 0 (the coating top surface) and y = h (the coating-substrate interface). See Figure 4.28.

4.9.3. Effect of Heat Treatments on Titanium Cold Spray Deposits

Heat treatments were carried out on the titanium deposits to investigate their effect on coating properties. Heat treatments were carried out at 400 °C, 600 °C, 800 °C and 1150 °C for one hour as described in Section 4.8.11. The same mechanical tests (for

example coating stiffness, porosity, rotating bend fatigue endurance limit and residual stress measurement) that had been previously used on the non-heat treated samples were used to characterise the heat treated coatings.

4.9.3.1. Coating Microstructure

Figure 4.47 shows the titanium coating microstructure after heat treatments of (a) 400 °C, (b) 800 °C and (c) 1150 °C for one hour. Higher magnification images of the coating microstructure after each heat treatment are shown in Figure 4.48.

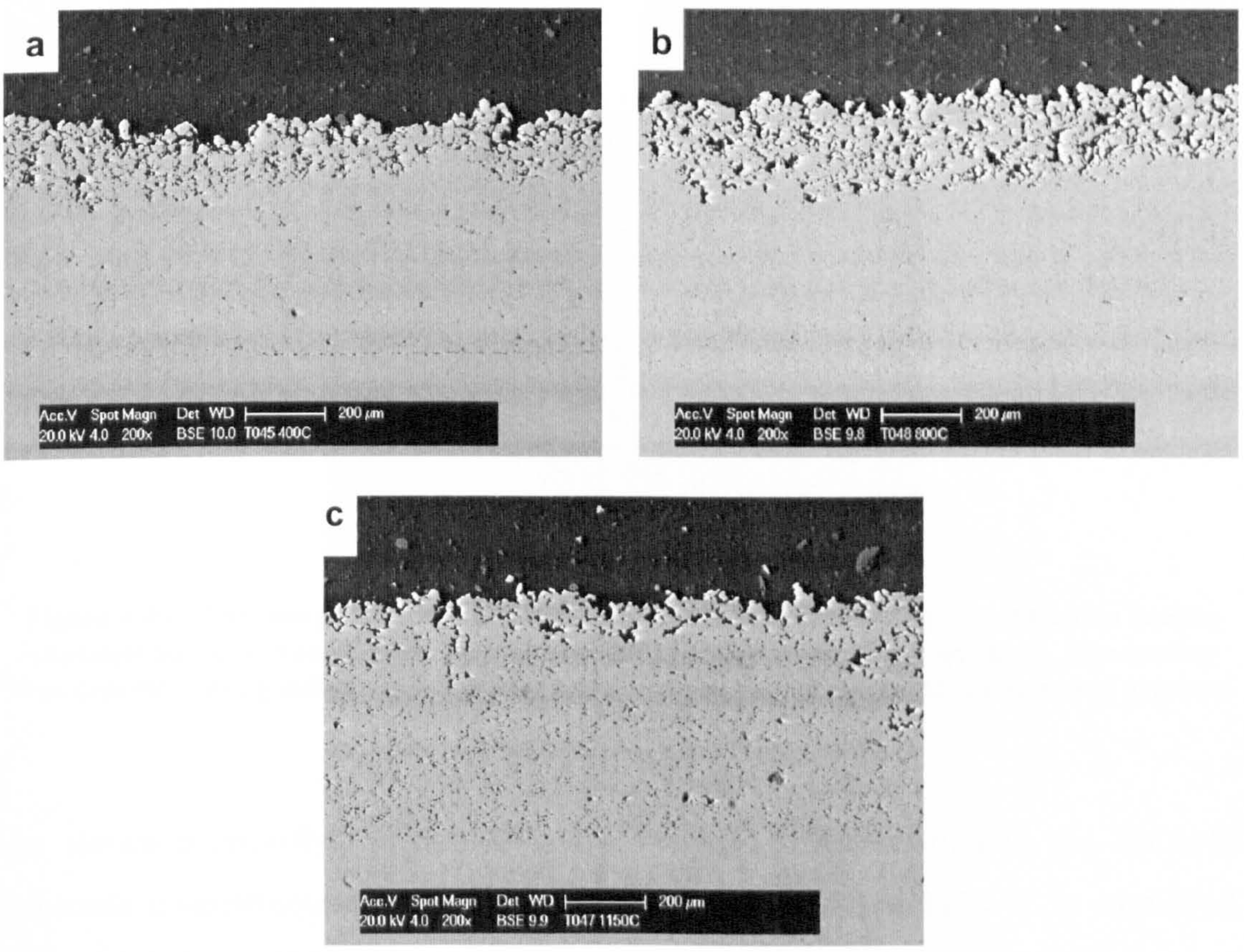

Figure 4.47 – BSE images of the titanium coating microstructure deposited onto a Ti6Al4V substrate and subsequently heat treated at (a) 400 °C, (b) 800 °C and (c) 1150 °C for one hour. The coating was deposited using helium as the primary gas at room temperature and a stagnation pressure of 29 bar.

It is found that there is minimal variation in the coating microstructure compared to the non-heat treated microstructure (Figure 4.32(b)) for heat treatments up to 800 °C (Figure 4.47(b)). After a heat treatment at 1150 °C, it becomes harder to identify individual particles as some of the defects that have been found previously, such as

interparticle boundaries, are no longer present. However, there also appears to be a greater amount of porosity of a more spherical nature and this is discussed in greater detail in the next section.

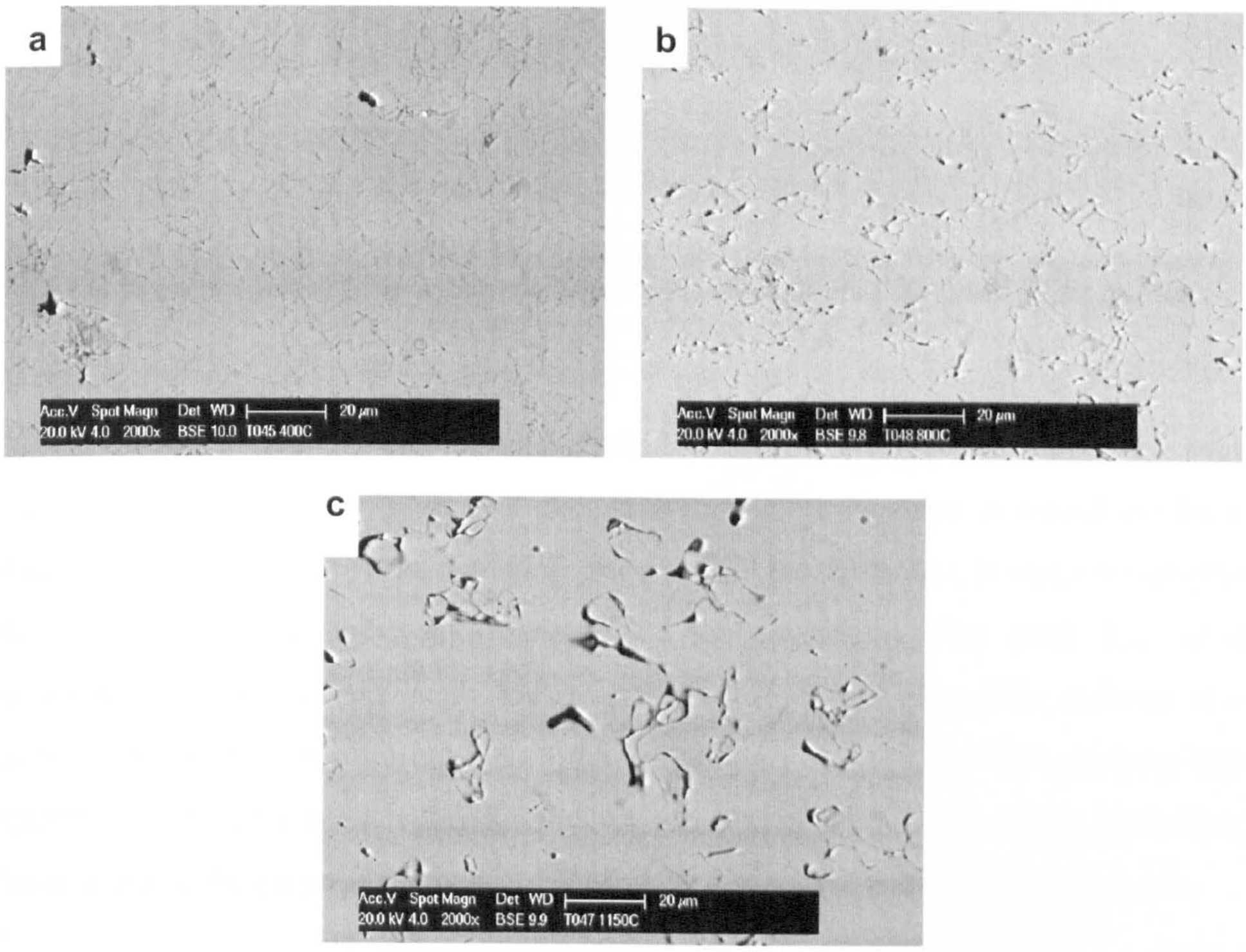

Figure 4.48 – BSE images showing the degree of inter-particle bonding for a titanium coating subsequently heat treated at (a) 400 °C, (b) 800 °C and (c) 1150 °C for one hour. The coating was deposited using helium as the primary gas at room temperature and a stagnation pressure of 29 bar.

As shown previously (Section 4.9.1.1.), there is little variation in the Ti6Al4V substrate microstructure until a heat treatment carried out at 1150 °C is employed. Figure 4.49 is an OM image of the etched coating substrate interface after being heat treated at 1150 °C for one hour. Growth of the grains from the substrate into the coating can be seen to have occurred and this was not observed for the other heat treatment temperatures.

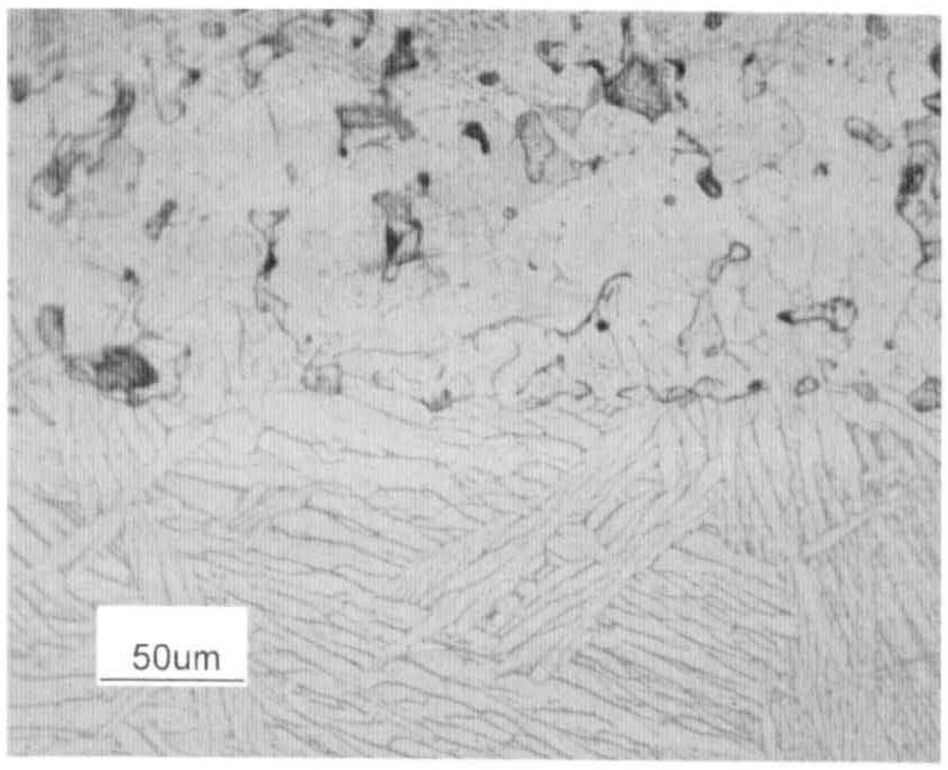

Figure 4.49 – OM image of the titanium coating / Ti6Al4V substrate after being heat treated at 1150 °C for one hour. The coating was deposited using helium as the primary gas at room temperature and a stagnation pressure of 29 bar.

Using EDX analysis, the amount of diffusion between the substrate and coating may be calculated. The Alkα peak was chosen as it was known that it would not have been found within the titanium coating prior to the heat treatment. It was not possible to accurately count the peak intensity of the vanadium Vkα peak due to it overlapping with the Tikβ peak. However, it is known that vanadium diffuses at a similar rate to that of aluminium in titanium (Figure 4.19) [12]. EDX analysis was carried out at 20 μm intervals up to 200 μm either side of the coating-substrate interface and the grey line shown in Figure 4.50 shows the results of this analysis.

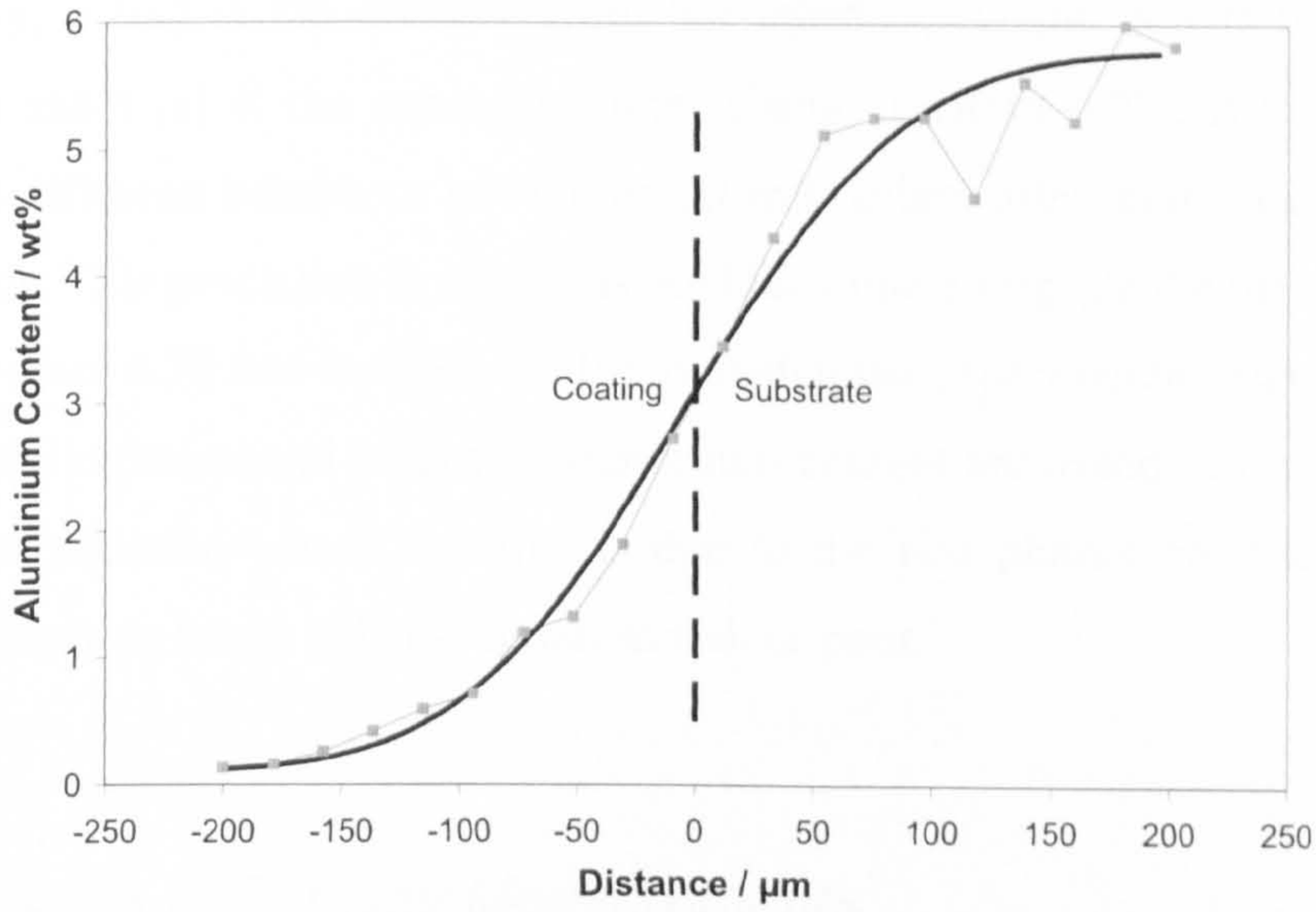

Figure 4.50 – Aluminium diffusion across the coating substrate interface for a heat treatment at 1150 °C for one hour. EDX measurements are indicated by the grey line and predicted values by the black line.

If the diffusion constant of an element within another material is known, it is possible to predict the rate of diffusion occurring when two specimens are joined together and heat treated. Diffusion coefficients were obtained from Figure 4.19 for the heat treatment temperatures used in this study and are summarised in Table 4.12.

Heat Treatment	Diffusion Coefficient / $m^2 s^{-1}$
600 °C	10^{-22}
800 °C	10^{-18}
1150 °C	10^{-13}

Table 4.12 – Diffusion coefficients for aluminium in titanium for a range of heat treatment temperatures [12].

For the heat treatment temperatures chosen below 1150 °C, the diffusion coefficients are very small, explaining why no measurable diffusion between the substrate and coating is identified for such heat treatment temperatures. By assuming that the two specimens are semi-infinite, the diffusion profile can be calculated from the following equation [137]:

$$C = \left(\frac{C_1 + C_2}{2}\right) - \left(\frac{C_1 - C_2}{2}\right) erf\left(\frac{x}{2\sqrt{Dt}}\right) \qquad \text{(Eq 4.27)}$$

Where C_1 and C_2 are the minimum and maximum aluminium compositions respectively, x (m) is the distance from the interface, D (m^2 s^{-1}) is the diffusion coefficient and t (s) is the annealing time. Using equation 4.27., it is possible to predict the diffusion behaviour of aluminium in titanium after annealing at 1150 °C for one hour. This prediction is shown as the black line alongside the measured EDX values in Figure 4.50 and is found to closely match the experimental data. Within the substrate, the experimental values of aluminium content are found to fluctuate either side of the predicted values and this is due to the two phases present within the Ti6Al4V substrate being either aluminium rich or poor.

4.9.3.2. Porosity Measurements

Table 4.9 shows the porosity measurements for heat treated cold sprayed titanium samples. For heat treatments up to 800 °C, a similar level of coating porosity was

found compared to the non-heat treated titanium cold spray coatings. Table 4.9 shows that for titanium coatings heat treated at 1150 °C an increase in coating porosity was measured.

Comparing a titanium coating heat treated at 1150 °C (Figure 4.48(c)) with a non heat treated titanium coating (Figure 4.32(b)) a difference in the pore aspect ratio is observed; for samples heat treated at 1150 °C, the pores appear to be of a more spherical nature. Measurement of the pore aspect ratio was carried out by image analysis as described in Section 4.8.3.5. and results are shown in Figure 4.51 for a non-heat treated and 1150 °C heat treated titanium coating. Measurements of the pore aspect ratio for samples heat treated at 400 °C, 600 °C and 800 °C were found to be similar to a non-heat treated sample. Figure 4.51 shows that the cold sprayed titanium coating heat treated at 1150 °C has a greater volume fraction of pores of aspect ratio 0.5 or higher compared to a non-heat treated sample.

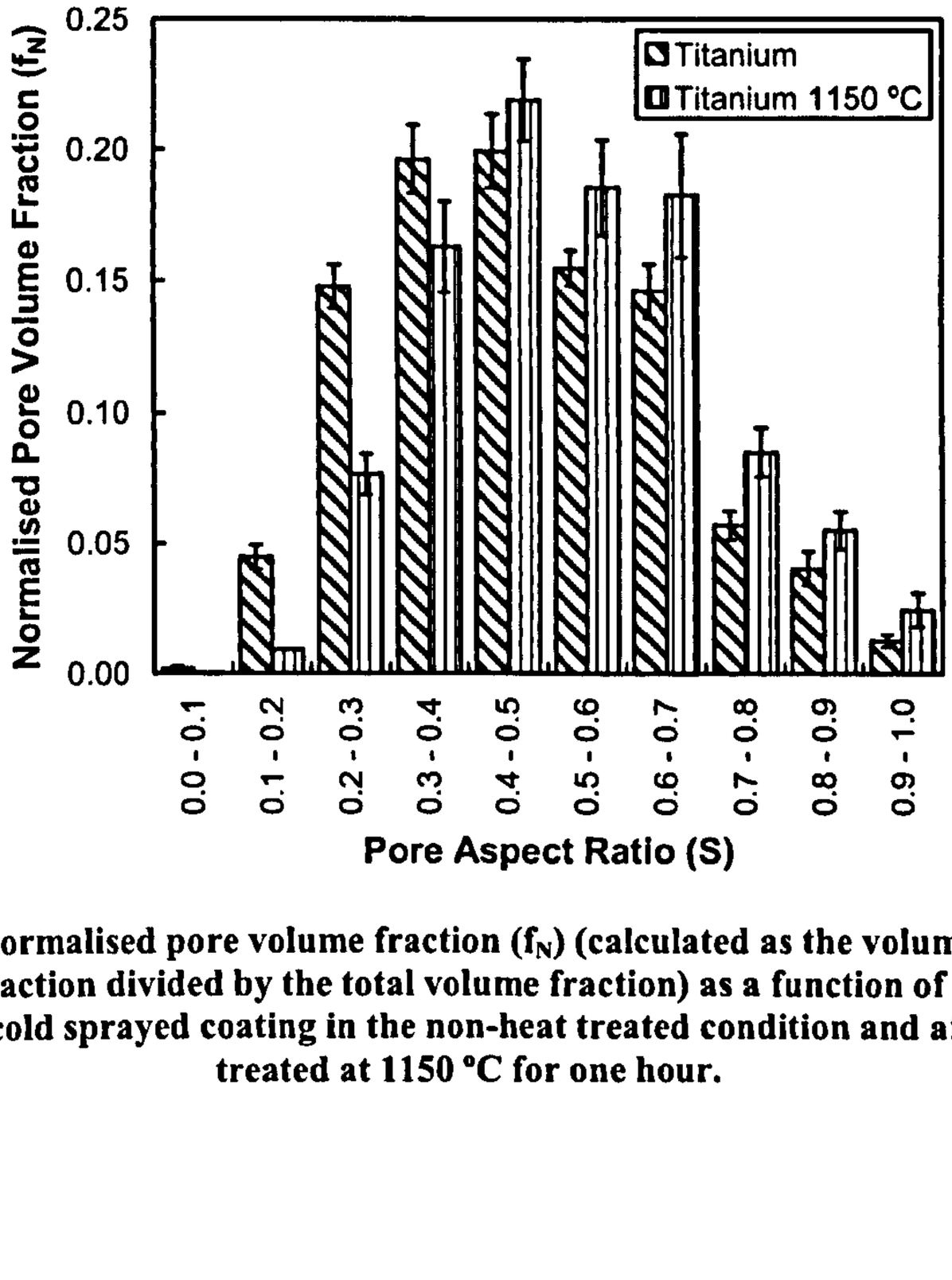

Figure 4.51 – Normalised pore volume fraction (f_N) (calculated as the volume fraction of a specific volume fraction divided by the total volume fraction) as a function of pore aspect ratio for a titanium cold sprayed coating in the non-heat treated condition and after being heat treated at 1150 °C for one hour.

4.9.3.3. Coating Stiffness

Table 4.9 shows the measured modulus values for the titanium coatings heat treated at the various temperatures. For heat treatment temperatures up to 800 °C, there is little change from the modulus ratio of 0.17 found for a titanium coating in the as-deposited state. After heat treatment at 1150 °C, the modulus ratio increases significantly to 0.36. Use of the Eshelby model, Figure 4.38, shows that this increase in modulus ratio may be due to an increase in the pore volume fraction of larger aspect ratio. Alternatively, it may also be due to improved bonding occurring due to diffusion bonding between particles, both within the coating and at the coating-substrate interface.

4.9.3.4. Coating Hardness

The average coating hardness, shown in Table 4.8, was found to increase with increasing heat treatment temperature. This is most likely due to increased levels of inter-particle bonding occurring with increasing heat treatment temperature.

4.9.3.5. Coating Bond Strength

It has been shown previously by EDX analysis, Figure 4.50, that diffusion has occurred between the Ti6Al4V substrate and titanium coating at a heat treatment temperature of 1150 ° C. No significant diffusion was measured or predicted to have occurred at heat treatment temperatures of 800 °C or lower. Transverse scratch testing was used to assess any changes in bond strength throughout the coating. Figure 4.52(a) and Figure 4.52(b) show transverse scratches with applied loads of 10 N and 70 N respectively, onto a titanium coating following heat treatment at 800 °C for one hour. Delamination at the coating substrate interface and cracks within the coating itself are found, similar to those previously shown for a non-heat treated sample (Figure 4.39(a) and Figure 4.39(b)). Therefore it is expected that no improvement in the coating bond strength results from heat treating up to 800 °C.

Figure 4.52(c) and Figure 4.52(d) show scratches with applied loads of 10 N and 70 N respectively for a coating heat treated at 1150 °C for one hour. For the higher load of 70 N (Figure 4.52(d)), there is a significant reduction in the amount of delamination and cracking occurring within the coating itself compared to samples heat treated at lower temperatures or in the as-deposited state.

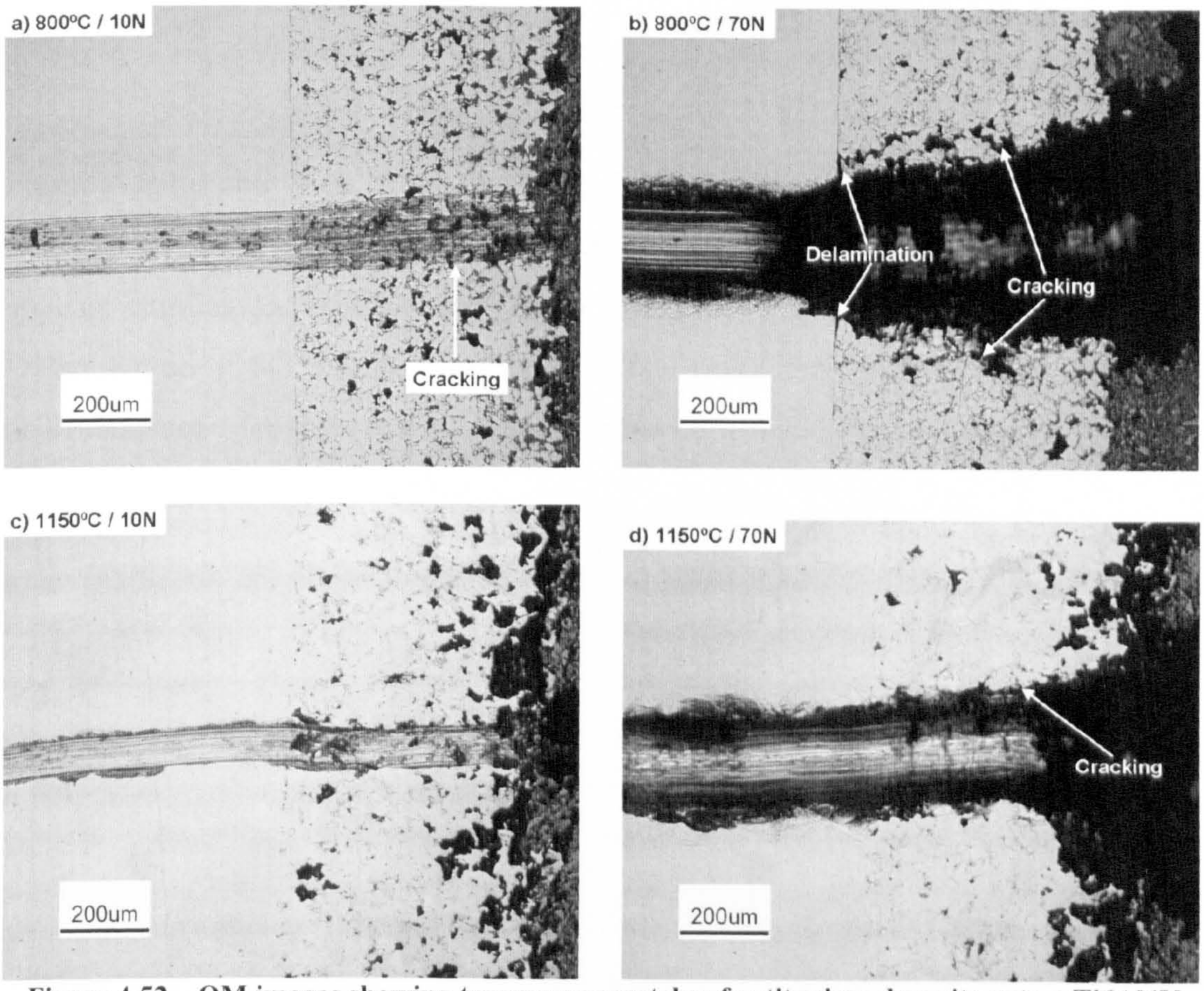

Figure 4.52 – OM images showing transverse scratches for titanium deposits onto a Ti6Al4V substrate and subsequently heat treated at, (a) and (b), 800 °C, and (c) and (d), 1150 °C for one hour. Scratches are generated by applied loads of 10 N and 70 N as indicated by each image. Scratch direction is from substrate into the coating (left to right). The coating was deposited using helium as the primary gas at room temperature and a stagnation pressure of 29 bar.

4.9.3.6. Fatigue Endurance Limit

Fatigue testing was carried out on titanium cold sprayed coatings deposited onto a Ti6Al4V substrate with an as-received surface finish and subsequently heat treated at 800 °C and 1150 °C for one hour. Measured fatigue endurance limits after 10^7 cycles are shown in Table 4.10. A reduction in fatigue endurance limit is found compared to the non-heat treated samples (Table 4.10). A heat treated substrate was found to have

a 59 % and 45 % decrease in fatigue endurance limit compared to the non-heat treated state after a heat treatment for one hour at 1150 °C and 800 °C respectively. Fatigue endurance limit reductions of approximately 60 % resulted when compared with coated samples in the heat treated and non-heat treated state. These reductions in fatigue endurance limit occurred despite minimal variation in the surface topography of the samples due to the heat treatment.

4.9.3.7. Analysis of Fracture Surfaces

Figure 4.53(a) shows an overview of the fatigue fracture surface for a cold sprayed sample heat treated at 800 °C. The fracture surface within the Ti6Al4V substrate appears similar to those found for a non-heat treated sample (Figure 4.42). Delamination of the coating from the substrate was identified to occur in the initial and final fracture regions and shown in Figure 4.53(b) and Figure 4.53(c).

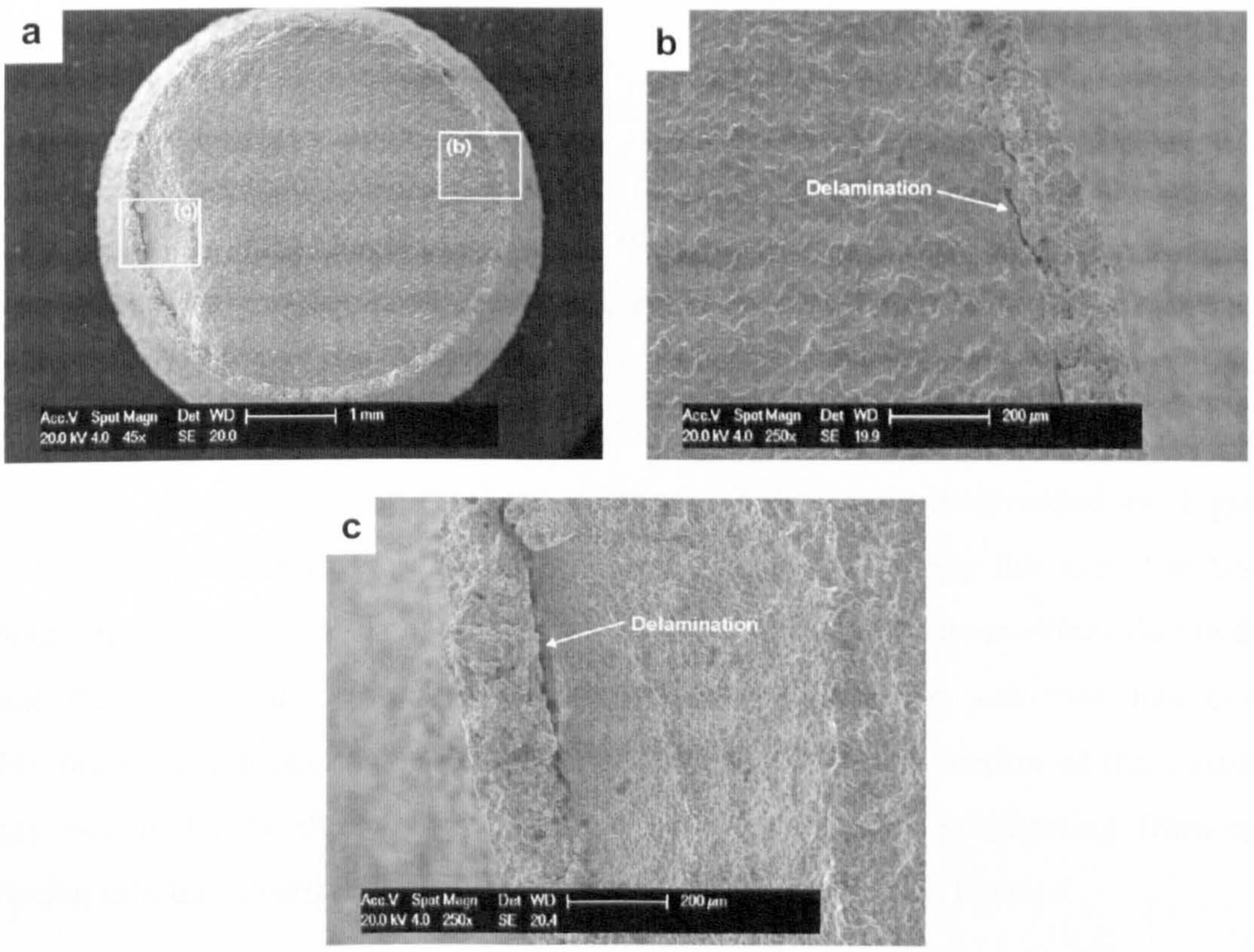

Figure 4.53 – SE image showing the (a) fatigue fracture surface of a Ti6Al4V substrate with an as-received surface finish and cold sprayed titanium coating subsequently heat treated at 800 °C for one hour and; (b) initial fracture point and (c) final fracture point both showing delamination of the coating from the substrate. The coating was deposited using helium as the primary gas at room temperature and a stagnation pressure of 29 bar.

Figure 4.54 is a cross-sectional image of the same sample showing the fatigue fracture. Large portions of the coating still appear well bonded to the coating substrate. At the fatigue fracture, the coating has broken into small sections on failure.

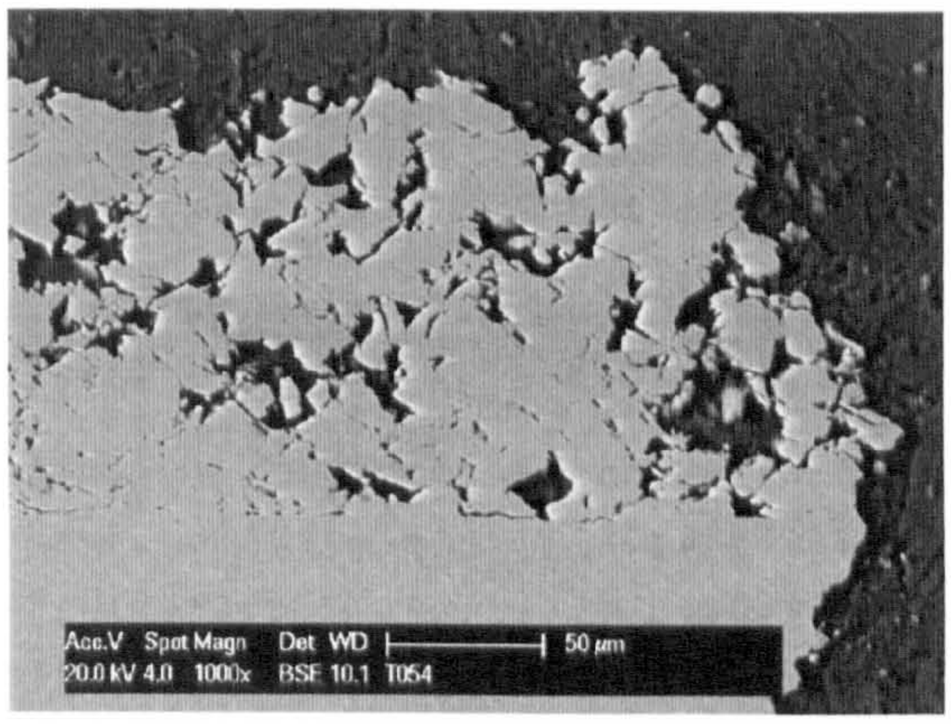

Figure 4.54 – BSE image of the cross-section at the fatigue fracture of a Ti6Al4V substrate and the titanium cold sprayed coating and heat treated at 800 °C for one hour (Stress = 217 MPa). The coating was deposited using helium as the primary gas at room temperature and a stagnation pressure of 29 bar.

Figure 4.55(a) shows the fatigue fracture surface for a cold sprayed sample heat treated at 1150 °C. The fracture surface is significantly different to those shown previously. It is hard to identify regions of Stage I and Stage II crack growth. The fracture surface appears brittle in nature. Figure 4.55(b) shows the typical coating-substrate interface found throughout the sample. The coating is shown to have remained well bonded to the substrate. This is most likely due to diffusion bonding processes occurring during the heat treatment. This fact is emphasised by Figure 4.56, a cross-sectional image of the same sample at the fatigue fracture. The BSE image shows grains that have formed across the coating-substrate interface due to the heat treatment and delamination between the coating and substrate has been eliminated. The reduction in fatigue endurance limit on application of the coating may potentially be due to the increased chance of cracks propagating from the coating into the substrate due to the improved bonding between the two.

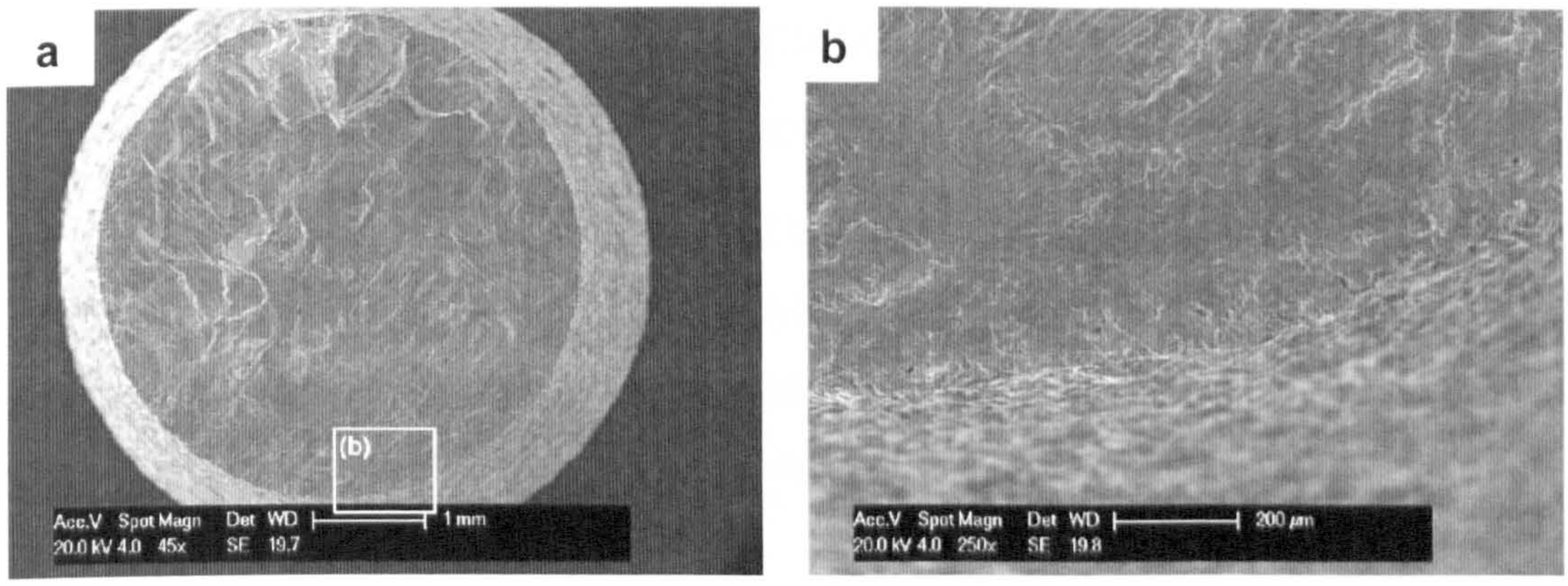

Figure 4.55 – SE image showing the (a) fatigue fracture surface of a Ti6Al4V substrate with an as-received surface finish and cold sprayed titanium coating subsequently heat treated at 1150 °C for one hour and (b) throughout the sample a high degree of bonding between the substrate and coating was found. The coating was deposited using helium as the primary gas at room temperature and a stagnation pressure of 29 bar.

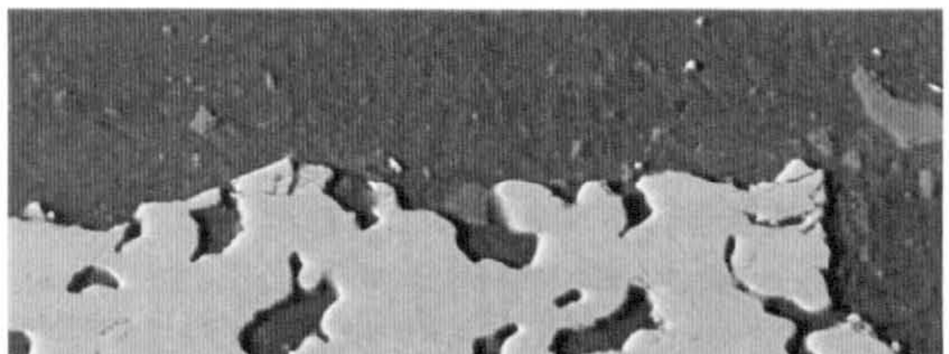

Figure 4.56 – BSE image of the cross-section at the fatigue fracture of a Ti6Al4V substrate and the titanium cold sprayed coating and heat treated at 1150 °C for one hour (Stress = 192 MPa). The coating was deposited using helium as the primary gas at room temperature and a stagnation pressure of 29 bar.

4.9.3.8. Residual stresses within heat treated deposits

The amount of induced specimen bending due to coating deposition was used to measure the residual stresses within the coating and substrate. Results are shown in Table 4.11. Residual stresses within the deposits were found to reduce with increasing heat treatment temperature due to the stress-relieving nature of heat treating.

4.9.4. Properties of Competitor Coating – Shrouded Arc Sprayed Titanium Deposits

The fatigue endurance limit, stiffness and induced residual stresses within a titanium coating, deposited by shrouded arc spraying, were measured to allow comparison between coatings created by the shrouded arc and cold spraying process. The shrouded arc titanium coating microstructure is also assessed to aid explanation of findings.

4.9.4.1. Coating Microstructure

The shrouded arc coating microstructure is shown in Figure 4.57. The titanium coating produced by shrouded arc spraying has a very different coating microstructure to a titanium coating produced by cold spraying (Figure 4.32). Despite the coating being produced within an inert atmosphere, individual titanium particles within the shrouded arc coating are typically separated by oxides, identified as intermediate grey levels within the BSE images. Porosity within the coating is found to be apparent and is able to form evenly at the coating top surface and close to the substrate-coating interface. Cracking at the coating top surface was found along the length of the sample and an example of this is shown Figure 4.57(b). Cracks were typically found to be no more than a couple of 100 μm in thickness. Cracks were not found within the coating close to the coating-substrate interface.

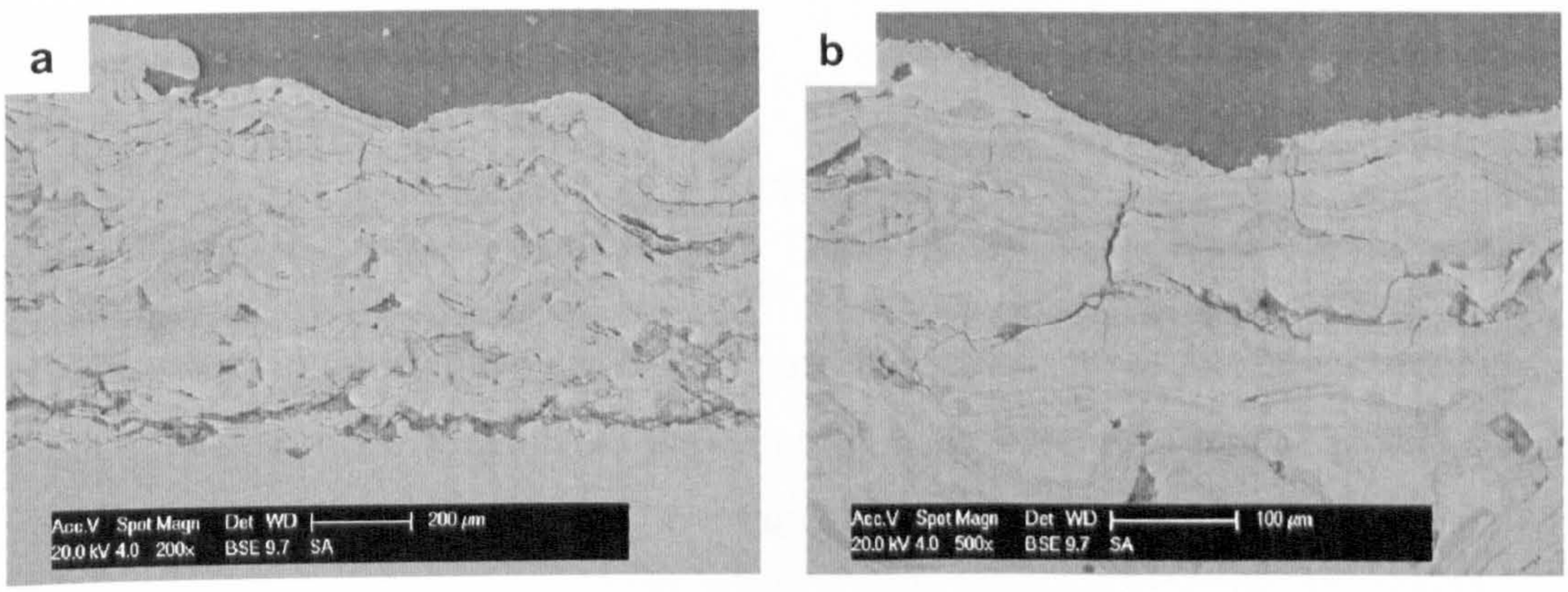

Figure 4.57 – BSE images of the cross-section of the shrouded arc titanium coating microstructure at (a) low magnification, (b) the coating top surface showing evidence of cracking occurring within the coating.

4.9.4.2. Coating Stiffness

The modulus of the shrouded arc coatings was measured as 41 ± 0.9 MPa. Using a modulus value of 120 GPa for titanium (from the metals handbook [13]), it is found that the modulus ratio of the shrouded arc coating is found to be approximately 0.33. This is significantly higher than the modulus ratio measured for the cold sprayed titanium coatings.

4.9.4.3. Fatigue Endurance Limit

Table 4.10 shows that samples that were grit blasted by the industrial partner were observed to have a 34 % reduction in fatigue endurance limit compared to the as received state. This is a larger reduction compared to samples grit blasted at the University of Nottingham and may be due to the higher surface roughness (Table 4.6) which gives an indication of the level of surface deformation that has occurred. An increase in surface deformation or surface roughness could create a greater number of surface stress raisers and initiation sites for cracks to develop, thus reducing the fatigue endurance limit. It is also noted that there are other factors determining the fatigue endurance limit of a sample and these are discussed in further detail in later sections. A further significant reduction in fatigue endurance limit was found on application of the shrouded arc sprayed coating. All samples failed before the fatigue endurance limit after 10^7 cycles could be measured. Therefore the table indicates an upper bound limit of the fatigue endurance limit for the shrouded arc samples of 182 MPa.

4.9.4.4. Analysis of Fracture Surfaces

Figure 4.58(a) shows the fatigue fracture of a shrouded arc sprayed sample. The substrate was found to have similar fracture features to those discussed previously (Figure 4.42). Evidence of the shrouded arc coating delaminating at the initial and final points of fracture is identified in Figure 4.58(b) and Figure 4.58(c) respectively.

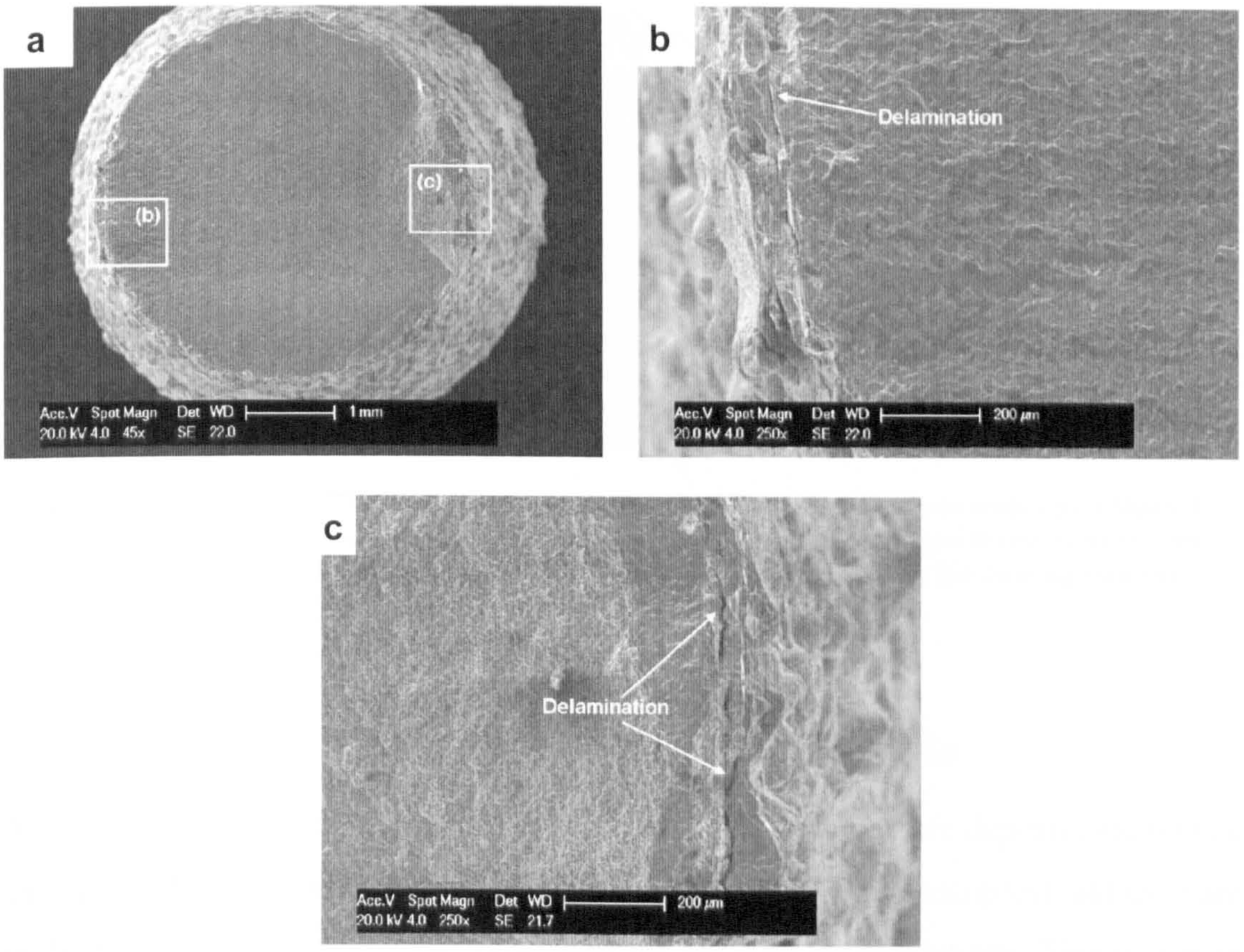

Figure 4.58 – SE image showing the (a) fatigue fracture surface of a Ti6Al4V substrate with a grit blasted surface finish and shrouded arc sprayed titanium coating and; (b) initial fracture point and (c) final fracture point.

Figure 4.59(a) is a cross-sectional image of the fatigue fracture. At the fracture point, a large portion of the coating has been removed. Parts of the remaining coating exhibit cracking, some of which continues into the substrate. These cracks are shown at a higher magnification in Figure 4.59(b). These cracks originated at the coating top surface having grown from pre-existing nucleation sites. Cracks were previously identified within the top third of the coating cross-section surface in Figure 4.57(b), for samples not used for fatigue testing. On application of the fatigue load, these cracks would have acted as stress raisers and grown and propagated into the substrate, causing premature failure.

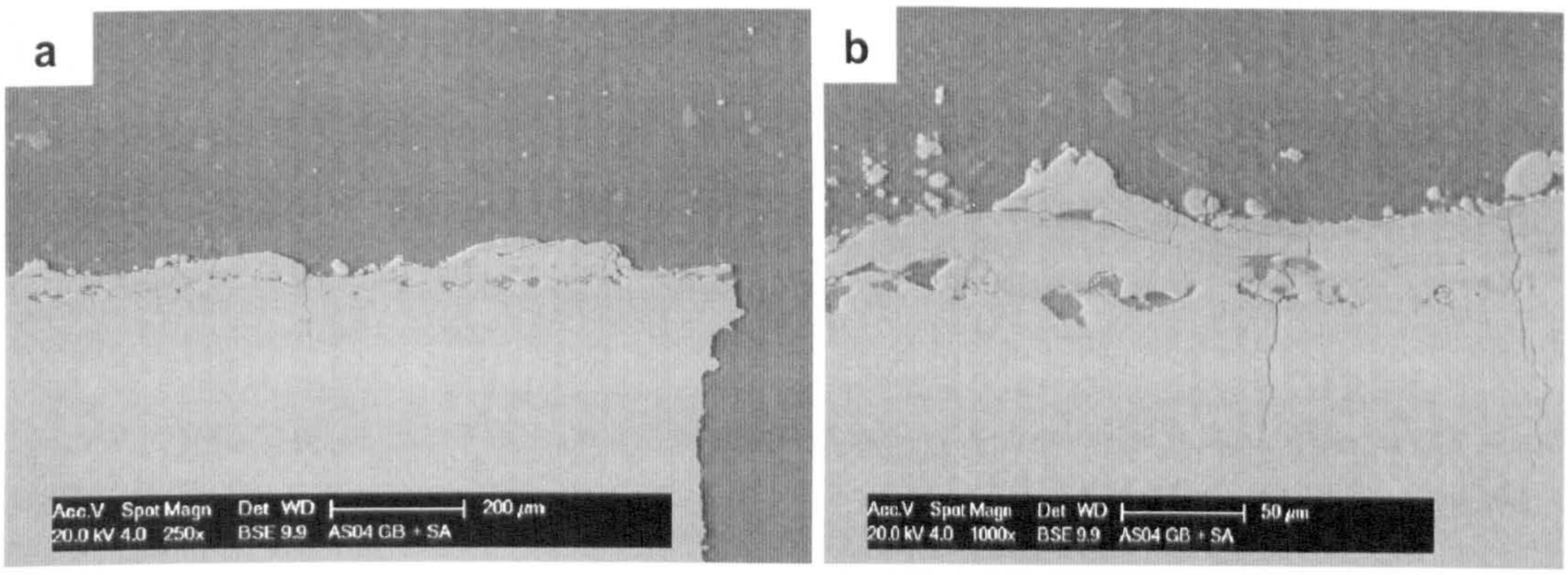

Figure 4.59 – BSE images of the cross section of the Ti6AL4V substrate with a grit blasted surface finish and the shrouded arc titanium coating close to the fatigue fracture at (a) low magnification and (b) high magnification. Cracking that runs from the coating into the substrate can be identified.

4.9.4.5. Residual Stresses within Deposits

Table 4.11 shows that residual stresses found in the shrouded arc deposits are tensile (as opposed to compressive stresses found in all cold spraying samples) and they are of higher magnitude than those measured for the cold spray coatings. This is due to the quenching stresses that are observed on cooling of the coating after deposition.

4.10. Discussion

The discussion section of this chapter is divided into two main sections. The first section discusses the results found for the Ti6Al4V substrate and the second section considers the results found for coatings experimentally tested during this study. The second section includes discussion on cold spray coatings, shrouded arc coatings and heat treated titanium cold spray coatings.

4.10.1. Substrate Properties

This section provides interpretation of the results previously described relating to the Ti6Al4V substrate and a comparison to results found by previous workers. The Ti6Al4V substrates were shown to have either a fine equiaxed or coarse microstructure in the as-received state. The Ti6Al4V alloy is used for many applications, predominantly aerospace, and therefore it is well characterised. The

mechanical properties measured in this study; hardness, stiffness, fatigue endurance limit, are all comparable to results from previous workers [13, 14, 118-120].

Figure 4.29(a) shows that a grain size of approximately 10 μm or less has been found for the Ti6Al4V substrate used for fatigue testing in the non-heat treated state. Table 4.10 shows the measured values of the fatigue endurance limit after 10^7 cycles of the Ti6Al4V substrate of 633 MPa for an as-received surface finish reducing to 418 MPa for a grit blasted surface finish. These values are comparable to other workers results, such as those shown by Wagner et al. [120] in Figure 4.12 for a 10 μm grain size. A 20% reduction in the fatigue endurance limit was measured after grit blasting carried out at the University of Nottingham due to the production of surface stress raisers from the grit blasting process. Greater reductions in the fatigue endurance limit were observed following grit blasting by the industrial partner. This is due to an increase in the surface roughness of the samples grit blasted by the industrial partner as shown in Table 4.6.

With increasing heat treatment temperature up to 800 °C, grain growth was found to occur. By heat treating above the α / β transformation temperature, shown to be approximately 1000 °C by Figure 4.1, a significant change in the substrate microstructure was found. The single phase beta field is separated from the two phase α / β field. By furnace cooling through the β transition temperature, the β phase transforms by nucleation and growth to leave a Widmanstätten α phase structure (Figure 4.31) [138]. The microstructural changes with increasing heat treatment give rise to a change in the mechanical properties of the Ti6Al4V substrate. A reduction in the substrate hardness (Table 4.8) is observed with increasing heat treatment temperature.

Up to a 59% reduction in the fatigue endurance limit of the Ti6Al4V substrate was found with increasing heat treatment temperature compared to the non-heat treated state (Table 4.10). The fatigue fractures of the Ti6Al4V substrate heat treated at 800 °C has a similar fatigue fracture surface to that of the non-heat treated sample. The 1150 °C heat treated samples showed a brittle fatigue fracture surface and this is

potentially due to oxygen embrittlement. A large increase in the diffusion rate of oxygen within Ti6Al4V occurs at heat treatment temperatures greater than 900 °C, as shown in Figure 4.19. The increase in the Young's modulus of Ti6Al4V with heat treatment temperature is a phenomenon that occurs with titanium alloys. It occurs because the modulus of the Ti6Al4V alloy is determined by the specific moduli of the phases present and their volume fractions. For the Ti6Al4V alloy, the volume fraction and compositions of the phases present depend on the prior heat treatment carried out and therefore as a consequence any prior heat treatment will influence the modulus of the titanium alloy [12, 132].

4.10.2. Cold Spray Coating Properties

This section provides interpretation of the results previously described and compares them to results found by previous workers.

4.10.2.1. Coating Microstructure

For the cold spray coatings, it is possible to identify pores, voids and defects between individual splats that make up the thickness of the coating. These defects are most easily identifiable within the titanium deposits (Figure 4.32(b)). Using porosity that is resolvable by the SEM (Table 4.9) as a quantifiable measurement of these defects, it has been shown that there are a greater number of these defects apparent in the titanium cold sprayed deposits compared to the aluminium (Figure 4.36(a)) and copper cold sprayed deposits (Figure 4.36(b)). For all types of deposit there appears to be a greater amount of porosity at the coating top surface than that found close to the coating-substrate interface. This is due to the way in which cold spray coatings are deposited. Particles that create the initial layers of the coating will be impacted by further impinging particles which would lead to compaction of particles that are already deposited. For particles that are deposited close to the top of the coating surface, there are fewer impinging particles that would lead to compaction of this section of the coating and therefore a more porous structure is expected.

Of the three deposited materials, and using their respective SEM images, copper may be expected to show the highest level of inter-particle bonding due to the low levels of defects and voids found within the coating microstructure. It was found that the copper coatings had the lowest coating porosity of the three materials deposited. It should, however, be noted that there may be other defects within the cold spray deposit that can not be resolved by the SEM and this is discussed in greater detail in further sections. The hardness of the titanium coatings was found to vary with coating depth as shown in Figure 4.41. At the coating top surface, a much lower coating hardness was measured than at the coating top surface as shown in Figure 4.32(a). A large number of pores and defects are found at the coating top surface due to the nature of the way in which a cold spray coating is created and this will influence hardness results in this portion of the coating.

It is expected that the defects identified within the deposits would affect the level of bonding occurring within the cold spray deposits and the coating stiffness of the cold spray deposits. The next section discusses the bonding strength and mechanisms found within cold spray deposits. Transverse scratch test images are discussed to assess the amount of bonding within the coating and a blended aluminium-copper powder was used to show visually the amount of inter-particle bonding found within cold spray deposits.

4.10.2.2. Bonding Strength and Mechanisms

It has been argued previously [47, 55, 93, 95] that upon impact, a shear instability results, which cleans the metal surfaces of oxides and leaves exposed metal surfaces which can be metallurgically bonded. The ability to form clean metal surfaces which are well bonded strongly depends upon both the conditions of impact (velocity, impact angle, temperature, local geometry) as well as upon the material in question (which will govern the nature of the shear instability and the nature of the pre-existing oxides upon the particle surfaces). During spray deposition of a coating, particles impact with a non-plane target which will be made up of particles which have been previously deposited. As such, each particle will experience different deformation conditions upon impact. Modelling of particle impact [47, 52] has

tended to examine only impact of spheres on plane targets, and as such does not adequately represent conditions observed in practice. Assadi et al. [93] briefly consider the interaction between multiple spherical particles impacting a surface. It was found that previous particle impacts to a substrate do affect the shear instabilities generated, by further impinging particles and that the strain and temperature distribution at the particle-particle impact interface is inhomogeneous; they suggested that this would indicate that bonding may be confined to a fraction of the interacting surfaces. In the modelling of impact, whilst shear and temperature effects can easily be considered, the role of the presence of surface oxides (both on the substrate material and on each individual particle) in modifying interface interactions has not been addressed (even though its role is widely recognised) [47].

To visually show the inhomogeneous bonding within cold spray deposits a blended aluminium-copper powder was used to produce coatings and subsequently heat treated (Section 4.8.2.2.). Following heat treatment, non-uniform intermetallic layers formed between the aluminium and copper particles form as shown by Figure 4.34. The reason for incomplete coverage of aluminium-copper interfaces with an intermetallic layer can be attributed to oxide layers on the surfaces of one or both original powder powders which act as a diffusion barrier. Aluminium, in particular, forms an oxide which is very stable and tenacious. Therefore bonding of aluminium and copper particles is potentially difficult, even at elevated temperature, unless this oxide film can be broken and intimate metal to metal contact obtained. In this respect the occurrence of shear instabilities on impact has a key role in breaking down oxide films and creating intimate metallic contact which will allow diffusion during elevated temperature annealing. The increase in fractional interface coverage, with increasing primary gas pressure, which was measured in this work (Figure 4.34) can be attributed to more extensive breakdown of oxide films at the higher pressure. This is because particle velocity increases with primary gas pressure, which in turn creates more extensive regions of shear instability as predicted by finite element modelling [93]. Thus it can be concluded that a higher particle velocity in the CGDS process causes a greater degree of direct metal contact between particles in the deposit. The phenomenon of localised regions of intermetallic layer formation, related to oxide breakdown, has also been observed in the context of studies on

diffusion bonding of aluminium and copper [135]. In their study, it was noted that an increase in bonding pressure increased the area over which intermetallics formed because of increased oxide break-up.

The intermetallic layer development during elevated temperature annealing can be explained in terms of a solute diffusion controlled process. It was established by Manna et al. [133] and Funamizu et al. [134] that the growth kinetics follow the following equation:

$$w = \sqrt{D \cdot t} \qquad \text{(Eq 4.28)}$$

where w is the intermetallic thickness, t is the dwell time of the heat treatment and D is the diffusion coefficient. D is temperature dependent and is given by:

$$D = D_o \cdot \exp\left(-\frac{Q}{R \cdot T}\right) \qquad \text{(Eq 4.29)}$$

where D_o is the pre-exponential constant, Q is the activation energy of the process, R is the gas constant and T is the absolute temperature. Data for calculating D are given in Table 4.13 for molten aluminium deposited by hot dipping onto a copper substrate with and without prior cold work [133]. Using the values given, the intermetallic thicknesses estimated for the present annealing treatment are ~ 1 and 6 μm for the assumption of 0 % and 40 % cold work respectively. These values are in reasonable agreement with those observed experimentally in this work, and shown in Figure 4.35.

Condition of copper substrate	**Pre-exponential factor (D_o) / $m^2\ s^{-1}$**	**Activation Energy (Q) / kJ mol^{-1}**
No prior deformation	0.9×10^{-4}	136.9
40% prior deformation	0.4×10^{-4}	116.6

Table 4.13 – Data used to calculate the intermetallic layer growth between aluminium and copper for following heat treatment. Taken from reference [133].

The increased intermetallic layer thickness obtained with the higher primary gas pressure can also be explained on the basis of the work of Manna et al. [133] in which growth kinetics were found to increase with increasing cold work due to crystal defects increasing solute diffusivity. It is well known that particles in cold sprayed deposits possess significant microstrain due to dislocations and other lattice

defects [139]. Since the degree of microstrain, i.e. defect density, is likely to increase with increased particle impact velocity if the primary gas pressure is increased, then this is expected to lead to an increase in intermetallic layer growth on annealing.

4.10.2.3. Coating Stiffness

In the case of thermally sprayed coatings, low modulus values have been attributed to porosity and microcrack formation resembling through thickness cracks within the coatings. Kuroda et al. [104] measured the range of pore volume fractions and, using an Eshelby model, the aspect ratios required to provide a satisfactory quantitative agreement with the measured modulus ratios were identified. However, no attempt was made to quantify the actual pore aspect ratios present within the deposits. The experimental results presented within this study indicate that in cold sprayed deposits, the elastic modulus is significantly reduced compared to that of the bulk materials. In this respect, the results confirm the findings of a number of other researchers [53, 55, 73, 82]. For the present study, the Eshelby model shows that defects of aspect ratio significantly less than unity are necessary to account for the low coating modulus found within the coatings considered. The Eshelby model (Figure 4.38) has shown that the defect aspect ratio has a significant effect on the coating modulus for a given defect volume fraction. Defects with an aspect ratio of 0.01 or lower (perpendicular to the force applied and representing through-thickness cracks or defects), with relatively small volume fractions present, cause a significant reduction in the modulus ratio of the coating material in the region of those observed experimentally (Table 4.9). Defects with an aspect ratio of 1 or higher (representing cracks or defects in the plane of the coating) cause only a slight change in the coating modulus from the original bulk value. The Eshelby model only considers defects that are of a single aspect ratio and that are orientated parallel to the substrate-coating interface (see Figure 4.11). In fact, defects of many different aspect ratios and at varying orientation may be expected to be found within a coating. Although the actual situation found within a coating is far more complex than the Eshelby model suggests, it does highlight the significant effect that defects resembling through-thickness cracks have on the coating modulus.

Figure 4.37(b) shows that for a pore aspect ratio of 0.2 or lower, the measured cumulative pore volume fraction was at most 0.05 of the total pore volume fraction (0.045 for titanium) measured by image analysis. It should be noted that the data obtained from image analysis and shown in Figure 4.37(a) and (b) takes no account of the pore orientation and assumes that all pores are aligned with the major axis perpendicular to the substrate-coating interface (the most detrimental pore orientation). In reality, only a proportion of the defects will be orientated in this manner and therefore an overestimation of the pore volume fraction for low aspect ratios may be expected. Therefore, when using the values from Figure 4.37(b) with the Eshelby model (Figure 4.38) an overestimation of the modulus reduction due to the pore aspect ratio may be expected. The Eshelby model (Figure 4.38), for titanium, predicts that for pores of an aspect ratio of 0.2 a total pore volume fraction of greater than 0.3 is required to give the measured modulus reduction. This value is far higher than the estimated pore volume fraction for the same aspect ratio measured by image analysis and thus it would appear that defects which can be resolved by SEM image analysis cannot, when coupled with an Eshelby type analysis, adequately explain the low modulus ratios measured experimentally. Other defects that cannot be resolved by metallographic preparation and SEM analysis are therefore suggested to be present. There are also other factors which might contribute to the modulus reduction and these are as follows:

i) There are potential experimental limitations that would lead to reduced modulus measurements. Low modulus ratios found for the aluminium, copper and titanium deposits may be partly due to lateral shear at the coating-substrate interface during four-point bend testing. The calculation of the coating modulus assumes perfect bonding at the interface and this assumption has limited the validity of the experiments conducted herein; accordingly, the actual Young's modulus of the coatings may be higher than that derived from the measurements and calculation methods employed. As such, the poor bonding at the interface for titanium coatings (manifested in the interface cracking observed in Figure 4.39(a) and (b)) may lead to reduced values of modulus being

reported. However, using the indentation method of modulus testing for a cold sprayed titanium coating [82] a modulus ratio of 0.19 was also obtained, suggesting that interface shear was not a dominant effect.

ii) Splats that may exhibit no visible gap between them as resolved by SEM, may still be poorly bonded to each other. These defects would therefore not be quantified by the SEM analysis and thus these types of defect will not be accounted for by this method. The actual defect content within the coating may be larger than the measured values. These defects will be of low aspect ratio, for example along splat interfaces where true metal to metal contact has not occurred and such defects have been previously identified in the deposit created by a blended aluminium and copper powder (Figure 4.34). Transverse scratch testing observations tend to support this argument as they have shown evidence for the presence of poorly bonded particles. Cracks have been found to occur along particle boundaries within coatings which are most noticeable in the titanium deposits as seen in Figure 4.39(a) and (b). Furthermore, many of these cracks are orientated as through-thickness cracks which are predicted by the Eshelby model to have the greatest influence on reducing the coating modulus.

In Section 4.9.2.2., it has been shown visually that incomplete disruption of oxide layers readily occurs within cold spray deposits which supports the arguments discussed above for a reduction in coating modulus due to inhomogeneous bonding. The copper cold sprayed coatings were found to have a significantly larger modulus ratio than the aluminium and titanium coatings sprayed in this study, see Table 4.9. The original sprayed microstructures (Figure 4.32 and Figure 4.36) show some evidence that there is porosity in the structures, with the titanium coating exhibiting defects which outlined individual splats, indicating that they may not be well bonded. Examination of the mechanical integrity of the interparticle boundaries by transverse scratch testing revealed that the particles in titanium were indeed more poorly bonded than the other two materials and that defects of much lower aspect

ratio do exist (Figure 4.39(a) and (b)); in contrast, it appeared from this test that the bonding in copper was relatively good in that no intersplat decohesion was observed (Figure 4.40(a) and (b)).

Aluminium and titanium are reactive metals, and, as such, will have well-bonded oxide layers on the surfaces of the particles being sprayed. The micrographs of the titanium coating (Figure 4.32(b)) showed that this material was relatively poorly densified during deposition; however, both the aluminium and copper coatings appeared to be very well densified (Figure 4.36(a) and (b)). The copper coatings have the highest modulus ratio of the three coatings examined within this study. The oxide layer on the copper particles is much less tenacious than the aluminium and titanium oxide layers and this is expected to aid the bonding process between splats, between the coating and the substrate, and therefore, improve the coating modulus. Accordingly, it has been proposed by Schmidt et al. [47] that copper requires the lowest critical velocity for bonding, of the coatings tested, to occur for the reasons described above (along with the fact that copper has the highest density for the three coating materials considered). It has been estimated [47] that a 25 μm copper particle requires a critical velocity of 470 – 500 m s^{-1} for bonding compared to greater than 600 m s^{-1} for bonding of similarly sized aluminium and titanium particles. The lower critical velocity indicates that the particles are more suited to cold spray deposition, due to both its ability to deform to form highly dense coatings and also due to the ease of disruption of interparticle oxides. Due to its dense microstructure following spraying, it is normally necessary to etch the copper coating to reveal the inter-splat boundaries and highlight the amount of localised deformation occurring [86, 88].

By comparing Table 4.4 and Table 4.9, it can be seen that McCune et al. [53] and Van Steenkiste et al. [55] found modulus ratios twice as large for corresponding cold sprayed copper and aluminium coatings than for those coatings deposited in this study. McCune et al. [53] indicated that the modulus ratio for their copper deposits was surprisingly high; whilst specific spray parameters are not reported in the paper, they indicate that the material was sprayed with gas at elevated temperature which may explain the high modulus ratio. In the case of the aluminium coatings [55],

heated air and larger particle sizes of size distribution +63 -106 μm were employed. By heating the main air supply an increase in gas velocity (and thus particle velocity) can be expected. Additionally, the larger particle size distribution would reduce the particle critical velocity for bonding to occur [47] but this effect is offset by a reduction in the actual particle velocity achieved in the gas stream. The use of cold gas in the present work may have resulted in particles achieving lower velocities on impact, giving rise to more regions of inhomogeneous bonding with thin oxide layers at a larger proportion of particle boundaries. Clearly, more work is required to systematically evaluate the effect of particle impact conditions on elastic modulus before further comparisons and conclusions may be drawn from results measured by other workers.

4.10.2.4. Residual Stresses

Residual stress measurements show low stresses generated within the titanium cold spray coatings and substrate. Residual stresses within the cold sprayed titanium coatings have been shown to be of compressive nature. The values found are comparable in magnitude to those found for a Ni-5wt%Al coating deposited by cold spraying [73]. Residual stresses of low magnitude are expected in cold spray coatings because there is no associated quenching stress that is associated with thermal spray methods. The compressive residual stresses within cold spray coatings are primarily due to the peening nature of the process. The compressive stresses in the coating lead to a prediction of a tensile residual stress in the substrate at the interface; however, it should be noted that this region is exposed to peening from the first deposited particles. This results in a compressive residual stress and moves the region of tensile residual stress deeper into the substrate.

It is noted that the size of the substrate used for the beam deflection method employed allowed stress relaxation due to deflection in the sample. If a sample or component was sprayed that did not allow significant stress relaxation to occur, for example the cylindrical dog bone samples used for fatigue testing, then the actual stresses generated would be expected to be higher than those shown in Table 4.11.

4.10.2.5. Fatigue

Application of cold sprayed titanium coatings has been shown to reduce the fatigue endurance limit by up to 15% for an as-received substrate surface finish (Table 4.10). This is due to a modification (roughening) of the substrate surface due to impinging high velocity particles and tensile residual stresses within the substrate at the substrate-coating interface. Moreover, the cylindrical dog bone fatigue substrates used were axisymmetric and would not be deflected during the spray process. Therefore the residual stress states in these samples will be different than those calculated by the beam deflection process, where relaxation can occur via bending. Compressive residual stresses found within coatings are usually associated with increased fatigue endurance limits; however those found within the cold sprayed titanium coatings are too low to prevent fatigue crack formation, and premature fatigue fracture also occurred.

Surface roughening of the substrate will increase the possible number of sites for cracks to nucleate. It is unknown if the cracks initiate at the substrate-coating interface or at the coating free-surface and at what point the coating delaminates from the substrate. Figure 4.44(a) and (b) show the significant effect of the fatigue testing on the bonding within the coating and at the interface. Near to the fracture, areas of the coating have de-bonded along splat boundaries and at the substrate-coating interface. At the shoulder of the sample, where applied stresses were lower, the coating shows little signs of degradation.

The fatigue endurance limit is similar for the grit blasted and grit blasted-and-sprayed samples. Both show a lower fatigue endurance limit than the as-received and sprayed samples. This is due to the grit blasting process deforming the substrate surface and creating more damaging stress raisers. It is notable that the addition of the coating to the as-received sample results in a reduction in fatigue endurance limit of ~96 MPa, whereas the addition of the coating to the grit blasted substrates results in a negligible change in the endurance limit. The stresses in the coatings and substrates for both substrate types are similar, differing by up to around 30 MPa (Table 4.11) and as such do not account for this difference. It must therefore be

concluded that the reduction in endurance limit for the grit blasted substrates is dominated by the stress raisers produced during blasting, leaving it relatively insensitive to any residual stresses resulting from the addition of the coating.

4.10.3. Effect of Heat Treatment on Titanium Coating Properties

The following section discusses the role of heat treatment temperature on the properties of the titanium cold spray coatings. Firstly, the effect that heat treatment temperature has on the coating microstructure and its bonding mechanisms is discussed. Next, the role that any microstructural changes have on the coatings mechanical properties, mainly the coating stiffness, residual stress and fatigue endurance limit of the titanium cold sprayed coating, is considered.

4.10.3.1. Coating Microstructure and Bonding Mechanisms

Heat treatment of the titanium cold spray coatings was found to affect the microstructural and mechanical properties of the deposits. With increasing heat treatment temperature there is an increase in the diffusion constants of various alloying elements within titanium as shown by Figure 4.19. By EDX analysis, the amount of aluminium that has diffused from the Ti6Al4V substrate into the titanium coating was measured. For heat treatments carried out at 800 °C or less, no measurable diffusion of aluminium was observed. At a heat treatment temperature of 1150 °C, diffusion of aluminium was able to occur, as shown by the five order of magnitude increase in the diffusion coefficient of aluminium within titanium shown in Table 4.12. The diffusion process occurring between the Ti6Al4V substrate and titanium coating is directly linked to the increased bond strength indicated by transverse scratch testing as shown in Section 4.8.3.5. Transverse scratch tests showed minimal cracking at the coating-substrate interface for samples heat treated at 1150 °C (Figure 4.52(d)) compared to samples heat treated at lower temperatures (Figure 4.52(b)) or not heat treated at all (Figure 4.39(b)). Etched images of the coating microstructure after a heat treatment at 1150 °C (Figure 4.49) show

significant grain growth across the coating-substrate interface and it is proposed that this is the primary reason for improved coating bond strength.

A similar amount of porosity was found for non-heat treated titanium coatings and titanium coatings heat treated up to 800 °C. For titanium coatings heat treated at 1150 °C, an increase in the amount of porosity measured was found (Table 4.9). Whilst it is not possible for the absolute amount of coating porosity to increase due to heat treatment, it is proposed that the amount of coating porosity resolvable by SEM analysis has increased. This is due to coalescence and 'sphericization' of the porosity; a feature previously observed by McCune et al. [53] and Li et al. [98] for heat treated copper cold spray deposits. Coalescence of pores is also known to readily occur when sintering powders at sufficiently high temperature [140]. In the sintering process, particles are pressed together and heated so that diffusion can readily occur at points where the particles are in contact. In the initial stages of sintering, the contact area between neighbouring particles will grow and necks between particles will form. Eventually these necks will grow sufficiently large so that they overlap, grain growth between the particles is able to occur and the surface areas of any residing pores will reduce [79]. This causes the powder to densify and any residual porosity remains as spherical holes by means of reducing the surface tension [79, 140]. Sintering of titanium and its alloys is typically carried out at temperatures in the range of 1000 °C to 1300 °C with a holding period of up to two hours [14, 79, 141, 142]. These conditions are similar to the highest heat treatment temperature used for this study and therefore similar mechanisms to those found during the sintering process may be expected to occur. For the coatings produced in this study it may be expected that during heat treating, pores and oxides are removed from areas of the coating microstructure where a high level of bonding is apparent by grain growth during the annealing process. The pores and oxides will eventually reside in areas of the coating microstructure where weaker bonding is apparent and the mechanisms required to remove the pores and oxides from these areas are not available. Evidence of coalescence of pores within titanium deposits is identified most clearly in deposits heat treated at 1150 °C (Figure 4.48(c)). Where coalescence of pores has not occurred, it is difficult to identify individual particles within the deposit, indicating improved bonding. For titanium deposits heat treated at 800 °C,

the microstructure shows some evidence of coalescence of pores (Figure 4.48(b)); however it is still possible for individual particles within the deposits to be identified as they are still surrounded by pores and defects resolvable by the SEM. Transverse scratch test images for a titanium coating heat treated at 800 °C (Figure 4.52(b)) showed significant cracking between particle boundaries, comparable in nature to the cracking observed within a non-heat treated sample (Figure 4.39(b)). Cracks are still able to readily form within deposits heat treated at 800 °C because coalescence of pores has not fully occurred, still leaving a significant fraction of particles within the coating surrounded by defects that will readily allow cracks to propagate throughout the coating microstructure. This is in stark contrast to a titanium coating heat treated at 1150 °C where minimal cracking was found to occur within the coating itself during transverse scratch testing (Figure 4.52(d)). It is therefore evident that heat treatment of the titanium coating above the β transus temperature of approximately 900 °C improves the bonding between individual particles.

Table 4.8 shows that the average coating hardness increases a small amount with heat treatment temperature. This is a direct consequence of improved bonding within the coating itself, due to recrystallisation. There is only a minor variation in the coating hardness after heat treatments were carried out at temperatures between 600 °C and 1150 °C. This indicates that a large proportion of the recrystallisation process readily occurs at a heat treatment temperature of 600 °C. The errors shown for the hardness results are large and highlight the fact that a large variation of the coating hardness was found throughout the samples. This indicates that despite heat treating a large variation in the bonding and number of defects within the coating may still be expected.

4.10.3.2. Coating Stiffness

A similar modulus ratio was measured for titanium coatings heat treated up to 800 °C compared to non-heat treated samples (Table 4.9). This is not surprising when considering the minor variations in the coatings microstructure and bonding between particles within the coatings themselves, highlighted by transverse scratch testing.

The modulus ratio was found to be approximately double for a titanium coating heat treated at 1150 °C.

The Eshelby model (Figure 4.38) identifies pores of low aspect ratio (i.e. those surrounding particles and orientated as through-thickness cracks) as being highly detrimental to the coating modulus. Heat treating the titanium coating samples at 1150 °C has reduced the number of pores and defects surrounding particles. By comparing the pore aspect ratio measured by image analysis of a titanium coating non-heat treated and heat treated at 1150 °C (Figure 4.51), fewer pores of small aspect ratio that may be resolvable by the SEM image analysis technique (Section 4.9.2.1.), were found within the coatings microstructure after heat treating at 1150 °C. Figure 4.38 shows that by reducing the volume fraction of pores with low aspect ratio an increase in the coating modulus ratio may be expected.

The increase in the modulus ratio after heat treating the titanium deposits at a heat treatment temperature of 1150 °C is expected to also be partly due to improved bonding at the coating-substrate interface and improved bonding within the coating itself as identified by transverse scratch testing in Figure 4.52(d). An improvement in bonding at the coating-substrate interface will prevent lateral shear from occurring during the four point bend modulus testing which would otherwise lead to a lower than actual coating modulus being measured, as discussed in Section 4.9.2.3. Furthermore, by improving bonding between individual particles within the coating itself, there are fewer defects within the coating that have zero stiffness on the application of a load, again leading to an increased coating modulus.

4.10.3.3. Coating Residual Stress and Fatigue Endurance Limit

The amount of beam deflection due to cold spraying was measured after deposition. Subsequent measurements of the amount of beam deflection were made after heat treatment. A reduction in the residual stresses found within the titanium coatings was found with increasing heat treatment temperature as shown in Table 4.11. Heat

treatment reduces the residual stresses measured within the samples due to relaxation of the sample occurring.

The original magnitude of the compressive residual stresses for non-heat treated samples is sufficiently low so that any benefit in preventing fatigue crack formation is expected to be minimal. In fact, a 15 % reduction in the fatigue endurance limit for a non-coated and coated Ti6Al4V substrate was found in the non-heat treated state. Heat treating led to a further reduction in the measured compressive residual stresses found within the coating and therefore it is not surprising that an even greater reduction in fatigue endurance limit was found due to the application of a cold spray coating which had been subsequently heat treated; for example up to a 37 % reduction in the fatigue endurance limit due to the cold sprayed coating for a sample heat treated at 800 °C was found.

It is noted that the technique used to measure residual stresses within the coating allows for stress relaxation to occur as the beam deflects due to spraying. Therefore higher residual stresses may be anticipated in the fatigue samples where no stress relaxation is able to occur. Accordingly during heat treating, stress relaxation, and therefore further reduction of the measured residual stresses within the sample, would not occur to the same degree within the fatigue samples. Therefore if the compressive residual stresses remain higher within the fatigue coated samples after heat treating, compared to the measured values shown in Table 4.11, there must be other reasons for the further reductions in their fatigue endurance limits. One possibility is that the heat treating process improves the bonding between the coating and substrate by diffusion bonding processes. Therefore, it may be expected that it would be easier for cracks which initiate at the coating top surface, due to stress raisers formed because of the rough coating surface, to propagate more readily from the coating into the substrate and cause premature failure.

By comparing Figure 4.53(a) with Figure 4.43(a) it is shown that fatigue samples heat treated at 800 °C show a similar fatigue fracture surface to non heat treated fatigue samples. A greater amount of coating delamination was found at the fatigue

fracture surface for samples heat treated at 800 °C but it is not clear if cracks were able to more readily propagate from the coating into the substrate. Furthermore, transverse scratch testing of titanium coatings heat treated at 800 °C (Figure 4.52(b)) appeared to show minimal improvement in bonding between the coating and substrate compared to a non-heat treated sample (Figure 4.39(b)). Therefore it can not be clearly ascertained if cracks were able to more readily propagate from the coating to the substrate and the fatigue failure mechanisms remains unclear for this case.

Figure 4.55(b) shows the fatigue fracture surface of a titanium coating heat treated at 1150 °C. Due to the heat treatment and diffusion bonding processes it is difficult to identify the coating-substrate interface. It has been shown previously by transverse scratch testing that bonding between the substrate and coating can be expected and this will make it easier for cracks that initiate on the coating top surface to propagate from the coating into the substrate and cause premature failure. More importantly, the fatigue fracture surface of the samples heat treated at 1150 °C shown in Figure 4.55(a) shows a brittle fracture surface and this is expected to be the predominant fracture mechanism in this case. Despite heat treatment occurring within an argon atmosphere it may be expected for some oxygen to be present within the furnace. Brittle fracture occurs due to diffusion of oxygen during the heat treatment process allowing oxygen embrittlement to occur.

4.10.4. Shrouded Arc Coating Properties

The shrouded arc coating microstructure is shown in Figure 4.57. The main microstructural difference between the shrouded arc coatings and cold spray coatings is the formation of oxides between particles found within the shrouded arc coatings. Oxides appear to have readily formed despite the use of a shrouded inert atmosphere. Porosity levels appear lower than the cold spray coatings and are evenly distributed around the coating cross section. In comparison, cold spray coatings tend to show a larger amount of porosity at the coating top surface, due to a reduction in compaction of the coating from further impinging particles. The shrouded arc coatings showed

evidence of cracking in the top portion of the coating surface. Cracks occur due to quenching stresses.

The shrouded arc samples had a measured modulus value of 40 GPa or approximately a third of the bulk modulus value. In plasma spraying, Kuroda and Clyne [104] show that coatings of a wide range of materials also have a modulus of approximately a third of the corresponding bulk value. The low modulus values found were attributed to the poor lateral bonding between individual splats [104].

A small tensile residual stress was found within the coating of the shrouded arc samples and is shown in Table 4.11. This is not unusual for thermally sprayed coatings and has been identified previously by other workers [73, 104]. Tensile residual stresses form within thermally sprayed coatings because of the build up of quenching stresses as the coating cools on impact.

A significantly lower fatigue endurance limit was found for the shrouded arc samples compared to the cold sprayed samples. Samples used for shrouded arc spraying were grit blasted by the industrial partner prior to spraying. The grit employed at by the industrial partner gave a greater substrate surface roughness to that grit blasted at the University of Nottingham as shown in Table 4.6. Therefore it is not surprising that samples grit blasted by the industrial partner had a lower fatigue endurance limit to those grit blasted at the University of Nottingham due to more damaging stress raisers at the substrate surface. In the case of the cold sprayed titanium samples, no further reduction in the fatigue endurance limit was found on the application of titanium cold sprayed coatings to a grit blasted substrate. However, at least a 56 % reduction in the fatigue endurance limit was found on application of a titanium shrouded arc coating (Table 4.10). The fatigue fracture surface of the shrouded arc sample, Figure 4.58, appears similar to those discussed previously for a cold sprayed titanium coating. It is proposed that the measured tensile residual stresses, commonly identified in thermally sprayed deposits, have allowed cracks to readily form and propagate through the coating. A cross-sectional image of the coating microstructure, Figure 4.57, and fatigue fracture, Figure 4.59, has shown cracks form on the coating top surface. On application of a fatigue load these cracks will act as initiation sites for further cracks to propagate and cause premature failure.

4.11. Conclusions

Titanium coatings have been successfully deposited using CGDS and a range of mechanical properties have been evaluated. Substrate condition, process parameters and post-spray heat treatment have all been found to influence the mechanical properties of the coatings produced. To increase general understanding of the CGDS process copper and aluminium coatings were also produced and compared to titanium coatings.

By microstructural examination, the titanium coatings appeared to be well bonded and of low porosity. Due to the nature of deposition, compressive residual stresses of low magnitude were measured for the CGDS coatings. These results were comparable to those found by others investigating CGDS coatings. Compressive residual stresses found within a coating are regarded as a favourable property, especially in the case of fatigue, where the compressive residual stresses may prevent fatigue crack nucleation. However, despite the compressive residual stress within the coating, a reduction in the fatigue endurance limit of a Ti6Al4V substrate of up to 15 % was measured when comparing coated and non-coated samples. This was due to induced tensile residual stresses within the substrate and the low magnitude of the compressive residual stresses within the coating being insufficient to prevent fatigue crack formation from occurring. The rough top surface of the coating would have also created preferential sites for fatigue cracks to propagate, stress-raisers, and therefore these will also reduce the fatigue endurance limit of the sample. This was also observed when comparing an as-received surface substrate condition with substrates that had been grit blasted and once again occurs due to stress-raisers being created at the sample surface.

By four point bend testing, titanium CGDS coatings were found to have a significantly lower modulus than bulk titanium. Using the same test procedure, copper and aluminium CGDS coatings were also found to have lower modulus values than their corresponding bulk material. The low modulus values found in all three coating types were attributed to poor bonding found between splats within the CGDS coatings. An Eshelby model was used to predict that defects and pores

surrounding particles and orientated as through-thickness cracks are the most detrimental in reducing a coatings modulus.

Transverse scratch testing was used to visually show the poor bonding between splats. Cracking was found to readily occur within the coating along splat boundaries. To investigate why poor bonding occurred at splat boundaries a method for characterising the bonding between splats within a CGDS coating was developed. CGDS coatings were produced using a blended aluminium-copper powder and subsequently heat treated. An intermetallic layer was observed to form at particle boundaries following a short annealing treatment at 400 °C. The coverage of particle interfaces was found to be non-uniform. This was attributed to the incomplete break-up of oxide films which act as diffusion barriers and provides a good indication of the degree of metal to metal contact in the as-sprayed deposit. By increasing particle velocity in the CGDS process a greater degree of direct metal contact between particles in the deposit was achieved.

The effect of heat treating titanium CGDS coatings was investigated and some improvements in the coating mechanical properties were made. For heat treatment temperatures of 800 °C or below minimal variation in the coating properties was measured. At a heat treatment temperature of 1150 °C diffusion bonding was found to readily occur at the substrate-coating interface and between splats within the coating itself. By transverse scratch testing this was visually shown to produce a coating that had significantly less coating break up between splats and at the coating-substrate interface compared to a non-heat treated coating. However, despite an argon furnace being used, oxygen embrittlement of the substrate was found to be a detrimental effect. Oxygen embrittlement led to brittle fracture of the substrate during four point bend testing, used to measure the coatings modulus.

In comparison to titanium coatings applied by a shrouded arc coating process, the properties of cold sprayed titanium coatings were found to be favourable. In particular, a significantly lower fatigue endurance limit was measured for shrouded arc titanium coatings and attributed to formation of tensile residual stresses within the coating on impact cooling.

Chapter 5 – Overall Conclusions and Future Work

This study has shown that titanium coatings may be successfully produced by the CGDS process. Various mechanical properties of the titanium coatings were evaluated to characterise the coatings produced. Of the mechanical properties measured of particular interest was the high coating to substrate bond strength, favourable compressive residual stresses within the coating, and a relatively low reduction in the fatigue endurance limit of the Ti6Al4V substrate compared to the application of a titanium coating produced by an alternative coating process, shrouded arc spraying.

General understanding of the CGDS coating process was furthered by depositing aluminium and copper coatings and assessing the coating stiffness and the level of bonding within the coating. A low coating modulus was found for all three coating types assessed and attributed to poor bonding between splats within the coating itself. The poor bonding within the CGDS coatings were shown visually by two methods; firstly, depositing a blended aluminium and copper powder and subsequently heat treating the produced coating. The heat treatment process allowed intermetallics to form between the aluminium and copper splats but this was found to occur only at a limited number of splat interfaces. Intermetallics would only form at regions where true metal to metal bonding had occurred during the deposition process and therefore indicated that bonding does not occur readily between splats within cold spray deposits. Secondly, transverse scratch testing showed that upon application of a load the coating was found to crack readily along splat interfaces. An improvement in the bonding within titanium deposits was made by heat treating, allowing diffusion bonding to occur between splats. However, improvements were only readily made at heat treatment temperatures of 1150 °C, and therefore this is not regarded as a particularly favourable method.

Particle velocities of a copper and titanium powder have been successfully measured by a PIV technique during deposition. Small particle sizes (typically less than 10 μm in diameter) were measured to have a lower particle velocity than larger particles. In some cases the particle velocity of these small particles was found to be sufficiently low that deposition would not be expected to occur. Therefore these results may be used in the future to optimise the size distribution of a powder size used as a feedstock for the CGDS process, leading to an increase in the deposition efficiency. Measured particle velocities were compared to the output from a model output and reasonable agreement between the two was found. The model was unable to predict the reduction in particle velocity for small particle sizes and was generally found to overestimate particle velocities. This may be explained by the assumptions made during the modelling process. Despite the limitations of model, when varying spray parameters, it was still able to predict similar trends to those measured by the PIV equipment. For these effects to be modelled successfully it is recommended that the use of CFD is employed to allow a model to be produced of greater accuracy to the one currently used.

A key advantage of cold spraying is that it allows coatings to be deposited at room temperature. This allows powders to be deposited that would normally require an inert atmosphere during deposition to prevent the formation of unwanted oxides. If only small increases (~ 500 °C) are made to the gas temperature, then powder properties that may be temperature dependent, oxide levels etc, are not expected to be affected due to the relatively small increase in gas temperature (remaining below the melting temperature of the powder) and the small time period that the powder is exposed to the temperature increase. If sufficient increases in gas velocity are made then there is the possibility for heated nitrogen gas to be employed. This is advantageous due to the high cost of helium gas, which as of January 2007, costs approximately ten times more than nitrogen. For the cold spraying process to be developed successfully, economically viable gases such as nitrogen or air must be developed. Therefore further modelling work and particle velocity measurements should also be made, using heated gas, to investigate their effect on particle impact velocity. If these results are favourable then coatings should be deposited utilising heated gas and their mechanical properties investigated.

Some techniques developed within this study could be further developed. For example, the methodology of investigating the bonding mechanisms within coatings using a blended aluminium-copper powder may also be used be used to investigate the level of bonding between a substrate and coating, if two dissimilar materials are employed and where an intermetallic layer is known to form during elevated temperature annealing. It is argued that initial particle impacts act to condition the substrate by removing pre-existing oxide layers and particles which arrive subsequently are then able to form a bond. It could thus be expected that oxide is not removed completely from the substrate surface and therefore bonding between substrate and depositing particles is not uniform but contains weak links. This methodology may also be used with other blended powders to investigation what variation in results is found.

Ultimately this project has shown that titanium coatings produced by the CGDS process show favourable coating properties. The next stage would be to develop these coatings in terms of their biomedical properties. HA has been described previously as being particularly advantageous in promoting bone growth and fixation to implants. It would therefore be of particular interest to determine the feasibility and optimisation of using the CGDS process to produce a blended titanium / HA powder. The mechanical properties of the blended titanium / HA coatings may be compared to the pure titanium coatings produced in this study as well as their biocompatibility assessed.

References

1. D. Rickerby and A. Matthews, *Advanced surface coatings: a handbook of surface engineering*. 1991, Glasgow: Blackie.
2. D. Williams, Revisiting the Definition of Biocompatibility. *Medical Device Technology,* 2003, Vol 14, p 10-13
3. J.Y. Rho, L. Kuhn-Spearing, and P. Zioupos, Mechanical properties and the hierarchical structure of bone. *Medical Engineering & Physics,* 1998, Vol 20, p 92-102
4. S.M. Kenny and M. Buggy, Bone cements and fillers: A review. *Journal Of Materials Science-Materials In Medicine,* 2003, Vol 14, p 923-938
5. M.J. Dalby, L. Di Silvio, E.J. Harper, and W. Bonfield, Increasing hydroxyapatite incorporation into poly(methylmethacrylate) cement increases osteoblast adhesion and response. *Biomaterials,* 2002, Vol 23, p 569-576
6. B.D. Ratner, A.S. Hoffman, F.J. Schoen, and J.E. Lemons, *Biomaterials Science - An Introduction to Materials in Medicine*. 1996, San Diego, California: Academic Press.
7. J.A. D'Antonio, W.N. Capello, M.T. Manley, and R. Geesink, Hydroxyapatite femoral stems for total hip arthroplasty - 10-to 13-year followup. *Clin. Orthop.,* 2001, p 101-111
8. G. Rizzi, A. Scrivani, M. Fini, and R. Giardino, Biomedical coatings to improve the tissue-biomaterial interface. *Int. J. Artificial Organs,* 2004, Vol 27, p 649-657
9. Y.Z. Yang, K.H. Kim, and J.L. Ong, Review on calcium phosphate coatings produced using a sputtering process - an alternative to plasma spraying. *Biomaterials,* 2005, Vol 26, p 327-337
10. H. Liang, B. Shi, A. Fairchild, and T. Cale, Applications of plasma coatings in artificial joints: an overview. *Vacuum,* 2004, Vol 73, p 317-326
11. D.J. Blackwood, Biomaterials: Past successes and future problems. *Corrosion Reviews,* 2003, Vol 21, p 97-124
12. G. Lütjering and J.C. Williams, *Titanium*. 2003, Berlin: Springer-Verlag.
13. J.R. Davis, *Metals handbook*. 2nd ed, ed. J.R. Davis. 1998, Materials Park, OH, USA: ASM International.
14. D.M. Brunette, P. Tengvall, M. Textor, and P. Thomsen, *Titanium in medicine: material science, surface science, engineering, biological responses and medical applications*. 2001, London: Springer-Verlag.
15. S.G. Steinemann, Titanium - the material of choice? *Periodontology 2000,* 1998, Vol 17, p 7-21
16. J. Dumbleton and M.T. Manley, Current concepts review - Hydroxyapatite-coated prostheses in total hip and knee arthroplasty. *J. Bone. Joint. Surg. Am.,* 2004, Vol 86A, p 2526-2540
17. P. Cheang and K.A. Khor, Addressing processing problems associated with plasma spraying of hydroxyapatite coatings. *Biomaterials,* 1996, Vol 17, p 537-544
18. Y.C. Tsui, C. Doyle, and T.W. Clyne, Plasma sprayed hydroxyapatite coatings on titanium substrates Part 1: Mechanical properties and residual stress levels. *Biomaterials,* 1998, Vol 19, p 2015-2029

19. C. Anderson Engh, C. Sychters, and C.E. Sr, Factors affecting femoral bone remodeling after cementless total hip arthroplasty. *The Journal of Arthroplasty,* 1999, Vol 14, p 637
20. J.L. Ong, M. Appleford, S. Oh, Y. Yang, W.H. Chen, J.D. Bunigardner, and W.O. Haggard, The characterization and development of bioactive hydroxyapatite coatings. *Jom,* 2006, Vol 58, p 67-69
21. L.M. Sun, C.C. Berndt, K.A. Gross, and A. Kucuk, Material fundamentals and clinical performance of plasma-sprayed hydroxyapatite coatings: A review. *Journal Of Biomedical Materials Research,* 2001, Vol 58, p 570-592
22. C.Y. Yang, R.M. Lin, B.C. Wang, T.M. Lee, E. Chang, Y.S. Hang, and P.Q. Chen, In vitro and in vivo mechanical evaluations of plasma-sprayed hydroxyapatite coatings on titanium implants: The effect of coating characteristics. *Journal Of Biomedical Materials Research,* 1997, Vol 37, p 335-345
23. Y.C. Tsui, C. Doyle, and T.W. Clyne, Plasma sprayed hydroxyapatite coatings on titanium substrates Part 2: optimisation of coating properties. *Biomaterials,* 1998, Vol 19, p 2031-2043
24. F.J. Gil, A. Padros, J.M. Manero, C. Aparicio, M. Nilsson, and J.A. Planell, Growth of bioactive surfaces on titanium and its alloys for orthopaedic and dental implants. *Materials Science & Engineering C-Biomimetic And Supramolecular Systems,* 2002, Vol 22, p 53-60
25. K. Hayashi, T. Inadome, H. Tsumura, Y. Nakashima, and Y. Sugioka, Effect of surface-Roughness of hydroxyapatite-coated titanium on the bone-implant interface shear-strength. *Biomaterials,* 1994, Vol 15, p 1187-1191
26. K. Gotfredsen, A. Wennerberg, C. Johansson, L.T. Skovgaard, and E. Hjortinghansen, Anchorage of TiO2-blasted, Ha-coated, and machined implants - An experimental-study with rabbits. *Journal Of Biomedical Materials Research,* 1995, Vol 29, p 1223-1231
27. A. Wennerberg, T. Albrektsson, C. Johansson, and B. Andersson, Experimental study of turned and grit-blasted screw-shaped implants with special emphasis on effects of blasting material and surface topography. *Biomaterials,* 1996, Vol 17, p 15-22
28. W.J. Donelly, W.J. Kobayashi, M.A.R. Freeman, T.W. Chin, H. Yeo, W. M., and G. Scott, Radiological and survival comparison of four methods of fixation of a proximal femoral stem. *J. Bone. Joint. Surg. Br.,* 1997, Vol 79-B, p 351-360
29. K. Hayashi, T. Mashima, and K. Uenoyama, The effect of hydroxyapatite coating on bony ingrowth into grooved titanium implants. *Biomaterials,* 1999, Vol 20, p 111-119
30. K.G. Nilsson, J. Karrholm, L. Carlsson, and T. Dalen, Hydroxyapatite coating versus cemented fixation of the tibial component in total knee arthroplasty - Prospective randomized comparison of hydroxyapatite-coated and cemented tibial components with 5-year follow-up using radiostereometry. *Journal Of Arthroplasty,* 1999, Vol 14, p 9-20
31. O. Mouzin, K. Soballe, and J.E. Bechtold, Loading improves anchorage of hydroxyapatite implants more than titanium implants. *Journal Of Biomedical Materials Research,* 2001, Vol 58, p 61-68
32. R.G.T. Geesink, Osteoconductive coatings for total joint arthroplasty. *Clin. Orthop.,* 2002, p 53-65

33. S.A. Hacking, M. Tanzer, E.J. Harvey, J.J. Krygier, and J.D. Bobyn, Relative contributions of chemistry and topography to the osseointegration of hydroxyapatite coatings. *Clin. Orthop.,* 2002, p 24-38
34. N. Aebli, J. Krebs, H. Stich, P. Schawalder, M. Walton, D. Schwenke, H. Gruner, B. Gasser, and J.C. Theis, In vivo comparison of the osseointegration of vacuum plasma sprayed titanium- and hydroxyapatite-coated implants. *J. Biomed. Mater. Res. Part A,* 2003, Vol 66A, p 356-363
35. A. Eckardt, H.M. Aberman, H.D. Cantwell, and J. Heine, Biological fixation of hydroxyapatite-coated versus grit- blasted titanium hip stems: a canine study. *Arch. Orthop. Trauma. Surg.,* 2003, Vol 123, p 28-35
36. V. Shukla, G.S. Elliott, B.H. Kear, and L.E. McCandlish, Hyperkinetic deposition of nanopowders by supersonic rectangular jet impingement. *Scripta Materialia,* 2001, Vol 44, p 2179-2182
37. R.C. McCune, A.N. Papyrin, J.N. Hall, W.L. Riggs II, and P.H. Zajchowski. An Exploration of the Cold Gas-Dynamic Spray Method for Several Materials Systems. in *8th National Thermal Spray Conference*. 1995. Houston, Texas: ASM International.
38. R.W. Smith and R.D. Fast, The Future Of Thermal Spray Technology. *Welding Journal,* 1994, Vol 73, p 43-50
39. A.E. Segall, A.N. Papyrin, J.C. Conway, and D. Shapiro, A cold-gas spray coating process for enhancing titanium. *Jom-Journal Of The Minerals Metals & Materials Society,* 1998, Vol 50, p 52-54
40. B. Wielage, A. Wank, H. Pokhmurska, T. Grund, C. Rupprecht, G. Reisel, and E. Friesen, Development and trends in HVOF spraying technology. *Surf. Coat. Technol.,* 2006, Vol 201, p 2032-2037
41. R. Halldearn. *Arc Spraying (Knowledge Summary)*. 2003; Available from: http://www.twi.co.uk/j32k/protected/band_3/ksrdh002.html.
42. R.C. Dykhuizen and M.F. Smith, Gas dynamic principles of cold spray. *J. Therm. Spray Technol.,* 1998, Vol 7, p 205-212
43. H. Kreye and T. Stoltenhoff. Cold Spraying - A Study of Process and Coating Characteristics. in *Thermal Spray: Surface Eng via Applied Research, ITSC*. 2000. Montreal, Quebec, Canada: ASM International.
44. C. Borchers, F. Gartner, T. Stoltenhoff, and H. Kreye, Microstructural bonding features of cold sprayed face centered cubic metals. *J. Appl. Phys.,* 2004, Vol 96, p 4288-4292
45. C.J. Li and W.Y. Li, Deposition characteristics of titanium coating in cold spraying. *Surf. Coat. Technol.,* 2003, Vol 167, p 278-283
46. J. Vlcek, H. Huber, H. Voggenreiter, A. Fischer, E. Lugscheider, H. Hallen, and G. Pache. Kinetic Powder Compaction Applying the Cold Spray Process A Study on Parameters. in *Thermal Spray 2001: New Surfaces for a New Millennium*. 2001. Singapore: ASM International.
47. T. Schmidt, F. Gartner, H. Assadi, and H. Kreye, Development of a generalized parameter window for cold spray deposition. *Acta Mater.,* 2006, Vol 54, p 729-742
48. T. Stoltenhoff, H. Kreye, and H.J. Richter, An analysis of the cold spray process and its coatings. *J. Therm. Spray Technol.,* 2002, Vol 11, p 542-550
49. H. Choi, S. Yoon, S. Uhm, and C. Lee, Characterization of the spraying beads deposited by the kinetic spraying process. *Surf. Coat. Technol.,* 2005, Vol 192, p 374-381

50. S.V. Klinkov, V.F. Kosarev, and M. Rein, Cold spray deposition: Significance of particle impact phenomena. *Aerospace Science And Technology,* 2005, Vol 9, p 582-591
51. M. Grujicic, C.L. Zhao, W.S. DeRosset, and D. Helfritch, Adiabatic shear instability based mechanism for particles/substrate bonding in the cold-gas dynamic-spray process. *Materials & Design,* 2004, Vol 25, p 681-688
52. M. Grujicic, J.R. Saylor, D.E. Beasley, W.S. DeRosset, and D. Helfritch, Computational analysis of the interfacial bonding between feed-powder particles and the substrate in the cold-gas dynamic-spray process. *Applied Surface Science,* 2003, Vol 219, p 211-227
53. R.C. McCune, W.T. Donlon, O.O. Popoola, and E.L. Cartwright, Characterization of copper layers produced by cold gas-dynamic spraying. *J. Therm. Spray Technol.,* 2000, Vol 9, p 73-82
54. T.H. Van Steenkiste, J.R. Smith, R.E. Teets, J.J. Moleski, D.W. Gorkiewicz, R.P. Tison, D.R. Marantz, K.A. Kowalsky, W.L. Riggs, P.H. Zajchowski, B. Pilsner, R.C. McCune, and K.J. Barnett, Kinetic spray coatings. *Surf. Coat. Technol.,* 1999, Vol 111, p 62-71
55. T.H. Van Steenkiste, J.R. Smith, and R.E. Teets, Aluminum coatings via kinetic spray with relatively large powder particles. *Surf. Coat. Technol.,* 2002, Vol 154, p 237-252
56. T.Y. Han, Z.B. Zhao, B.A. Gillispie, and J.R. Smith, Effects of spray conditions on coating formation by the kinetic spray process. *J. Therm. Spray Technol.,* 2005, Vol 14, p 373-383
57. J. Lee, S. Shin, H. Kim, and C. Lee, Effect of gas temperature on critical velocity and deposition characteristics in kinetic spraying. *Applied Surface Science,* 2007, Vol 253, p 3512-3520
58. P. Oosthuizen, H. and W. Carscallen, E., *Compressible Fluid Flow*. 1st ed. 1997, New York: McGraw Hill.
59. T. Stoltenhoff, H. Kreye, H.J. Richter, and H. Assadi. Optimisation of the Cold Spray Process. in *Thermal Spray 2001: New Surfaces for a new Millennium*. 2001. Singapore: ASM International.
60. R. Clift, J.R. Grace, and M.R. Weber, *Bubbles, Drops and Particles*. 1978, New York: Academic Press.
61. A.B. Bailey and J. Hiatt, Sphere drag coefficients for a broad range of mach and reynolds-numbers. *Aiaa J.,* 1972, Vol 10, p 1436-&
62. M.J. Walsh, Drag Coefficient Equations For Small Particles In High-Speed Flows. *Aiaa J.,* 1975, Vol 13, p 1526-1528
63. C.B. Henderson, Drag coefficients of spheres in continuum and rarefied flows. *Aiaa J.,* 1976, Vol 14, p 707-708
64. M.J. Walsh, Drag Coefficient Of Spheres In Continuum And Rarefied Flows - Reply. *Aiaa J.,* 1977, Vol 15, p 893-894
65. T. Marrocco, D.G. McCartney, P.H. Shipway, and A.J. Sturgeon, Production of titanium deposits by cold-gas dynamic spray: Numerical modeling and experimental characterization. *J. Therm. Spray Technol.,* 2006, Vol 15, p 263-272
66. T. Stoltenhoff, J. Voyer, and H. Kreye. Cold spraying - state of the art and applicability. in *International Thermal Spray Conference*. 2002. Essen, Germany: DVS Deutscher Verband für Schweißen.

67. B. Jodoin, F. Raletz, and M. Vardelle, Cold spray modeling and validation using an optical diagnostic method. *Surf. Coat. Technol.*, 2006, Vol 200, p 4424-4432
68. M. Grujicic, C.L. Zhao, C. Tong, W.S. Derosset, and D. Helfritch, Analysis of the impact velocity of powder particles in the cold-gas dynamic-spray process. *Mater. Sci. Eng. A,* 2004, Vol 368, p 222-230
69. J. Prehm and K. Hartz, Diagnostics in Thermal Spraying Processes, in *Modern Surface Technology*, F.-W. Bach, A. Laarmann, and T. Wenz, Editors. 2006, Wiley-VCH: Weinheim, Germany. p 191-203.
70. D.L. Gilmore, R.C. Dykhuizen, R.A. Neiser, T.J. Roemer, and M.F. Smith, Particle velocity and deposition efficiency in the cold spray process. *J. Therm. Spray Technol.,* 1999, Vol 8, p 576-582
71. J.W. Wu, H.Y. Fang, S. Yoon, H. Kim, and C. Lee, Measurement of particle velocity and characterization of deposition in aluminum alloy kinetic spraying process. *Applied Surface Science,* 2005, Vol 252, p 1368-1377
72. F. Raletz, M. Vardelle, and G. Ezo'o, Critical particle velocity under cold spray conditions. *Surf. Coat. Technol.,* 2006, Vol 201, p 1942-1947
73. S. Sampath, X.Y. Jiang, J. Matejicek, L. Prchlik, A. Kulkarni, and A. Vaidya, Role of thermal spray processing method on the microstructure, residual stress and properties of coatings: an integrated study for Ni-5 wt.%Al bond coats. *Mater. Sci. Eng. A,* 2004, Vol 364, p 216-231
74. H. Fukanuma, N. Ohno, B. Sun, and R.Z. Huang, In-flight particle velocity measurements with DPV-2000 in cold spray. *Surf. Coat. Technol.,* 2006, Vol 201, p 1935-1941
75. J. Vlcek, J. Zwick, H. Huber, U. Schnaut, E. Lugscheider, Ottobrunn, and D. Aachen. Spray Forging of Powder Material Applying the Cold Spray Process. in *International Thermal Spray Conference*. 2002. Essen, Germany: DVS Deutscher Verband für Schweißen.
76. G. Mauer, R. Vassen, and D. Stover, Comparison and applications of DPV-2000 and accuraspray-g3 diagnostic systems. *J. Therm. Spray Technol.,* 2007, Vol 16, p 414-424
77. D.R. Lide, *CRC handbook of chemistry and physics: a ready-reference book of chemical and physical data.* 82nd ed. 2001, Boca Raton, Florida: CRC Press.
78. J. Karthikeyan, C.M. Kay, and J. Lindeman. Cold Spray Processing of Titanium Powder. in *Thermal Spray: Surface Eng via Applied Research, ITSC*. 2000. Montreal, Quebec, Canada: ASM International.
79. R.M. German, *A-Z of Powder Metallurgy*. 1st ed. 2005, Oxford: Elsevier.
80. D.C. Montgomery, *Applied statistics and probability for engineers*, ed. D.C. Montgomery and G.C. Runger. 2007, Hoboken, N.J.: John Wiley & Sons.
81. B.V. Liengme, *A Guide to Microsoft Excel for Scientists and Engineers*. 2nd ed. 2000, Oxford: Butterworth-Heinemann.
82. R.S. Lima, A. Kucuk, C.C. Berndt, J. Karthikeyan, C.M. Kay, and J. Lindemann, Deposition efficiency, mechanical properties and coating roughness in cold-sprayed titanium. *J. Mater. Sci. Lett.,* 2002, Vol 21, p 1687-1689
83. T. Novoselova, P. Fox, R. Morgan, and W. O'Neill, Experimental study of titanium/aluminium deposits produced by cold gas dynamic spray. *Surf. Coat. Technol.,* 2006, Vol 200, p 2775-2783

84. R. Morgan, P. Fox, J. Pattison, C. Sutcliffe, and W. O'Neill, Analysis of cold gas dynamically sprayed aluminium deposits. *Mater. Lett.*, 2004, Vol 58, p 1317-1320
85. R.C. Dykhuizen, M.F. Smith, D.L. Gilmore, R.A. Neiser, X. Jiang, and S. Sampath, Impact of high velocity cold spray particles. *J. Therm. Spray Technol.*, 1999, Vol 8, p 559-564
86. C. Borchers, F. Gartner, T. Stoltenhoff, H. Assadi, and H. Kreye, Microstructural and macroscopic properties of cold sprayed copper coatings. *J. Appl. Phys.*, 2003, Vol 93, p 10064-10070
87. T. Van Steenkiste and J.R. Smith, Evaluation of coatings produced via kinetic and cold spray processes. *J. Therm. Spray Technol.*, 2004, Vol 13, p 274-282
88. T. Stoltenhoff, C. Borchers, F. Gartner, and H. Kreye, Microstructures and key properties of cold-sprayed and thermally sprayed copper coatings. *Surf. Coat. Technol.*, 2006, Vol 200, p 4947-4960
89. M. Peters, J. Hemptenmacher, J. Kumpfert, and C. Leyens, Structure and Properties of Titanium and Titanium Alloys, in *Titanium and Titanium Alloys: fundamentals and applications*, C. Leyens and M. Peters, Editors. 2003, Wiley-VCH: Weinheim. p 1-36.
90. S. Shin, S. Yoon, Y. Kim, and C. Lee, Effect of particle parameters on the deposition characteristics of a hard/soft-particles composite in kinetic spraying. *Surf. Coat. Technol.*, 2006, Vol 201, p 3457-3461
91. Y. Xu and I.M. Hutchings, Cold spray deposition of thermoplastic powder. *Surf. Coat. Technol.*, 2006, Vol 201, p 3044-3050
92. C.J. Li, W.Y. Li, Y.Y. Wang, G.J. Yang, and H. Fukanuma, A theoretical model for prediction of deposition efficiency in cold spraying. *Thin Solid Films,* 2005, Vol 489, p 79-85
93. H. Assadi, F. Gartner, T. Stoltenhoff, and H. Kreye, Bonding mechanism in cold gas spraying. *Acta Mater.*, 2003, Vol 51, p 4379-4394
94. V.K. Champagne, D. Helfritch, P. Leyman, S.G. Ahl, and B. Klotz, Interface material mixing formed by the deposition of copper on aluminum by means of the cold spray process. *J. Therm. Spray Technol.*, 2005, Vol 14, p 330-334
95. J.W. Wu, H.Y. Fang, S. Yoon, H. Kim, and C. Lee, The rebound phenomenon in kinetic spraying deposition. *Scripta Materialia,* 2006, Vol 54, p 665-669
96. K. Balani, A. Agarwal, S. Seal, and J. Karthikeyan, Transmission electron microscopy of cold sprayed 1100 aluminum coating. *Scripta Materialia,* 2005, Vol 53, p 845-850
97. K. Balani, T. Laha, A. Agarwal, J. Karthikeyan, and N. Munroe, Effect of carrier gases on microstructural and electrochemical behavior of cold-sprayed 1100 aluminum coating. *Surf. Coat. Technol.*, 2005, Vol 195, p 272-279
98. W.Y. Li, C.J. Li, and H.L. Liao, Effect of annealing treatment on the microstructure and properties of cold-sprayed Cu coating. *J. Therm. Spray Technol.*, 2006, Vol 15, p 206-211
99. E. Calla, D.G. McCartney, and P.H. Shipway, Effect of deposition conditions on the properties and annealing behavior of cold-sprayed copper. *J. Therm. Spray Technol.*, 2006, Vol 15, p 255-262
100. T. Van Steenkiste and D.W. Gorkiewicz, Analysis of tantalum coatings produced by the kinetic spray process. *J. Therm. Spray Technol.*, 2004, Vol 13, p 265-273

101. R.E. Blose, B.H. Walker, R.M. Walker, and S.H. Froes. Depositing titanium alloy additive features to forgings and extrusions using the cold spray process. in *International Thermal Spray Conference Proceedings*. 2006. Seattle, Washington, USA: ASM International.
102. J.W. Wu, J.G. Yang, H.Y. Fang, S. Yoon, and C. Lee, The bond strength of Al-Si coating on mild steel by kinetic spraying deposition. *Applied Surface Science,* 2006, Vol 252, p 7809-7814
103. R.S. Lima, J. Karthikeyan, C.M. Kay, J. Lindemann, and C.C. Berndt, Microstructural characteristics of cold-sprayed nanostructured WC-Co coatings. *Thin Solid Films,* 2002, Vol 416, p 129-135
104. S. Kuroda and T.W. Clyne, The Quenching Stress In Thermally Sprayed Coatings. *Thin Solid Films,* 1991, Vol 200, p 49-66
105. S.H. Leigh, C.K. Lin, and C.C. Berndt, Elastic response of thermal spray deposits under indentation tests. *J. Am. Ceram. Soc.,* 1997, Vol 80, p 2093-2099
106. J.P. Singh, M. Sutaria, and M. Ferber, Use of indentation technique to measure elastic modulus of plasma-sprayed zirconia thermal barrier coating. *Ceramic Engineering & Science Proceedings,* 1997, Vol 18, p 191-200
107. T.S. Price, P.H. Shipway, and D.G. McCartney, Effect of cold spray deposition of a titanium coating on fatigue behavior of a titanium alloy. *J. Therm. Spray Technol.,* 2006, Vol 15, p 507-512
108. T. Gnaeupel-Herold, H.J. Prask, J. Barker, F.S. Biancaniello, R.D. Jiggetts, and J. Matejicek, Microstructure, mechanical properties, and adhesion in IN625 air plasma sprayed coatings. *Mater. Sci. Eng. A,* 2006, Vol 421, p 77-85
109. M. Kachanov, I. Tsukrov, and B. Shafiro, Effective moduli of solids with cavities of various shapes. *Applied Mechanics Reviews,* 1994, Vol 47, p S151-S174
110. L.P. Chao, J.H. Huang, and Y.S. Huang, The influence of aspect ratio of voids on the effective elastic moduli of foamed metals. *Journal Of Composite Materials,* 1999, Vol 33, p 2002-2016
111. S.H. Leigh and C.C. Berndt, Modelling of elastic constants of plasma spray deposits with ellipsoid-shaped voids. *Acta Mater.,* 1999, Vol 47, p 1575-1586
112. I. Sevostianov and M. Kachanov, Modeling of the anisotropic elastic properties of plasma-sprayed coatings in relation to their microstructure. *Acta Mater.,* 2000, Vol 48, p 1361-1370
113. K.Y. Lee and D.R. Paul, A model for composites containing three-dimensional ellipsoidal inclusions. *Polymer,* 2005, Vol 46, p 9064-9080
114. J.D. Eshelby, The elastic field outside an ellipsoidal inclusion. *Proceedings Of The Royal Society Of London Series A-Mathematical And Physical Sciences,* 1959, Vol 252, p 561-569
115. J.D. Eshelby, The determination of the elastic field of an ellipsoidal inclusion, and related problems. *Proceedings Of The Royal Society Of London Series A-Mathematical And Physical Sciences,* 1957, Vol 241, p 376-396
116. T.W. Clyne and P.J. Withers, *An introduction to metal matrix composites*. 1993, Cambridge: Cambridge University Press.
117. *Methods of fatigue testing - part 2: Rotating bending fatigue tests*. 1962.
118. N.G. Turner and W.T. Roberts, Fatigue Behaviour of Titanium. *Transactions of the Metallurgical Society of AIME,* 1968, Vol 242, p 1223-1230

119. R.S. Bellows, S. Muju, and T. Nicholas, Validation of the step test method for generating Haigh diagrams for Ti-6Al-4V. *Int. J. Fatigue,* 1999, Vol 21, p 687-697
120. L. Wagner and J.K. Bigoney, Fatigue of Titanium Alloys, in *Titanium and Titanium Alloys: fundamentals and applications*, C. Leyens and M. Peters, Editors. 2003, Wiley-VCH: Weinheim, Germany. p 153-186.
121. K. Sakaki, Cold spray process - Overview and application trends, in *Designing, Processing And Properties Of Advanced Engineering Materials, Pts 1 And 2*. 2004. p 1305-1308.
122. E.P. Popov and T.A. Balan, *Engineering Mechanics of Solids*. 2nd ed. 1999, New Jersey: Prentice-Hall, Inc.
123. T.W. Clyne and S.C. Gill, Residual stresses in thermal spray coatings and their effect on interfacial adhesion: A review of recent work. *J. Therm. Spray Technol.,* 1996, Vol 5, p 401-418
124. L.C. Erickson, R. Westergard, U. Wiklund, N. Axen, H.M. Hawthorne, and S. Hogmark, Cohesion in plasma-sprayed coatings - A comparison between evaluation methods. *Wear,* 1998, Vol 214, p 30-37
125. F. Beltzung, G. Zambelli, E. Lopez, and A.R. Nicoll, Fracture-toughness measurement of plasma sprayed ceramic coatings. *Thin Solid Films,* 1989, Vol 181, p 407-415
126. E. Lopez, F. Beltzung, and G. Zambelli, Measurement Of Cohesion And Adhesion Strengths In Alumina Coatings Produced By Plasma Spraying. *J. Mater. Sci. Lett.,* 1989, Vol 8, p 346-348
127. M. Baleani, M. Viceconti, and A. Toni, The effect of sandblasting treatment on endurance properties of titanium alloy hip prostheses. *Artificial Organs,* 2000, Vol 24, p 296-299
128. D.C. Maxwell and T. Nicholas. A Rapid Method for Generation of a Haigh Diagram for High Cycle Fatigue. in *29th National Symposium on Fatigue and Fracture Mechanics*. 1999. Stanford, California, USA: ASM International.
129. S.R. Thompson, J.J. Ruschau, and T. Nicholas, Influence of residual stresses on high cycle fatigue strength of Ti-6Al-4V subjected to foreign object damage. *Int. J. Fatigue,* 2001, Vol 23, p S405-S412
130. T. Nicholas, Step loading for very high cycle fatigue. *Fatigue Fract. Eng. Mater. Struct.,* 2002, Vol 25, p 861-869
131. T. Fry. *Residual stress measurement: XRD depth profiling using successive material removal*. 2002 21st April[cited 2004 21st April]; Available from: http://midas.npl.co.uk/midas/content/ma34.html.
132. Y.T. Lee and G. Welsch, Youngs Modulus And Damping Of Ti-6al-4v Alloy As A Function Of Heat-Treatment And Oxygen Concentration. *Mater. Sci. Eng. A,* 1990, Vol 128, p 77-89
133. I. Manna and J.D. Majumdar, Enhanced kinetics of diffusion coating of aluminum on copper by boundary diffusion. *J. Mater. Sci. Lett.,* 1993, Vol 12, p 920-922
134. Y. Funamizu and K. Watanabe, Interdiffusion in Al-Cu system. *Transactions Of The Japan Institute Of Metals,* 1971, Vol 12, p 147-152
135. F.A. Calvo, A. Urena, J.M.G. Desalazar, and F. Molleda, Special features of the formation of the diffusion bonded joints between copper and aluminum. *J. Mater. Sci.,* 1988, Vol 23, p 2273-2280
136. G.E. Dieter, *Mechanical metallurgy*. 3rd ed. 1986, New York: McGraw-Hill.

137. D.A. Porter and K.E. Easterling, *Phase Transformations in Metals and Alloys*. 2nd ed. 1992, London: Chapman and Hall.
138. V.A. Joshi, *Titanium Alloys - An Atlas of Structures and Fracture Features*. 2006, Boca Raton, Florida: CRC Press.
139. E. Calla, D.G. McCartney, and P.H. Shipway. Effect of heat treatment on the structure and properties of cold sprayed copper. in *Thermal Spray 2005: Advances in Technology and Application*. 2005. Basel, Switzerland: DVS.
140. M.F. Ashby and D.R.H. Jones, *Engineering Materials 2: An introduction to microstructures, processing and design*. 2001, Woburn, USA: Butterworth-Heinemann.
141. B.B. Panigrahi, Sintering behaviour of Ti-2Ni and Ti-5Ni elemental powders. *Mater. Lett.*, 2007, Vol 61, p 152
142. M.M. Dewidar and J.K. Lim, Properties of solid core and porous surface Ti-6Al-4V implants manufactured by powder metallurgy. *Journal of Alloys and Compounds,* 2008, Vol 454, p 442
143. F.M. White, *Fluid Mechanics*. 4th ed. 1999, Singapore: McGraw Hill.
144. B.D. Cullity and S.R. Stock, *Elements of x-ray diffraction*. 3rd ed. 2001, New Jersey: Prentice Hill.
145. B. Eigenmann, B. Scholtes, and E. Macherauch, Determination of residual stresses in ceramics and ceramic-metal composites by x-ray diffraction methods. *Materials Science & Engineering,* 1989, Vol A118, p 1-17
146. O.T. Iancu, D. Munz, B. Eigenmann, B. Scholtes, and E. Macherauch, Residual-stress state of brazed ceramic metal-compounds, determined by analytical methods and x-ray residual-stress measurements. *J. Am. Ceram. Soc.,* 1990, Vol 73, p 1144-1149

Appendix 1

This appendix describes in greater detail determining the calculation of gas velocity whilst travelling within a de Laval nozzle and is primarily based on the text book "Compressible Fluid Flow" by Oosthuizen and Carscallen [58].

Background Knowledge

The perfect gas law states that [58]:

$$P = \rho RT \tag{A1}$$

The specific gas constant is determined by the specific heat with constant pressure and specific heat with constant volume of the gas.

$$R = C_p - C_v \tag{A2}$$

Manipulation of equation A1 shows that between two points of flow:

$$\frac{P_1}{\rho_1 T_1} = \frac{P_2}{\rho_2 T_2} \tag{A3}$$

When this is applied between the inlet and outlet of a differentially short control volume:

$$\frac{P}{\rho T} = \frac{P + dP}{(\rho + d\rho)(T + dT)} \tag{A4}$$

Rearrangement gives:

$$\frac{P}{\rho T} = \frac{1 + \frac{dP}{P}}{\left(1 + \frac{d\rho}{\rho}\right)\left(1 + \frac{dT}{T}\right)} \tag{A5}$$

And binomial expansion gives:

$$\frac{P}{\rho T} = \frac{P}{\rho T}\left(1 + \frac{dP}{P}\right)\left(1 - \frac{d\rho}{\rho}\right)\left(1 - \frac{dT}{T}\right) \tag{A6}$$

$$\frac{dP}{P} - \frac{d\rho}{\rho} - \frac{dT}{T} = 0 \tag{A7}$$

Equation A7 shows how the changes in pressure, density and temperature are interrelated in compressible flows. For a compressible fluid passing through a De Laval nozzle the flow is assumed as quasi one dimensional and isentropic.

Quasi One Dimensional Flow

Strictly speaking, the equation of one dimensional flow is only applicable to flow in a pipe of constant cross sectional area. However, the equations of one dimensional flow can still be used for many other situations, for example a de Laval nozzle, relatively accurately if the rate of change of area and the curvature are small enough for one component of the velocity vector to remain dominant over the other two components. Such flows, in which the flow area is changing but in which the flow at any section can be treated as one dimensional, are commonly referred to as quasi one-dimensional flows.

Isentropic Processes

An isentropic flow is a flow that is adiabatic and frictionless. Adiabatic means a reversible thermodynamic process that occurs without gain or loss of heat. It can therefore be stated that dQ_{rev}, the amount of reversible heat transfer, will be zero.

If we consider that the small change of entropy of a fluid, dS, it is defined as:

$$dS = \frac{dQ_{rev}}{T} \qquad \text{(A8)}$$

Therefore an isentropic process will also have no change in entropy, hence dS equals zero. As the flow is characterised as isentropic, an equation can be derived for the behaviour of the gas.

Classic Thermodynamics and Steady Flow Energy Equations

A thermodynamic system is that part of the universe that is under consideration. A real or imaginary boundary separates the system from the rest of the universe, which is referred to as the environment. A useful classification of thermodynamic systems is based on the nature of the boundary and the flows of matter, energy and entropy through it.

The enthalpy of a system, also known as heat content, is defined as the change in energy of a reaction. It is defined by the equation:

$$H = U + PV \tag{A9}$$

The change in enthalpy between two states is:

$$dH = dU + PdV + VdP \tag{A10}$$

The change in internal energy, U, of a system between two states is equal to the difference in heat transfer into the system and work done by the system:

$$dU = dQ + dW \tag{A11}$$

The work and heat transfer of the system depend on the process used to change the state. As there is constant pressure between the two states, the work done by the gas is given as:

$$dW = -PdV \tag{A12}$$

Inserting equations A11 and A12 into equation A10 gives:

$$dH = dQ + VdP \tag{A13}$$

By considering equation A10 again for a constant pressure process the change in enthalpy between two states is in fact:

$$dH = dU + PdV \tag{A14}$$

Equation A14 shows that the enthalpy and internal energy of a system change but the pressure remains constant. The change of enthalpy of a system is also equal to the heat transfer of a constant pressure process:

$$dH = C_p dT \tag{A15}$$

The steady flow energy equation is applied through a differentially short control volume. As flow is steady, the conservation of momentum requires that for this control volume the net force in direction x be equal to the rate at which momentum leaves the control volume in the x direction minus the rate at which it enters in the x direction. Gravitational forces are neglected. Therefore if a fluid enters at section 1

of the control volume with velocity u_1 and with enthalpy H_1 per unit mass, and leaves through section 2 with velocity u_2 and enthalpy H_2 then:

$$H_2 + \frac{u_2^2}{2} = H_1 + \frac{u_1^2}{2} + Q - W \qquad \text{(A16)}$$

Assuming no work is done and therefore W is zero and applying equation A15 to A16 gives:

$$C_p T_2 + \frac{u_2^2}{2} = C_p T_1 + \frac{u_1^2}{2} + Q \qquad \text{(A17)}$$

Applying this equation to the flow through a differentially short control volume gives:

$$C_p T + \frac{u^2}{2} + dQ = C_p (T + dT) + \frac{(u + du)^2}{2} \qquad \text{(A18)}$$

By neglecting higher order terms, i.e. If du^2 is neglected because the length of the control volume, dx, is very small then equation A18 becomes:

$$C_p dT + u du = dQ \qquad \text{(A19)}$$

Equation A19 indicates that in compressible flows, changes in velocity, will in general, include changes in temperature and that heat addition can cause velocity changes also.

If the flow is adiabatic then equation A16 gives:

$$C_p T_2 + \frac{u_2^2}{2} = C_p T_1 + \frac{u_1^2}{2} \qquad \text{(A20)}$$

And therefore equation A19 for an adiabatic flow would be:

$$C_p dT + u du = 0 \qquad \text{(A21)}$$

Equation A21 shows that in adiabatic flow, an increase in velocity will be accompanied by a decrease in temperature.

Entropy Considerations

The entropy of a flow must be considered as it places limitations on which flow processes are physically possible and which are physically excluded.

Combining equations A13 and A15 gives:

$$C_p dT = dQ + VdP \tag{A22}$$

Inserting equation A8 gives:

$$C_p dT = TdS + VdP \tag{A23}$$

Rearranging gives:

$$dS = C_p \frac{dT}{T} - \frac{V}{T} dP \tag{A24}$$

The equation of state for an ideal gas states:

$$PV = nRT \tag{A25}$$

By inserting equation A25 into equation A24:

$$dS = C_p \frac{dT}{T} - R\frac{dP}{P} \tag{A26}$$

Integrating between two points gives:

$$S_2 - S_1 = C_p \ln\left(\frac{T_2}{T_1}\right) - R\ln\left(\frac{P_2}{P_1}\right) \tag{A27}$$

For an isentropic process dS equals zero and therefore:

$$\ln\left(\frac{T_2}{T_1}\right) = \left(\frac{R}{C_p}\right)\ln\left(\frac{P_2}{P_1}\right) \tag{A28}$$

And therefore:

$$\frac{T_2}{T_1} = \left(\frac{P_2}{P_1}\right)^{\frac{R}{C_p}} \tag{A29}$$

The difference between the specific heats of a gas of constant pressure and constant volume equals the specific gas constant:

$$C_p - C_V = R \tag{A30}$$

Manipulation of equation A30 gives:

$$C_p - C_v = R$$

$$1 - \frac{C_v}{C_p} = \frac{R}{C_p}$$

$$1 - \frac{1}{\gamma} = \frac{R}{C_p}$$

$$\frac{\gamma - 1}{\gamma} = \frac{R}{C_p} \tag{A31}$$

Inserting equation A31 into A29 gives:

$$\frac{T_2}{T_1} = \left(\frac{P_2}{P_1}\right)^{\frac{\gamma-1}{\gamma}} \tag{A32}$$

Applying the perfect gas law to the right hand side of equation A32:

$$\frac{P_2}{P_1}\frac{\rho_1}{\rho_2} = \left(\frac{P_2}{P_1}\right)^{1}\left(\frac{P_2}{P_1}\right)^{-\frac{1}{\gamma}} \tag{A33}$$

And therefore:

$$\left(\frac{\rho_1}{\rho_2}\right)^{\gamma} = \frac{P_1}{P_2} \quad \text{and} \quad \frac{T_1}{T_2} = \left(\frac{\rho_1}{\rho_2}\right)^{\gamma-1} \tag{A34}$$

Therefore in isentropic flows $\frac{P}{\rho^{\gamma}}$ is a constant.

Applying equation A27 between the inlet and exit of a differentially short volume gives:

$$(S + dS) - S = C_p \ln\left(\frac{T + dT}{T}\right) - R \ln\left(\frac{P + dP}{P}\right) \tag{A35}$$

If ε is a small quantity, ln(1+ε) is to the first order equal to ε. Therefore equation A35 gives:

$$dS = C_p \frac{dT}{T} - R\frac{dP}{P} \tag{A36}$$

Insertion of equation A31 and manipulating gives:

$$\frac{dS}{C_p} = \frac{dT}{T} - \left(\frac{\gamma - 1}{\gamma}\right)\frac{dP}{P} \tag{A37}$$

For an isentropic flow equation A36 gives:

$$C_p dT = \frac{RT}{P} dP \tag{A38}$$

Using the perfect gas law (equation A1) and inserting into equation A38 gives:

$$C_p dT = \frac{dP}{\rho} \tag{A39}$$

However when considering an isentropic flow the energy equation (equation A21) which using equation A39 gives:

$$\frac{dP}{\rho} + udu = 0 \tag{A40}$$

Equation A40 is the same as would be calculated if conservation of momentum considerations were used. Thus by assuming isentropic flow of a gas, one of the conservation equations (energy or momentum) becomes redundant and it is not necessary to consider conservation of energy and conservation of momentum.

Mach Number

The Mach number is equal to the ratio of the gas velocity to the speed of sound in the gas.

$$Ma = \frac{u}{a} \tag{A41}$$

The speed of sound in a perfect gas is given by:

$$a = \sqrt{\gamma RT} \tag{A42}$$

If Ma<1 the flow is said to be subsonic, if Ma>1 then the flow is said to be supersonic. When the speed of gas is Ma=1 then:

$$u = \sqrt{\gamma RT} \tag{A43}$$

One Dimensional Isentropic Flow

By definition the change in entropy remains constant in an isentropic flow. Equations A33 and A34 state:

$$\frac{P_2}{P_1}\frac{\rho_1}{\rho_2} = \left(\frac{P_2}{P_1}\right)^{1}\left(\frac{P_2}{P_1}\right)^{-\frac{1}{\gamma}} \quad \text{and} \quad \left(\frac{\rho_1}{\rho_2}\right)^{\gamma} = \frac{P_1}{P_2} \quad \text{and} \quad \frac{T_1}{T_2} = \left(\frac{\rho_1}{\rho_2}\right)^{\gamma-1}$$

Using equation A42 it follows that:

$$\frac{a_2}{a_1} = \left(\frac{T_2}{T_1}\right)^{\frac{1}{2}} = \left(\frac{\rho_2}{\rho_1}\right)^{\frac{\gamma-1}{2}} = \left(\frac{P_2}{P_1}\right)^{\frac{\gamma-1}{2\gamma}} \tag{A44}$$

Equations A44 are called the isentropic state relationships. Then by considering energy conservation between two points (Equation A20):

$$C_p T_1 + \frac{u_1^2}{2} = C_p T_2 + \frac{u_2^2}{2}$$

Combining equations A44 and A20 gives:

$$\frac{T_2}{T_1} = \frac{1 + \frac{\left(u_1^2\right)}{2C_p T_1}}{1 + \frac{\left(u_2^2\right)}{2C_p T_2}} \tag{A45}$$

But:

$$\frac{u^2}{2C_p T} = \left[\frac{u^2}{2\gamma RT}\right]\left[\frac{\gamma R}{C_p}\right] = \frac{\gamma - 1}{2} Ma^2 \tag{A46}$$

And therefore:

$$\frac{T_2}{T_1} = \frac{1+\frac{1}{2}(\gamma-1)Ma_1^2}{1+\frac{1}{2}(\gamma-1)Ma_2^2} \tag{A47}$$

This equation applies in adiabatic flow. As the flow is regarded as isentropic, friction effects are negligible. Therefore using equations A47 and A43 the pressure and density of the gas can be found in terms of the Mach number at points one and two similar to the equation above for the gas temperature.

$$\frac{P_2}{P_1} = \left[\frac{1+\frac{1}{2}(\gamma-1)Ma_1^2}{1+\frac{1}{2}(\gamma-1)Ma_2^2}\right]^{\frac{\gamma}{\gamma-1}} \quad \text{and} \quad \frac{\rho_2}{\rho_1} = \left[\frac{1+\frac{1}{2}(\gamma-1)Ma_1^2}{1+\frac{1}{2}(\gamma-1)Ma_2^2}\right]^{\frac{1}{\gamma-1}} \tag{A48}$$

The continuity equation gives

$$\left(\frac{\rho_1}{\rho_2}\right)\left(\frac{u_2}{u_1}\right) = \frac{A_1}{A_2}$$

The above equations are, together, sufficient to determine the characteristics of one-dimensional isentropic flow in terms of the associated mach number of the gas.

Stagnation Conditions

Stagnation conditions exist isentropically when the flow is brought to rest. A large reservoir of gas can be considered as possessing stagnation conditions. Stagnation conditions are denoted with the subscript $_0$, for example P_0, T_0, ρ_0.

Critical Conditions

Critical conditions for an isentropic flow exist when the mach number equals one. Critical conditions are denoted by an asterisk, for example P*, T*, ρ*. Using equations A47 and A48 and setting Ma_2 to 1, relationships for the critical conditions can be found:

$$\frac{T^*}{T} = \left[\frac{2}{\gamma+1} + \frac{\gamma-1}{\gamma+1}Ma^2\right] \tag{A49}$$

$$\frac{a^*}{a} = \left[\frac{2}{\gamma+1} + \frac{\gamma-1}{\gamma+1}Ma^2\right]^{\frac{1}{2}} \quad \text{(A50)}$$

$$\frac{P^*}{P} = \left[\frac{2}{\gamma+1} + \frac{\gamma-1}{\gamma+1}Ma^2\right]^{\frac{\gamma}{\gamma-1}} \quad \text{(A51)}$$

$$\frac{\rho^*}{\rho} = \left[\frac{2}{\gamma+1} + \frac{\gamma-1}{\gamma+1}Ma^2\right]^{\frac{1}{\gamma-1}} \quad \text{(A52)}$$

By then setting Ma to zero in equations A49 to A52 the relationship between the critical and stagnation conditions can be found:

$$\frac{T^*}{T_0} = \frac{2}{\gamma+1} \quad \text{(A53)}$$

$$\frac{a^*}{a_0} = \sqrt{\frac{2}{\gamma+1}} \quad \text{(A54)}$$

$$\frac{P^*}{P_0} = \left(\frac{2}{\gamma+1}\right)^{\frac{\gamma}{\gamma-1}} \quad \text{(A55)}$$

$$\frac{\rho^*}{\rho_0} = \left(\frac{2}{\gamma+1}\right)^{\frac{1}{\gamma-1}} \quad \text{(A56)}$$

Variable Area Flow

To calculate the affect of a flow passing through a variable cross sectional area duct we assume:

i) Isentropic flow.

ii) Flow is one dimensional at all areas along the duct ie. cross section does not change rapidly with distance along the duct.

iii) Steady flow rate.

A steady flow rate means that within the duct [143]:

$$\rho(x)A(x)u(x) = \dot{m} = \text{mass flow rate} = \text{constant} \qquad \text{(A57)}$$

The differential form of equation A57 is:

$$\frac{d\rho}{\rho} + \frac{dA}{A} + \frac{du}{u} = 0 \qquad \text{(A58)}$$

The speed of sound of a fluid is defined as:

$$a^2 = \frac{dP}{d\rho} \qquad \text{(A59)}$$

The isentropic energy flow, equation A40, states:

$$\frac{dP}{\rho} + udu = 0$$

By eliminating dP and dρ between equations A59 and A40 to obtain the following relationship between velocity change and area change in an isentropic duct flow [143].

$$\frac{du}{u} = \frac{dA}{A}\frac{1}{Ma^2 - 1} = -\frac{dP}{\rho u^2} \qquad \text{(A60)}$$

This equation shows property changes are of opposite sign for subsonic and supersonic flow because of the term Ma^2-1. There are four combinations of area change and Mach number summarised below.

i) dA > 0 (Increasing duct area) and Ma < 1 (Subsonic)

Then du < 0 (deceleration) and dp > 0 (Increasing pressure)

ii) dA > 0 (Increasing duct area) and Ma > 1 (Supersonic)

Then du > 0 (acceleration) and dp < 0 (Decreasing pressure)

iii) dA < 0 (Decreasing duct area) and Ma < 1 (Subsonic)

Then du > 0 (acceleration) and dp < 0 (Decreasing pressure)

iv) dA < 0 (Decreasing duct area) and Ma > 1 (Supersonic)

Then $du < 0$ (deceleration) and $dp > 0$ (Increasing pressure)

For the case of a De Laval nozzle option ii) occurs after the gas has passed through the throat of the nozzle. This will cause the gas to continue acceleration as it passes along the nozzle.

Area-Mach Relationships

Fluid flow originating from a large reservoir is assumed to have stagnation conditions exist in the reservoir. The equations governing the flow at some arbitrary section, 1, is the continuity equation:

$$\rho_1 u_1 A_1 = \dot{m} \tag{A61}$$

And the energy equation:

$$u_1^2 + \frac{2}{(\gamma - 1)} a_1^2 = \frac{2}{(\gamma - 1)} a_0^2 \tag{A62}$$

Or

$$u_1^2 = \left(\frac{2}{\gamma - 1}\right) a_0^2 \left[1 - \left(\frac{a_1}{a_0}\right)^2\right] \tag{A63}$$

Also the isentropic relations apply at all points throughout the duct (equation A44):

$$\frac{a_1}{a_0} = \left(\frac{T_1}{T_0}\right)^{\frac{1}{2}} = \left(\frac{\rho_1}{\rho_0}\right)^{\frac{\gamma-1}{2}} = \left(\frac{P_1}{P_0}\right)^{\frac{\gamma-1}{2\gamma}}$$

Combining equations A63 and A44 gives:

$$u_1 = \left\{\left(\frac{2a_0^2}{\gamma - 1}\right) 1 - \left(\frac{P_1}{P_0}\right)^{\frac{\gamma-1}{\gamma}}\right\}^{\frac{1}{2}} \tag{A64}$$

Which becomes:

$$u_1 = \left\{ \left(\frac{2\gamma}{\gamma - 1} \right) \left(\frac{P_0}{\rho_0} \right) \left[1 - \left(\frac{P_1}{P_0} \right)^{\frac{\gamma-1}{\gamma}} \right] \right\}^{\frac{1}{2}} \tag{A65}$$

Substituting equation A65 into equation A61 and then using the isentropic relations gives:

$$\dot{m} = \rho_0 u_1 A_1 \frac{\rho_1}{\rho_0}$$

$$\dot{m} = \rho_0 A_1 \left(\frac{P_1}{P_0} \right)^{\frac{1}{\gamma}} \left\{ \left(\frac{2\gamma}{\gamma - 1} \right) \left(\frac{P_0}{\rho_0} \right) \left[1 - \left(\frac{P_1}{P_0} \right)^{\frac{\gamma-1}{\gamma}} \right] \right\}^{\frac{1}{2}} \tag{A66}$$

As the mass flow rate is constant across the duct, equation A66 can be used to relate the pressure at any point in the duct to the area. So if subscript 2 refers to any point along the duct then:

$$\dot{m} = \rho_0 A_2 \left(\frac{P_2}{P_0} \right)^{\frac{1}{\gamma}} \left\{ \left(\frac{2\gamma}{\gamma - 1} \right) \left(\frac{P_0}{\rho_0} \right) \left[1 - \left(\frac{P_2}{P_0} \right)^{\frac{\gamma-1}{\gamma}} \right] \right\}^{\frac{1}{2}} \tag{A67}$$

Dividing equation A67 by A66 gives:

$$\frac{A_2}{A_1} = \left(\frac{P_1}{P_2} \right)^{\frac{1}{\gamma}} \left[\frac{1 - \left(\frac{P_1}{P_0} \right)^{\frac{\gamma-1}{\gamma}}}{1 - \left(\frac{P_2}{P_0} \right)^{\frac{\gamma-1}{\gamma}}} \right]^{\frac{1}{2}} \tag{A68}$$

Equation A68 relates the pressures at any two sections of the duct to the areas of the respective sections.

Equation A68 can be related to a point in the duct where Ma=1, i.e., the critical conditions. There may not actually be a point in the duct where Ma=1, but the conditions at such a point are convenient to use for reference purposes. Expressions

for the pressure and velocity at Ma=1 have been previously derived (Equations A53 to A56).

$$a^{*2} = \frac{2}{\gamma+1} a_0^2 \tag{A54}$$

Another way of writing this is:

$$\left(\frac{a^*}{a_0}\right)^2 = \frac{T^*}{T_0} = \frac{2}{\gamma+1} \tag{A69}$$

Using the isentropic relations allows equation A69 to be written as:

$$\frac{P^*}{P_0} = \left(\frac{2}{\gamma+1}\right)^{\frac{2}{\gamma-1}} \tag{A70}$$

Substituting equation A70 into A67 gives, with rearrangement:

$$A^* = \frac{\dot{m}}{\sqrt{\gamma P_0 \rho_0}} \left(\frac{2}{\gamma+1}\right)^{-\frac{\gamma+1}{2(\gamma-1)}} \tag{A71}$$

The area at any point within the duct, expressed in terms of A*, can be related to the pressure by substituting equation A70 into equation A68. With manipulation this gives:

$$\frac{A}{A^*} = \frac{\left(\frac{2}{\gamma+1}\right)^{\frac{\gamma+1}{2(\gamma-1)}} \left(\frac{\gamma-1}{2}\right)^{\frac{1}{2}}}{\left\{\left(\frac{P}{P_0}\right)^{\frac{2}{\gamma}} - \left(\frac{P}{P_0}\right)^{\frac{\gamma+1}{\gamma}}\right\}^{\frac{1}{2}}} \tag{A72}$$

Applying equations A65, A66 and A72 it is possible to generate an equation relating the exit throat duct area and the overall pressure ratio (P_e/P_0)

$$u_e = \left\{\left(\frac{2\gamma}{\gamma-1}\right)\left(\frac{P_0}{\rho_0}\right)\left[1 - \left(\frac{P_e}{P_0}\right)^{\frac{\gamma-1}{\gamma}}\right]\right\}^{\frac{1}{2}} \tag{A73}$$

$$\dot{m} = \rho_0 A_e \left(\frac{P_e}{P_0}\right)^{\frac{1}{\gamma}} \left\{ \left(\frac{2\gamma}{\gamma-1}\right)\left(\frac{P_0}{\rho_0}\right)\left[1-\left(\frac{P_e}{P_0}\right)^{\frac{\gamma-1}{\gamma}}\right]\right\}^{\frac{1}{2}} \tag{A74}$$

This can be rearranged to give:

$$A^* = \frac{\dot{m}}{\sqrt{\gamma P_0 \rho_0}} \left(\frac{2}{\gamma+1}\right)^{-\frac{\gamma+1}{2(\gamma-1)}} \tag{A75}$$

$$\frac{A_e}{A^*} = \frac{\left(\frac{2}{\gamma+1}\right)^{\frac{\gamma+1}{2(\gamma-1)}}\left(\frac{\gamma-1}{2}\right)^{\frac{1}{2}}}{\left\{\left(\frac{P_e}{P_0}\right)^{\frac{2}{\gamma}}-\left(\frac{P_e}{P_0}\right)^{\frac{\gamma+1}{\gamma}}\right\}^{\frac{1}{2}}} \tag{A76}$$

Equation A73 to A76 allow the exit velocity, exit cross sectional area and the throat area to be found. It would also be convenient to express the variable area relations in terms of the mach number, Ma. Equation A62 gives:

$$u_1^2 + \frac{2}{(\gamma-1)}a_1^2 = \frac{2}{(\gamma-1)}a_0^2$$

Which gives:

$$u_1 = Ma_0\left\{1+\left(\frac{\gamma-1}{2}\right)Ma_1^2\right\}^{-\frac{1}{2}} \tag{A77}$$

Using the energy equations and the isentropic relations gives:

$$\left(\frac{a}{a_0}\right)^2 = \left\{1+\left(\frac{\gamma-1}{2}\right)Ma^2\right\}^{-1} \tag{A78}$$

And

$$\left(\frac{\rho}{\rho_0}\right) = \left\{1+\left(\frac{\gamma-1}{2}\right)Ma^2\right\}^{-\frac{1}{\gamma-1}} \tag{A79}$$

Due to constant mass flow rate, equation A61, and using equations A77 to A79 it follows that:

$$\frac{\dot{m}}{A} = \frac{\rho_0 A_0 Ma}{\left\{1+\left(\frac{\gamma-1}{2}\right)Ma^2\right\}^{\frac{\gamma+1}{2(\gamma-1)}}} \qquad \text{(A80)}$$

Applying equation A80 between any two points within the duct where the mass flow rate must be the same we get:

$$\frac{A_2}{A_1} = \left(\frac{Ma_1}{Ma_2}\right)\left\{\frac{1+\left(\frac{\gamma-1}{2}\right)Ma_2^2}{1+\left(\frac{\gamma-1}{2}\right)Ma_1^2}\right\}^{\frac{\gamma+1}{2(\gamma-1)}} \qquad \text{(A81)}$$

Writing this equation in terms of the cross sectional area at where the critical conditions exist (where Ma=1) gives:

$$\left(\frac{A}{A^*}\right) = \frac{1}{Ma}\left[\frac{2}{\gamma+1}\left(1+\frac{\gamma-1}{2}Ma^2\right)\right]^{\frac{\gamma+1}{2(\gamma-1)}} \qquad \text{(A82)}$$

Equation A82 is called the area-Mach number relation and shows that the Mach number at any location in the duct is a function of the local duct area to the sonic throat area. This equation also allows the throat area to be calculated for sonic flow to occur if all other variables are known.

Appendix 2

To convert from a volumetric size distribution to a number size distribution the following equation is used:

$$Num = \frac{Vol\%}{BinVol} \tag{A83}$$

The number of particles measured within each bin, *Num*, is calculated by dividing, *Vol%,* the volume percent of particles for that bin (the original data output from the laser diffractometer), with, *BinVol*, the volume of a single particle of diameter equal to the mid-point of the bin range. The number percent of particles found for each bin range may then be calculated by dividing the number of particles for each bin with the total number of particles of all bin ranges. A summary of the volumetric size distribution data for the copper powder and the conversion process to a number distribution is shown in Table A1.

Bin Range / µm	Mid-point of Bin / µm	Volume of Single Particle / μm^3	Vol%	Vol% / Volume of Single Particle	Num%
2.26 - 2.49	2.4	7.0	0.0	0.005	1.6
2.49 - 2.75	2.6	9.4	0.1	0.007	2.1
2.75 - 3.03	2.9	12.7	0.1	0.008	2.5
3.03 - 3.34	3.2	17.0	0.2	0.010	3.2
3.34 - 3.69	3.5	22.7	0.3	0.013	4.2
3.69 - 4.07	3.9	30.5	0.5	0.016	5.1
4.07 - 4.48	4.3	40.9	0.8	0.019	5.9
4.48 - 4.94	4.7	54.8	1.1	0.021	6.6
4.94 - 5.45	5.2	73.5	1.7	0.023	7.4
5.45 - 6.01	5.7	98.6	2.5	0.025	8.0
6.01 - 6.63	6.3	132.1	3.5	0.027	8.4
6.63 - 7.31	7.0	177.2	4.7	0.027	8.4
7.31 - 8.06	7.7	237.6	5.9	0.025	7.9
8.06 - 8.89	8.5	318.5	7.0	0.022	7.0
8.89 - 9.80	9.3	427.0	7.9	0.019	5.9
9.80 - 10.81	10.3	572.5	8.4	0.015	4.7
10.81 - 11.92	11.4	767.6	8.7	0.011	3.6
11.92 - 13.14	12.5	1029.2	8.9	0.009	2.7
13.14 - 14.49	13.8	1379.8	8.4	0.006	1.9
14.49 - 15.98	15.2	1850.1	7.2	0.004	1.2
15.98 - 17.62	16.8	2480.5	6.0	0.002	0.8
17.62 - 19.42	18.5	3325.7	4.9	0.001	0.5
19.42 - 24.42	20.4	4458.9	3.7	0.001	0.3
24.42 - 23.62	22.5	5978.0	2.6	0.000	0.1
23.62 - 26.04	24.8	8015.0	1.8	0.000	0.1
26.04 - 28.72	27.4	10746.1	1.2	0.000	0.0
28.72 - 31.67	30.2	14408.2	0.3	0.000	0.0
31.67 - 34.92	33.3	19317.9	0.0	0.000	0.0
34.92 - 38.50	36.7	25899.9	0.0	0.000	0.0

Table A1– Conversion process from the volumetric size distribution, produced by the laser diffractometer, to a number size distribution for the spherical copper powder.

Appendix 3

This section comprises of a selection of plots of the raw particle velocity data. The raw particle velocity data plotted within this appendix are shown in Table A2.

Powder	Gas Type	Stand Off Distance	Stagnation Pressure	Corresponding Fig. Nos.	
Copper +5-25 µm	Helium	20 mm	10 bar	Figure 3.25(a)	Figure A1
			29 bar	Figure 3.25(a)	Figure A2
		1 mm	29 bar	Figure 3.27(a)	Figure A3
	Nitrogen	20 mm	10 bar	Figure 3.25(b)	Figure A4
			29 bar	Figure 3.25(b)	Figure A5
		1 mm	29 bar	Figure 3.27(b)	Figure A6
Titanium +5-45 µm	Helium	20 mm	10 bar	Figure 3.30(a)	Figure A7
			29 bar	Figure 3.30(b)	Figure A8

Table A2 – Table of process parameters that raw particle velocity data is available for and shown in this appendix. All measurements are made at a y-axis position of 0 mm.

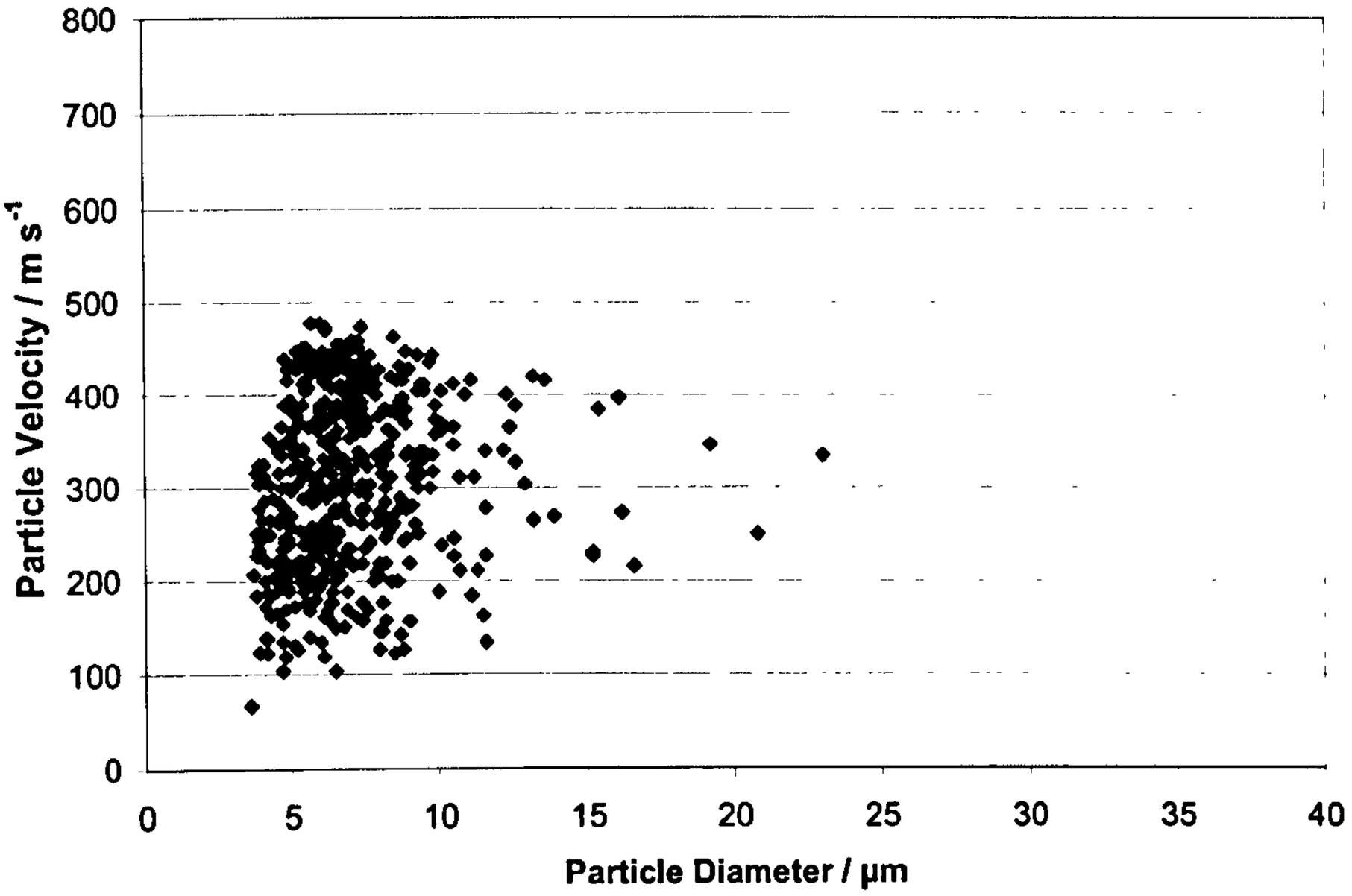

Figure A1 – Influence of particle diameter on particle velocity for the +5 -25 µm copper powder travelling with a helium gas flow at stagnation pressure 10 bar. Data for 500 individual particles was collected at a stand off distance of 20 mm and within the centre of the gas plume.

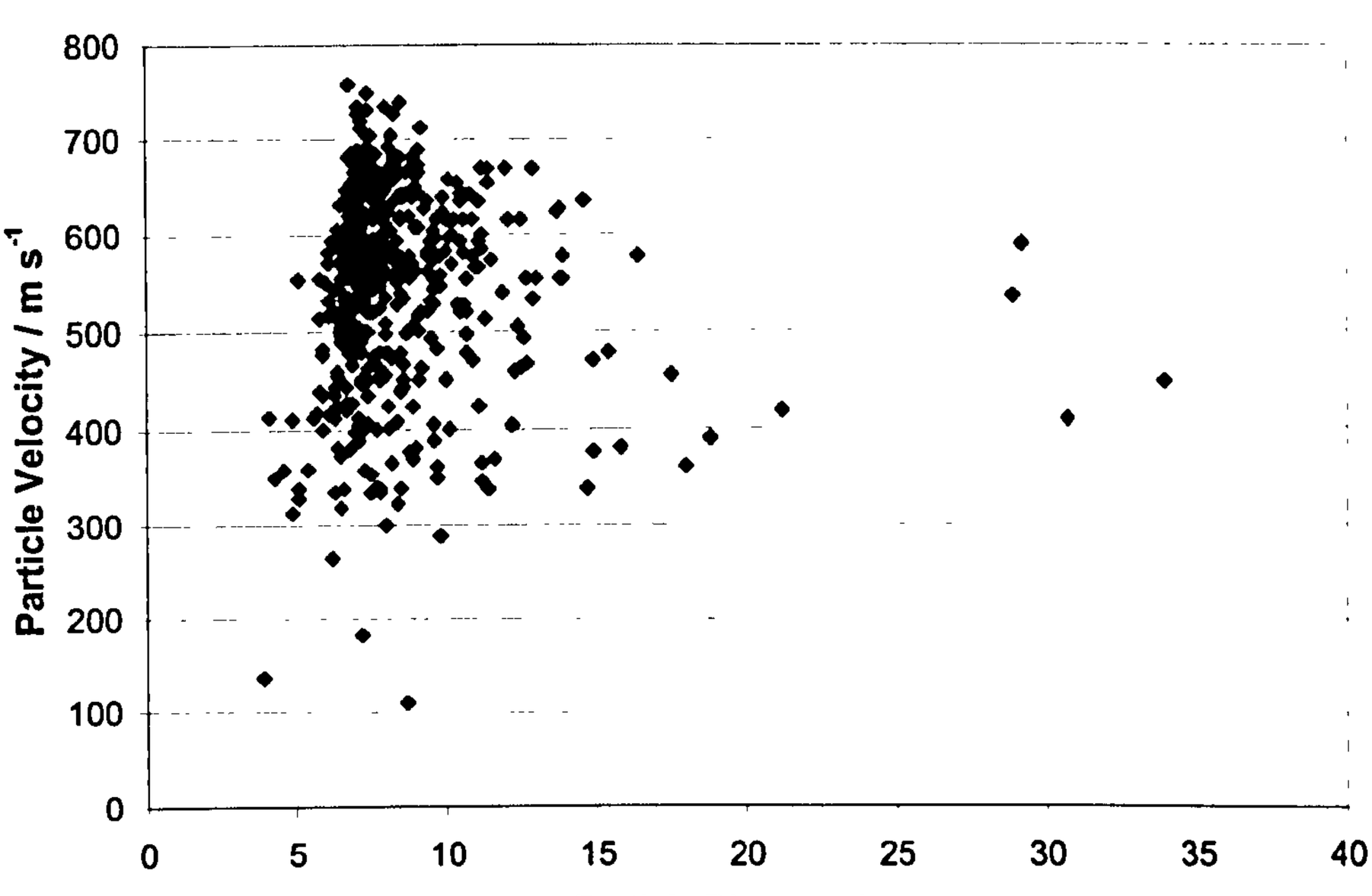

Figure A2 – Influence of particle diameter on particle velocity for the +5 -25 µm copper powder travelling with a helium gas flow at stagnation pressure 29 bar. Data for 500 individual particles was collected at a stand off distance of 20 mm and within the centre of the gas plume.

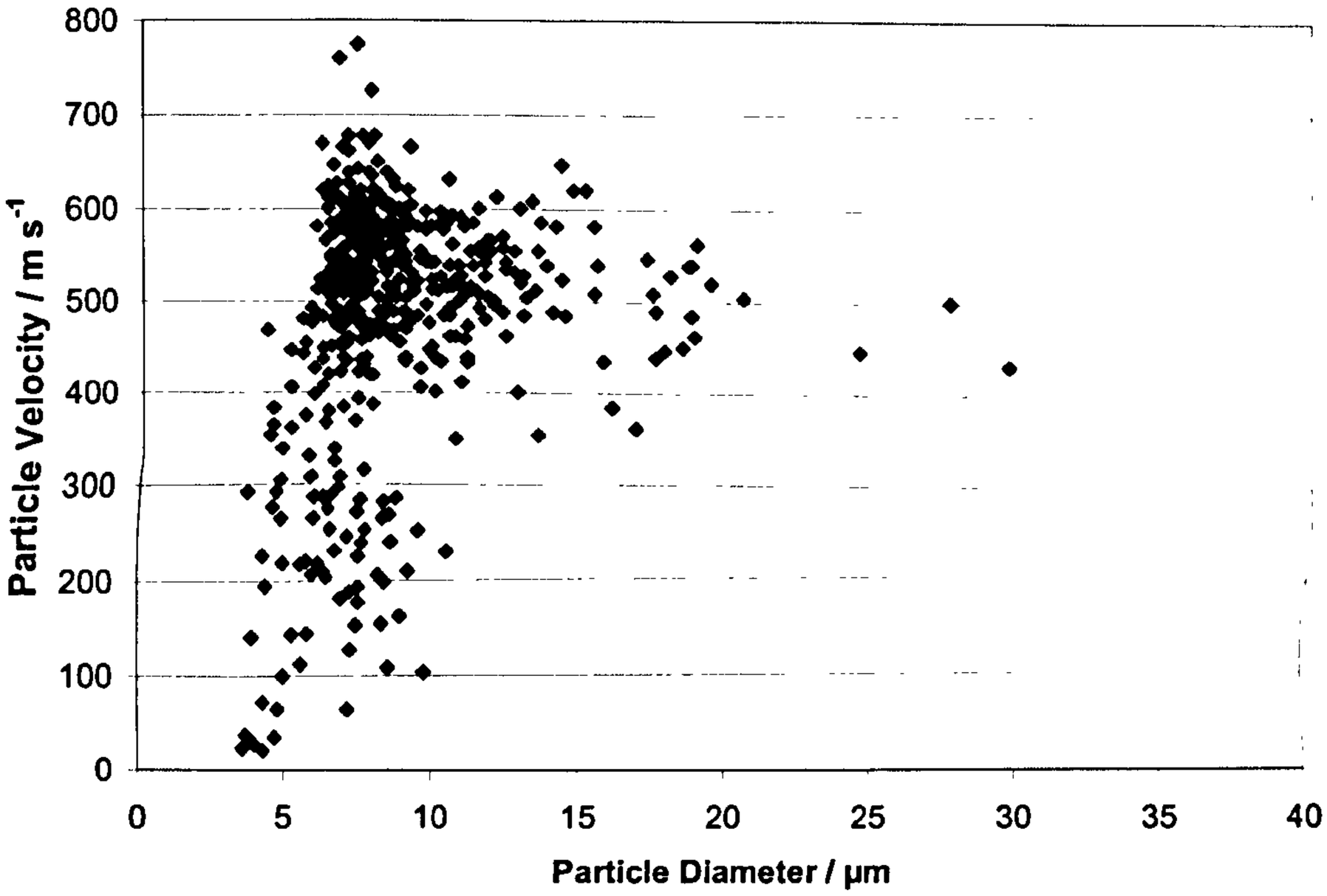

Figure A3 – Influence of particle diameter on particle velocity for the +5 -25 µm copper powder travelling with a helium gas flow at stagnation pressure 29 bar. Data for 500 individual particles was collected at a stand off distance of 1 mm and within the centre of the gas plume.

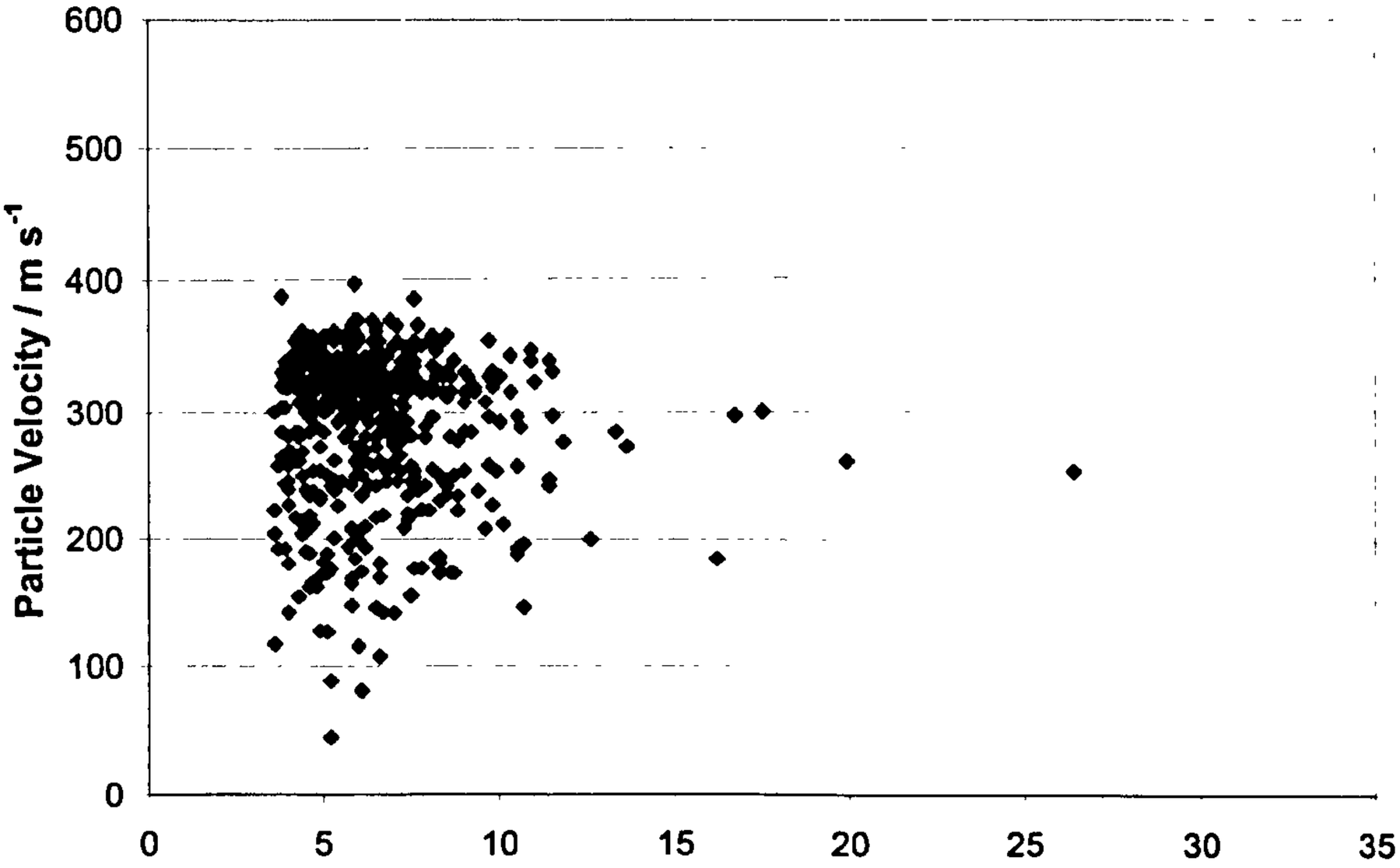

Figure A4 – Influence of particle diameter on particle velocity for the +5 -25 µm copper powder travelling with a nitrogen gas flow at stagnation pressure 10 bar. Data for 500 individual particles was collected at a stand off distance of 20 mm and within the centre of the gas plume.

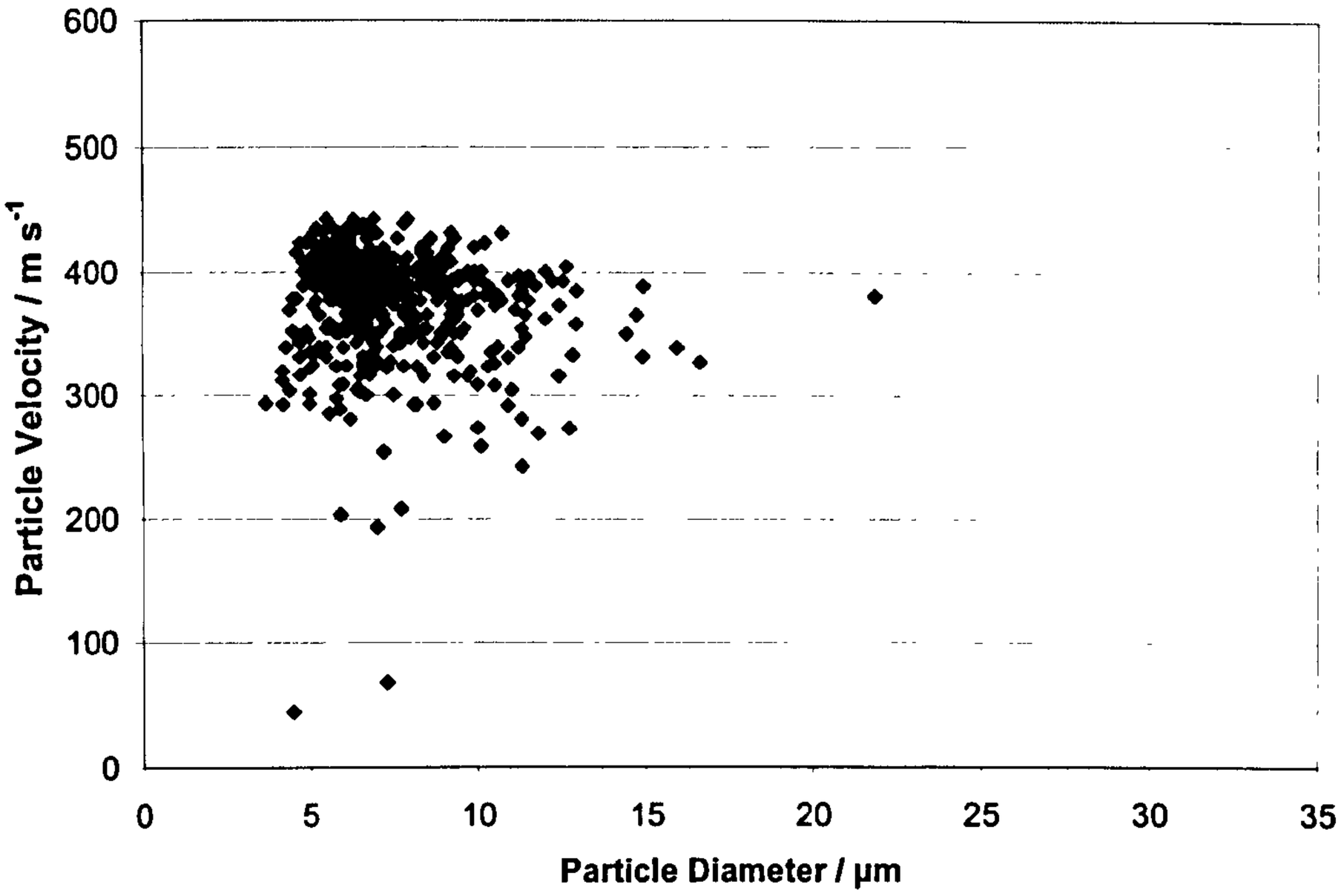

Figure A5 – Influence of particle diameter on particle velocity for the +5 -25 µm copper powder travelling with a nitrogen gas flow at stagnation pressure 29 bar. Data for 500 individual particles was collected at a stand off distance of 20 mm and within the centre of the gas plume.

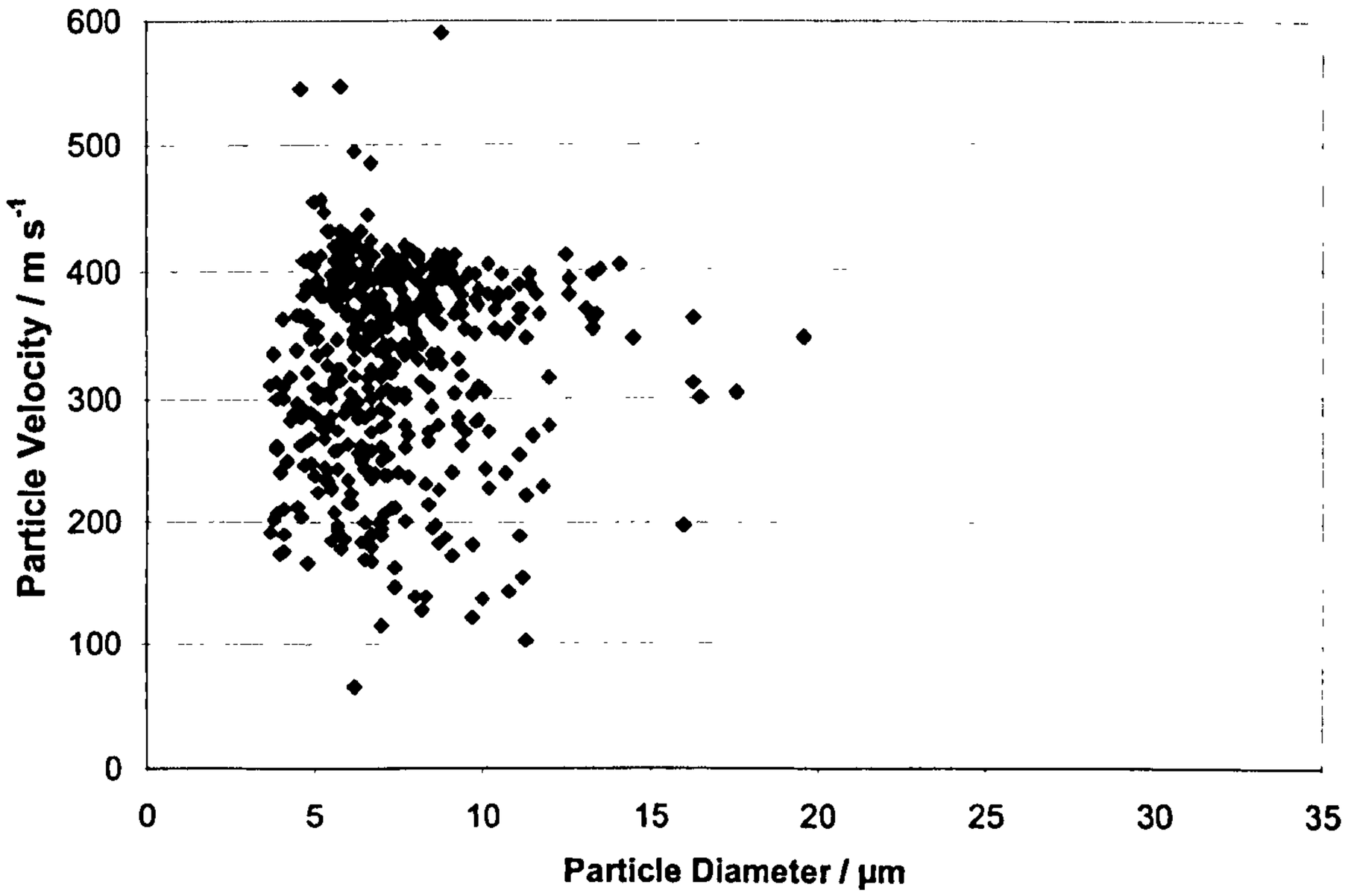

Figure A6 – Influence of particle diameter on particle velocity for the +5 -25 µm copper powder travelling with a nitrogen gas flow at stagnation pressure 29 bar. Data for 500 individual particles was collected at a stand off distance of 1 mm and within the centre of the gas plume.

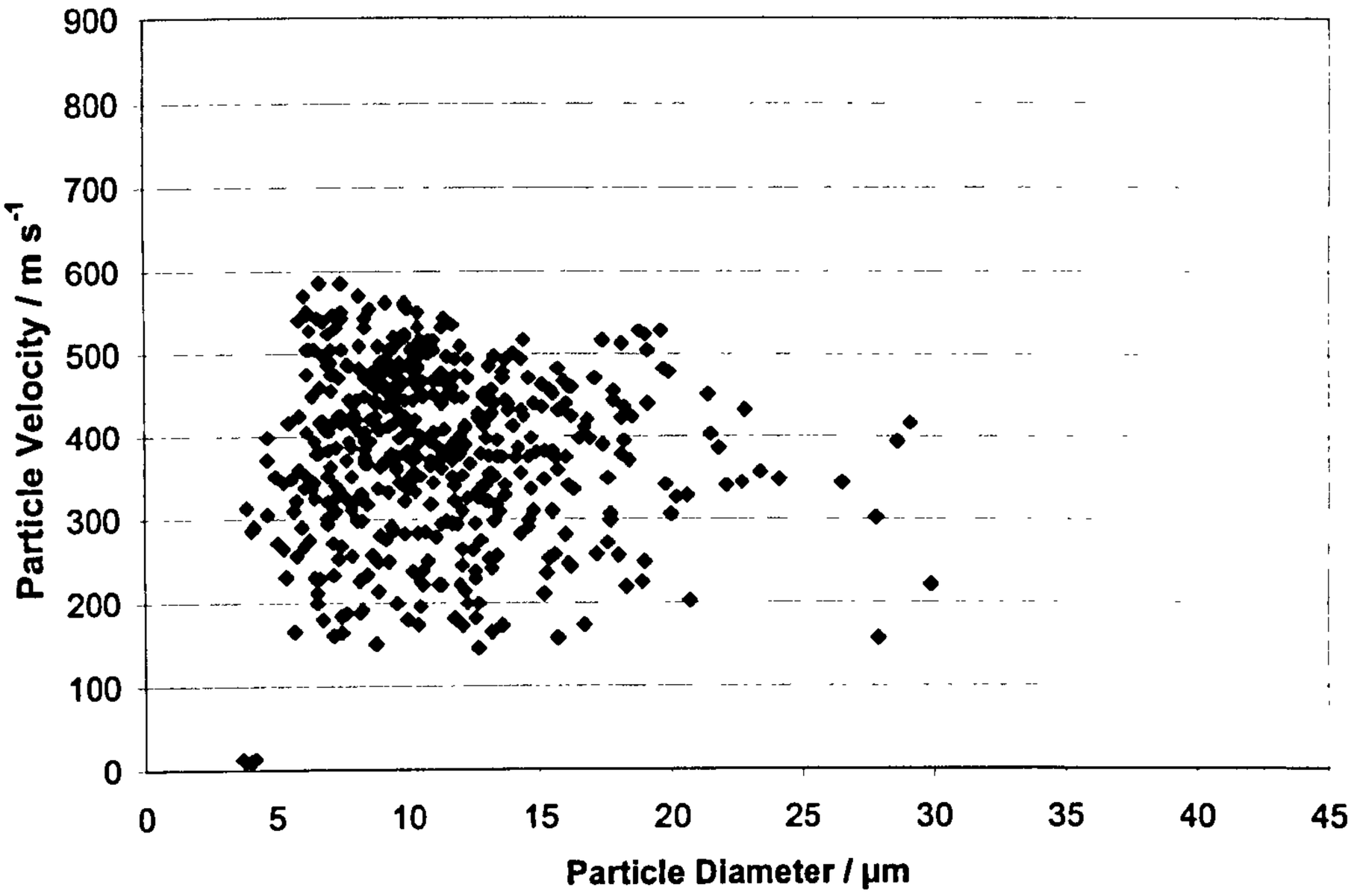

Figure A7 – Influence of particle diameter on particle velocity for the +5 -45 µm titanium powder travelling with a helium gas flow at stagnation pressure 10 bar. Data for 500 individual particles was collected at a stand off distance of 20 mm and within the centre of the gas plume.

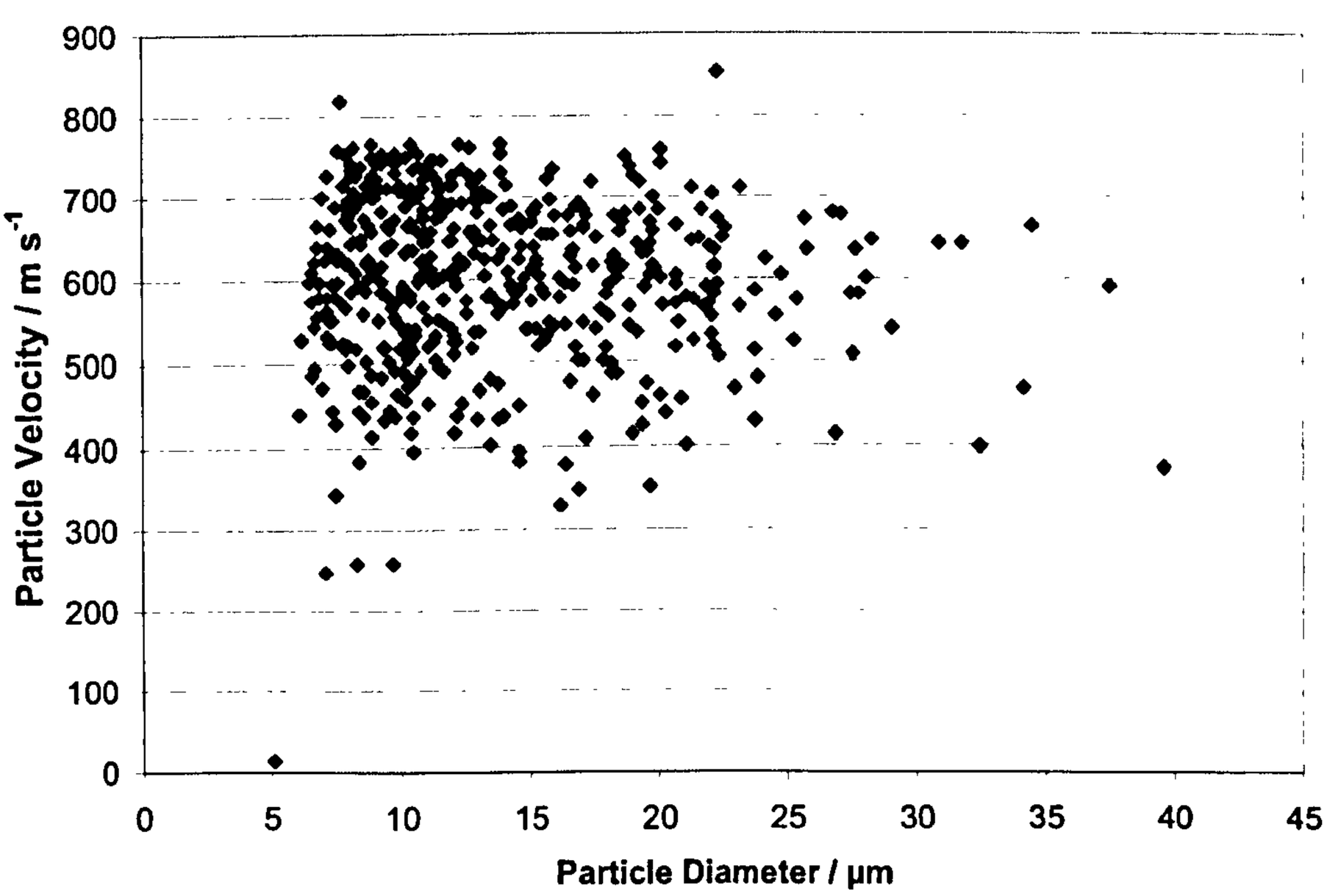

Figure A8 – Influence of particle diameter on particle velocity for the +5 -45 µm titanium powder travelling with a helium gas flow at stagnation pressure 29 bar. Data for 500 individual particles was collected at a stand off distance of 20 mm and within the centre of the gas plume.

Appendix 4

This section explains the theory behind calculating residual stresses using X-ray diffractometry. Figure A9 shows a bar in tension having stress acting upon it, σ_y, which produces a strain, ε_y, given by:

$$\varepsilon_y = \frac{\Delta L}{L} = \frac{L_f - L_o}{L_o} \tag{A84}$$

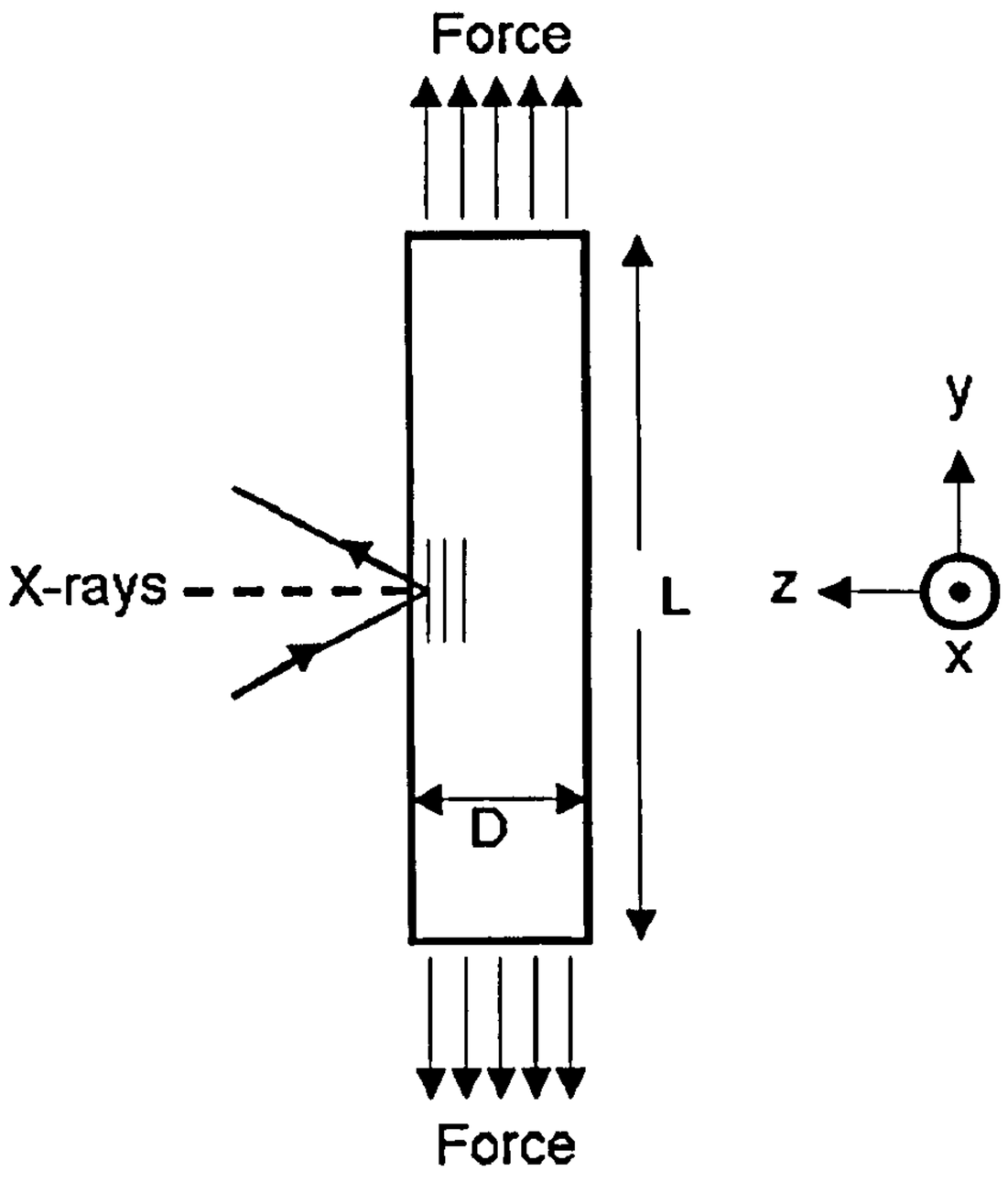

Figure A9 – Bar in pure tension, with diffraction planes parallel to axis [144].

Where L_f and L_o and the final and original lengths of the bar. Strain is related to the stress by:

$$\sigma_y = E\varepsilon_y \tag{A85}$$

Where E is the Young's modulus of the bar. The strains in the x and z directions are given by:

$$\varepsilon_x = \varepsilon_z = \frac{D_f - D_o}{D_o} \tag{A86}$$

Where D_f and D_o and the final and original diameters of the bar. If the bar is isotropic, these strains are related by the equation:

$$\varepsilon_x = \varepsilon_z = \upsilon - \varepsilon_y \tag{A87}$$

Where ν is the Poisson's ratio for the material. ε_z can be measured by x-rays by detecting the variation in spacing between crystal lattice planes before and during a force is applied. It can be shown that:

$$\varepsilon_z = \frac{d_n - d_o}{d_o} \qquad \text{(A88)}$$

Where d_n is the spacing of the planes parallel to the bar axis under stress, and d_o is the spacing of the same planes in the absence of stress [144]. Combining equations A85, A87 and A88 gives:

$$\sigma_y = -\frac{E}{\upsilon}\left(\frac{d_n - d_o}{d_o}\right) \qquad \text{(A89)}$$

Equation A89 requires the precise measurement of d_o, the distance between crystal plane lattices when no stress is applied. For a sample with residual stresses this is not possible. It is not sufficient to use d_o values from materials handbooks due to even a small variation in levels of impurities will influence the d_o parameter.

Often analysis is required on a plane surface and not a cylindrical rod. The calculations described above have to be altered to apply to a plane surface where a biaxial or even triaxial stress system will often occur. No longer looking at a rod (as described previously), but a surface along the planes of the principal axis, x and y, as shown by Figure A10. It may be assumed that a state of plane stress exists, ie σ_z=0, and that the stresses are biaxial, therefore:

$$\varepsilon_x = \varepsilon_y = -\upsilon\varepsilon_z = \frac{-\upsilon\sigma_y}{E} \qquad \text{(A90)}$$

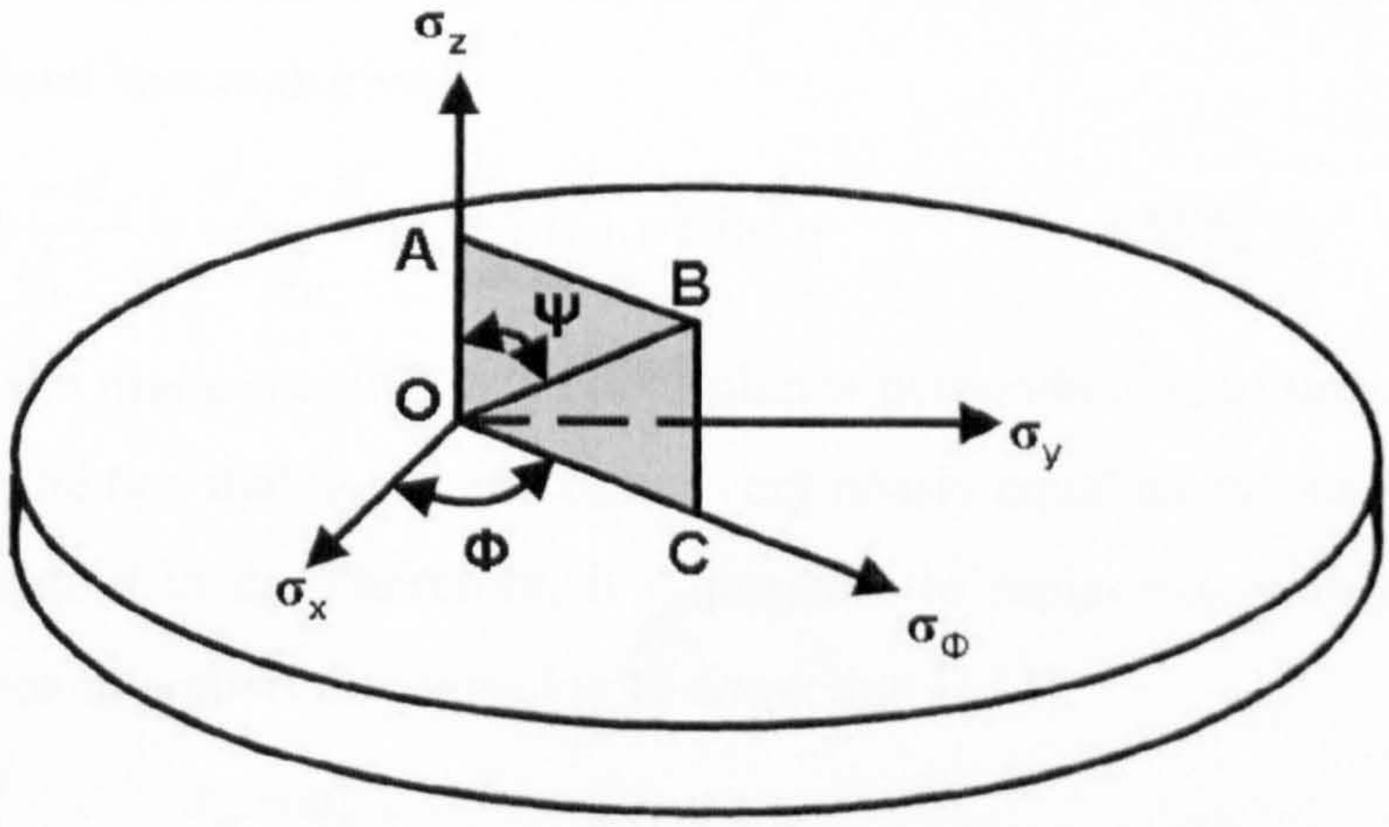

Figure A10 – Residual stresses at the surfaces of a stressed body. $\sigma_z = 0$. The stress to be measured is σ_Φ [144].

If we assume at the surface of the material, where the x-ray measurement is considered to be made, that σ_z=0 then:

$$\varepsilon_z = -\upsilon(\varepsilon_x + \varepsilon_y) = -\frac{\upsilon}{E}(\sigma_x + \sigma_y) \qquad \text{(A91)}$$

Combining equations A89 and A91 gives:

$$\frac{d_n - d_o}{d_o} = -\frac{\upsilon}{E}(\sigma_x + \sigma_y) \qquad \text{(A92)}$$

Similar to equation A89, equation A92 also requires the precise measurement of d_o. It is not guaranteed that the maximum stress within the sample will lie along one of the principal axis. Therefore when carrying out residual stress measurements, using x-ray diffractometry, the sample must be examined for various Φ angles as shown by Figure A10. When a single stress in some direction along the surface, σ_Φ, as shown by Figure A10, the line OC is measured. By tilting the sample the spacings of crystal planes at various Ψ angles can be measured. In the case of the angle Ψ, shown in Figure A10, spacings of crystal planes perpendicular to line OB will be calculated. Elasticity theory for an isotropic solid shows that the strain along an inclined line, ε_ψ (Figure A10), is [144-146]:

$$\varepsilon_\psi = \frac{1+\upsilon}{E}\sigma_\phi \sin^2\psi - \frac{\upsilon}{E}(\sigma_x + \sigma_y) \qquad \text{(A93)}$$

Subtraction of equation A91 from A93 gives:

$$\varepsilon_\psi - \varepsilon_z = \frac{\sigma_\phi}{E}(1+\upsilon)\sin^2\psi \qquad \text{(A94)}$$

Equation A94 shows that the difference between two strains in a stressed specimen depends only on the stress acting in the plane of those strains. Expressing the strains in terms of plane spacings gives:

$$\frac{d_\psi - d_o}{d_o} - \frac{d_n - d_o}{d_o} = \frac{d_\psi - d_o}{d_o} = \frac{\sigma_\phi}{E}(1+\upsilon)\sin^2\psi \qquad \text{(A95)}$$

Where d_Ψ is the plane spacing for crystal planes perpendicular to line OB in Figure A10. Due to the fact that d_Ψ, d_n and d_o are very nearly equal to one another, $(d_\Psi - d_n)$ is small compared to d_o. Therefore, it is possible to replace d_o with d_Ψ or d_n with negligible error. It is therefore possible to show that [144]:

$$\sigma_\phi = \frac{E}{(1+\upsilon)\sin^2\psi}\left(\frac{d_\psi - d_n}{d_n}\right) \qquad \text{(A96)}$$

The most commonly used method for stress determination is the $sin^2\psi$ method. A number of XRD measurements are made at different ψ angles between 0 and 45 degrees. The inter-planar spacing or 2θ peak position is measured and plotted on a graph of d values against $sin^2\psi$. By assuming that σ_z=0 then the gradient of the line produced can be used to calculate the residual stress in the specimen with knowledge of the elastic constants of the specimen.

$$\sigma_\phi = \left(\frac{E}{1+\upsilon}\right)m \tag{A97}$$

Where m is the gradient of the slope.